

# **Numerical Investigation on the Performance of Double Layered H-Rotor Darrieus Turbine**

*Submitted by*

**S.M. Rakibul Hassan**

*Student ID: 0413102055*

*Supervisor*

**Dr. Mohammad Ali**

*Professor*

*Department of Mechanical Engineering.*

*A thesis submitted to the*

*Department of Mechanical Engineering*

*in partial fulfillment of the requirements for the degree*

*of*

**MASTER OF SCIENCE IN MECHANICAL ENGINEERING**



**BANGLADESH UNIVERSITY OF ENGINEERING AND  
TECHNOLOGY, DHAKA**



**NUMERICAL INVESTIGATION ON THE PERFORMANCE OF  
DOUBLE LAYERED H-ROTOR DARRIEUS TURBINE**

Submitted by

**S.M. Rakibul Hassan**

Student ID: 0413102055

Supervisor

**Dr. Mohammad Ali**

Professor

Department of Mechanical Engineering

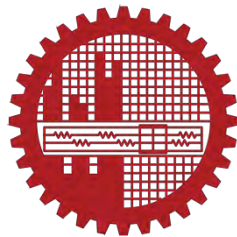
*A thesis submitted to the*

*Department of Mechanical Engineering*

*in partial fulfillment of the requirements for the degree*

*of*

MASTER OF SCIENCE IN MECHANICAL ENGINEERING



Department of Mechanical Engineering






**BANGLADESH UNIVERSITY OF ENGINEERING AND TECHNOLOGY,  
DHAKA**

**February, 2018**



The thesis titled “Numerical Investigation on the Performance of Double Layered H-Rotor Darrieus Turbine” submitted by S.M. RAKIBUL HASSAN, Roll No.: 0413102055, Session: April 2013 has been accepted as satisfactory in partial fulfillment of the requirements for the degree of Master of Science in Mechanical Engineering on 17 February, 2018.

#### BOARD OF EXAMINERS

-   
1 Dr. Mohammad Ali  
Professor  
Dept. of Mechanical Engineering,  
Bangladesh University of Engineering and Technology,  
Dhaka-1000  
Chairman  
(Supervisor)
-   
2 Dr. Mohammad Ali  
Professor & Head of the Dept. of Mechanical  
Engineering  
Bangladesh University of Engineering and Technology,  
Dhaka-1000  
Member  
(Ex- Officio)
-   
3 Dr. Mohammad Arif Hasan Mamun  
Professor  
Dept. of Mechanical Engineering,  
Bangladesh University of Engineering and Technology,  
Dhaka-1000  
Member
-   
4 Dr. Mohammad Mamun  
Professor  
Dept. of Mechanical Engineering,  
Bangladesh University of Engineering and Technology,  
Dhaka-1000  
Member
-   
5 Dr. Md. Quamrul Islam  
Professor  
Dept. of Mechanical Engineering,  
Military Institute of Science and Technology, Mirpur  
Cantonment, Dhaka  
Member  
(External)

## DECLARATION

The contents presented herein are the result of an M.Sc. thesis performed at Bangladesh University of Engineering and Technology (BUET), Dhaka. It has been done by S.M. Rakibul Hassan (Student No. 0413102055) under the supervision of Professor Dr. Mohammad Ali and has not been submitted anywhere for the award of any degree or diploma.

*S.M. Rakibul Hassan*

**S.M. Rakibul Hassan**

Student ID: 0413102055

**Supervisor:**

**Dr. Mohammad Ali**

Professor

Department of Mechanical Engineering

BUET

## **ACKNOWLEDGMENT**

I would like to express my heartfelt gratitude, sincere appreciation and great indebtedness to my honorable thesis supervisor Professor Dr. Mohammad Ali, Department of Mechanical Engineering, BUET for his valuable suggestions, inspiration, encouragement and support throughout the Thesis.

I am grateful to the Department of Mechanical Engineering, BUET for providing all the facilities to perform this thesis. I devote sincere gratitude to the numerous researchers for paving the pathway for me by sharing their knowledge and experience on respective fields.

## ABSTRACT

Performance of wind turbine has been investigated for a long period of time. As a result, the design of both Horizontal Axis Wind Turbine and Vertical Axis Wind Turbine has been improved. However, still there is opportunity to increase its efficiency. The Vertical Axis Wind Turbine (VAWT) has the advantage over Horizontal Axis Wind Turbine (HAWT) for working on omnidirectional air flow without any additional control system. A double layered H-rotor Darrieus type VAWT is investigated numerically in this thesis, which is a lift based wind turbine. The effect of solidity (i.e. chord length x no. of blades / radius of turbine) on power coefficient ( $C_p$ ) of H-rotor for different tip speed ratios has been numerically simulated and studied. The study has been conducted using unsteady RANS equations and SST  $k-\omega$  turbulence model. SIMPLE algorithm is used for pressure-velocity coupling and the second order upwind discretization scheme is chosen for getting accurate solution. Different parameters are compared, which depict the performance of the double layered H-rotor Darrieus type VAWT. The double layered H-Darrieus VAWT is found to be a higher speed lower torque machine compared to the single layered H-Darrieus VAWT, which can generate power at higher maximum power coefficient for higher solidity vertical axis wind turbines. Double Layered staggered H-Darrieus VAWT offers more stable power coefficient than the Double Layered in-line H-Darrieus VAWT with solidity  $\zeta=1.5$  near the tip speed ratio for maximum power coefficient.



## TABLE OF CONTENTS

<b>DECLARATION.....</b>	<b>iii</b>
<b>ACKNOWLEDGMENT .....</b>	<b>iv</b>
<b>ABSTRACT.....</b>	<b>v</b>
<b>TABLE OF CONTENTS.....</b>	<b>vi</b>
<b>LIST OF FIGURES .....</b>	<b>ix</b>
<b>LIST OF TABLES .....</b>	<b>xiv</b>
<b>NOMENCLATURE.....</b>	<b>xv</b>
<b>INTRODUCTION.....</b>	<b>1</b>
1.1 Introduction.....	2
1.2 Motivation.....	6
1.3 Scope and Objectives.....	6
1.4 Outline of the research.....	7
<b>BACKGROUND LITERATURE.....</b>	<b>8</b>
<b>THEORY .....</b>	<b>14</b>
3.1. Aerodynamic Forces .....	15
3.1.1 Drag force .....	15
3.1.2 Lift .....	17
3.1.3 Normal force or Radial Force .....	17
3.1.4 Tangential force .....	18
3.2 Dimensionless Parameters .....	19
3.2.1 Reynolds Number .....	19
3.2.2 Drag Coefficient .....	20
3.2.3 Torque Coefficient.....	21
3.2.4 Power Coefficient .....	22
3.2.5 Solidity.....	22
3.2.6 Tip Speed Ratio .....	23
3.3 Relation between the Angle of Attack and Angle of Rotation of Blade.....	23
3.4 Theories for Performance Analysis of Vertical Axis Wind Turbine .....	24
3.5 Blade Element Theory .....	24
3.6 Single Streamtube Model.....	28
3.7 Double Multiple Stream Tube Theory .....	29
3.7.1 Single layered H-rotor VAWT .....	30
3.7.2 Double layered H-rotor VAWT .....	31

<b>MATHEMATICAL MODELING.....</b>	<b>34</b>
4.1 Governing equations .....	35
4.1.1 Continuity equation .....	35
4.1.2 Momentum equation.....	35
4.1.3 Reynolds Average Navier-Stokes Equation.....	36
4.2 Finite Volume Method and Staggered Grid.....	37
4.3 Second order upwind discretization scheme .....	39
4.4 SIMPLE Pressure-Velocity Coupling.....	40
4.5 Under-relaxation Factor .....	42
4.6 Shear Stress Transport (SST) $k-\omega$ Turbulence Modeling .....	42
<b>COMPUTATIONAL MODEL .....</b>	<b>46</b>
5.1 Geometric Model .....	47
5.2 Computational Domain.....	48
5.3 Mesh Generation.....	48
5.4 Boundary Conditions .....	50
5.5 Numerical Method .....	51
<b>RESULTS AND DISCUSSIONS .....</b>	<b>53</b>
6.1 Validation and Grid independence Test.....	54
6.1.1 Validation .....	54
6.1.2 Grid Independence Test.....	55
6.2 Performance of Single Layered H-Darrieus Vertical Axis Wind Turbine.....	56
6.2.1 Relationship between torque coefficient and tip speed ratio .....	56
6.2.2 Relationship between power coefficient and tip speed ratio.....	58
6.2.3 Relationship between torque coefficient and angle of rotation.....	60
6.2.4 Velocity Contour and Velocity Vectors.....	63
6.2.5 Pressure Contour.....	75
6.2.6 Lift and Drag Coefficient.....	79
6.3 Performance of Double Layered H-Darrieus Vertical Axis Wind Turbine .....	80
6.3.1 Relationship between torque coefficient and tip speed ratio .....	80
6.3.2 Relationship between power coefficient and tip speed ratio.....	82
6.3.3. Contribution of inner and outer layer to the power coefficient.....	83
6.3.4 Relationship between torque coefficient and angle of rotation.....	87
6.3.5 Velocity Contour and Velocity Vectors.....	90
6.3.6 Pressure Contour.....	112
6.3.7 Lift and Drag Coefficient.....	116
6.4 Comparison between single layered and double layered H-Darrieus VAWT .....	116

6.5 Performance of Double Layered H-Darrieus VAWT with Staggered Layers .....	119
6.5.1 Relationship between torque coefficient and tip speed ratio .....	119
6.5.2 Relationship between power coefficient and tip speed ratio.....	120
6.5.3. Contribution of inner and outer layer blades to the power coefficient .....	121
6.5.4 Relationship between torque coefficient and angle of rotation.....	123
6.5.5 Velocity Contour and Velocity Vectors.....	124
6.5.6 Pressure Contour.....	131
6.5.7 Lift and Drag Coefficient.....	133
<b>CONCLUSION.....</b>	<b>134</b>
7.1 Conclusion .....	135
<b>RECOMMENDATIONS: .....</b>	<b>137</b>
<b>REFERENCES.....</b>	<b>138</b>

## LIST OF FIGURES

<b>Fig. 1.1:</b> Different types of horizontal axis wind turbine [1] .....	2
<b>Fig. 1.2:</b> Different Type of Vertical Axis Wind Turbine [1] .....	3
<b>Fig. 1.3:</b> Comparison of Power Coefficient of Different Wind Turbines .....	4
<b>Fig. 1.4:</b> Wind Data .....	6
<b>Fig. 1.5:</b> Wind Turbine (a) Single Layered VAWT (b) Double Layered in-line VAWT (c) Double Layered Staggered VAWT .....	7
<b>Fig. 3.1:</b> Aerodynamic forces on an airfoil .....	17
<b>Fig. 3.2:</b> Normal and Tangential force on a wind turbine blade .....	18
<b>Fig. 3.3:</b> Velocity and force components on a wind turbine blade (airfoil) .....	18
<b>Fig. 3.4:</b> Forces and velocities in a H-rotor Darrieus turbine [23] .....	23
<b>Fig. 3.5:</b> $\alpha$ vs. $\theta$ at different value of $\lambda$ .....	24
<b>Fig. 3.6:</b> Elemental Force Element on a Blade Element of H-rotor VAWT .....	25
<b>Fig. 3.7:</b> Velocity diagram on the blade element of H-rotor VAWT .....	25
<b>Fig. 3.8:</b> Single stream tube model for single layered Vertical Axis Wind Turbine .....	28
<b>Fig. 3.9:</b> Double multiple stream tube model for single layered rotor showing velocities and angle .....	30
<b>Fig. 3.10:</b> Double Multiple Stream Tube Model for double layered Vertical Axis H-Darrieus Turbine .....	31
<b>Fig. 4.1:</b> Staggered Grid [25] .....	38
<b>Fig. 4.2:</b> Second Order Discretization Scheme .....	39
<b>Fig. 4.3:</b> Flow Chart for SIMPLE pressure velocity coupling method .....	41
<b>Fig. 5.1:</b> Geometric Model of Vertical Axis Wind Turbine (a) 3 Bladed, Single Layered (b) 6 Bladed, Double Layered (In-line) (c) 6 Bladed, Double Layered (Staggered) .....	47
<b>Fig. 5.2:</b> Computational Domain of Vertical Axis Wind Turbine[15] .....	48
<b>Fig. 5.3:</b> Generated Mesh (a) full domain (b) mesh near interface zone (c) around airfoil (d) very close to airfoil .....	49
<b>Fig 5.4:</b> Boundary Types .....	50
<b>Fig. 6.1:</b> (a) Comparison of $C_p$ vs. $\lambda$ curve for validation .....	54
<b>Fig. 6.2:</b> Grid Independence Test .....	55
<b>Fig. 6.3:</b> $C_t$ vs. $\lambda$ for single layered 3 bladed H-rotor VAWT .....	56
<b>Fig. 6.4:</b> $C_p$ vs. $\lambda$ for single layered 3 bladed VAWT .....	60
<b>Fig. 6.5:</b> $C_t$ vs. $\theta$ for $\zeta=0.5$ Single layered H-Darrieus VAWT (max $C_p$ at $\lambda =3.25$ ) .....	61
<b>Fig. 6.6:</b> $C_t$ vs. $\theta$ for $\zeta=0.7$ Single layered H-Darrieus VAWT (max $C_p$ at $\lambda =2.5$ ) .....	62
<b>Fig. 6.7:</b> $C_t$ vs. $\theta$ for $\zeta=1.0$ Single layered H-Darrieus VAWT (max $C_p$ at $\lambda =2.25$ ) .....	62
<b>Fig. 6.8:</b> Velocity contour of 3 Bladed Single layered H – Rotor VAWT; Solidity 0.5, $\lambda=3.25$ (0 degree) .....	63
<b>Fig. 6.9:</b> Velocity contour of 3 Bladed Single layered H – Rotor VAWT; Solidity 0.5, $\lambda=3.25$ (60 degree) .....	64
<b>Fig. 6.10:</b> Velocity contour of 3 Bladed Single layered H – Rotor VAWT; Solidity 0.7, $\lambda=2.5$ (0 degree) .....	64
<b>Fig. 6.11:</b> Velocity contour of 3 Bladed Single layered H – Rotor VAWT; Solidity 0.7, $\lambda= 2.5$ (60 degree) .....	65
<b>Fig. 6.12:</b> Velocity contour of 3 Bladed Single layered H – Rotor VAWT; Solidity 1.0, $\lambda=2.25$ (0 degree) .....	65
<b>Fig. 6.13:</b> Velocity contour of 3 Bladed Single layered H – Rotor VAWT; Solidity 1.0, $\lambda=2.25$ (60 degree) .....	66
<b>Fig. 6.14(a):</b> Velocity vector of 3 Bladed Single layered H – Rotor VAWT; Solidity 0.5, $\lambda=3.25$ (blade at 0 degree) .....	66
<b>Fig. 6.14(b):</b> Velocity vector of 3 Bladed Single layered H – Rotor VAWT; Solidity 0.5, $\lambda=3.25$ (blade at 60 degree) .....	67
<b>Fig. 6.14(c):</b> Velocity vector of 3 Bladed Single layered H – Rotor VAWT; Solidity 0.5, $\lambda=3.25$ (blade at 120 degree) .....	67

<b>Fig. 6.14(d):</b> Velocity vector of 3 Bladed Single layered H – Rotor VAWT; Solidity 0.5, $\lambda=3.25$ (blade at 180 degree) .....	68
<b>Fig. 6.14(e):</b> Velocity vector of 3 Bladed Single layered H – Rotor VAWT; Solidity 0.5, $\lambda=3.25$ (blade at 240 degree) .....	68
<b>Fig. 6.14(f):</b> Velocity vector of 3 Bladed Single layered H – Rotor VAWT; Solidity 0.5, $\lambda=3.25$ (blade at 300 degree) .....	69
<b>Fig. 6.15(a):</b> Velocity vector of 3 Bladed Single layered H – Rotor VAWT; Solidity 0.7, $\lambda= 2.5$ (blade at 0 degree) .....	69
<b>Fig. 6.15(b):</b> Velocity vector of 3 Bladed Single layered H – Rotor VAWT; Solidity 0.7, $\lambda= 2.5$ (blade at 60 degree) .....	70
<b>Fig. 6.15(c):</b> Velocity vector of 3 Bladed Single layered H – Rotor VAWT; Solidity 0.7, $\lambda= 2.5$ (blade at 120 degree) .....	70
<b>Fig. 6.15(d):</b> Velocity vector of 3 Bladed Single layered H – Rotor VAWT; Solidity 0.7, $\lambda= 2.5$ (blade at 180 degree) .....	71
<b>Fig. 6.15(e):</b> Velocity vector of 3 Bladed Single layered H – Rotor VAWT; Solidity 0.7, $\lambda= 2.5$ (blade at 240 degree) .....	71
<b>Fig. 6.15(f):</b> Velocity vector of 3 Bladed Single layered H – Rotor VAWT; Solidity 0.7, $\lambda= 2.5$ (blade at 300 degree) .....	72
<b>Fig. 6.16(a):</b> Velocity vector of 3 Bladed Single layered H – Rotor VAWT; Solidity 1.0, $\lambda=2.25$ (blade at 0 degree) .....	72
<b>Fig. 6.16(b):</b> Velocity vector of 3 Bladed Single layered H – Rotor VAWT; Solidity 1.0, $\lambda=2.25$ (blade at 60 degree) .....	73
<b>Fig. 6.16(c):</b> Velocity vector of 3 Bladed Single layered H – Rotor VAWT; Solidity 1.0, $\lambda=2.25$ (blade at 120 degree) .....	73
<b>Fig. 6.16(d):</b> Velocity vector of 3 Bladed Single layered H – Rotor VAWT; Solidity 1.0, $\lambda=2.25$ (blade at 180 degree) .....	74
<b>Fig. 6.16(e):</b> Velocity vector of 3 Bladed Single layered H – Rotor VAWT; Solidity 1.0, $\lambda=2.25$ (blade at 240 degree) .....	74
<b>Fig. 6.16(f):</b> Velocity vector of 3 Bladed Single layered H – Rotor VAWT; Solidity 1.0, $\lambda=2.25$ (blade at 300 degree) .....	75
<b>Fig. 6.17:</b> Pressure contour of 3 Bladed single layered H – Rotor VAWT; Solidity 0.5 at $\lambda=3.25$ .....	76
<b>Fig. 6.18:</b> Pressure contour of 3 Bladed single layered H – Rotor VAWT; Solidity 0.7, $\lambda=2.5$ .....	77
<b>Fig. 6.19:</b> Pressure contour of 3 Bladed single layered H – Rotor VAWT; Solidity 1.0, $\lambda=2.25$ .....	78
<b>Fig 6.20:</b> $C_l$ and $C_d$ vs. $\theta$ for Double Layered (In-line) H-Darrieus VAWT; Solidity 1.0 at $\lambda=2.25$ .....	79
<b>Fig. 6.21:</b> $C_l$ vs. $\lambda$ for double layered 6 bladed H-rotor VAWT .....	80
<b>Fig. 6.22:</b> $C_p$ vs. $\lambda$ for double layered 6 bladed VAWT .....	83
<b>Fig. 6.23:</b> Inner layer power coefficient, outer layer power coefficient and total power coefficient for $\zeta=0.75$ .....	84
<b>Fig. 6.24:</b> Inner layer power coefficient, outer layer power coefficient and total power coefficient for $\zeta=1.05$ .....	85
<b>Fig. 6.25:</b> Inner layer power coefficient, outer layer power coefficient and total power coefficient for $\zeta=1.0$ .....	86
<b>Fig. 6.26:</b> $C_l$ vs. $\theta$ for $\zeta=0.5$ Double layered H-Darrieus VAWT (max $C_p$ at $\lambda =4.0$ ) .....	87
<b>Fig. 6.27:</b> $C_l$ vs. $\theta$ for $\zeta=1.05$ Double layered H-Darrieus VAWT (max $C_p$ at $\lambda =3.75$ ) .....	88
<b>Fig. 6.28:</b> $C_l$ vs. $\theta$ for $\zeta=1.5$ Double layered H-Darrieus VAWT (max $C_p$ at $\lambda = 3.0$ ) .....	88
<b>Fig. 6.29:</b> Velocity contour of 6 Bladed Double layered H – Rotor VAWT; Solidity 0.75, $\lambda=4.5$ (0 degree) .....	91
<b>Fig. 6.30:</b> Velocity contour of 6 Bladed Double layered H – Rotor VAWT; Solidity 0.75, $\lambda=4.5$ (60 degree) .....	91
<b>Fig. 6.31:</b> Velocity contour of 6 Bladed Double layered H – Rotor VAWT; Solidity 1.05, $\lambda=3.75$ (0 degree) .....	91

<b>Fig. 6.32:</b> Velocity contour of 6 Bladed Double layered H – Rotor VAWT; Solidity 1.05, $\lambda=3.75$ (60 degree) .....	92
<b>Fig. 6.33:</b> Velocity contour of 6 Bladed Double layered H – Rotor VAWT; Solidity 1.5, $\lambda=3$ (0 degree) .....	93
<b>Fig. 6.34:</b> Velocity contour of 6 Bladed Double layered H – Rotor VAWT; Solidity 1.5, $\lambda=3$ (60 degree) .....	93
<b>Fig. 6.35(a):</b> Velocity vector of 6 Bladed Double layered H – Rotor VAWT; Solidity 0.75, $\lambda=4.5$ (outer layer blades at 0 degree) .....	94
<b>Fig. 6.35(b):</b> Velocity vector of 6 Bladed Double layered H – Rotor VAWT; Solidity 0.75, $\lambda=4.5$ (outer layer blades at 60 degree) .....	94
<b>Fig. 6.35(c):</b> Velocity vector of 6 Bladed Double layered H – Rotor VAWT; Solidity 0.75, $\lambda=4.5$ (outer layer blades at 120 degree) .....	95
<b>Fig. 6.35(d):</b> Velocity vector of 6 Bladed Double layered H – Rotor VAWT; Solidity 0.75, $\lambda=4.5$ (outer layer blades at 180 degree) .....	95
<b>Fig. 6.35(e):</b> Velocity vector of 6 Bladed Double layered H – Rotor VAWT; Solidity 0.75, $\lambda=4.5$ (outer layer blades at 240 degree) .....	96
<b>Fig. 6.35(f):</b> Velocity vector of 6 Bladed Double layered H – Rotor VAWT; Solidity 0.75, $\lambda=4.5$ (outer layer blades at 300 degree) .....	96
<b>Fig. 6.36(a):</b> Velocity vector of 6 Bladed Double layered H – Rotor VAWT; Solidity 0.75, $\lambda=4.5$ (inner layer blade at 0 degree) .....	97
<b>Fig. 6.36(b):</b> Velocity vector of 6 Bladed Double layered H – Rotor VAWT; Solidity 0.75, $\lambda=4.5$ (inner layer blade at 60 degree) .....	97
<b>Fig. 6.36(c):</b> Velocity vector of 6 Bladed Double layered H – Rotor VAWT; Solidity 0.75, $\lambda=4.5$ (inner layer blade at 120 degree) .....	98
<b>Fig. 6.36(d):</b> Velocity vector of 6 Bladed Double layered H – Rotor VAWT; Solidity 0.75, $\lambda=4.5$ (inner layer blade at 180 degree) .....	98
<b>Fig. 6.36(e):</b> Velocity vector of 6 Bladed Double layered H – Rotor VAWT; Solidity 0.75, $\lambda=4.5$ (inner layer blade at (a) 240 degree) .....	99
<b>Fig. 6.36(f):</b> Velocity vector of 6 Bladed Double layered H – Rotor VAWT; Solidity 0.75, $\lambda=4.5$ (inner layer blade at 300 degree) .....	99
<b>Fig. 6.37(a):</b> Velocity vector of 6 Bladed Double layered H – Rotor VAWT; Solidity 1.05, $\lambda=3.75$ (inner layer blades at 0 degree) .....	100
<b>Fig. 6.37(b):</b> Velocity vector of 6 Bladed Double layered H – Rotor VAWT; Solidity 1.05, $\lambda=3.75$ (inner layer blades at 60 degree) .....	100
<b>Fig. 6.37(c):</b> Velocity vector of 6 Bladed Double layered H – Rotor VAWT; Solidity 1.05, $\lambda=3.75$ (inner layer blades at 120 degree) .....	101
<b>Fig. 6.37(d):</b> Velocity vector of 6 Bladed Double layered H – Rotor VAWT; Solidity 1.05, $\lambda=3.75$ (inner layer blades at 180 degree) .....	101
<b>Fig. 6.37(e):</b> Velocity vector of 6 Bladed Double layered H – Rotor VAWT; Solidity 1.05, $\lambda=3.75$ (inner layer blades at 240 degree) .....	102
<b>Fig. 6.37(f):</b> Velocity vector of 6 Bladed Double layered H – Rotor VAWT; Solidity 1.05, $\lambda=3.75$ (inner layer blades at 300 degree) .....	102
<b>Fig. 6.38(a):</b> Velocity vector of 6 Bladed Double layered H – Rotor VAWT; Solidity 1.05, $\lambda=3.75$ (outer layer blades at 0 degree) .....	103
<b>Fig. 6.38(b):</b> Velocity vector of 6 Bladed Double layered H – Rotor VAWT; Solidity 1.05, $\lambda=3.75$ (outer layer blades at 60 degree) .....	103
<b>Fig. 6.38(c):</b> Velocity vector of 6 Bladed Double layered H – Rotor VAWT; Solidity 1.05, $\lambda=3.75$ (outer layer blades at 120 degree) .....	104
<b>Fig. 6.38(d):</b> Velocity vector of 6 Bladed Double layered H – Rotor VAWT; Solidity 1.05, $\lambda=3.75$ (outer layer blades at 180 degree) .....	104
<b>Fig. 6.38(e):</b> Velocity vector of 6 Bladed Double layered H – Rotor VAWT; Solidity 1.05, $\lambda=3.75$ (outer layer blades at 240 degree) .....	105

<b>Fig. 6.38(f):</b> Velocity vector of 6 Bladed Double layered H – Rotor VAWT; Solidity 1.05, $\lambda=3.75$ (outer layer blades at 300 degree) .....	105
<b>Fig. 6.39(a):</b> Velocity vector of 6 Bladed Double layered H – Rotor VAWT; Solidity 1.5, $\lambda=3.0$ (inner layer blades at 0 degree) .....	106
<b>Fig. 6.39(b):</b> Velocity vector of 6 Bladed Double layered H – Rotor VAWT; Solidity 1.5, $\lambda=3.0$ (inner layer blades at 60 degree) .....	106
<b>Fig. 6.39(c):</b> Velocity vector of 6 Bladed Double layered H – Rotor VAWT; Solidity 1.5, $\lambda=3.0$ (inner layer blades at 120 degree) .....	107
<b>Fig. 6.39(d):</b> Velocity vector of 6 Bladed Double layered H – Rotor VAWT; Solidity 1.5, $\lambda=3.0$ (inner layer blades at 180 degree) .....	107
<b>Fig. 6.39(e):</b> Velocity vector of 6 Bladed Double layered H – Rotor VAWT; Solidity 1.5, $\lambda=3.0$ (inner layer blades at 240 degree) .....	108
<b>Fig. 6.39(f):</b> Velocity vector of 6 Bladed Double layered H – Rotor VAWT; Solidity 1.5, $\lambda=3.0$ (inner layer blades at 300 degree) .....	108
<b>Fig. 6.40(a):</b> Velocity vector of 6 Bladed Double layered H – Rotor VAWT; Solidity 1.5, $\lambda=3.0$ (outer layer blades at 0 degree) .....	109
<b>Fig. 6.40(b):</b> Velocity vector of 6 Bladed Double layered H – Rotor VAWT; Solidity 1.5, $\lambda=3.0$ (outer layer blades at 60 degree) .....	109
<b>Fig. 6.40(c):</b> Velocity vector of 6 Bladed Double layered H – Rotor VAWT; Solidity 1.5, $\lambda=3.0$ (outer layer blades at 120 degree) .....	110
<b>Fig. 6.40(d):</b> Velocity vector of 6 Bladed Double layered H – Rotor VAWT; Solidity 1.5, $\lambda=3.0$ (outer layer blades at 180 degree) .....	110
<b>Fig. 6.40(e):</b> Velocity vector of 6 Bladed Double layered H – Rotor VAWT; Solidity 1.5, $\lambda=3.0$ (outer layer blades at 240 degree) .....	111
<b>Fig. 6.40(f):</b> Velocity vector of 6 Bladed Double layered H – Rotor VAWT; Solidity 1.5, $\lambda=3.0$ (outer layer blades at 300 degree) .....	111
<b>Fig. 6.41:</b> Pressure contour of 6 Bladed Double layered H – Rotor VAWT; Solidity 0.75 at $\lambda=4.5$ .....	112
<b>Fig. 6.42:</b> Pressure contour of 6 Bladed double layered H – Rotor VAWT; Solidity 1.05 at $\lambda=3.75$ .....	114
<b>Fig. 6.43:</b> Pressure contour of 6 Bladed double layered H – Rotor VAWT; Solidity 1.5 at $\lambda=3$ .....	115
<b>Fig 6.44:</b> $C_t$ and $C_d$ vs. $\theta$ for Double Layered (In-line) H-Darrieus VAWT; Solidity 1.5 at $\lambda=3.0$ .....	116
<b>Fig 6.45:</b> Comparison of $C_t$ for $(C_p)_{max}$ with the change of solidity .....	117
<b>Fig 6.46:</b> Comparison of $\lambda$ for $(C_p)_{max}$ with the change of solidity .....	118
<b>Fig 6.47:</b> Comparison of $(C_p)_{max}$ with the change of solidity .....	118
<b>Fig. 6.48:</b> $C_t$ vs. $\lambda$ for different H-Darrieus VAWT at $\zeta=1.5$ .....	119
<b>Fig. 6.49:</b> $C_p$ vs. $\lambda$ for different H-Darrieus VAWT at $\zeta=1.5$ .....	120
<b>Fig. 6.50:</b> Inner layer power coefficient, outer layer power coefficient and total power coefficient for Double Layered (staggered) VAWT with $\zeta=1.5$ .....	121
<b>Fig. 6.51:</b> Inner layer power coefficient and outer layer power coefficient for Double Layered VAWTs with $\zeta=1.5$ .....	122
<b>Fig. 6.52:</b> $C_t$ vs. $\theta$ for Double layered (Staggered) H-Darrieus VAWT with $\zeta=1.5$ .....	123
<b>Fig. 6.53:</b> Velocity contour of 6 Bladed Double layered H – Rotor VAWT; Solidity 1.0, $\lambda=3.0$ (0 degree) .....	124
<b>Fig. 6.54:</b> Velocity contour of 6 Bladed Double layered H – Rotor VAWT; Solidity 1.0, $\lambda=3.0$ (60 degree) .....	124
<b>Fig. 6.55(a):</b> Velocity vector of 6 Bladed Double layered Staggered H – Rotor VAWT; Solidity 1.5, $\lambda=3.0$ (inner layer blades at 0 degree) .....	125
<b>Fig. 6.55(b):</b> Velocity vector of 6 Bladed Double layered Staggered H – Rotor VAWT; Solidity 1.5, $\lambda=3.0$ (inner layer blades at 60 degree) .....	125
<b>Fig. 6.55(c):</b> Velocity vector of 6 Bladed Double layered Staggered H – Rotor VAWT; Solidity 1.5, $\lambda=3.0$ (inner layer blades at 120 degree) .....	126
<b>Fig. 6.55(d):</b> Velocity vector of 6 Bladed Double layered Staggered H – Rotor VAWT; Solidity 1.5, $\lambda=3.0$ (inner layer blades at 180 degree) .....	126

<b>Fig. 6.55(e):</b> Velocity vector of 6 Bladed Double layered Staggered H – Rotor VAWT; Solidity 1.5, $\lambda=3.0$ (inner layer blades at 240 degree).....	127
<b>Fig. 6.55(f):</b> Velocity vector of 6 Bladed Double layered Staggered H – Rotor VAWT; Solidity 1.5, $\lambda=3.0$ (inner layer blades at 300 degree).....	127
<b>Fig. 6.56(a):</b> Velocity vector of 6 Bladed Double layered Staggered H – Rotor VAWT; Solidity 1.5, $\lambda=3.0$ (outer layer blades at 0 degree).....	128
<b>Fig. 6.56(b):</b> Velocity vector of 6 Bladed Double layered Staggered H – Rotor VAWT; Solidity 1.5, $\lambda=3.0$ (outer layer blades at 60 degree).....	128
<b>Fig. 6.56(c):</b> Velocity vector of 6 Bladed Double layered Staggered H – Rotor VAWT; Solidity 1.5, $\lambda=3.0$ (outer layer blades at 120 degree).....	129
<b>Fig. 6.56(d):</b> Velocity vector of 6 Bladed Double layered Staggered H – Rotor VAWT; Solidity 1.5, $\lambda=3.0$ (outer layer blades at 180 degree).....	129
<b>Fig. 6.56(e):</b> Velocity vector of 6 Bladed Double layered Staggered H – Rotor VAWT; Solidity 1.0, $\lambda=3.0$ (outer layer blades at 240 degree).....	130
<b>Fig. 6.56(f):</b> Velocity vector of 6 Bladed Double layered Staggered H – Rotor VAWT; Solidity 1.5, $\lambda=3.0$ (outer layer blades at 300 degree).....	130
<b>Fig 6.57:</b> Pressure contour of outer layer blades of Double layered staggered H – Rotor VAWT; Solidity 1.5 at $\lambda=3.0$ .....	131
<b>Fig 6.58:</b> Pressure contour of outer layer blades of Double layered staggered H – Rotor VAWT; Solidity 1.5 at $\lambda=3.0$ .....	132
<b>Fig 6.59:</b> $C_1$ and $C_d$ vs. $\theta$ for Double layered (Staggered) H-Darrieus VAWT; Solidity 1.5 at $\lambda=3.0$ .....	133



## LIST OF TABLES

Table 5.1: Mesh Sizing .....	50
Table 5.2: Values for Numerical Calculation. ....	52
Table 6.2: Relationship between $C_i$ and $C_p$ with $\lambda$ for Single Layered VAWT with $\zeta = 0.5$ .....	58
Table 6.3: Relationship between $C_i$ and $C_p$ with $\lambda$ for Single Layered VAWT with $\zeta = 0.7$ .....	58
Table 6.4: Relationship between $C_i$ and $C_p$ with $\lambda$ for Single Layered VAWT with $\zeta = 1.0$ .....	58
Table 6.5: Relationship between $C_i$ and $C_p$ with $\lambda$ for Double Layered VAWT with $\zeta = 0.5$ .....	81
Table 6.6: Relationship between $C_i$ and $C_p$ with $\lambda$ for Double Layered VAWT with $\zeta = 0.7$ .....	81
Table 6.7: Relationship between $C_i$ and $C_p$ with $\lambda$ for Double Layered VAWT with $\zeta = 1.0$ .....	81
Table 6.8: Calculation of $C_p$ of double layered 6 bladed VAWT with solidity 0.5 .....	84
Table 6.9: Calculation of $C_p$ of double layered 6 bladed VAWT with solidity 0.7 .....	85
Table 6.10: Calculation of $C_p$ of double layered 6 bladed VAWT with solidity 1.0 .....	86
Table 6.10: $C_i$ and $C_p$ of different type of H-Darrieus VAWT with unit solidity .....	119

## NOMENCLATURE

<b>Symbol</b>	<b>Symbol Description</b>
A	Frontal Area of Wind Turbine
$C_d$	Coefficient of Drag
$C_l$	Coefficient of Lift
$C_t$	Coefficient of torque
$C_p$	Coefficient of Power
F	Force
L	Length
P	Pressure
Re	Reynolds Number
R	Radius of the Turbine
v	Velocity
$\mu$	Dynamic viscosity
$\nu$	Kinematic viscosity
$\rho$	Density
$\theta$	Angle of Rotation or Azimuth Angle
k	Kinetic Energy
$\omega$	Specific Dissipation Rate
$\lambda$	Tip Speed Ratio (tsr) of Wind Turbine
$\Omega$	Rotational Velocity (rad/s)
$\alpha$	Angle of Attack
$\sigma$	Solidity Ratio

CHAPTER:1

# **INTRODUCTION**

## 1.1 Introduction

Wind is a natural source of power which has been used to sail boats and ships, pump water and many other purposes from long back. Day by day the use of wind power has increased and people tried to improve the wind machines. In order to make life easier, Scientists and Engineers were always trying to convert wind energy to the necessary form of energy. Due to advent of modern technologies now-a-days it has got more and more attention towards harnessing more energy. On that respect, wind turbines have gained extensive engineering concern. At different times, people invented and worked on different types of wind turbine which can be classified as below.

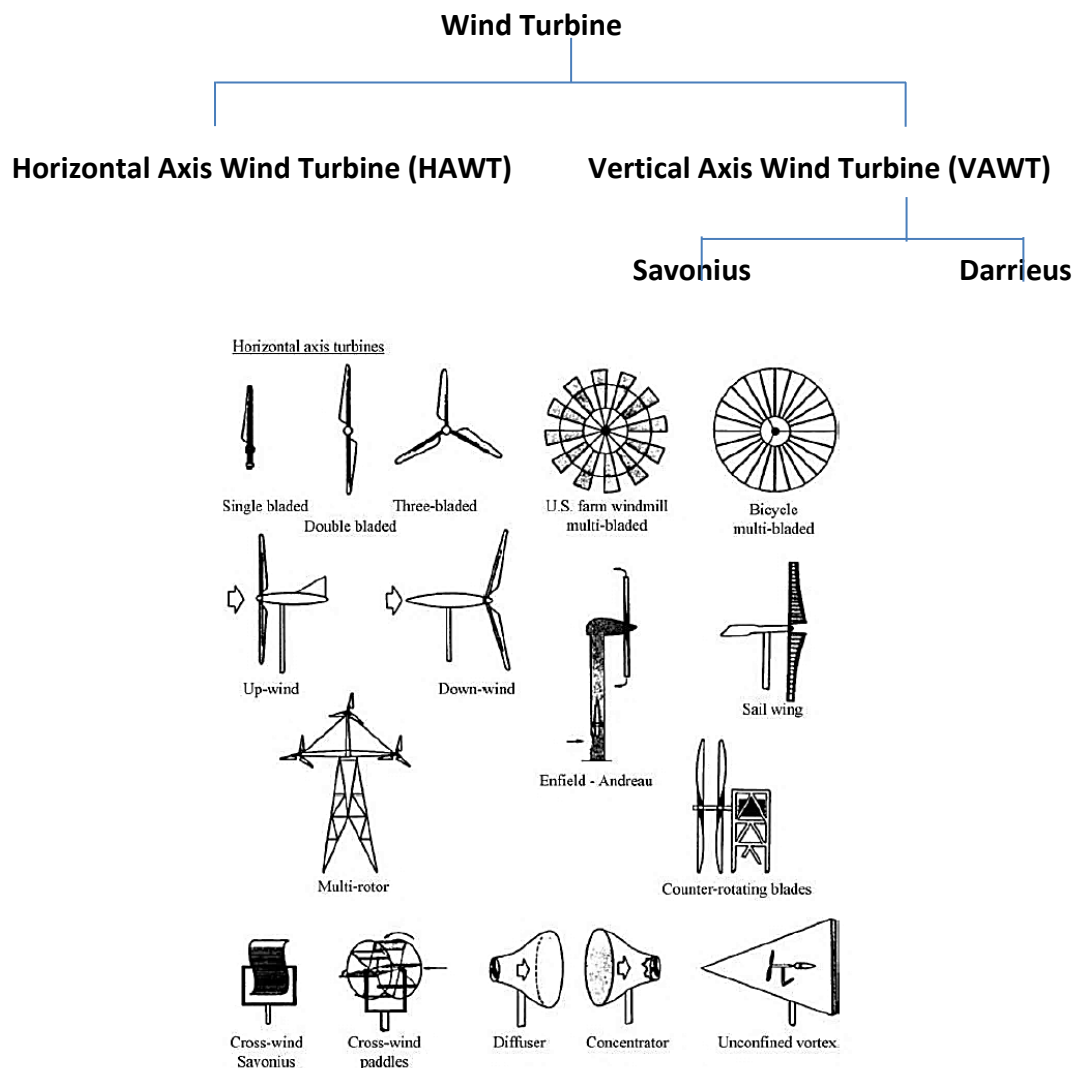


**Fig. 1.1:** Different types of horizontal axis wind turbine [1]

Different types of horizontal axis wind turbines and vertical axis wind turbines are shown in Fig 1.1 and Fig 1.2 respectively.

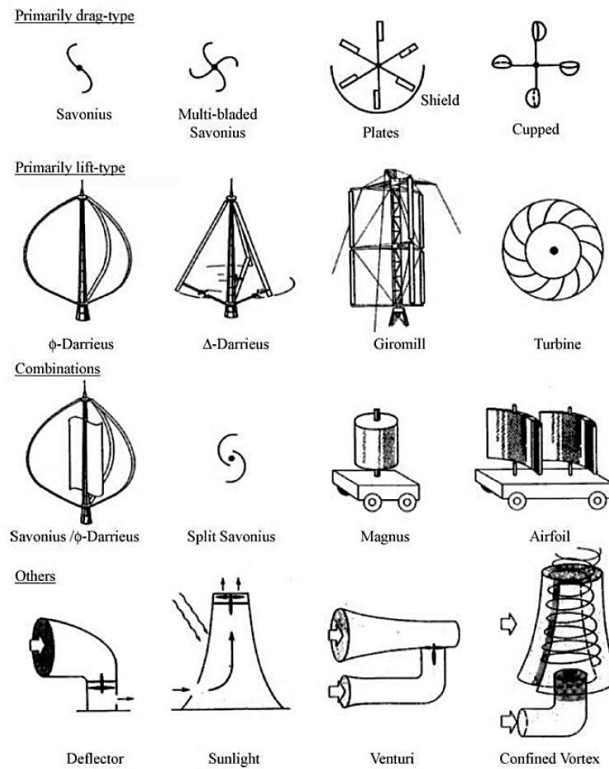


**Fig. 1.2:** Different Type of Vertical Axis Wind Turbine [1]

Theoretically, the maximum power that can be harnessed from the wind, independent of the design of wind turbine in an open flow, is defined by Betz's law and the theoretical maximum limit is 59.3% of the available wind power. However, practically, wind turbine can achieve 75~80% of Betz's limit. Relation of power coefficient for different types of wind turbines at different tip speed ratios are shown in Fig. 1.3.

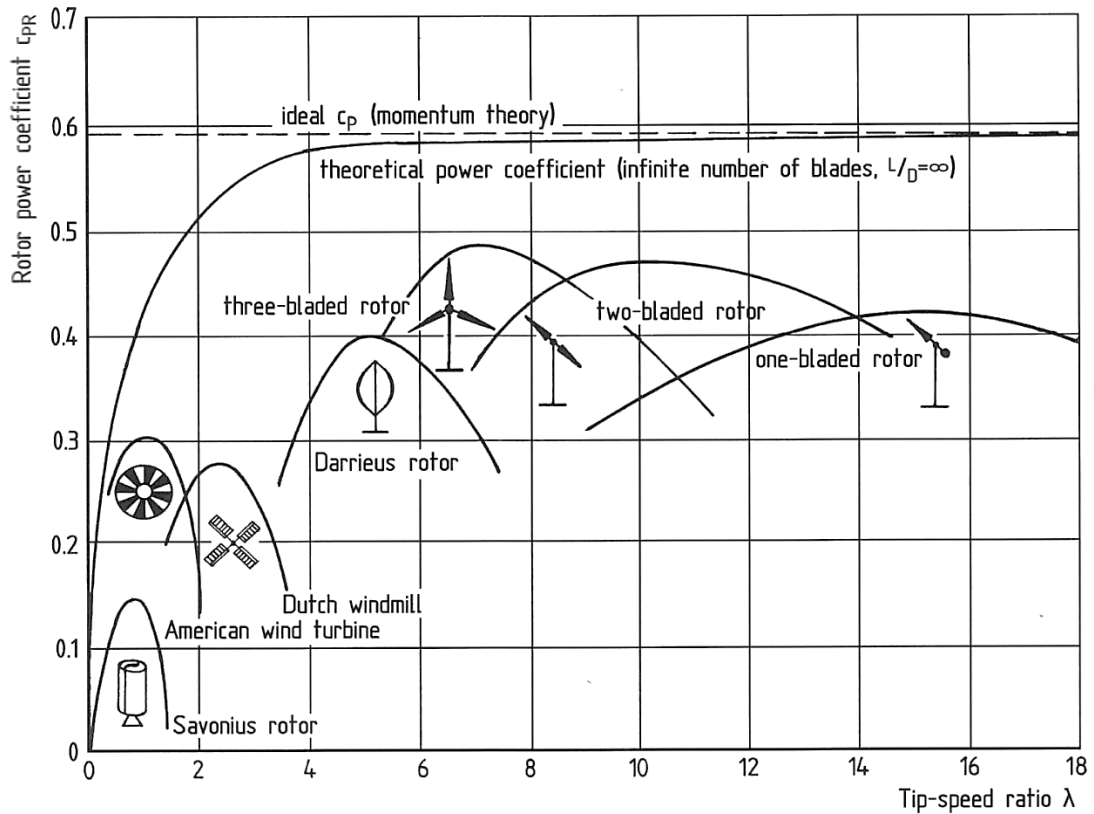


**Fig. 1.3:** Comparison of Power Coefficient of Different Wind Turbines

Now-a-days, engineers are consistently doing research in order to improve the scenario. As a result of continuous research and developments, the wind farms consist of Horizontal Axis Wind Turbine (HAWT) now can generate megawatts of electricity efficiently. However, horizontal axis wind turbines need special arrangements to align itself into the direction of wind.

On the other hand, the Vertical Axis Wind Turbine (VAWT) can extract power from the low speed omni-directional wind which is again of two types. One is drag basis and the other is lift basis VAWT. The Savonius type VAWT is a low speed, high torque, drag basis wind turbine and the Darrieus type VAWT is a high speed, low torque, lift basis wind turbine. Nevertheless, the Darrieus turbines need high starting torque. Sometimes, Savonius rotor is attached to Darrieus wind turbine in order to generate the higher starting torque.

Wind Speed Chart (in m/s) made from 29 Years of Recorded Data of Bangladesh Meteorological

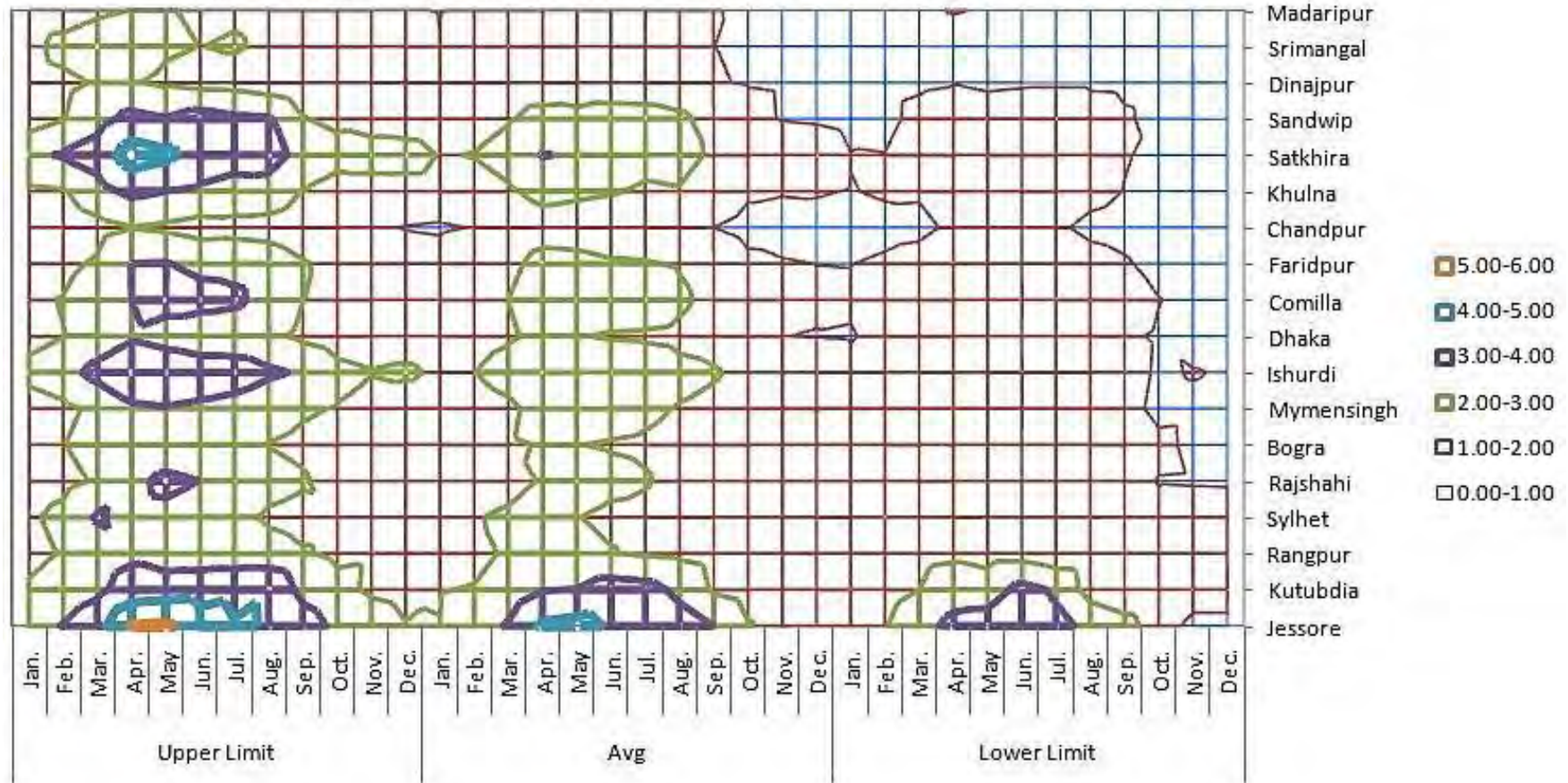


Fig. 1.4: Wind Data

## 1.2 Motivation

The demand of clean energy is increasing day by day as the environmental pollution due to burning the fossil fuel is being demotivated all over the world. Wind is one of the major sources of clean energy. However, wind is not uniform everywhere and in some places like Bangladesh the average velocity of wind is also low. Wind speed distribution at different places in Bangladesh is shown in Fig. 1.4. For the low speed omnidirectional wind vertical axis wind turbines are good solution for harnessing power.

## 1.3 Scope and Objectives

The main objectives of the present research work can be summarized as follows:

1. To study the characteristics of Darrieus type Vertical Axis Wind Turbine (VAWT) by numerical simulations.
2. To study the effect of solidity on Power coefficient of double layered Darrieus VAWT.
3. To compare the relations between maximum power coefficient and tip speed ratio of single layered and double layered Darrieus VAWT.
4. To study the effect of inner layer blades on the performance of outer layer blades.

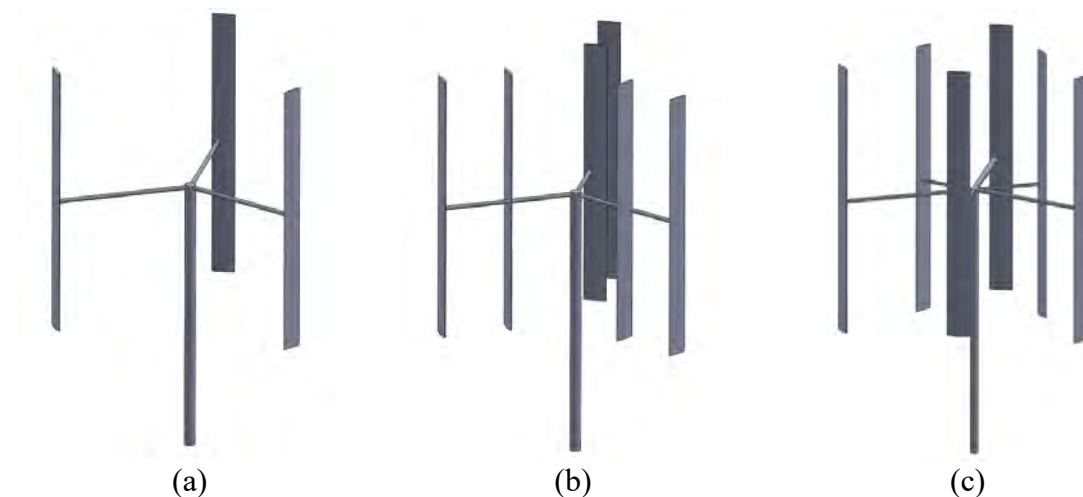


**Fig. 1.5:** Wind Turbine (a) Single Layered VAWT (b) Double Layered in-line VAWT (c) Double Layered Staggered VAWT



In this thesis report, the performances of three different types of H-rotor VAWT as shown in Fig.1.5 are going to be investigated.

#### **1.4 Outline of the research**

The thesis is presented in following direction.

1. A brief description on outcomes of previous researches is presented.
2. Theory of Vertical Axis Wind Turbine is presented.
3. The methods of the research; mathematical modeling, governing equations, experimental and the outlines of numerical methodology are discussed
4. Discussion on the result yielded from the numerical investigation.
5. Finally the current study is concluded and few scopes for further researches are recommended.

CHAPTER:2

# **BACKGROUND LITERATURE**

Vertical Axis Wind Turbine (VAWT) has got more engineering concern in order to improve its efficiency. Hence, scientists are always trying to analyze its performance theoretically, numerically and experimentally.

Theoretically, the vertical axis wind turbines were studied using streamtube theories [2]. Single streamtube model was the first attempt of the theoretical modeling of the vertical axis wind turbine. This was introduced by Templin et al. [3] in the year 1974. In this model the whole turbine rotor was enclosed within a single streamtube. Wilson and Lissaman [4] in 1974 and Strickland in 1975 [5] used multiple streamtube model for the performance analysis of vertical axis wind turbine. In that approach, a series of streamtubes parallel to the free stream were assumed. The multiple streamtube model gave rise to a velocity distribution through the rotor both in vertical and horizontal directions. Another model named Double Multiple Streamtube Model was presented by Paraschivoiu in the year 1981 [6]. In that model, the rotor was divided into upstream half and downstream half. All streamtubes were divided into these two halves and then analysis was performed in each half separately.

A.C. Mandal and M.Q. Islam [7] investigated the performance of Darrieus turbine theoretically. They considered the effect of chord to radius ratio and blade pitching in their study. For a high chord-radius ratio, the local angle of attack on a straight blade of a Darrieus wind turbine changes along the chord length. As a result, the flow on the airfoil becomes curvilinear. They found that consideration of flow curvature effect could predict the performance of VAWT more accurately even for small chord to radius ratio.

Gosselin et al. [8] numerically investigated the effect of blade aspect ratio and use of end plates of VAWT using U-RANS simulation. They found due to smaller aspect ratio

efficiency dropped about 60% and the effect of end plates was positive on power extraction. They also found the solidity of the most efficient fixed pitch turbine was 0.2 and for higher solidity turbines, the blade pitching was required to achieve higher efficiency.

Beri and Yao [9] compared the CFD result and the results for double multiple streamtube model and found power coefficient at lower tip speed ratio were higher for CFD than Double Multiple Stream Tube (DMST) result. CFD was also lower than  $(C_p)_{\max}$  for DMST. Moreover, at lower tip speed ratio, negative torque was found in the calculation by DMST model while positive torque was found in the CFD simulation result.

An analytical model based on multiple streamtube theory was proposed by Conaill et al. [10] in order to calculate the rotor performance and aerodynamic forces on rotor blades of Variable Pitch Vertical Axis Wind Turbines. Flow curvature, flow expansion, tip loss and dynamic stall were considered in this model. They found sinusoidal blade pitching may increase the power coefficient about 5.4% to 26.7% at different tip speed ratio. They suggested that, as there was a coupling between the upstream energy extraction and downstream energy extraction, pitching effect on the performance of the whole turbine at any specific azimuthal location must be considered for optimized pitching.

R. Lanzafame et al. [11] developed the unsteady 2D CFD model and investigated the performance of H-rotor. They showed the development of vortex along the wake. Each blade generated different level of turbulence depending on its azimuthal position and on the interference of blade motion with the turbulence along the wake.

I. Malael & H. Dumitrescu [12] found that, URANS method could correctly assess the blade vortex interactions. Hence, URANS (Unsteady Reynolds Average Navier-Stokes) methods could predict the performance of VAWT more accurately than RANS (Reynolds Average Navier-Stokes) equations. They recommended SST  $k-\omega$  turbulence model for numerical study in their research. Malael, Dumitrescu and Cardos [13] investigated a particular dynamic stall phenomenon associated with unsteady flow around a NACA 0018 airfoil rotor at high angle of attack and at low speed,  $Re_c = 10^{-5}$ . They found that, special configuration of blade vortex interaction produced drag dynamic stall. The drag dynamic stall process was triggered by a certain unsteadiness level inside rotor.

In 1982 Paul G. Migliore and John R Fritschen [14] experimented on different airfoil shapes and found the thinner symmetric airfoils could achieve higher maximum power coefficient,  $(C_p)_{max}$  than the thicker symmetric airfoils. NACA Symmetric airfoils achieve peak  $C_p$ 's of 0.45 for NACA 0012, 0.4 for NACA 0018. That implies thinner airfoils were better for achieving higher  $C_p$ 's. The NACA 63<sub>b</sub>-0XX airfoil achieves  $(C_p)_{max}$  of 0.44 to 0.46. However, for NACA 63 series, higher  $(C_p)_{max}$  were associated with larger thickness. So NACA 63<sub>2</sub>-015 and 63<sub>3</sub>-018 airfoils were better than NACA 0015 airfoil. From their experimental study, it was evident that for very low solidities, the maximum power coefficient decreased with the decrease in solidity.

Later on, the effect of thickness was also investigated by Danao et al. [15] and Chen et al. [16] and similar result was found. Danao et al. [15] studied the blade thickness as well as camber effects and found the cambered airfoil produced higher torque in both upwind and downwind while inverted cambered airfoil generate torque mostly in upwind region. Danao et al. also showed that, SST  $k-\omega$  turbulence model was the most

appropriate turbulence model to use in case of unsteady airfoil motion. Chen et al. [16] also found that, for low tip speed ratio, the power coefficient was affected by the vortex and blade interaction and increased until the number of blades equal to three.

In 2012 M.H. Mohamed [17] numerically studied 20 nos. of H-rotor wind turbine made of different airfoils and found S-1046 airfoil promising for the wind energy generation. Wind turbine consists of three S-1046 airfoil shaped blade achieved  $(C_p)_{\max}$  26.83% higher than the  $(C_p)_{\max}$  of VAWT using symmetric NACA airfoils. This led to 10.87% increase in absolute efficiency of VAWT. He also recommended low solidity H-rotor Darrieus VAWT for wider operating range. In his numerical analysis of the H-rotor VAWT, unsteady Reynolds Average Navier-Stokes equations was solved for more accurate result. Later, in 2015 Mohamed et al. [18] used SST k- $\omega$  turbulence model for numerical analysis for investigating the performance of 25 airfoils as Vertical axis wind turbine blade and found LS(1)-0413 more efficient than S-1046.

Taher et al. [19] studied the effect of number of blades and blade chord length on the performance of Straight Bladed VAWT. They found that, the max power coefficient is increased with increasing the chord length and decreasing the number of blades, while keeping the solidity unchanged. For the same no. of blades the solidity is increased by increasing the chord length.  $(C_p)_{\max}$  increases with the solidity upto a certain limit. If the solidity is (i.e. chord length) increased further,  $(C_p)_{\max}$  decreases. For the wind turbines having blades of same chord length, they also found that,  $(C_p)_{\max}$  increases with the increase in nos. of blades up to a certain limit, then decreases again. Torque ripple factor is inversely proportional to the no. of blades and hence, the chord length. Moreover, the normal (radial) force decreases with increasing the no. of blades and decreasing chord length at same solidity. Dominy et al. [20] showed three bladed H-

rotor has better self-starting capability than two bladed H-rotor because of its orientation independency.

Shengmao and Yen [21] found in their study that, for larger solidity SB-VAWT,  $(C_p)_{\max}$  increased with increasing the solidity, which was achieved at lower tip speed ratio ( $\lambda$ ). The increase in solidity and tip speed ratio affected the flow fields which resulted the decrement of wind speed passing through the interior of the turbine rotor. This phenomenon affected the performance of Straight Bladed VAWT (SB-VAWT).

Castelli et al. [22] performed 2D CFD analysis to observe the effect of blade number on the SB-VAWT of solidity 0.5, 0.67 and 0.83. They also found that, due to increasing no. of blade i.e. due to increasing the solidity,  $(C_p)_{\max}$  decreased and it was achieved at lower tip speed ratio ( $\lambda$ ). Besides,  $(C_p)_{\max}$  became lower and frequency of oscillation in torque increased, as for increasing the no. of blades meaning the increasing no. of periods in one complete rotation. The maximum torque values were generated during the upstream half-cycle (approximately  $(0^\circ$  to  $90^\circ)$  and where the angle of attack of the turbine blades were larger than the stall limit, the torque coefficient becomes negative.

CHAPTER: 3

# **THEORY**



### 3.1. Aerodynamic Forces

As a real flow is not a potential or inviscid flow, there develops some forces during flow around a body. Due to the pressure on the body (normal force) and viscosity effect (shear force) aerodynamic forces arise. Pressure acts locally, normal to the surface, and shear force acts locally, parallel to the surface. These aerodynamic forces are commonly resolved into two components:

- 1) Drag Force
- 2) Lift Force

#### 3.1.1 Drag force

Drag force is the force component parallel to the direction of relative motion or the free stream velocity. It is a resistive force opposite to the direction of a moving body. In fluid dynamics, the drag equation is a formula used to calculate the force of drag experienced by an object due to movement through a fully enclosing fluid. The formula is accurate only under certain conditions: the objects must have a blunt form factor and the fluid must have a large enough Reynolds number to produce turbulence behind the object. The equation is

$$F_D = \frac{1}{2} \rho v^2 C_D A \quad (3.1)$$

Where,

$F_D$  is the drag force

$\rho$  is the mass density of the fluid

$v$  is the velocity of the object relative to the fluid,

$A$  is the reference area, and

$C_D$  is the drag coefficient which is a dimensionless coefficient related to the object's geometry and taking into account both skin friction and form drag.

Drag force can be classified as:

- 1) Profile Drag
  - a. Skin Friction Drag
  - b. Form Drag
  - c. Interference Drag
- 2) Induced Drag

Skin friction drag results from the frictional forces that exist between a body and the air through which it is moving. Its value depends on the viscous effect, surface roughness, platform area and the state of boundary layer. Form drag is the resistance created by the shape of the body subject to the airflow. The general shape and size of the body is the most important factor in form drag. If the shape of the body encourage the airflow to separate from the surface, create eddies and so the streamline flow is disturbed then a turbulent wake is formed behind the body which increases drag called form drag. Interference drag is the result of interference occurs at the viscous junction of the surfaces. Whenever two surfaces meet at a sharp angle on an object, the airflow has a tendency to form a vortex. Accelerating the air into this vortex causes increase in drag. It can be reduced by using proper fillets and eliminating sharp angles. If pressure difference exists between upper and lower surface of a body such as an airfoil, a vortex or whirling occurs at the tip which increase drag called induced drag.

In case of a bluff the skin friction drag is relatively higher than the form drag, where form drag is higher than skin friction drag in case of a streamlined body. So in case of studying a bluff body form drag is the most important and dominant one and in case of a streamlined body friction drag become the main concern in aerodynamic studies. Form drag can be reduced by streamlining the body though then skin friction drag increases as surface area increases.

### 3.1.2 Lift

Lift is the force component acts perpendicularly upward to the direction of relative motion or the free stream velocity. Its direction depends on the shape of a body and rotation. Force in opposite direction of lift force (in downward direction) is called the downforce.

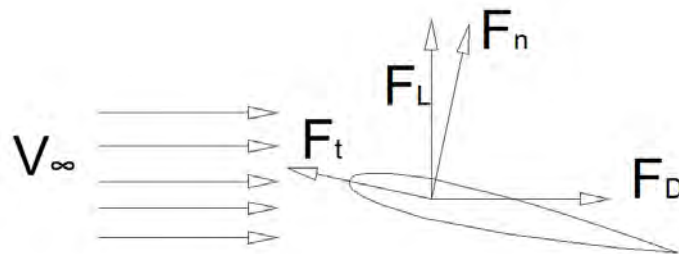


**Fig. 3.1:** Aerodynamic forces on an airfoil

### 3.1.3 Normal force or Radial Force

Normal force or radial force is the force component acting on the wind turbine blade along the radius of vertical axis wind turbine. It is considered as positive when the force acts outward in radial direction.

### 3.1.4 Tangential force

Tangential force is the force component acting on the wind turbine blade tangent to the periphery of vertical axis wind turbine or perpendicular to the radius of VAWT.

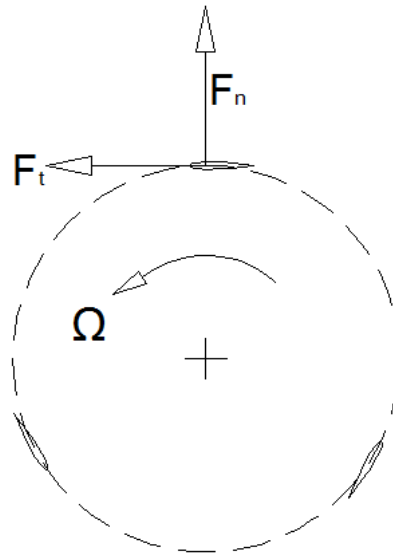


**Fig. 3.2:** Normal and Tangential force on a wind turbine blade

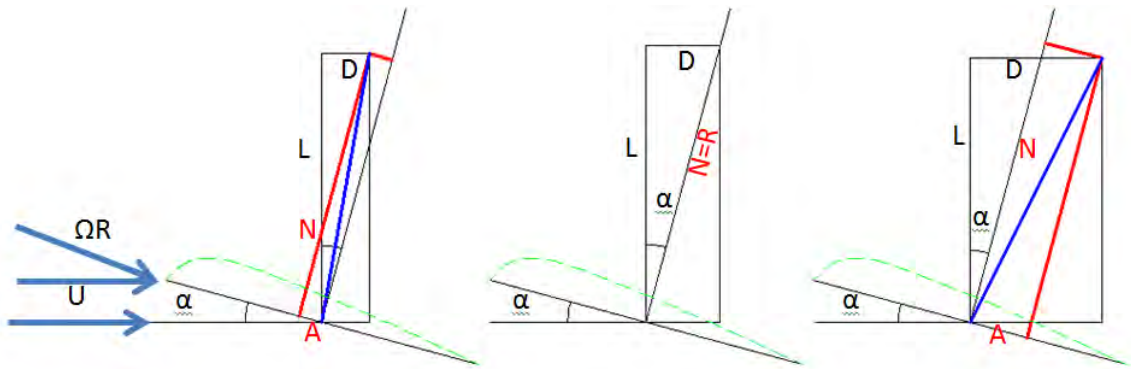


**Fig. 3.3:** Velocity and force components on a wind turbine blade (airfoil)

From the Fig. 3.3, for positive axial force lift force should be higher such that,  $\frac{D}{L} \leq \tan \alpha$ , where  $\alpha$  is the angle of attack.

### **3.2 Dimensionless Parameters**

The non-dimensionalization of the governing equations of fluid flow is important for both theoretical and computational reasons. Non-dimensional scaling provides a method for developing dimensionless groups that can provide physical insight into the importance of various terms in the system of governing equations. Computationally, dimensionless forms have the added benefit of providing numerical scaling of the system discrete equations, thus providing a physically linked technique for improving the ill-conditioning of the system of equations. Moreover, dimensionless forms also allow us to present the solution in a compact way. To minimize the experimental effort, the dependent variables are group together to form dimensionless parameters. Some of the important dimensionless numbers used in fluid mechanics and heat transfer are given below.

#### **3.2.1 Reynolds Number**

In fluid mechanics, the Reynolds number ( $Re$ ) is a dimensionless number that gives a measure of the ratio of inertial forces to viscous forces and consequently quantifies the relative importance of these two types of forces for given flow conditions.

Reynolds number can be defined for a number of different situations where a fluid is in relative motion to a surface. These definitions generally include the fluid properties of density and viscosity, plus a velocity and a characteristic length or characteristic dimension. This dimension is a matter of convention – for example a radius or diameter is equally valid for spheres or circles, but one is chosen by convention. For aircraft or ships, the length or width can be used. For flow in a pipe or a sphere moving in a fluid the internal diameter is generally used today. Other shapes such as rectangular pipes or

non-spherical objects have an *equivalent diameter* defined. For fluids of variable density such as compressible gases or fluids of variable viscosity such as non-Newtonian fluids, special rules apply. The velocity may also be a matter of convention in some circumstances, notably stirred vessels. With these conventions, the Reynolds number is defined as

$$Re = \frac{\rho v L}{\mu} = \frac{v L}{\nu} \quad (3.2)$$

Where,

- $v$  is the mean velocity of the object relative to the fluid
- $L$  is a characteristic linear dimension
- $\mu$  is the dynamic viscosity of the fluid
- $\nu$  is the kinematic viscosity
- $\rho$  is the density of the fluid

### 3.2.2 Drag Coefficient

Drag coefficient ( $C_D$ ) is a dimensionless quantity that is used to quantify the drag or resistance of an object in a fluid environment such as air or water. It is used in the drag equation, where a lower drag coefficient indicates the object will have less aerodynamic or hydrodynamic drag. The drag coefficient is always associated with a particular surface area.

The drag coefficient  $C_D$  is defined as

$$C_D = \frac{F_D}{\frac{1}{2}\rho v^2 A} \quad (3.3)$$

$$F_D = \int P dA \cos\theta \quad (3.4)$$

Where,

P is the Pressure on the surface

$F_D$  is the drag force,

$\rho$  is the mass density of the fluid,

v is the speed of the object relative to the fluid and

A is the reference area.

### 3.2.3 Torque Coefficient

Torque coefficient is the ratio of torque generated by the wind turbine to the available torque due to wind velocity. It is represented by  $C_Q$ .

$$C_Q = \frac{Q}{\frac{1}{2}\rho A v_\infty^2 R} \quad (3.5)$$

Where,

Q = Torque of the wind turbine

$\rho$  = Air density

$v_\infty$  = free stream velocity

R = radius of the wind turbine

A = Reference area.

### 3.2.4 Power Coefficient

Power coefficient is the ratio of power extracted by wind turbine to the available power in wind. It is represented by  $C_p$

$$C_p = \frac{P}{\frac{1}{2}\rho A v_\infty^3} \quad (3.6)$$

Where,

$P$  = Power extracted by the wind turbine

$\rho$  = Air density

$v_\infty$  = free stream velocity

$A$  = Reference area.

### 3.2.5 Solidity

Solidity ( $\zeta$ ) is the solid blockage area of the wind turbine. It is generally defined as the fraction of the circumference blocked by the rotor. For vertical axis wind turbine, it is defined as below,

$$\text{For Single layered VAWT} \quad \sigma = \frac{NC}{R} \quad (3.7.a)$$

$$\text{For Double Layered VAWT} \quad \sigma = \frac{N_i C_i}{R_i} + \frac{N_o C_o}{R_o} \quad (3.7.b)$$

Where,  $N$  = Number of blades;  $C$  = Chord length of blade;  $R$  = Radius of rotor

$N_i$  = Number of inner layer blades;  $C_i$  = Chord length of inner layer blade;  $R_i$  = Radius of inner layer rotor

$N_o$  = Number of outer layer blades;  $C_o$  = Chord length of outer layer blade;  $R_o$  = Radius of outer layer rotor



### 3.2.6 Tip Speed Ratio

Tip speed ratio ( $\lambda$ ) is the ratio of the velocity at the tip of wind turbine to the free stream velocity.

$$\lambda = \frac{R\Omega}{v_{\infty}} \quad (3.7)$$

Here,  $\Omega$  = Rotational velocity of wind turbine (rad/s)

### 3.3 Relation between the Angle of Attack and Angle of Rotation of Blade

The angle of attack depends on the induced wind velocity and the rotational speed of the wind turbine. If we consider the induced velocity ( $v_a$ ) is same in upstream and downstream side or at any angle of rotation of the VAWT and equal to the free stream velocity, then the change of angle of attack ( $\alpha$ ) with the rotational angle ( $\theta$ ) is as shown in Fig. 3.4. In this figure free stream velocity is represented by  $U_{\infty}$ .

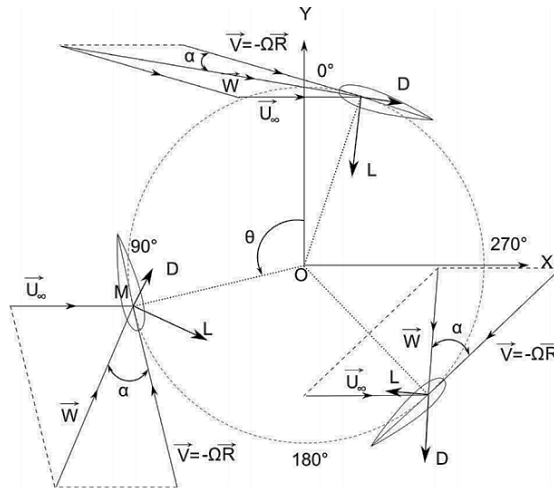


**Fig. 3.4:** Forces and velocities in a H-rotor Darrieus turbine [23]

From geometric considerations, the incidence angle  $\alpha$  are given by,

$$\alpha = \tan^{-1}\left(\frac{\sin \theta}{\lambda + \cos \theta}\right)$$

The equation for resultant velocity can be written as below.

$$\vec{W} = \vec{U}_\infty + \vec{V}$$

And the value of  $\vec{W}$  is,  $W = \sqrt{U_\infty^2 + (\Omega R)^2 + 2U_\infty\Omega R \cos \theta}$

The change of angle of attack with the angle of rotation is for different tip speed ratio is shown in Fig. 3.5.

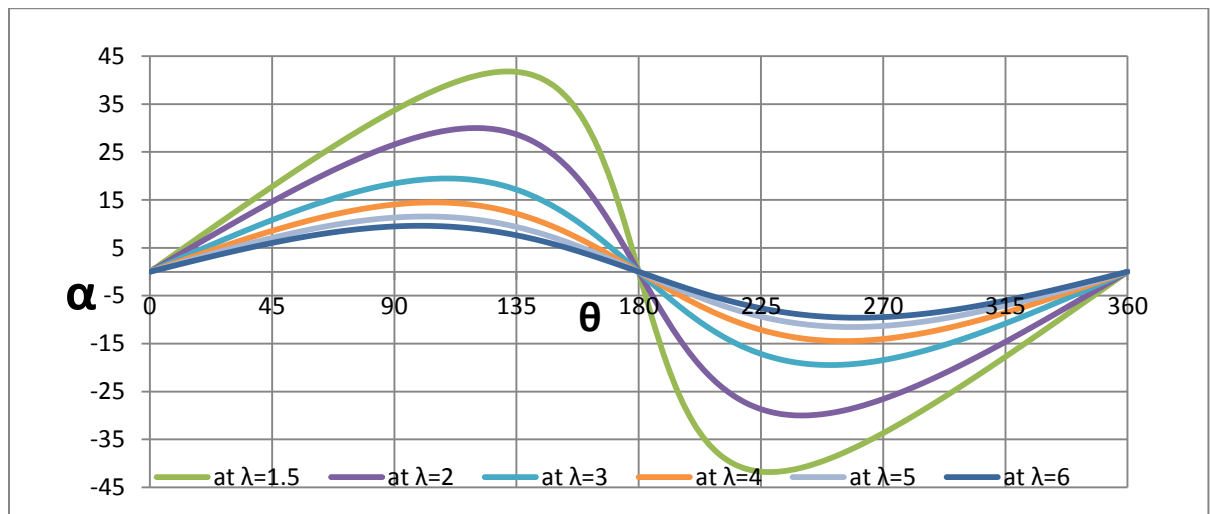


**Fig. 3.5:**  $\alpha$  vs.  $\theta$  at different value of  $\lambda$

However, practically the induced velocity never remains equal to the free stream velocity and unchanged with the rotational angle.

### 3.4 Theories for Performance Analysis of Vertical Axis Wind Turbine

In order to analyze the performance of vertical axis wind turbine, many theories have been established. In this thesis, we are analyzing the performance of single layer H-rotor VAWT and double layered H-rotor VAWT. Their performance may be predicted theoretically by the conventional momentum theories as below.

### 3.5 Blade Element Theory

Blade element theory involves breaking a blade down into several small parts then determining the forces on each of these small blade elements. These forces are then

integrated along the entire blade and over one rotor revolution in order to obtain the forces and moments produced by the entire propeller or rotor. [24] Elemental force and velocity diagram on the blade element are shown in Fig. 3.6 and Fig. 3.7 respectively.

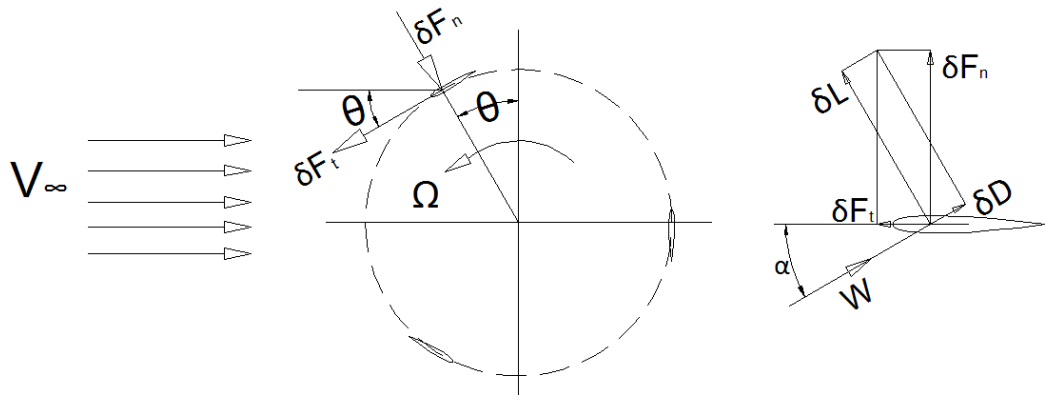


**Fig. 3.6:** Elemental Force Element on a Blade Element of H-rotor VAWT

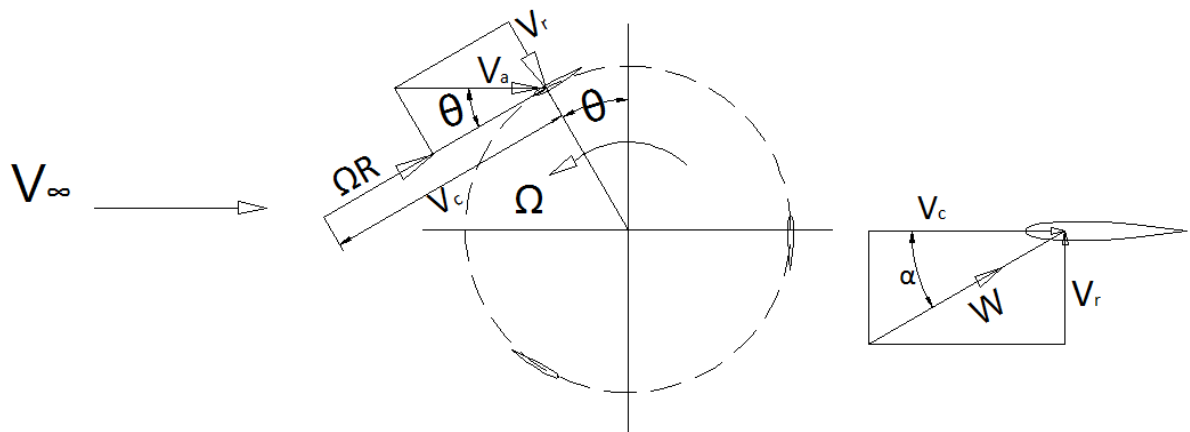


**Fig. 3.7:** Velocity diagram on the blade element of H-rotor VAWT

According to Glauert Actuator disc theory, the induced velocity (i.e. the uniform velocity through the rotor) is,

$$v_a = \frac{v_\infty + v_w}{2} \quad (3,8)$$

Where,  $V_w$  is the wake velocity.

From Fig. 3.7, the velocity in the chordal component is,  $v_c = v_a \cos\theta + R\Omega$

And the velocity in radial direction,  $v_r = v_a \sin\theta$

Hence, Resultant velocity  $W$  can be expressed as below,

$$W^2 = v_c^2 + v_r^2 = (v_a \cos\theta + R\Omega)^2 + (v_a \sin\theta)^2$$

$$\text{OR, } W^2 = v_a^2 + (\Omega R)^2 + 2v_a \Omega R \cos\theta$$

And the local angle of attack can be expressed as below,

$$\tan\alpha = \frac{v_r}{v_c} = \frac{v_a \sin\theta}{v_a \cos\theta + R\Omega}$$

So,

$$\alpha = \tan^{-1}\left(\frac{v_a \sin\theta}{v_a \cos\theta + R\Omega}\right)$$

Now considering the tip speed ratio ( $\lambda = R\Omega/v_\infty$ ), above equations can be written in non-dimensional form as below,

$$\frac{W}{v_a} = \sqrt{(\cos\theta + \lambda \frac{v_\infty}{v_a})^2 + (\sin\theta)^2} \quad (3.9)$$

$$\text{Or, } \frac{W}{v_a} = \sqrt{1 + (\lambda)^2 \left(\frac{v_\infty}{v_a}\right)^2 + 2\lambda \frac{v_\infty}{v_a} \cos\theta} \quad (3.10)$$

And

$$\alpha = \tan^{-1}\left(\frac{\sin\theta}{\cos\theta + \lambda \frac{v_\infty}{v_a}}\right) \quad (3.11)$$

The elemental normal force  $\delta F_n$  is perpendicular to the airfoil chord line and the elemental tangential force  $\delta F_t$  is parallel to the airfoil chord line. The elemental normal and tangential forces are defined as,

$$\delta F_n = C_n \frac{1}{2} \rho W^2 C \delta s \quad (3.12)$$

$$\text{And } \delta F_t = C_t \frac{1}{2} \rho W^2 C \delta s \quad (3.13)$$

Where,  $C$  is the chord length of blade airfoil and  $\delta s$  is the elemental blade length.

Now the relation between the elemental lift force  $\delta L$ , elemental drag forces  $\delta D$ , elemental normal force  $\delta F_n$  and elemental tangential force  $\delta F_t$  are defined as below with the help of Fig. 3.6.

$$\delta F_n = \delta L \cos \alpha + \delta D \sin \alpha \quad (3.14)$$

$$\text{and } \delta F_t = \delta L \sin \alpha - \delta D \cos \alpha \quad (3.15)$$

Where,

$$\delta L = C_l \frac{1}{2} \rho W^2 C \delta s \quad (3.16)$$

$$\text{and, } \delta D = C_d \frac{1}{2} \rho W^2 C \delta s \quad (3.17)$$

Here,  $C_d$  and  $C_l$  are drag and lift coefficient respectively.

So, using equations (3.12) to (3.17), we can write,

$$C_n = C_l \cos\alpha + C_d \sin\alpha \quad (3.18)$$

$$\text{and } C_t = C_l \sin\alpha - C_d \cos\alpha \quad (3.19)$$

The torque coefficient is a function of lift coefficient, drag coefficient and angle of attack. As the ratio of tip speed to induced velocity increases the angle of attack decreases. For  $\alpha \rightarrow 0$ ,  $\sin \alpha \approx 0$ . This leads to very small torque coefficient. An airfoil performs at higher lift coefficient and lower drag coefficient when the angle of attack is below critical angle of attack. So the angle of attack is optimum when it is lower than and very close to the critical angle of attack. Hence, the tip speed ratio is optimum when, it creates an angle of attack close to the critical angle of attack.

### 3.6 Single Streamtube Model

Single stream tube model is the simplest model for theoretical analysis of Vertical Axis Wind Turbine (VAWT). In this model rotor is assumed inside a single stream tube as shown in Fig. 3.8. Axial flow velocity (induced velocity) is assumed to be constant and related to the undisturbed stream velocity by equating the streamwise drag force to the momentum change of air through the rotor.

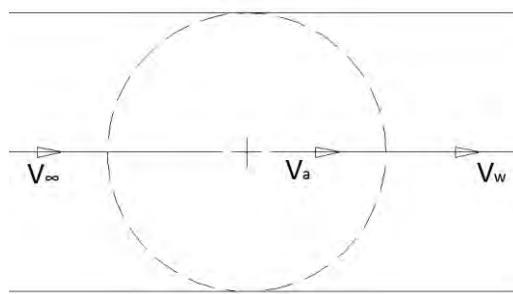


**Fig. 3.8:** Single stream tube model for single layered Vertical Axis Wind Turbine

The elemental tangential force on the rotor blade,

$$\delta F_t = C_t \frac{1}{2} \rho W^2 C \delta s \quad (3.20)$$

$$\text{And the elemental torque, } \delta Q = R \delta F_t \quad (3.21)$$

Assuming infinite nos. of blade distribution, we can replace  $C$  with  $\frac{NC\delta\theta}{2\pi}$  in equation (1).

Then integrating equation (2) we get the total torque output form wind turbine as below,

$$Q = R \frac{1}{2} \rho \frac{NC}{2\pi} \int_0^H \int_0^{2\pi} C_t W^2 d\theta ds \quad (3.20)$$

$$\Rightarrow Q = \frac{NC}{4\pi} R \rho H \int_0^{2\pi} C_t W^2 d\theta \quad (3.21)$$

Hence, power output can be calculated as,  $P = Q\Omega$

$$\text{So, } P = \frac{NC}{4\pi} \Omega R \rho H \int_0^{2\pi} C_t W^2 d\theta \quad (3.22)$$

The power coefficient of a wind turbine is defined as the ratio of extracted power from wind to the available power in wind. And the equation can be written as below,

$$C_P = P/P_{av}$$

$$\text{Where available power } P_{av} = \frac{1}{2} \rho A v_\infty^3$$

$$\text{So, } C_P = \frac{2}{\rho A v_\infty^3} \times \frac{NC}{4\pi} \Omega R \rho H \int_0^{2\pi} C_t W^2 d\theta \quad (3.23)$$

$$\Rightarrow C_P = \frac{NC}{4\pi v_\infty^3} \Omega \int_0^{2\pi} C_t W^2 d\theta ; \quad [as, A = 2RH] \quad (3.24)$$

### 3.7 Double Multiple Stream Tube Theory

Double multiple stream tube theory describes the performance of VAWT better than the single stream tube theory. Here the turbine is divided in upstream and downstream side for the separate analysis. In order to find the induced velocity in upstream and

downstream side, the principle of two actuator discs in tandem is used [2].

Assumptions are as below:

Assumptions:

1. Velocity is constant in horizontal direction.
2. Wake velocity of upstream half is the free stream velocity for the downstream half-cycle.
3. All induced and wake velocities are considered as axial.
4. Considering the H-rotor is installed high above the boundary layer, the change of height is insignificant and hence, the effect of height in free stream velocity is assumed to absent in this thesis.

### 3.7.1 Single layered H-rotor VAWT

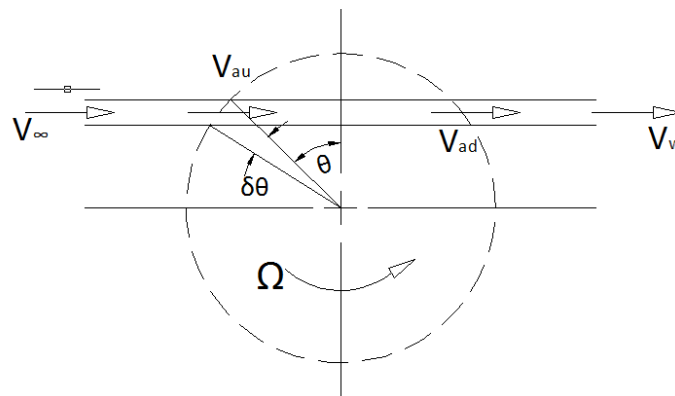


**Fig. 3.9:** Double multiple stream tube model for single layered rotor showing velocities and angle

From the Fig.3.9 equation of resultant velocity at upstream and downstream side can be written as below,

Resultant velocity at upstream side, 
$$W_u^2 = v_{au}^2 + (\Omega R)^2 + 2v_{au}\Omega R \cos\theta \quad (3.25)$$



Resultant velocity at downstream side,  $W_d^2 = v_{ad}^2 + (\Omega R)^2 + 2v_{ad}\Omega R \cos\theta$  (3.26)

Here,  $V_{au}$  and  $V_{ad}$  are induced velocities at the upstream and downstream side respectively.

Power coefficient can be calculated in similar way as shown above for single multiple stream tube model and can be written as below.

For upstream half,  $C_{Pu} = \frac{NC}{4\pi v_\infty^3} \Omega \int_0^\pi C_t w_u^2 d\theta$  (3.27)

And for downstream half,  $C_{Pd} = \frac{NC}{4\pi v_\infty^3} \Omega \int_0^\pi C_t w_d^2 d\theta$  (3.28)

Hence, total power coefficient,  $C_p = C_{pu} + C_{pd}$  (3.29)

### 3.7.2 Double layered H-rotor VAWT

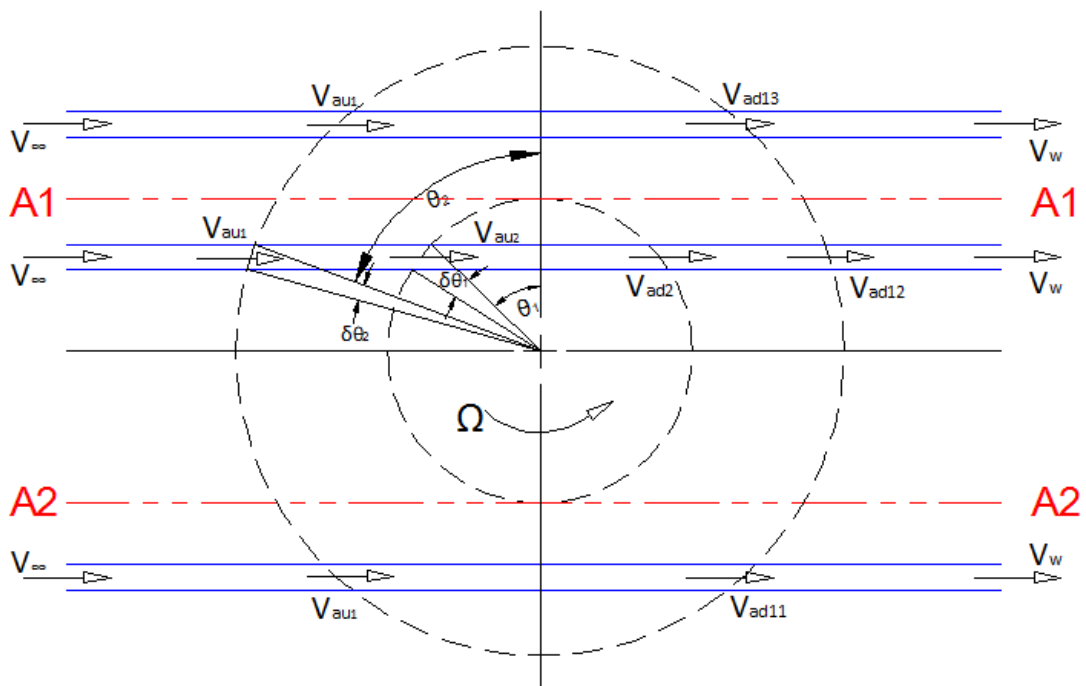


**Fig. 3.10:** Double Multiple Stream Tube Model for double layered Vertical Axis H-Darrieus Turbine

For double layered H-rotor,  $V_{au1}$  and  $V_{au2}$  are induced velocities at the upstream side for outer layer and inner layer respectively. The induced velocity for inner layer at downstream side is  $V_{ad2}$ . As a part of outer layer at the downstream side is blocked by the inner layer, the induced velocity of outer layer is not same everywhere at downstream side. The induced velocity is symbolized with  $V_{ad12}$  where the outer layer is blocked by the inner layer at downstream. This zone is between the lines A1-A1 and A2-A2. Elsewhere at downstream, the induced velocity is considered as  $V_{ad11}$  and  $V_{ad13}$ . For the simplicity  $V_{ad11}$  and  $V_{ad13}$  are considered equal.

Therefore, the equations of resultant velocities can be written as below.

$$w_{u1}^2 = v_{au1}^2 + (\Omega R_o)^2 + 2v_{au1}\Omega R_o \cos\theta_2 \quad (3.30)$$

$$w_{u2}^2 = v_{au2}^2 + (\Omega R_i)^2 + 2v_{au2}\Omega R_i \cos\theta_1 \quad (3.31)$$

$$w_{d2}^2 = v_{ad2}^2 + (\Omega R_i)^2 + 2v_{ad2}\Omega R_i \cos\theta_1 \quad (3.32)$$

$$w_{d11}^2 = v_{ad11}^2 + (\Omega R_o)^2 + 2v_{ad11}\Omega R_o \cos\theta_2 \quad (3.33)$$

$$w_{d12}^2 = v_{ad12}^2 + (\Omega R_o)^2 + 2v_{ad12}\Omega R_o \cos\theta_2 \quad (3.34)$$

$$w_{d13}^2 = v_{ad13}^2 + (\Omega R_o)^2 + 2v_{ad13}\Omega R_o \cos\theta_2 \quad (3.35)$$

Power coefficient for outer layer of upstream side

$$C_{Pu1} = \frac{N_1 C}{4\pi v_\infty^3} \omega \int_0^\pi C_t w_{u1}^2 d\theta_2 \quad (3.36)$$

Power coefficient for inner layer of upstream side,

$$C_{Pu2} = \frac{N_2 C}{4\pi v_\infty^3} \omega \int_0^\pi C_t w_{u2}^2 d\theta_1 \quad (3.37)$$

Power coefficient for inner layer of downstream side,

$$C_{Pd2} = \frac{N_2 C}{4\pi v_\infty^3} \omega \int_\pi^{2\pi} C_t w_{d2}^2 d\theta_1 \quad (3.38)$$

Power coefficient for outer layer of upstream side

$$C_{Pu1} = \frac{N_1 C}{4\pi v_\infty^3} \omega \int_0^\pi C_t w_{u1}^2 d\theta_2 \quad (3.39)$$

Power coefficient for outer layer of downstream side

$$C_{Pd1} = \frac{N_1 C}{4\pi v_\infty^3} \omega \left[ \int_\pi^{4\pi/3} C_t w_{d11}^2 d\theta_2 + \int_{4\pi/3}^{5\pi/3} C_t w_{d12}^2 d\theta_2 + \int_{5\pi/3}^{2\pi} C_t w_{d11}^2 d\theta_2 \right] \quad (3.40)$$

$$\text{Now, the total power coefficient, } C_p = C_{pu1} + C_{pu2} + C_{pd2} + C_{pd1} \quad (3.41)$$

CHAPTER: 4

# **MATHEMATICAL MODELING**

## 4.1 Governing equations

### 4.1.1 Continuity equation

In fluid dynamics, the continuity equation states that, the rate at which mass enters into a system is equal to the rate at which mass leaves the system plus the accumulation of mass within the system. The differential form of the continuity equation is:

$$\frac{\partial \rho}{\partial t} + \nabla \cdot (\rho \mathbf{u}) = 0 \quad (4.1)$$

where

- $\rho$  is fluid density,
- $t$  is time,
- $\mathbf{u}$  is the flow velocity vector field.

The time derivative can be understood as the accumulation (or loss) of mass in the system, while the divergence term represents the difference in flow in versus flow out.

### 4.1.2 Momentum equation

Conservation of momentum in an inertial reference frame is,

$$\frac{\partial(\rho \mathbf{u})}{\partial t} + \nabla \cdot (\rho \mathbf{u} \mathbf{u}) = -\nabla p + \nabla \cdot \boldsymbol{\tau} + \rho \mathbf{g} + \mathbf{F} \quad (4.2)$$

Where,  $p$ =static pressure

$\rho \mathbf{g}$  = gravitational body force

$\mathbf{F}$  = external body force

Stress tensor,  $\boldsymbol{\tau} = \mu \left[ (\nabla \mathbf{u} + \nabla \mathbf{u}^T) - \frac{2}{3} \nabla \cdot \mathbf{u} \mathbf{I} \right]$

$\mu$  = molecular viscosity

$I =$  unit tensor

The second term of right hand side of equation for stress tensor represents the effect of volume dilation. These continuity and momentum equations are combined together, called the Navier-Stokes equations.

#### 4.1.3 Reynolds Average Navier-Stokes Equation

For the analysis of turbulent flow and its fluctuating variables the Navier-Stokes equations are averaged. In case of averaging the variables are divided into mean value and fluctuating value.

For example, if we consider velocity component  $\mathbf{u}$ , then  $\mathbf{u} = \bar{\mathbf{u}} + \mathbf{u}'$ .

Substituting this type of forms in Navier-Stokes equations and taking a time average Reynolds average Navier-Stokes equation can be derived. In this research, time averaged Navier-Stokes equations are used.

The time averaged Navier-Stokes equations can be written as below:

$$\frac{\partial \rho}{\partial t} + \frac{\partial}{\partial x_i} (\rho u_i) = 0 \quad (4.3)$$

$$\begin{aligned} \frac{\partial}{\partial t} (\rho u_i) + \frac{\partial}{\partial x_j} (\rho u_i u_j) \\ = -\frac{\partial p}{\partial x_i} + \frac{\partial}{\partial x_j} \left[ \mu \left( \frac{\partial u_i}{\partial x_j} + \frac{\partial u_j}{\partial x_i} - \frac{2}{3} \delta_{ij} \frac{\partial u_l}{\partial x_l} \right) \right] + \frac{\partial}{\partial x_j} (-\rho \overline{u'_i u'_j}) \end{aligned} \quad (4.4)$$

In the above equation, the term  $-\rho \overline{u'_i u'_j}$  represents the Reynolds Stress term, which characterizes the effect of turbulence. These Reynolds stresses must be modeled to

close the above equation and this can lead to the creation different types of turbulence modeling. In this research, Shear Stress Transport (SST)  $k$ - $\omega$  turbulence model is used.

#### **4.2 Finite Volume Method and Staggered Grid**

In finite volume method, the whole computational domain is divided into many small control volumes. Then the governing equations are integrated over those small control volumes. For numerical simulation, these integral forms of governing equations are discretized with the help of discretization scheme. Velocity and pressure are considered at different nodes of control volume. It is described by Versteeg and Malalasekara [25] that, if velocities and pressure both are defined at the nodes of an ordinary control volume then a highly non-uniform pressure field can act like a uniform field in the discretized momentum equations. Besides, the influence of pressure is not properly represented in the discretized momentum equations. For this particular reason staggered grid for velocity component [26] is needed to be used. In this case the scalar variables (pressure, density, temperature etc.) are evaluated at ordinary nodal points and velocity components are calculated on staggered grids centered on the cell face as shown in Fig.4.1.

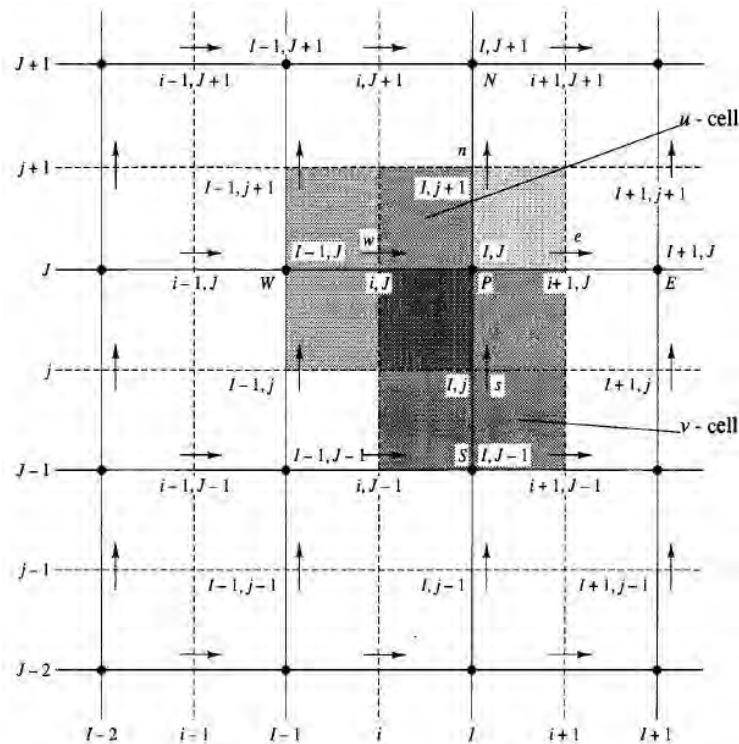


**Fig. 4.1:** Staggered Grid [25]

The momentum equations are non-linear equations. At the same time, in order to calculate the value of pressure and to get the pressure curve over the complete domain by performing numerical simulation, an equation relating the velocity components and pressure field is needed. This method is known as pressure-velocity coupling. The discretized momentum equations are solved with a guessed pressure field first to obtain the velocity components. Then a pressure correction term is used to correct the pressure and velocity components. These correction values are used to solve the continuity equation to obtain the new pressure correction value. Thus through iterations it is possible to get the correct values for pressure and velocity components. In summary, pressure-velocity coupling method is the method to couple velocity components and pressure fields so that one can be used to verify other and run the simulation to find the correct values of pressure field and velocity components.



### 4.3 Second order upwind discretization scheme

In this research, the Second Order Upwind discretization scheme is used for discretizing the integral form of governing equations because of its lower numerical diffusivity and reliability. Another benefit of this scheme is it can achieve the second order accuracy.

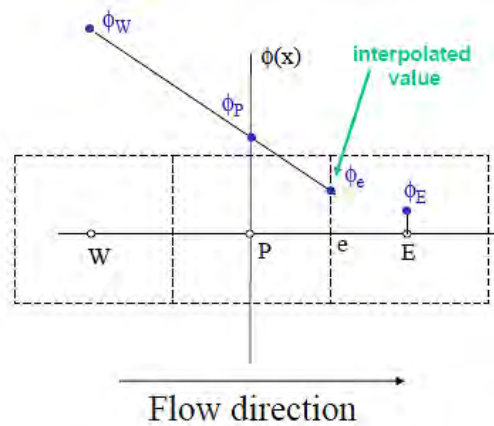


**Fig. 4.2:** Second Order Discretization Scheme

In this approach, the higher-order accuracy is achieved at cell faces through a Taylor series expansion of the cell-centered solution about the cell centroid. Thus when the second-order upwinding is selected, the face value is computed using the cell centered value and its gradient in upstream cells as shown in Fig.4.2. The expression of the value of variable at face can be written as below.

$$\phi_{f,sou} = \phi + \nabla\phi \cdot \mathbf{r} \quad (4.5)$$

Where,  $\phi$  and  $\nabla\phi$  are the cell-centered value and its gradient in the upstream cell, and  $\mathbf{r}$  is the displacement vector from the upstream cell centroid to the face centroid. This formulation requires the determination of the gradient  $\nabla\phi$  in each cell. Finally, the gradient  $\nabla\phi$  is limited so that no new maxima or minima are introduced. The correction equation is controlled by a factor named relaxation factor.

#### 4.4 SIMPLE Pressure-Velocity Coupling

In this research, the Semi Implicit Method for Pressure-Linked Equation (SIMPLE) is the used as the pressure-velocity coupling method. It was introduced by Patankar and Spalding in the year 1972. For velocity and pressure, two adjacent staggered cells are considered as discussed above. The algorithm for the Semi Implicit Method for Pressure-Linked Equation (SIMPLE) is shown in Fig. 4.3.

In Ansys Fluent, the face values are momentum-weighted averaged instead of linear averaging in order to avoid unphysical checker-boarding of pressure [25] as ascribed by Rhie and Chow [28]. Ansys Fluent uses weighting factor based on  $a_p$  coefficients of discretized momentum equations and thus the face mass flux can be written as below:

$$\begin{aligned} J_f &= \rho_f \frac{a_{p,c_0} v_{n,c_0} + a_{p,c_1} v_{n,c_1}}{a_{p,c_0} + a_{p,c_1}} + d_f \left( \left( p_{c_0} + (\nabla p)_{c_0} \cdot \vec{r}_0 \right) - \left( p_{c_1} + (\nabla p)_{c_1} \cdot \vec{r}_1 \right) \right) \\ &= \hat{J}_f + d_f (p_{c_0} - p_{c_1}) \end{aligned} \quad (4.6)$$

Where,  $P_{c_0}$ ,  $P_{c_1}$  and  $v_{n,c_0}$ ,  $v_{n,c_1}$  are the pressures and normal velocities, respectively, within the two cells on either side of the face, and  $\hat{J}_f$  contains the influence of velocities in these cells. The term  $d_f$  is a function of  $\bar{a}_p$ , the average of the momentum equation  $a_p$  coefficients for the cells on either side of face  $f$ .

As per SIMPLE algorithm, the momentum equation is at first solved with a guessed pressure field,  $p^*$  and the resulting mass flux,  $J_f^*$  computed from the equation-4.7. If the values of face flux do not satisfy the continuity equation, then a correction  $J_f'$  is added to the face flux  $J_f^*$  so that the corrected face flux can be written as equation-4.8.

$$J_f^* = \hat{J}_f^* + d_f (p_{c_0}^* - p_{c_1}^*) \quad (4.7)$$

$$J_f = J_f^* + J_f' \quad (4.8)$$

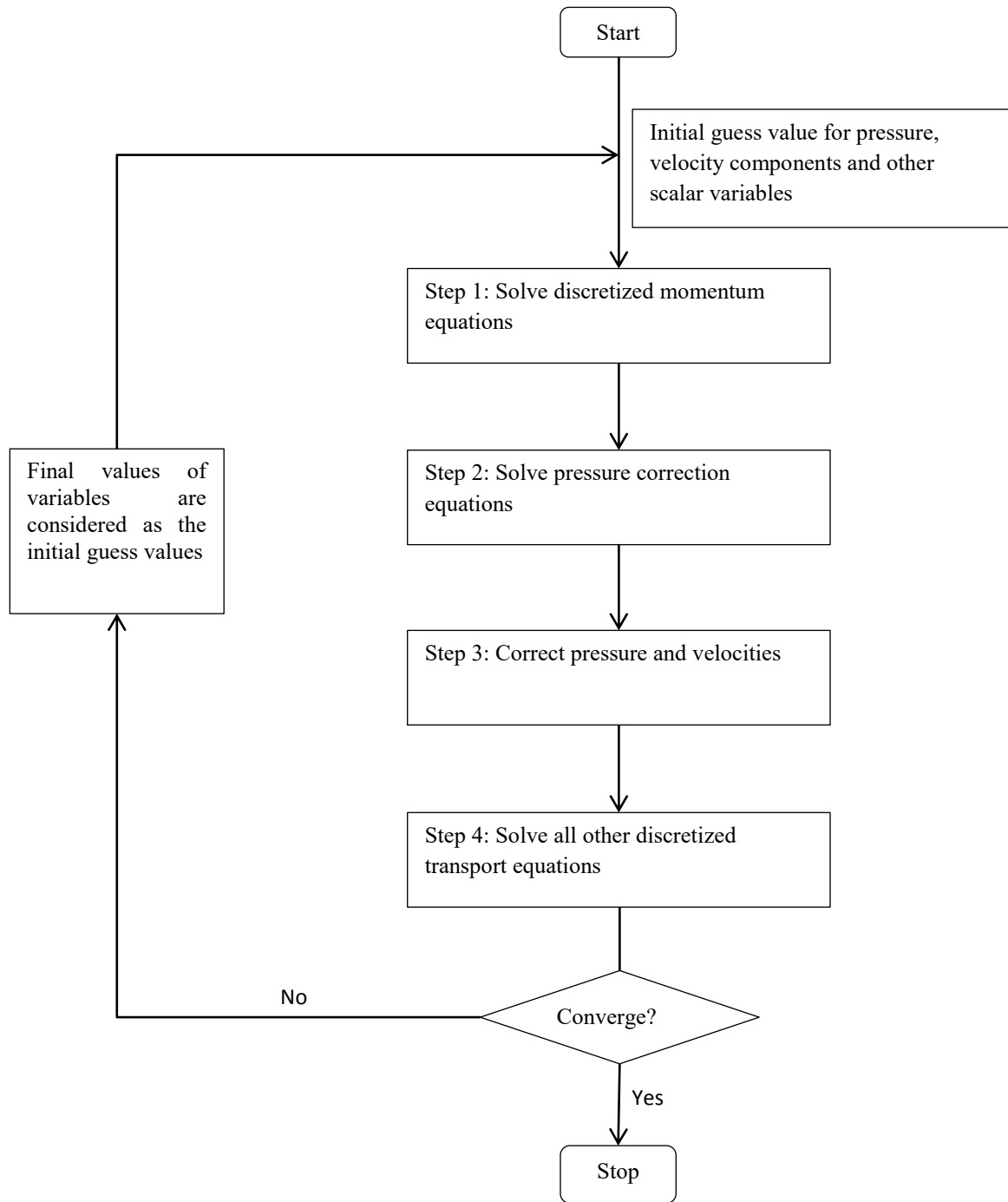


**Fig. 4.3:** Flow Chart for SIMPLE pressure velocity coupling method

The SIMPLE algorithm postulates that  $J_f'$  be written as

$$J_f' = d_f (p'_{c0} - p'_{c1}) \quad (4.9)$$

Where,  $p'$  is the cell pressure correction.

The SIMPLE algorithm substitutes the flux correction equations (Equation 4.8 and Equation 4.9) into the discrete continuity equation to obtain a discrete equation for the pressure correction  $p'$  in the cell. Once a solution is obtained, the cell pressure and the face mass flux are corrected using the following equations.

$$p = p^* + \alpha_p p' \quad (4.10)$$

$$J_f = J_f^* + d_f (p'_{c0} - p'_{c1}) \quad (4.11)$$

Here  $\alpha_p$  is the under-relaxation factor for pressure. The corrected face flux  $J_f$ , satisfies the discrete continuity equation identically during each iteration.

#### 4.5 Under-relaxation Factor

Under relaxation factor is used to control the correction equations. As shown in the pressure correction equation 4.10, if the value of under relaxation factor is large and if the guessed value is far away from final correct value, then the computation may be unstable. Larger values of under relaxation factors may also lead to divergence. But if it is too small, it will take too long time to converge. Hence, the under relaxation factor has to be large enough to move the iterative improvement forward and at the same time it has to be small enough to ensure stable computation and convergence.

#### 4.6 Shear Stress Transport (SST) $k-\omega$ Turbulence Modeling

The SST  $k-\omega$  model was developed by Menter in 1994. It is a two equation eddy viscosity turbulence model. This model predicts the turbulence by two partial differential variables, turbulent kinetic energy ( $k$ ) and specific rate of dissipation of the turbulence kinetic energy  $k$  into internal thermal energy ( $\omega$ ). The  $k-\omega$  model has the robust and accurate formulation to describe the near-wall region. The SST  $k-\omega$  model is

the blend of k- $\omega$  model at near-wall region and k- $\epsilon$  model at the free-stream region. The k- $\epsilon$  model is less sensitive to the inlet free-stream turbulence properties than the k- $\omega$  model. Hence, it is better to use k- $\epsilon$  model at free-stream or at far field.

The two transport equations for the SST k- $\omega$  model [27] is,

$$\frac{\partial}{\partial t}(\rho k) + \frac{\partial}{\partial x_i}(\rho k u_i) = \frac{\partial}{\partial x_j} \left[ \left( \mu + \frac{\mu_t}{\sigma_k} \right) \frac{\partial k}{\partial x_j} \right] + G_k - \rho \beta^* k \omega + S_k \quad (4.12)$$

and

$$\begin{aligned} \frac{\partial}{\partial t}(\rho \omega) + \frac{\partial}{\partial x_j}(\rho \omega u_j) \\ = \frac{\partial}{\partial x_j} \left[ \left( \mu + \frac{\mu_t}{\sigma_\omega} \right) \frac{\partial \omega}{\partial x_j} \right] + \frac{\alpha}{\nu_t} G_k - \rho \beta_i \omega^2 + 2(1 - F_1) \frac{\rho}{\omega \sigma_{\omega,2}} \frac{\partial k}{\partial x_j} \frac{\partial \omega}{\partial x_j} + S_\omega \end{aligned} \quad (4.13)$$

Where,

$\zeta_k$  and  $\zeta_\omega$  are turbulent Prandtl numbers for k and  $\omega$  respectively. They can be defined as

$$\sigma_k = \frac{1}{\frac{F_1}{\sigma_{k,1}} + \frac{1 - F_1}{\sigma_{k,2}}} \quad (4.14)$$

and

$$\sigma_\omega = \frac{1}{\frac{F_1}{\sigma_{\omega,1}} + \frac{1 - F_1}{\sigma_{\omega,2}}} \quad (4.15)$$

Also,  $\mu_t = \text{Turbulent viscosity} = \frac{\rho k}{\omega \max\left[\frac{1}{\alpha^*}, \frac{SF_2}{a_1 \omega}\right]}$ ; where S is the strain rate magnitude and

the coefficient  $\alpha^*$  damps the turbulent viscosity causing a low-Reynolds number correction.

$$\alpha^* = \alpha_\infty^* \left( \frac{\alpha_0^* + \frac{Re_t}{R_k}}{1 + \frac{Re_t}{R_k}} \right); \text{ here, } R_k = 6, Re_t = \frac{\rho k}{\mu \omega}, R_\omega = 2.95 \alpha^*, \alpha_0^* = \frac{\beta_i}{3}$$

$F_1$  and  $F_2$  are blending functions.

$$F_1 = \tanh(\Phi_1^4)$$

$$\Phi_1 = \min \left[ \max \left( \frac{\sqrt{k}}{0.09 \omega y}, \frac{500 \mu}{\rho y^2 \omega} \right), \frac{4 \rho k}{\sigma_{\omega,2} D_\omega^+ y^2} \right]$$

$$F_2 = \tanh(\Phi_2^4)$$

$$\Phi_2 = \max \left( 2 \frac{\sqrt{k}}{0.09 \omega y}, \frac{500 \mu}{\rho y^2 \omega} \right)$$

$D_\omega^+$  is the positive portion of the cross-diffusion term and  $y$  is the distance to the next surface.

The SST  $k$ - $\omega$  model is the blend of the standard  $k$ - $\omega$  and the standard  $k$ - $\epsilon$  model. To blend them together, the standard  $k$ - $\epsilon$  model has been transformed in equations based on  $k$  and  $\omega$ , which introduces the term called cross-diffusion term and symbolized with  $D_\omega$ .

$$D_\omega = 2(1 - F_1) \rho \frac{1}{\omega \sigma_{\omega,2}} \frac{\partial k}{\partial x_j} \frac{\partial \omega}{\partial x_j} \quad (4.16)$$

and

$$D_\omega^+ = \max \left[ 2 \rho \frac{1}{\omega \sigma_{\omega,2}} \frac{\partial k}{\partial x_j} \frac{\partial \omega}{\partial x_j}, 10^{-10} \right] \quad (4.17)$$

$G_k$  = generation of turbulence kinetic energy due to mean velocity gradients

$$= \min \left( -\rho \overline{u_i u_j} \frac{\partial u_j}{\partial x_i}, 10 \rho \beta^* k \omega \right)$$

$G_\omega =$  generation of  $\omega = \frac{\alpha}{\nu_t} G_k$  ; here,  $\nu_t$ =kinematic eddy viscosity,  $\alpha = \frac{\alpha_\infty}{\alpha^*} \left( \frac{\alpha_0 + \frac{Re_t}{R_\omega}}{1 + \frac{Re_t}{R_\omega}} \right)$  and

$$R_\omega = 2.95\alpha^*$$

For SST k- $\omega$  model,  $\alpha_\infty$  is given by,

$$\alpha_\infty = F_1\alpha_{\infty,1} + (1 - F_1)\alpha_{\infty,2}$$

Where,

$$\alpha_{\infty,1} = \frac{\beta_{i,1}}{\beta_\infty^*} - \frac{\kappa^2}{\sigma_{w,1}\sqrt{\beta_\infty^*}}$$

$$\text{And } \alpha_{\infty,2} = \frac{\beta_{i,2}}{\beta_\infty^*} - \frac{\kappa^2}{\sigma_{w,2}\sqrt{\beta_\infty^*}}$$

$$\kappa=0.41$$

Note that in the high-Reynolds number form of the k- $\omega$  model,  $\alpha = \alpha_\infty = 1$  and  $\alpha^* =$

$$\alpha_\infty^* = 1$$

$$\beta_i = F_1\beta_{i,1} + (1 - F_1)\beta_{i,2}$$

The values of constants are,

$$\zeta_{k,1} = 1.176, \zeta_{\omega,1} = 2.0, \zeta_{k,2} = 1.0, \zeta_{\omega,2} = 1.168, \alpha_1 = 0.31, \beta_{i,1} = 0.075, \beta_{i,2} = 0.0828, \alpha_0 = 1/9, \alpha_\infty = 0.52, \alpha_\infty^* = 1, R_\beta = 8, \zeta^* = 1.5, M_{t0} = 0.25, \beta_\infty^* = 0.09$$

CHAPTER: 5

# **COMPUTATIONAL MODEL**



## 5.1 Geometric Model

Performance of three different models of H-rotor VAWT is studied in this thesis. These models are shown in Fig. 5.1. Single Layered H-Rotor VAWT consists of 3 blades is shown in Fig. 5.1(a). In Fig 5.1(b) and Fig. 5.1(c) six bladed double layered H-rotor VAWTs are presented. All the models are consists of same NACA 0012 blades as the thin airfoils are more efficient than thick airfoil. Chord lengths of all the NACA 0012 blades are also equal and the value is 85.8mm.

The Double Layered H-Darrieus VAWT concept is novel in the field of Vertical Axis Wind Turbine. For the Double Layered H-Darrieus VAWTs as shown in Fig. 5.1(b) and 5.1(c), the inner layer radius is considered half of the outer layer radius.

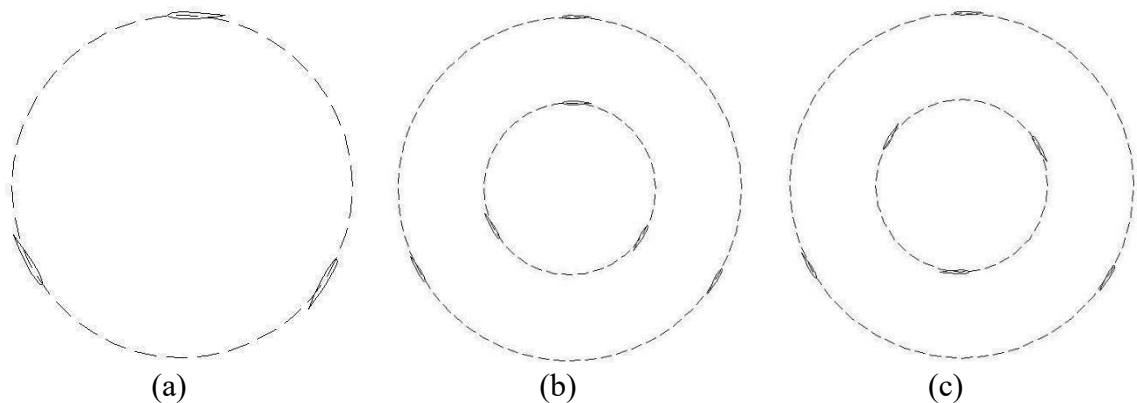


**Fig. 5.1:** Geometric Model of Vertical Axis Wind Turbine (a) 3 Bladed, Single Layered (b) 6 Bladed, Double Layered (In-line) (c) 6 Bladed, Double Layered (Staggered)

The inner layer and outer layer blades are in same angular position for 6 Bladed, Double Layered (In-line) VAWT as shown in Fig. 5.1(b). But for 6 Bladed, Double Layered (Staggered), as shown in Fig. 5.1(c), the inner layer blades are  $60^\circ$  ahead than the outer layer blades

## 5.2 Computational Domain

The size of the computational domain should be larger enough to allow the vortices to shed off and at the same time it should be smaller enough to save computational time and expense. In this research, the computational domain is 10 times wider and 15 times longer than the turbine diameter. The downstream of the domain is 10D away from the center of the turbine.

For solving the rotational vertical axis wind turbine, the entire computational domain is divided into two different zones; Stationary zone and Rotating zone. These two zones are connected at interface boundary. The diameter of rotational zone is 1.25 times of the turbine diameter as shown in Fig. 5.2.

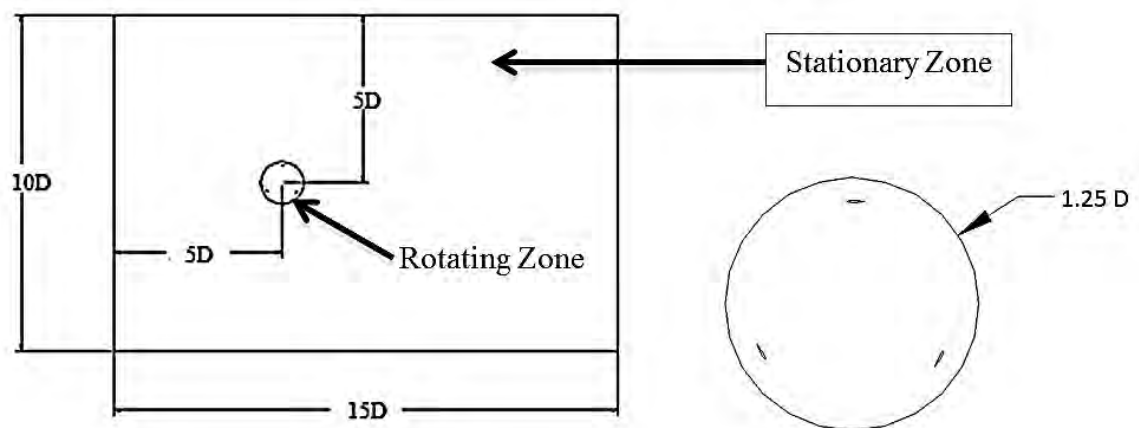


**Fig. 5.2:** Computational Domain of Vertical Axis Wind Turbine [15]

## 5.3 Mesh Generation

Whole computational domain is divided into control volumes using tri-mesh technique. Gambit is used for Meshing. Density of mesh is higher near the airfoil region. No. of mesh on a blade surface is about 1720 with mesh size 0.1 mm. Mesh size increases from the airfoil surface to outer direction as shown in table 5.1. The generated mesh is shown in Fig. 5.3.

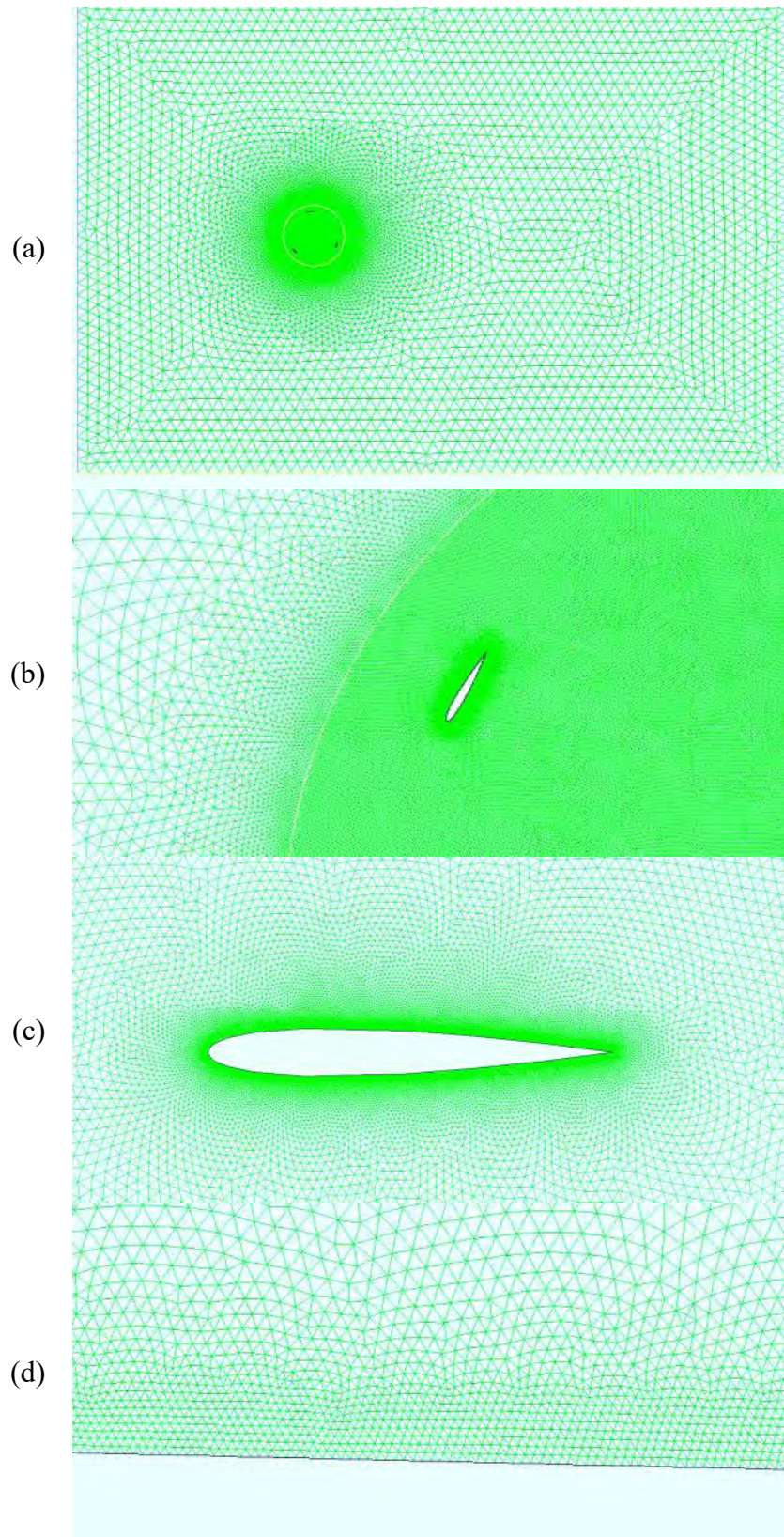


**Fig. 5.3:** Generated Mesh (a) full domain (b) mesh near interface zone (c) around airfoil (d) very close to airfoil

**Table 5.1:** Mesh Sizing

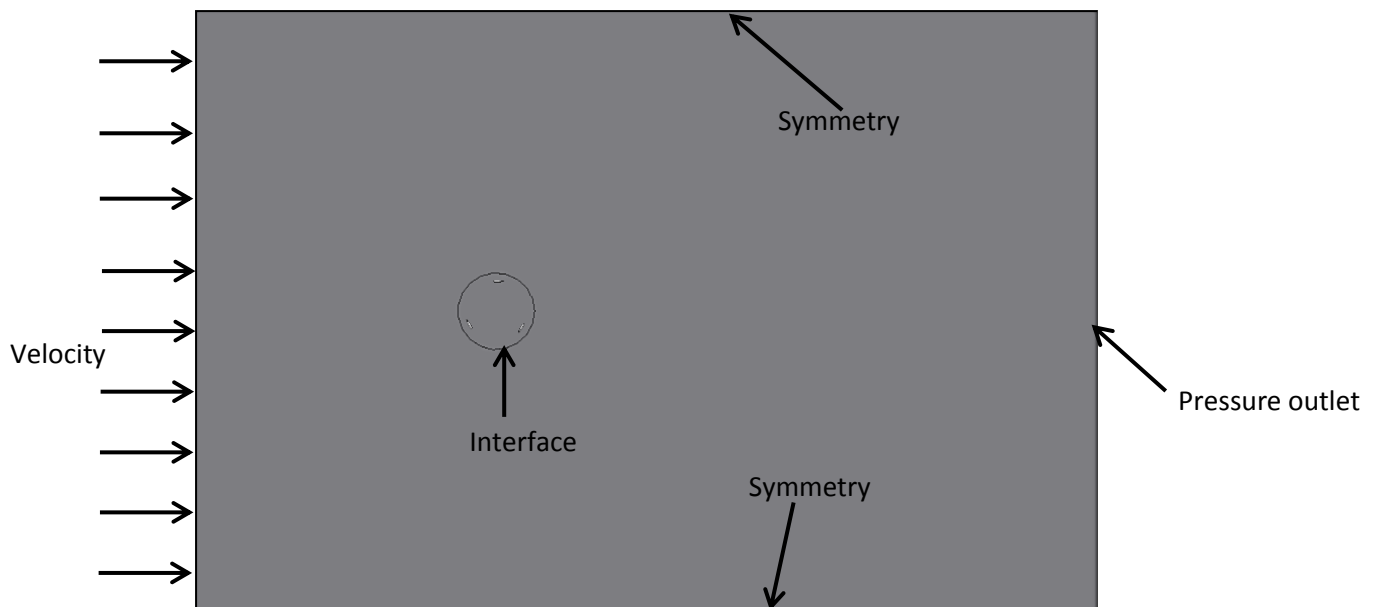
	For Rotating Zone:	For Stationary Zone
Start size	0.0001 m (at airfoil)	0.003 m (at interface)
Growth Rate	1.1	1.1
Size Limit	0.003 m	0.250m

**Table 5.2:** Total no. of Cells

Type of VAWT	Solidity	Total no. of cells
Three bladed Single Layered VAWT	0.5	493,016
	0.7	317,952
	1.0	183,014
Six bladed Double Layered In-Line VAWT	0.75	1,596,274
	1.05	946,324
	1.5	609,280
Six bladed Double Staggered VAWT	1.5	608,188

#### 5.4 Boundary Conditions

The boundary types considered for the numerical simulation is shown in Fig. 5.4. Velocity Inlet and Pressure outlet are used as boundary types respectively for upstream and downstream boundaries of the computational domain. Both top and bottom boundaries are defined as Symmetry. The interface of the Rotating and Stationary zones is assigned as Interface type boundary. All blades are defined as wall type boundary.

**Fig 5.4:** Boundary Types

For k- $\omega$  method, value of kinetic energy (k) and specific dissipation rate ( $\omega$ ) at inlet boundary are required for simulation. Following equations are used to find these values at inlet.

Kinetic Energy at Inlet,

$$= \frac{1}{2} (u_x^2 + u_y^2 + u_z^2)$$

Dissipation Rate at Inlet,

$$\omega = \frac{\varepsilon}{k\beta^*}$$

$$\text{Where, } \varepsilon = c_\mu^{3/4} \beta^{3/2} l^{-1}$$

Here,  $c_\mu = \beta^* = 0.009$  and  $l = 0.07 \times \text{Characteristic length}$  (i.e. chord length)

Inlet Velocity,  $u = u_x = 4\text{m/s}$ ; Outlet Pressure: 1 atm; Inlet Kinetic energy,  $k = 8 \text{ m}^2/\text{s}^2$

Inlet Specific Dissipation Rate,  $\omega = 1528.97\text{s}^{-1}$

## 5.5 Numerical Method

For numerical analysis of the H-rotor VAWT, unsteady Reynolds Average Navier-Stokes equations is solved. Considering the turbulence present in the system, k- $\omega$  SST (Shear Stress Transport) turbulence model is preferred over other turbulence model as recommended by different researchers [11, 17]. This is more reliable and effective to get precise result. This model has the combined advantages of achieving good result in the inner parts of boundary layer by using k- $\omega$  formulation and maintaining the far-field stability by switching to k- $\varepsilon$  model in free-stream. Second order upwind discretization scheme is used for all cases because of its lower numerical diffusivity and reliability. SIMPLE pressure-velocity coupling is considered for the simulation.

In order to solve the rotating body of VAWT, moving mesh technique is used. The time steps was chosen such that, each rotation of rotating zone is about three degree. The required values for numerical calculation are shown below in table 5.2.

**Table 5.2:** Values for Numerical Calculation.

No. of Layers	no. of blades, N	Solidity, $\sigma$	inner layer radius, $R_i$ (m)	Outer layer radius, $R_o$ (m)	tip speed ratio, $\lambda$	rotational speed, $\Omega = u\lambda/R_o$ (rad/s)		
2	6	0.75	0.515	1.03	3.25	12.62626		
					4	15.54002		
					4.5	17.48252		
					4.75	18.45377		
					5.25	20.39627		
		1.05	0.3677	0.7354	3.21	17.45921		
					3.5	19.03652		
					3.75	20.39627		
					4	21.75602		
					4.25	23.11577		
		1.5	0.2575	0.515	1	7.77001		
					2	15.54002		
					2.5	19.42502		
					3	23.31002		
					3.5	27.19503		
1	3	0.5	N/A	0.515	2	15.53398		
					2.5	19.41748		
					3	23.31002		
					3.25	25.25253		
					3.5	27.19503		
		0.7	N/A	0.3677	4.5	34.96503		
					2	21.75602		
					2.5	27.19503		
		1	N/A	0.2575	3	32.63403		
					1.5	23.30097		
					2.25	34.95146		
							2.5	38.83495

For present calculation, the convergence criterion is set to  $10^{-4}$ . Moment created by the turbine is also monitored to ensure the convergence of solution. The moment created by the turbine gives a periodic curve. The solution is considered as converged, when difference in amplitude is less than 5%. In order to achieve this accuracy, the numerical simulation is run for 8-10 revolutions approximately [12].

CHAPTER: 6

# **RESULTS AND DISCUSSIONS**

## 6.1 Validation and Grid independence Test

### 6.1.1 Validation

The present numerical technique is validated by comparing the result of numerical simulation on H-rotor VAWT with the results found by Gosselin et al. [8] considering the same blade profile (NACA 0015) and the same boundary conditions. The inlet boundary is considered as „Uniform Velocity Inlet“, top and bottom boundary are considered as „Symmetry“, Outlet boundary is considered as „Pressure Outlet“ and blade surfaces are considered as „Wall“ type boundary condition. The wind turbine solidity is considered as 0.5486 and k- $\omega$  SST turbulence model is chosen for the numerical simulation. These are also same as used in the numerical simulation performed by Gosselin et al. [8]. The result with convergence criteria  $10^{-4}$  shows the qualitative agreement with the result of Gosselin et al., which can be observed in table 6.1 and Fig. 6.1(a). Thus the present numerical code is used for next numerical analysis.

**TABLE 6.1.** Comparative result for wind turbine with NACA 0015

$\lambda$	$C_t$	$C_p$	$C_p$ -Gosselin
2.75	0.094196	0.259038	0.25
3	0.119667	0.359	0.36
3.25	0.109591	0.35617	0.362
3.5	0.092186	0.322652	0.34
4	0.061882	0.247528	0.26

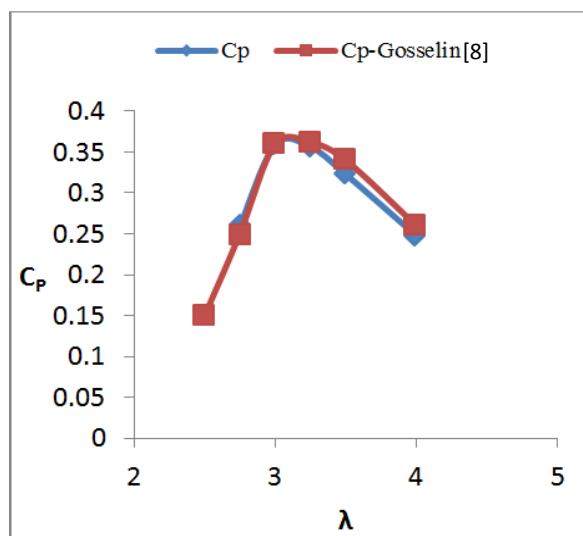


**Fig. 6.1:** (a) Comparison of  $C_p$  vs.  $\lambda$  curve for validation



### 6.1.2 Grid Independence Test

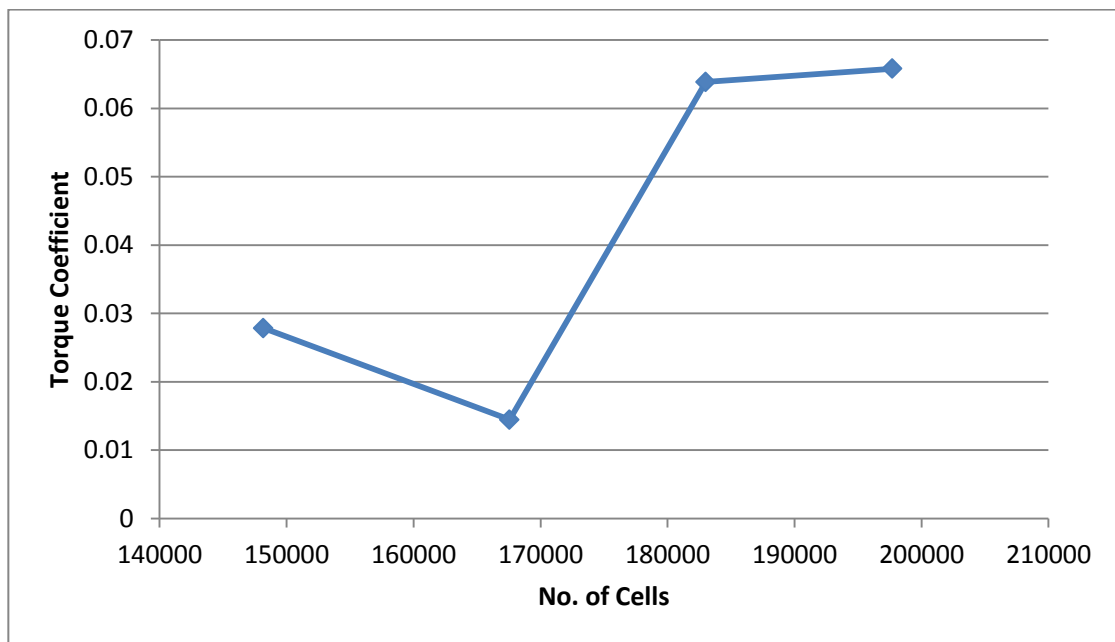


**Fig. 6.2:** Grid Independence Test

There are 183,014 no of cells present in the mesh is generated as per the description in article 5.3 and table 5.2. The independence of the mesh is checked for this numerical study. Fig.6.2 is showing the comparison of torque coefficient and the nos. of cells in the numerical model. It can be depicted that, if the no of cells is more than 183,014, the output of torque coefficient will not change significantly. Hence, this meshing technique and size as mentioned in table 5.1 and 5.2 can be applied for the present numerical study.

## 6.2 Performance of Single Layered H-Darrieus Vertical Axis Wind Turbine

### 6.2.1 Relationship between torque coefficient and tip speed ratio

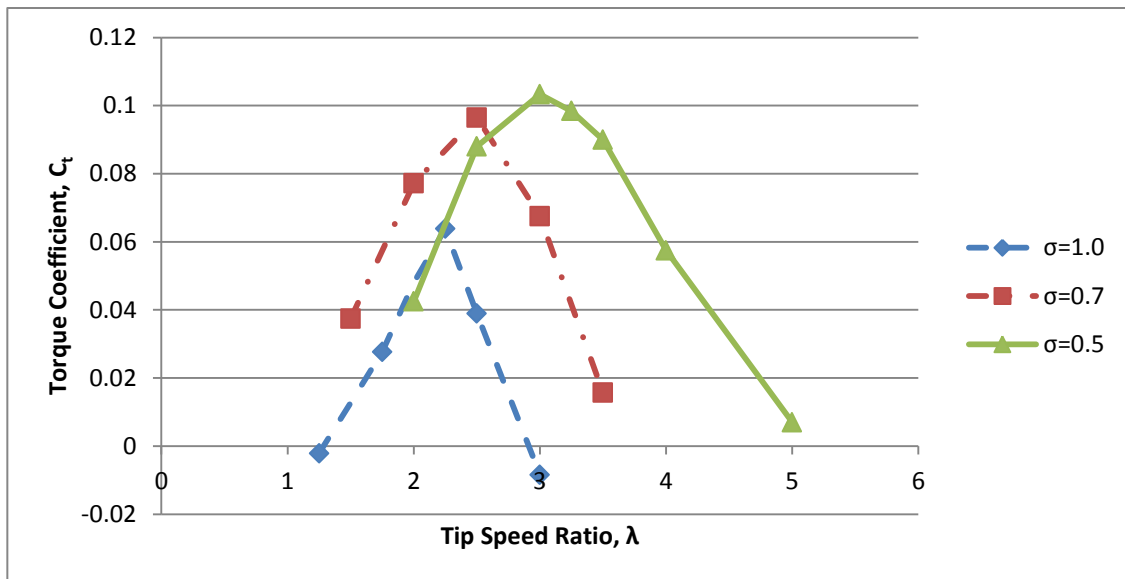


**Fig. 6.3:**  $C_t$  vs.  $\lambda$  for single layered 3 bladed H-rotor VAWT

The performance analysis of the Single Layered H-Darrieus VAWT with solidity 0.5, 0.7 and 1.0 is studied in this thesis. The torque coefficient found in the study is shown in Fig. 6.3 with respect to the tip speed ratio for different solidities. The trend visible in the Fig 6.3 is that, at first the torque coefficient increases with the increase in tip speed ratio up to a certain limit and then decreases with further increase in tip speed ratio. For Single layered H-Darrieus VAWT with solidity  $\zeta=0.5$ , the torque coefficient  $C_t$  is found as 0.0425 at a tip speed ratio,  $\lambda=2$ . It is also shown from Fig. 6.3, the torque coefficient increases with the tip speed ratio until a maximum value,  $(C_t)_{\max} = 0.1033$  at  $\lambda=3$  and further increment in tip speed ratio reduces the torque coefficient. At  $\lambda=5$ , the torque coefficient is found 0.007.

For solidity  $\zeta=0.7$ , the torque coefficient is maximum at  $\lambda=2.5$  and the value of  $(C_t)_{\max}$  is 0.0965336. At tip speed ratios either lower of higher than  $\lambda=2.5$ , the torque

coefficient is lower. At  $\lambda=1.5$ , the torque coefficient  $C_t$  is equal to 0.3747133 and at  $\lambda=3.5$ ,  $C_t$  is equal to 0.1571857.

The  $C_t$  vs.  $\lambda$  curve for single layered H-rotor VAWT from Fig. 6.3 with the solidity,  $\zeta=1.0$  also shows the similar nature. At  $\lambda=1.75$ , the torque coefficient  $C_t$  is equal to 0.00276594. The maximum torque coefficient  $(C_t)_{\max}= 0.063864$  is achieved at  $\lambda=2.25$ . Then at  $\lambda=2.5$ , the torque coefficient  $C_t$  is equal to 0.0389556.

It is visible from the  $C_t$  vs.  $\lambda$  curves that, at first the torque coefficient increases up to a certain limit and then it reduces with the increase in tip speed ratio. Basically, when a blade goes through the wind, it leaves turbulence behind it. Hence, the tip speed ratio is required to be low enough so that the disturbed wind gets sufficient time to be uniform again before the next blade faces that wind. On the contrary, if the tip speed is too high, then the rotating blades will act like a solid wall and obstruct the wind flow. This again reduces the torque coefficient [29]. This is the reason for the bell shaped  $C_t$  vs.  $\lambda$  curves as shown in Fig. 6.3. Moreover, another reason behind this is also discussed in article 3.5.

From the Fig. 6.3, it can be observed that, maximum torque coefficient of single layered VAWT is the highest for the H-rotor with solidity 0.5. Then with the increase in solidity the maximum torque coefficient decreases and achieved at lower tip speed ratio. It can be observed from the figure that, torque coefficient of wind turbine is proportional to the tip speed ratio, however inversely proportional to the solidity.

**Table 6.2:** Relationship between  $C_t$  and  $C_p$  with  $\lambda$  for Single Layered VAWT with  $\zeta = 0.5$ 

$\lambda$	$C_t$	$C_p$
2	0.0425	0.085
2.5	0.088	0.22
3	<b>0.103333</b>	0.31
<b>3.25</b>	0.098462	<b>0.32</b>
3.5	0.09	0.315
4	0.0575	0.23
5	0.007	0.035

**Table 6.3:** Relationship between  $C_t$  and  $C_p$  with  $\lambda$  for Single Layered VAWT with  $\zeta = 0.7$ 

$\lambda$	$C_t$	$C_p$
1.5	0.03747133	0.056207
2	0.077214	0.154428
<b>2.5</b>	<b>0.0965336</b>	<b>0.241334</b>
3	0.06754967	0.202649
3.5	0.01571857	0.055015

**Table 6.4:** Relationship between  $C_t$  and  $C_p$  with  $\lambda$  for Single Layered VAWT with  $\zeta = 1.0$ 

$\lambda$	$C_t$	$C_p$
1.25	-0.0021184	-0.002648
1.75	0.00276594	0.0048404
<b>2.25</b>	<b>0.063864</b>	<b>0.143694</b>
2.5	0.0389556	0.097389
3	-0.00841	-0.02523

### 6.2.2 Relationship between power coefficient and tip speed ratio

The change of power coefficient ( $C_p$ ) with the change in tip speed ratio ( $\lambda$ ) for a single layered H-Darrieus VAWT is shown in Fig. 6.4. This figure is showing  $C_p$  vs.  $\lambda$  curve for three different solidity ( $\zeta=1.0$ , 0.7 and 0.5). From the  $C_p$  vs.  $\lambda$  curve for  $\zeta=1.0$ , it can be seen that, at  $\lambda=1.75$ , the power coefficient ( $C_p$ ) is equal to 0.0048404. The power coefficient rises up to 0.143694 at  $\lambda=2.25$ . Then the power coefficient starts to fall with further increase in tip speed ratio.

For H-rotor VAWT with solidity  $\zeta=0.7$ , the power coefficient is 0.056207 at  $\lambda=1.5$ . Then it increases to  $C_p=0.241334$  at  $\lambda=2.5$ . Further increase in tip speed ratio, power coefficient decreases to  $C_p=0.055015$  at  $\lambda=3.5$ .

For the H-Darrieus vertical axis wind turbine with solidity 0.5, the similar pattern of  $C_p$  vs.  $\lambda$  curve is observed. The maximum  $C_p$  is 0.32 and this maximum power coefficient is achieved at  $\lambda=3.25$ . This H-rotor VAWT with  $\zeta=0.7$  is studied from  $\lambda=2$  to  $\lambda=5$ . It is also clear from the Fig. 6.4 that the range of tip speed ratio for positive power coefficient is wider for H-rotor VAWT with lower solidity.

The maximum power coefficient for H-rotor VAWT with  $\zeta=0.5$  is the highest among the H-rotor VAWTs with other different solidity values. The maximum power coefficient for H-Darrieus VAWT with  $\zeta=0.7$  is 40.46% higher than the maximum  $C_p$  for H-Darrieus VAWT with  $\zeta=1.0$  and 55.1% lower than the  $(C_p)_{\max}$  of H-Darrieus VAWT with  $\zeta=0.5$ . Therefore, it can be said that with the decrease in solidity, the maximum power coefficient of a Vertical Axis Wind Turbine increases.

It is also evident that, the maximum power coefficient for  $\zeta=1.0$ ,  $\zeta=0.7$  and  $\zeta=0.5$  are achieved at tip speed ratio  $\lambda=2.25$ ,  $\lambda=2.5$  and  $\lambda=3.25$  respectively. So, it is completely understandable that, as the solidity of the vertical axis H-Darrieus wind turbine increases, the VAWT achieves its maximum  $C_p$  at lower tip speed ratio.

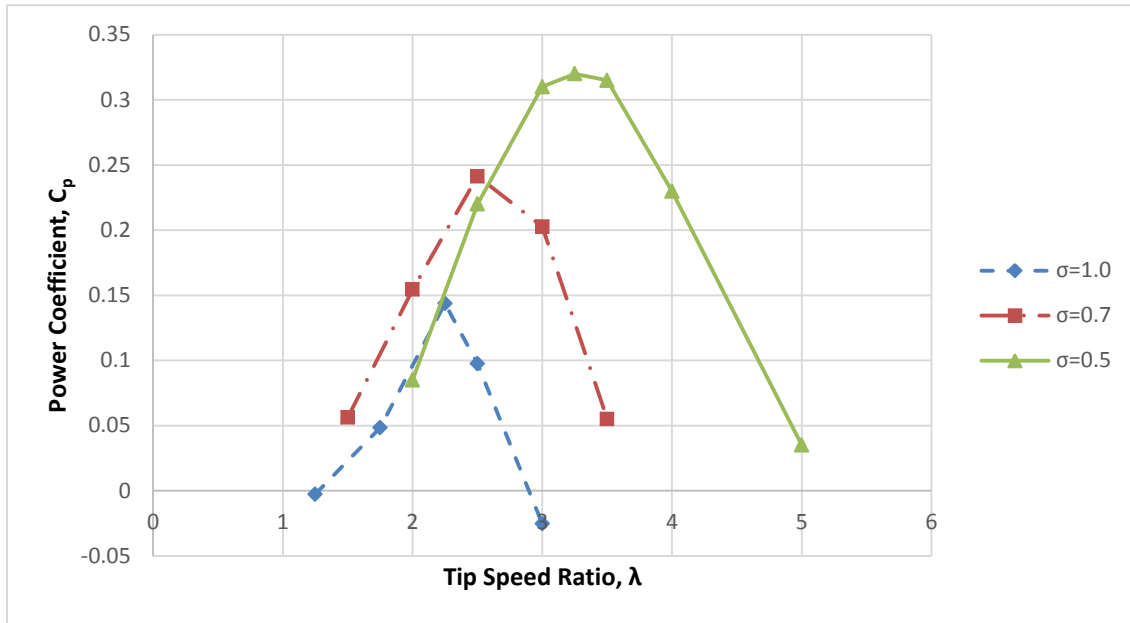


**Fig. 6.4:**  $C_p$  vs.  $\lambda$  for single layered 3 bladed VAWT

### 6.2.3 Relationship between torque coefficient and angle of rotation

For the Single layered H-Darrieus VAWT with  $\zeta=0.5$ , peak  $C_t=0.41265$  is achieved at the tip speed ratio,  $\lambda=3.25$  and the blade angular position  $\theta=79.9^\circ$ . For the solidity  $\zeta=0.7$ , the peak  $C_t$  is found 0.23197 at  $\lambda=3$  &  $\theta=99^\circ$  and at the same time for the solidity  $\zeta=1.0$ , the peak  $C_t$  is 0.2864 at  $\lambda=2.25$  and  $\theta=99^\circ$ . At this tip speed ratio  $\lambda=2.25$ , the  $C_t$  and  $C_p$  for single layered VAWT with  $\zeta=1.0$  are also maximum as shown in fig 6.3 and fig 6.4 respectively. However, for  $\zeta=0.5$  and  $\zeta=0.7$ , though the peak values of the torque coefficients of an individual blade are achieved at  $\lambda=3.25$  and  $\lambda=3$  respectively, values of  $(C_t)_{\max}$  of the vertical axis wind turbine are found at  $\lambda=3$  and  $\lambda=2.5$ . Because when the turbines with solidity  $\zeta=0.5$  and  $\zeta=0.7$  rotates at  $\lambda=3.25$  and  $\lambda=3$ , each blade consumes torque and power in downstream side. This reduces the average torque generation by a single blade and hence the torque coefficient of the turbine is also reduced.

For these single layered VAWTs, torque is mainly generated at the upstream side of the turbine. In the downstream side, the torque coefficient of an individual blade is negative. Only exception is the single layered VAWT with  $\zeta=0.7$  at  $\lambda=2$ , where it generates very small positive torque. That means, the blade at downstream side of single layered VAWT uses the torque generated by the upstream side blades to rotate. Hence the downstream side can be said as the consumption side of the turbine.

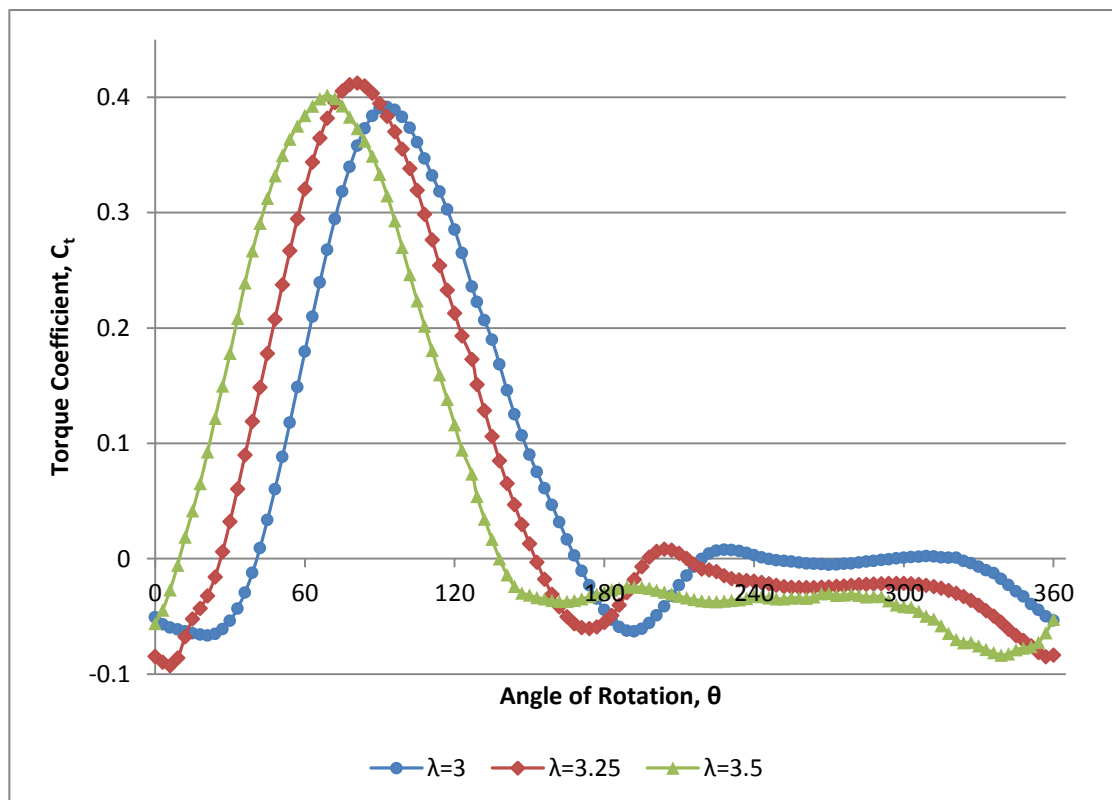


**Fig. 6.5:**  $C_t$  vs.  $\theta$  for  $\zeta=0.5$  Single layered H-Darrieus VAWT (max  $C_p$  at  $\lambda=3.25$ )

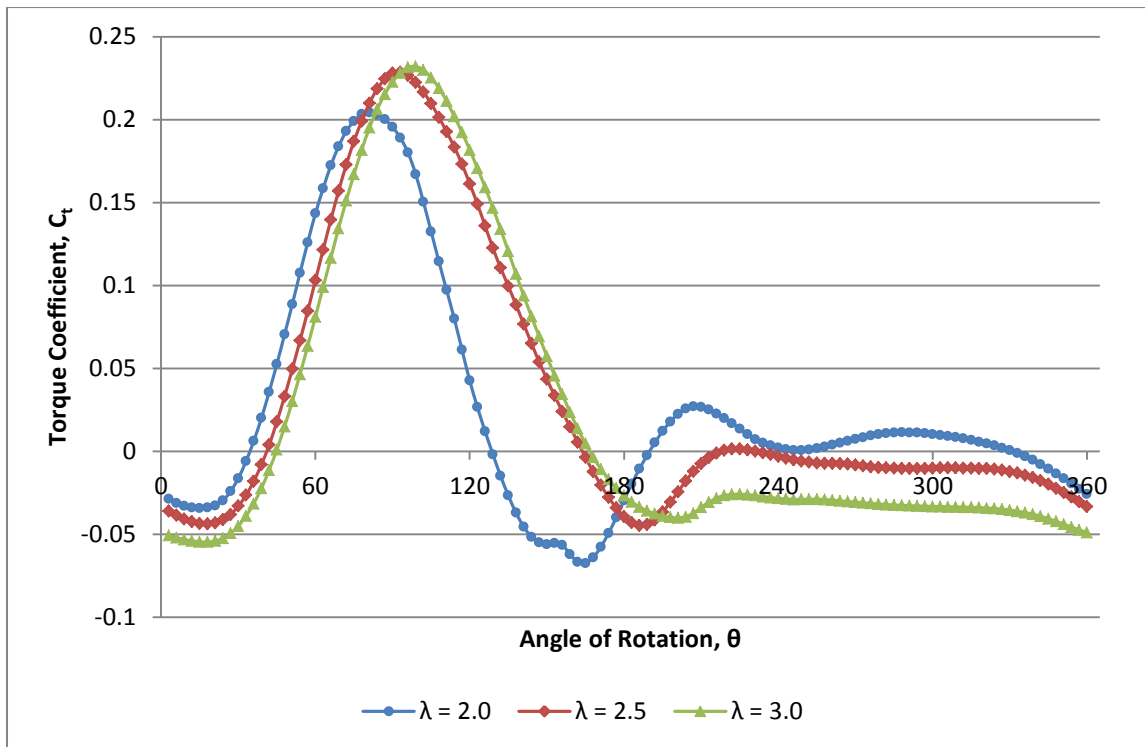


**Fig. 6.6:**  $C_t$  vs.  $\theta$  for  $\zeta=0.7$  Single layered H-Darrieus VAWT (max  $C_p$  at  $\lambda=2.5$ )

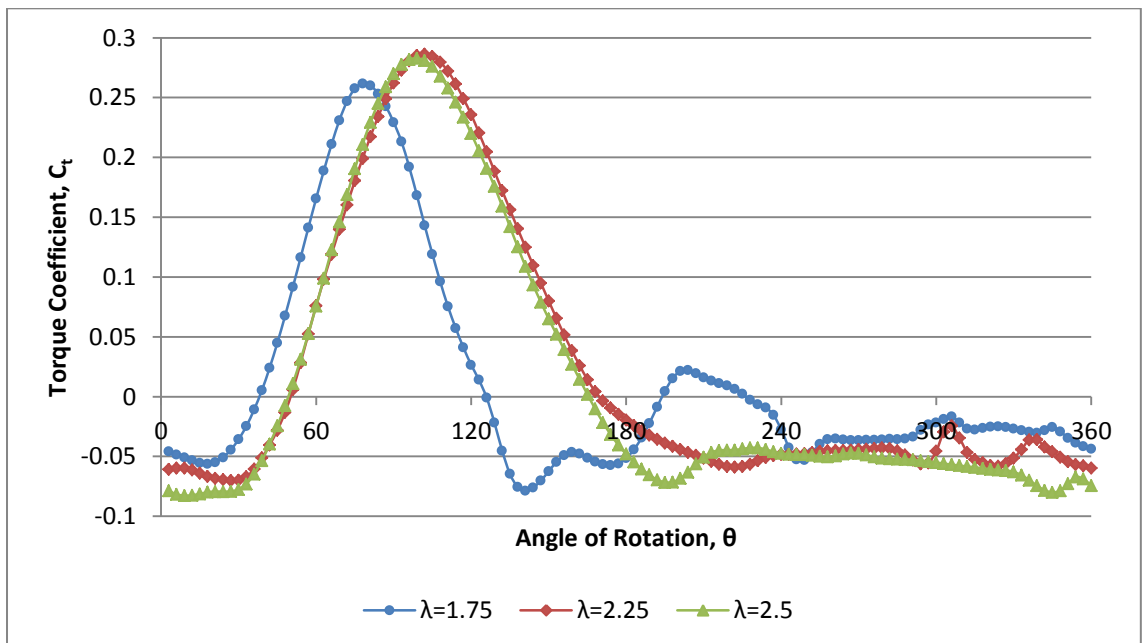


**Fig. 6.7:**  $C_t$  vs.  $\theta$  for  $\zeta=1.0$  Single layered H-Darrieus VAWT (max  $C_p$  at  $\lambda=2.25$ )

It can also be observed from Fig. 6.5 to Fig. 6.7 that, an individual blade consumes less torque when it rotates at lower tip speed ratio. Even for some cases, an individual blade may generate torque, when it rotates at a tip speed ratio lower than the tip speed ratio for  $(C_p)_{\max}$ . For this reason, the average torque coefficient of VAWT becomes



maximum at  $\lambda=3$  for single layered H-rotor VAWT with  $\zeta=0.7$  and at  $\lambda=2.5$  for single layered H-rotor VAWT with  $\zeta=0.5$ .

#### 6.2.4 Velocity Contour and Velocity Vectors

The velocity contours depicted in the figures for Fig. 6.8 to Fig. 6.13 show that, at downstream side the velocity of wind decreases. Because a portion of the kinetic energy of wind is used by the upstream turbine blades for generating torque and power. Due to this fact, the blades in downstream side get less available kinetic energy to generate power. More over when a blade rotates at a higher speed and the power is not present in the wind then it use the power and torque generated by the upstream blades. The higher the speed is, the higher the torque consumed by the blades at downstream side of VAWT.

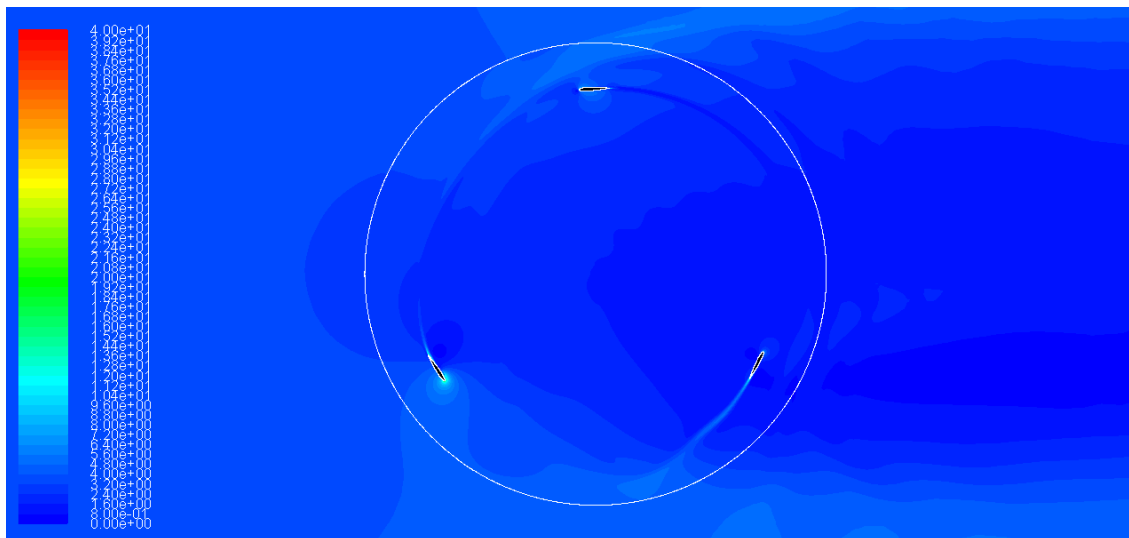


**Fig. 6.8:** Velocity contour of 3 Bladed Single layered H – Rotor VAWT; Solidity 0.5,  $\lambda=3.25(0 \text{ degree})$

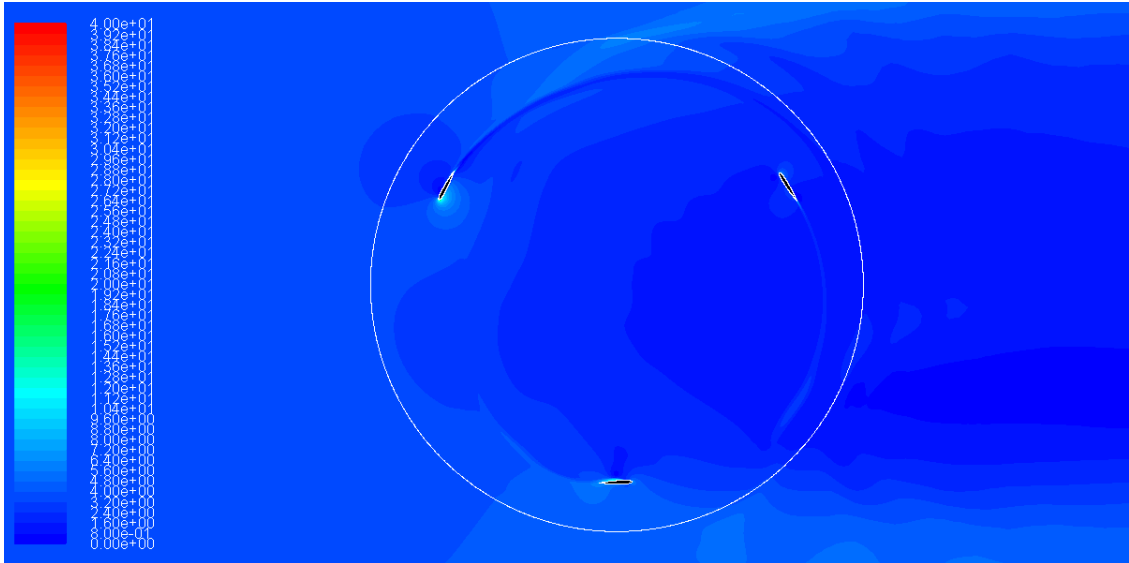


**Fig. 6.9:** Velocity contour of 3 Bladed Single layered H – Rotor VAWT; Solidity 0.5,  $\lambda=3.25(60 \text{ degree})$

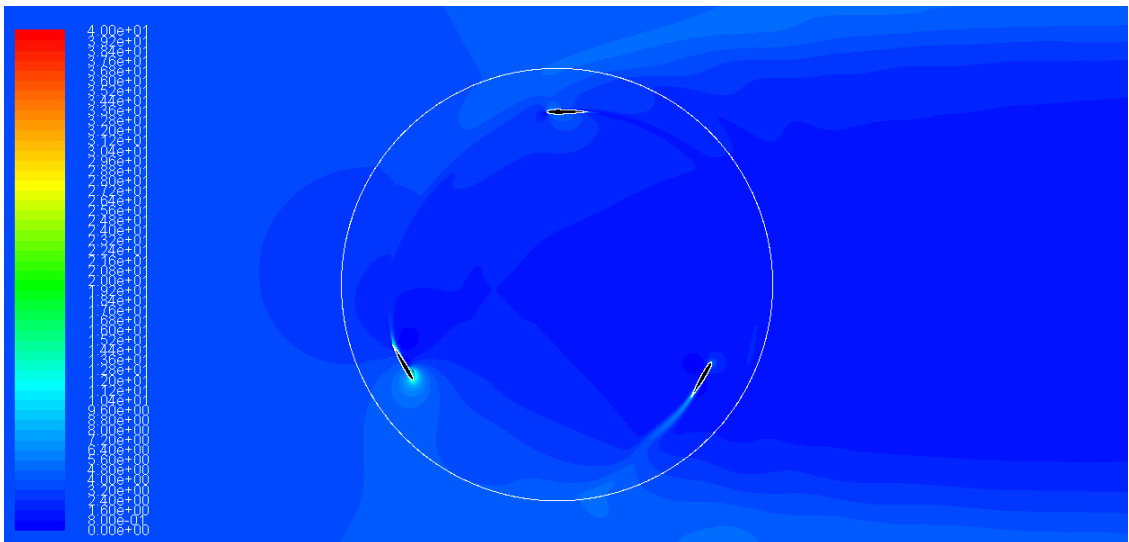


**Fig. 6.10:** Velocity contour of 3 Bladed Single layered H – Rotor VAWT; Solidity 0.7,  $\lambda=2.5(0 \text{ degree})$

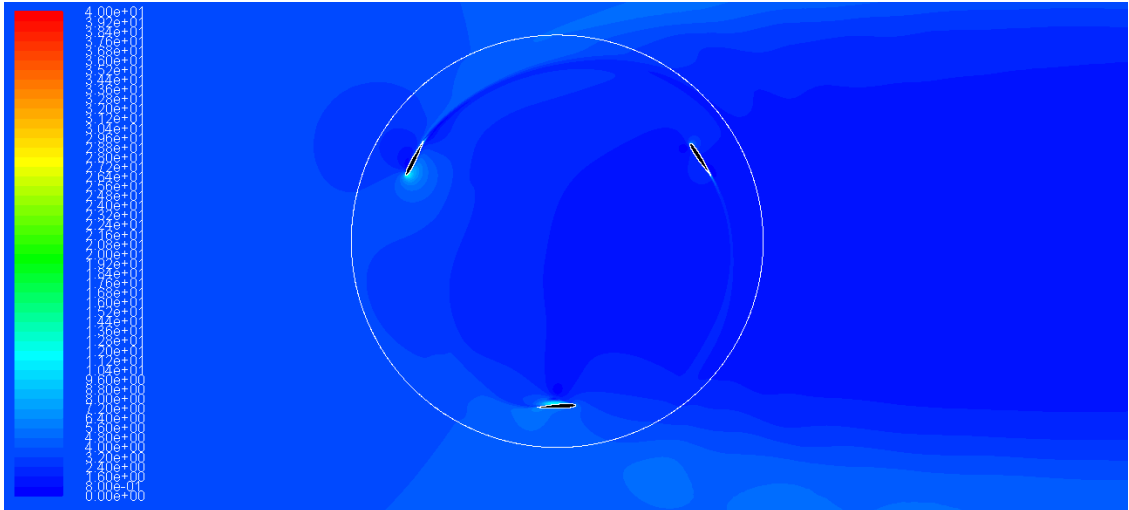


**Fig. 6.11:** Velocity contour of 3 Bladed Single layered H – Rotor VAWT; Solidity 0.7,  
 $\lambda=2.5$ (60 degree)

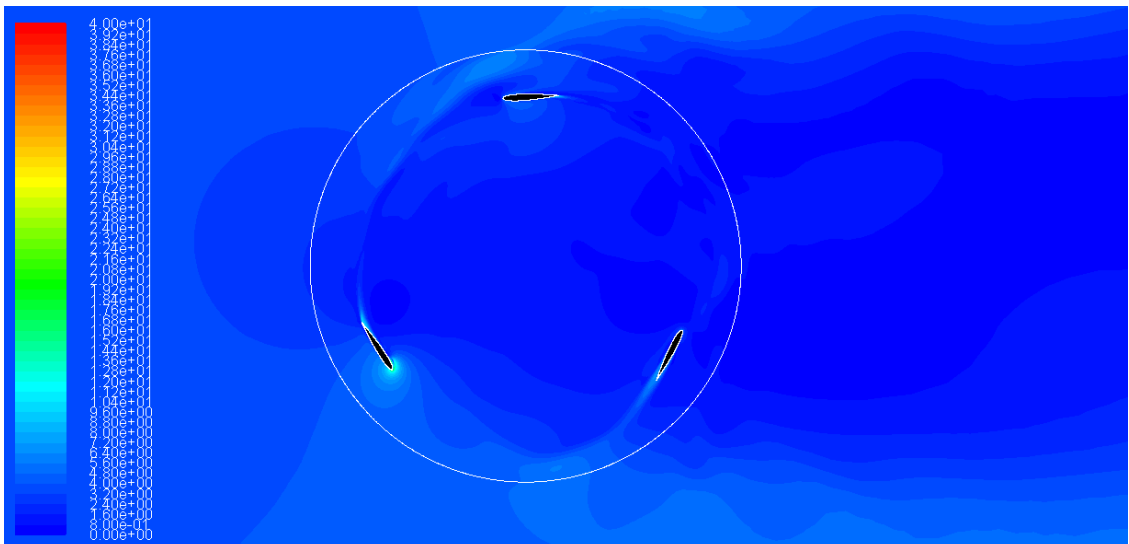


**Fig. 6.12:** Velocity contour of 3 Bladed Single layered H – Rotor VAWT; Solidity 1.0,  
 $\lambda=2.25$  (0 degree)

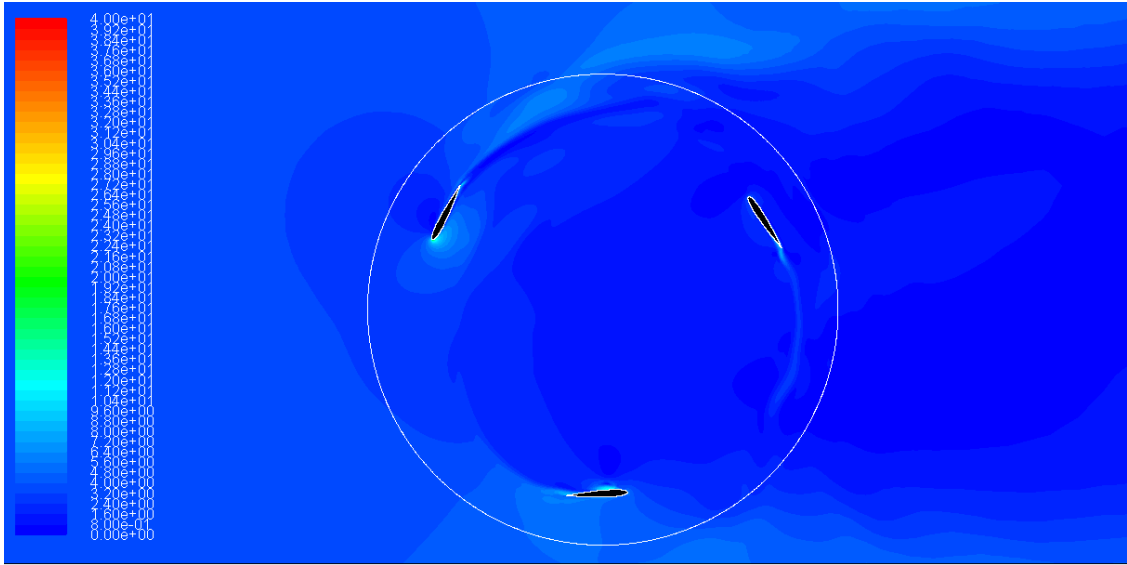


**Fig. 6.13:** Velocity contour of 3 Bladed Single layered H – Rotor VAWT; Solidity 1.0,  $\lambda=2.25$  (60 degree)

The Velocity vectors around the blade are shown in Fig 6.14 to Fig 6.16.

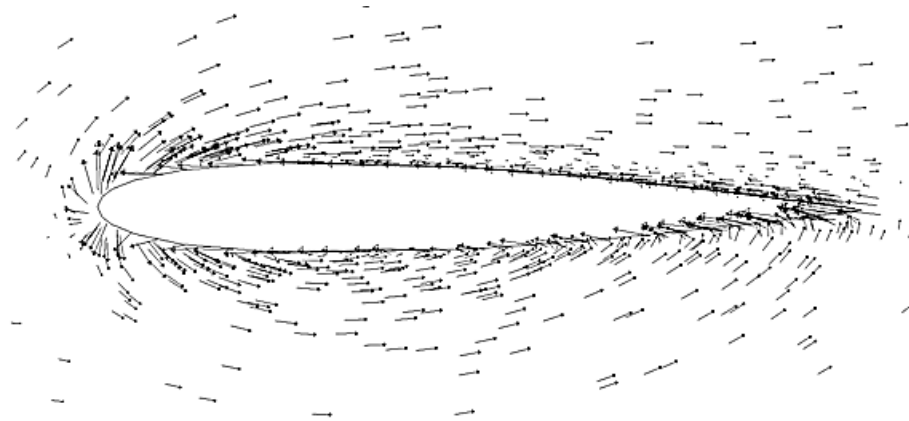


**Fig. 6.14(a):** Velocity vector of 3 Bladed Single layered H – Rotor VAWT; Solidity 0.5,  $\lambda=3.25$ (blade at 0 degree)

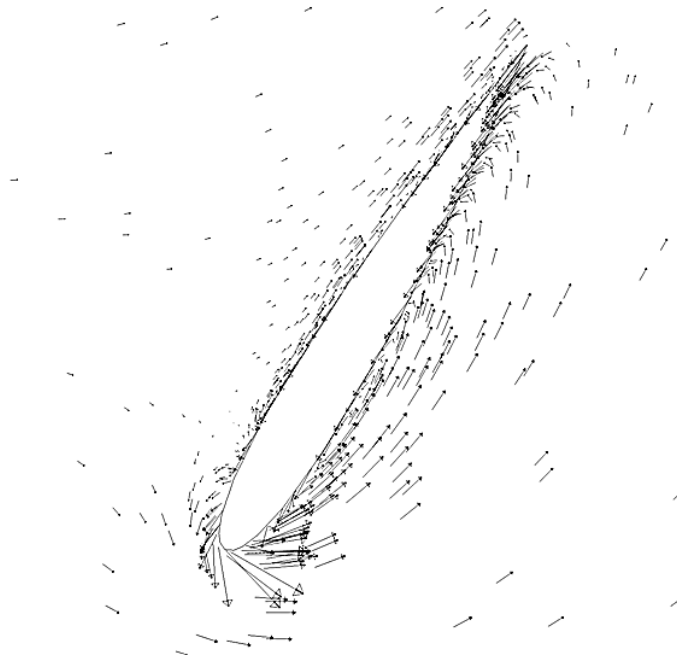


**Fig. 6.14(b):** Velocity vector of 3 Bladed Single layered H – Rotor VAWT; Solidity 0.5,  $\lambda=3.25$ (blade at 60 degree)

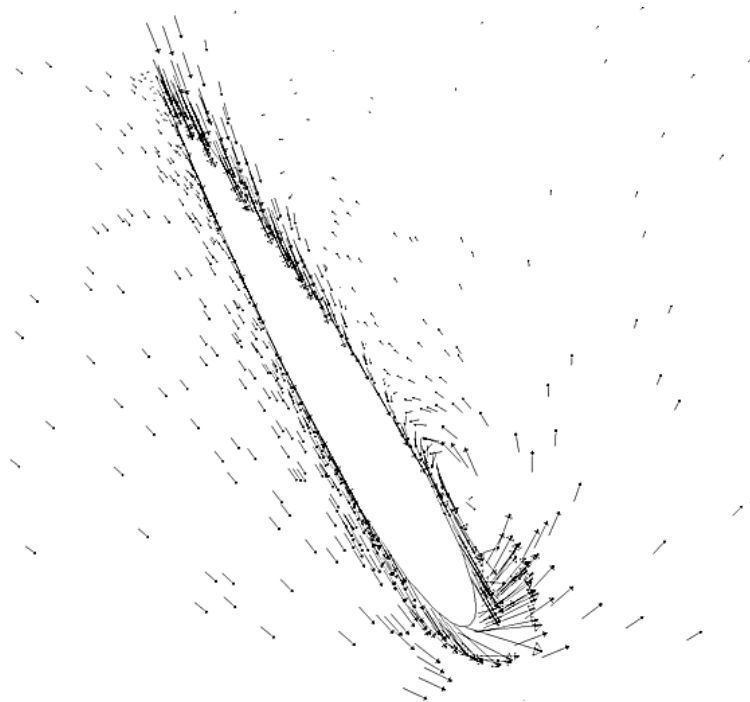


**Fig. 6.14(c):** Velocity vector of 3 Bladed Single layered H – Rotor VAWT; Solidity 0.5,  $\lambda=3.25$ (blade at 120 degree)

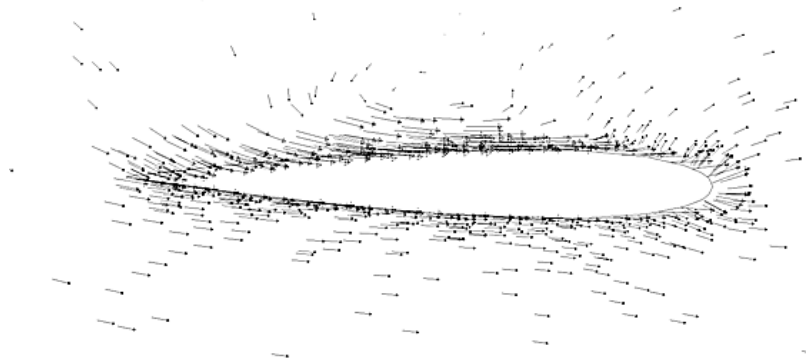


**Fig. 6.14(d):** Velocity vector of 3 Bladed Single layered H – Rotor VAWT; Solidity 0.5,  $\lambda=3.25$ (blade at 180 degree)

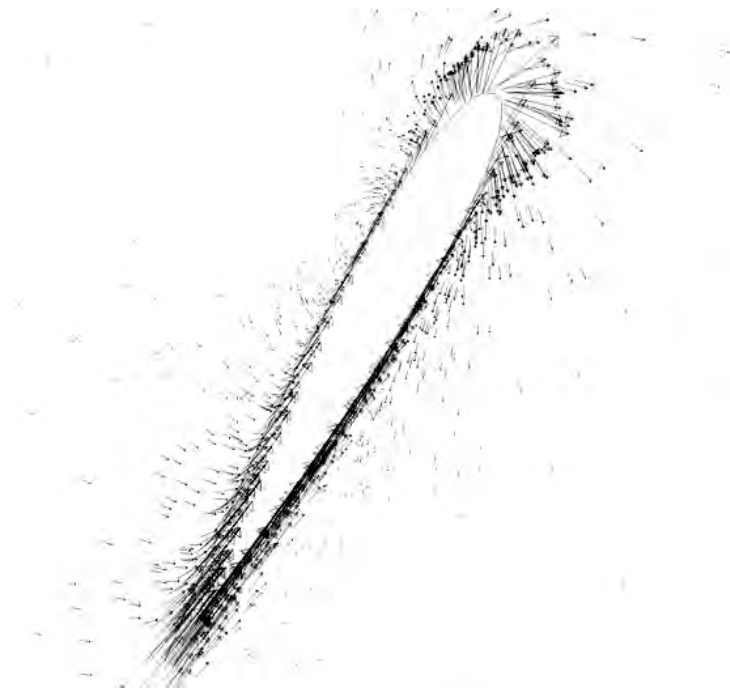


**Fig. 6.14(e):** Velocity vector of 3 Bladed Single layered H – Rotor VAWT; Solidity 0.5,  $\lambda=3.25$ (blade at 240 degree)

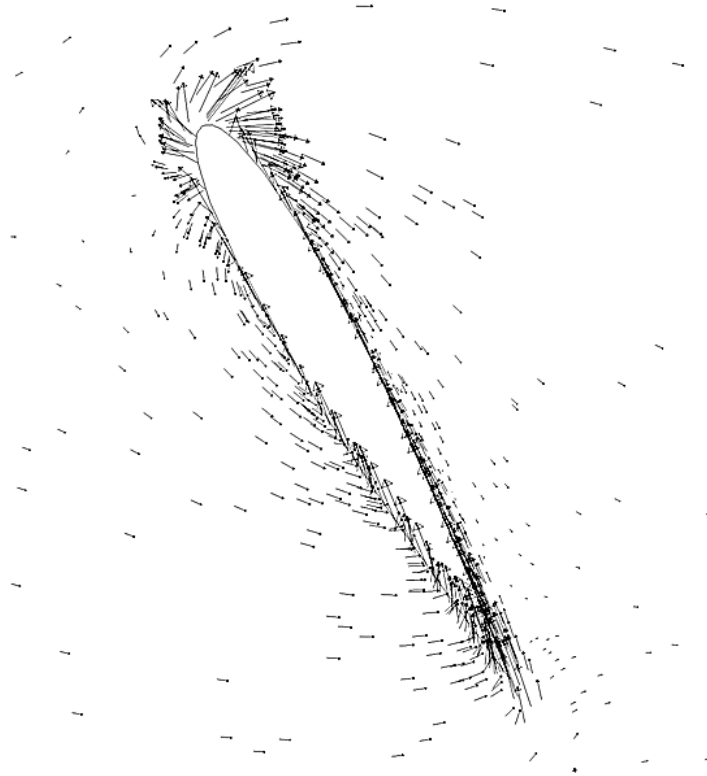


**Fig. 6.14(f):** Velocity vector of 3 Bladed Single layered H – Rotor VAWT; Solidity 0.5,  $\lambda=3.25$ (blade at 300 degree)

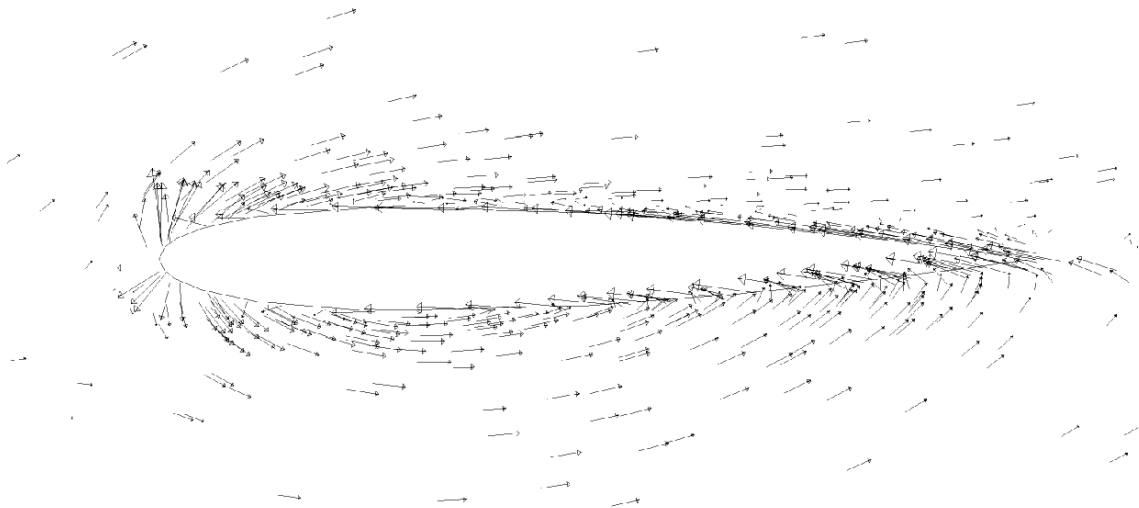


**Fig. 6.15(a):** Velocity vector of 3 Bladed Single layered H – Rotor VAWT; Solidity 0.7,  $\lambda= 2.5$ (blade at 0 degree)

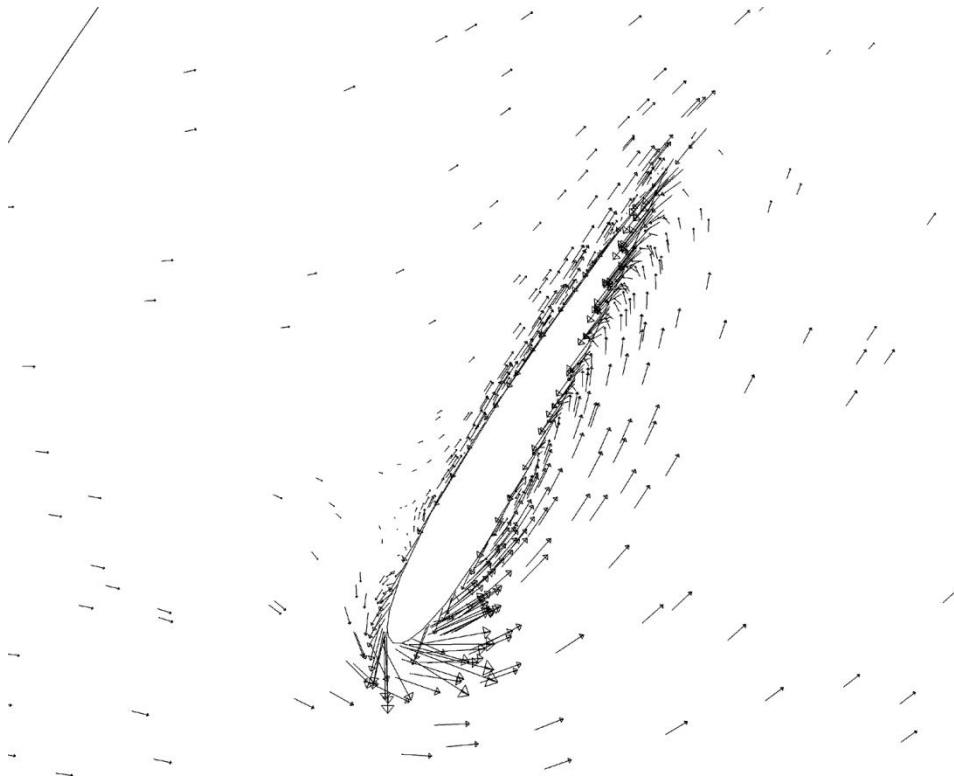


**Fig. 6.15(b):** Velocity vector of 3 Bladed Single layered H – Rotor VAWT; Solidity 0.7,  $\lambda=2.5$ (blade at 60 degree)

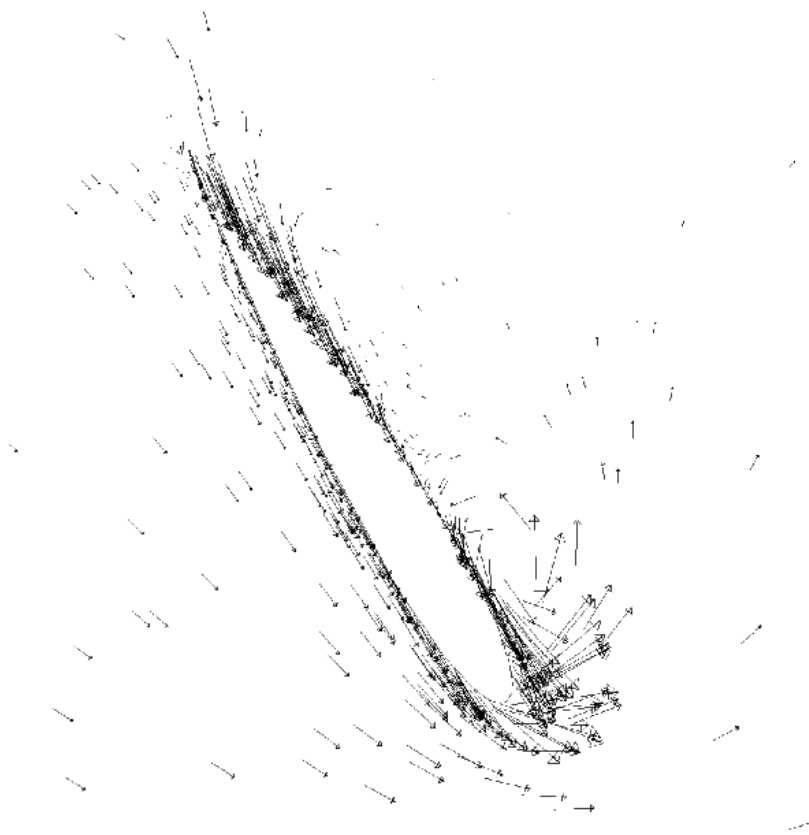


**Fig. 6.15(c):** Velocity vector of 3 Bladed Single layered H – Rotor VAWT; Solidity 0.7,  $\lambda=2.5$ (blade at 120 degree)



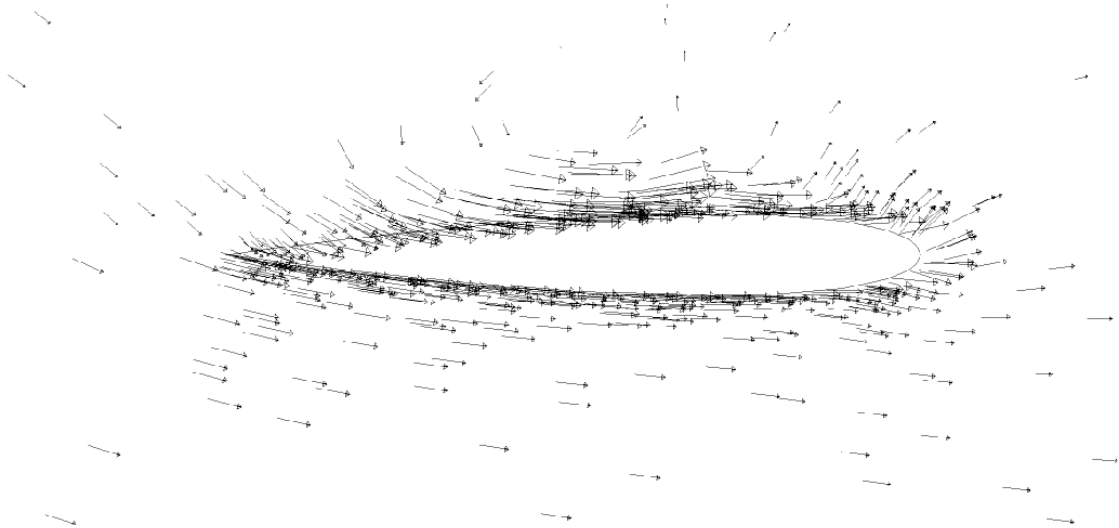


**Fig. 6.15(d):** Velocity vector of 3 Bladed Single layered H – Rotor VAWT; Solidity 0.7,  $\lambda= 2.5$ (blade at 180 degree)

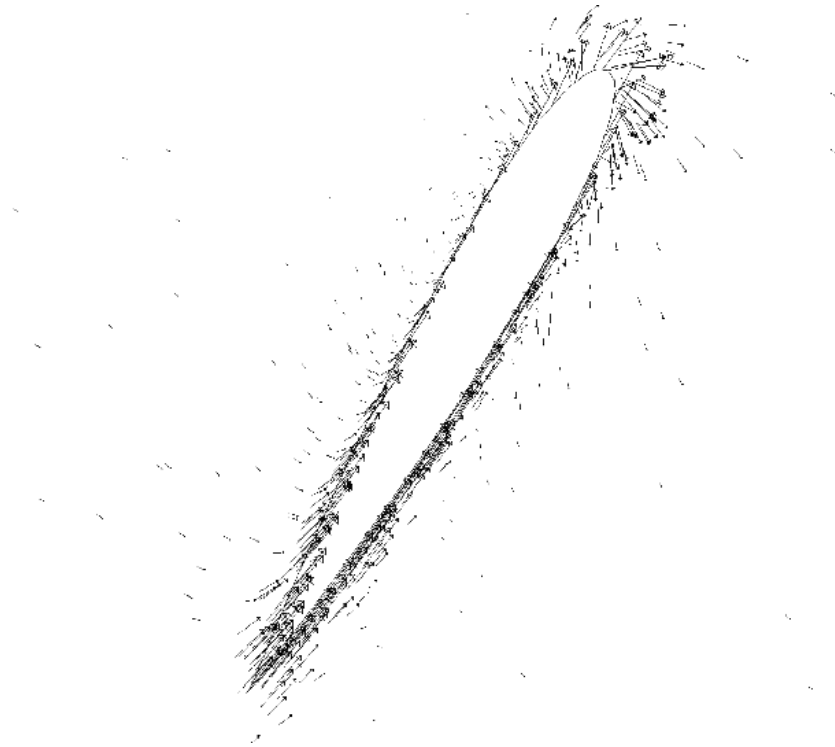


**Fig. 6.15(e):** Velocity vector of 3 Bladed Single layered H – Rotor VAWT; Solidity 0.7,  $\lambda= 2.5$ (blade at 240 degree)



**Fig. 6.15(f):** Velocity vector of 3 Bladed Single layered H – Rotor VAWT; Solidity 0.7,  $\lambda=2.5$ (blade at 300 degree)

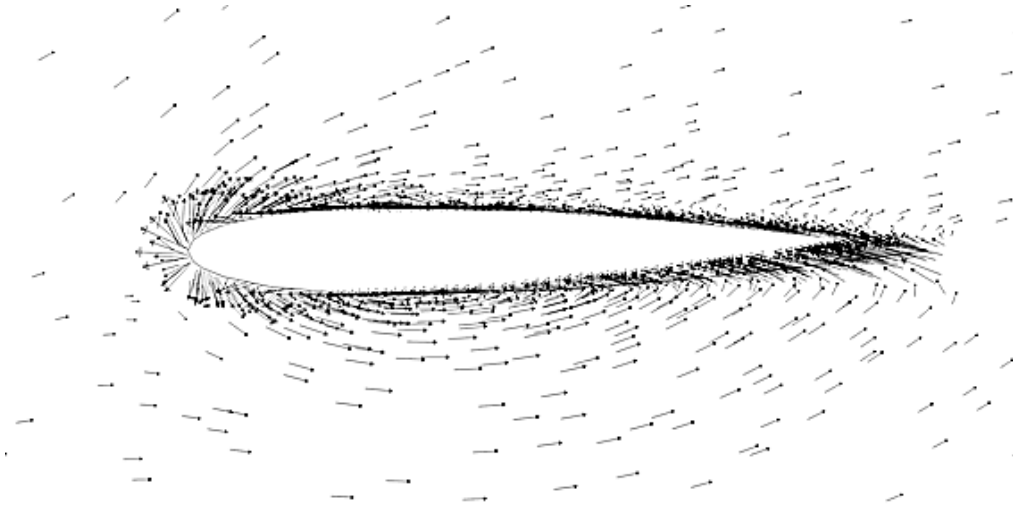


**Fig. 6.16(a):** Velocity vector of 3 Bladed Single layered H – Rotor VAWT; Solidity 1.0,  $\lambda=2.25$  (blade at 0 degree)

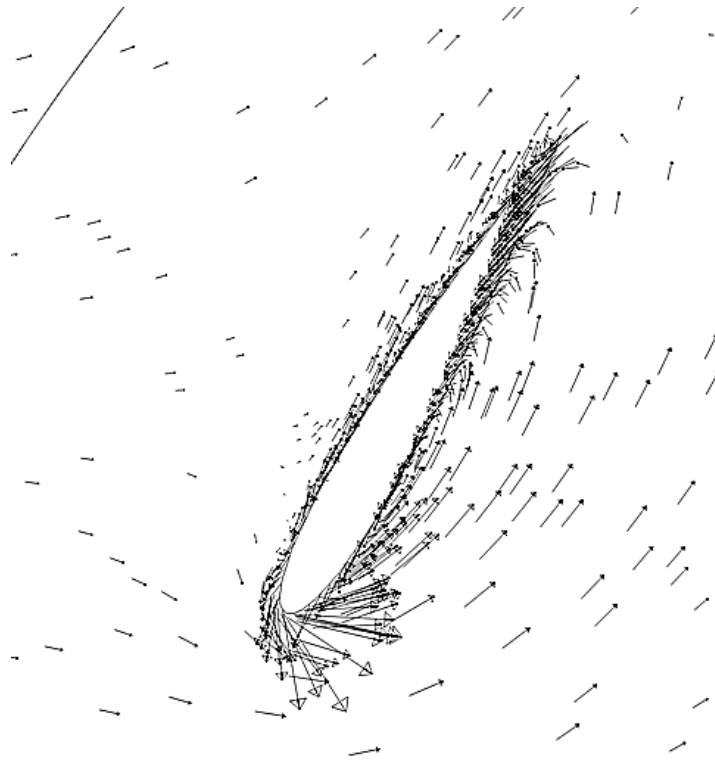


**Fig. 6.16(b):** Velocity vector of 3 Bladed Single layered H – Rotor VAWT; Solidity 1.0,  $\lambda=2.25$  (blade at 60 degree)

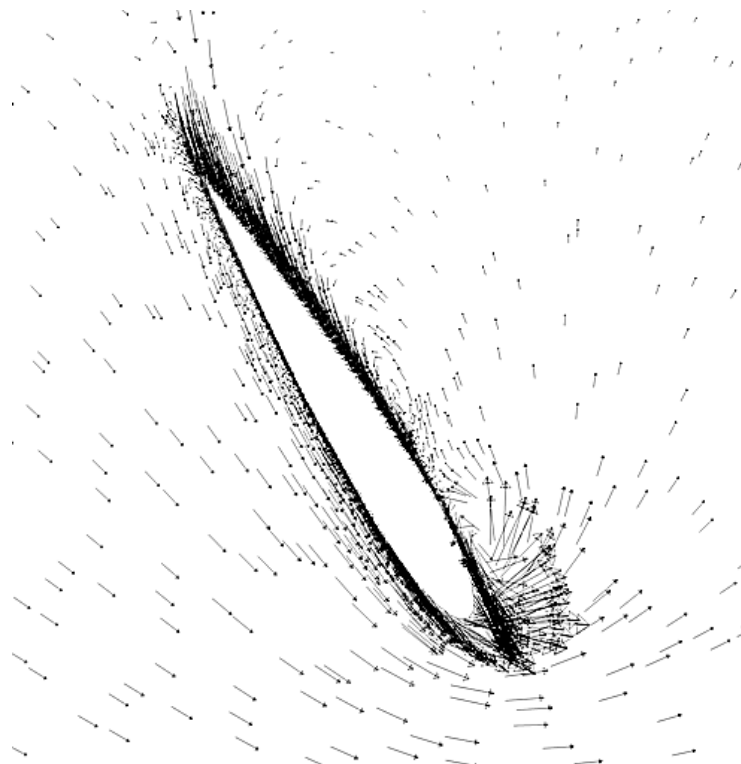


**Fig. 6.16(c):** Velocity vector of 3 Bladed Single layered H – Rotor VAWT; Solidity 1.0,  $\lambda=2.25$  (blade at 120 degree)



**Fig. 6.16(d):** Velocity vector of 3 Bladed Single layered H – Rotor VAWT; Solidity 1.0,  $\lambda=2.25$  (blade at 180 degree)

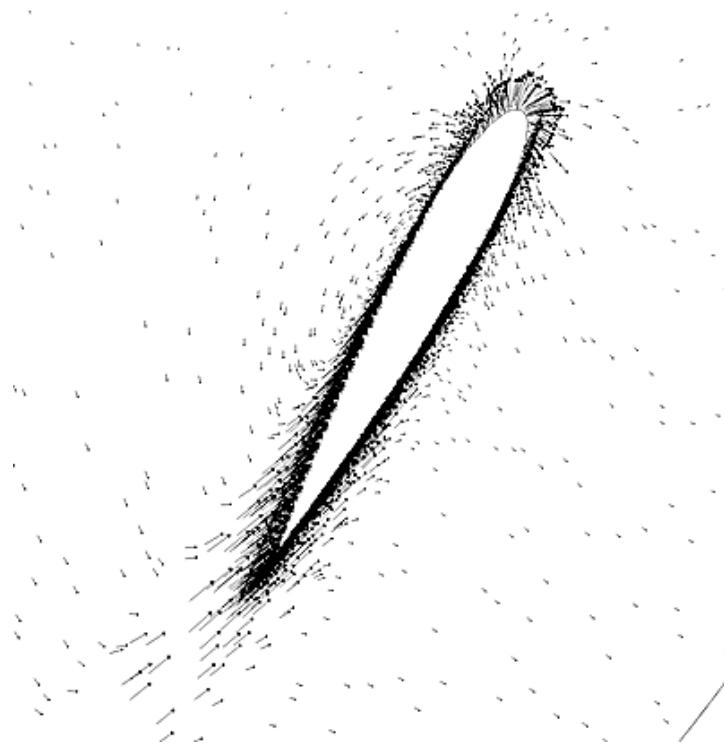


**Fig. 6.16(e):** Velocity vector of 3 Bladed Single layered H – Rotor VAWT; Solidity 1.0,  $\lambda=2.25$  (blade at 240 degree)

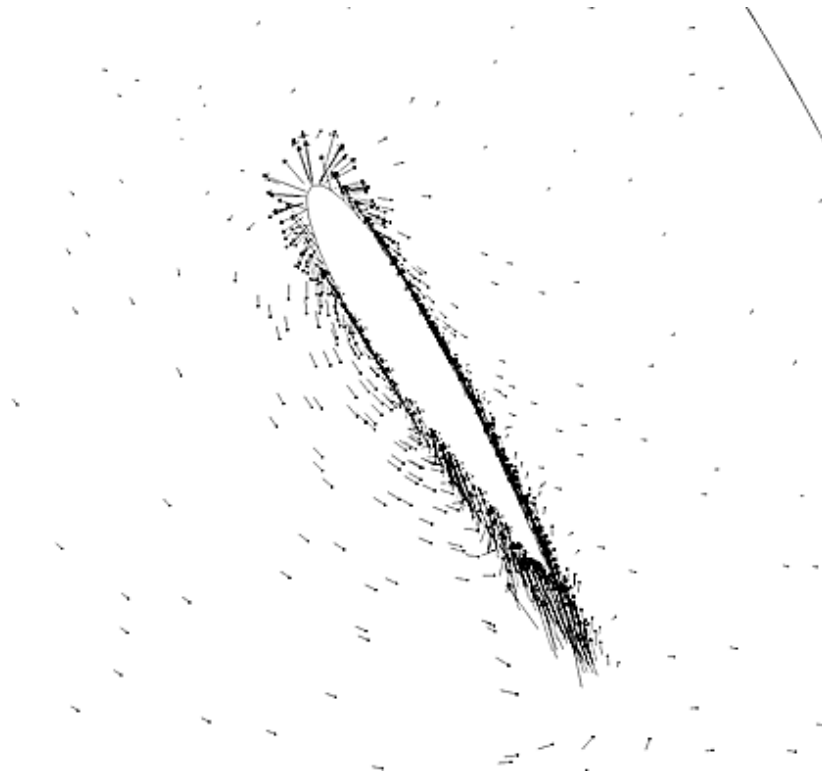


**Fig. 6.16(f):** Velocity vector of 3 Bladed Single layered H – Rotor VAWT; Solidity 1.0,  $\lambda=2.25$  (blade at 300 degree)

### 6.2.5 Pressure Contour

The Pressure contours for single layered H-rotor VAWTs are shown in Fig 6.17 to Fig 6.19. At angle,  $\theta=0^0$  a high pressure zone is in front of the turbine blades causes negative axial force and thereby creates negative  $C_t$ . At  $\theta=60^0$ , the high pressure zone is found at the outer side of the blade and low pressure is found at inner side which creates positive axial force in front of the blade, hence, positive  $C_t$ . At  $\theta=120^0$ , the low pressure zone becomes bigger and the higher pressure near the tip falls, which causes higher  $C_t$ . At  $\theta=180^0$ ,  $\theta=240^0$  and  $\theta=300^0$  the high pressure zone is present in front of the turbine blade and thereby causes negative axial force and hence, negative  $C_t$ .

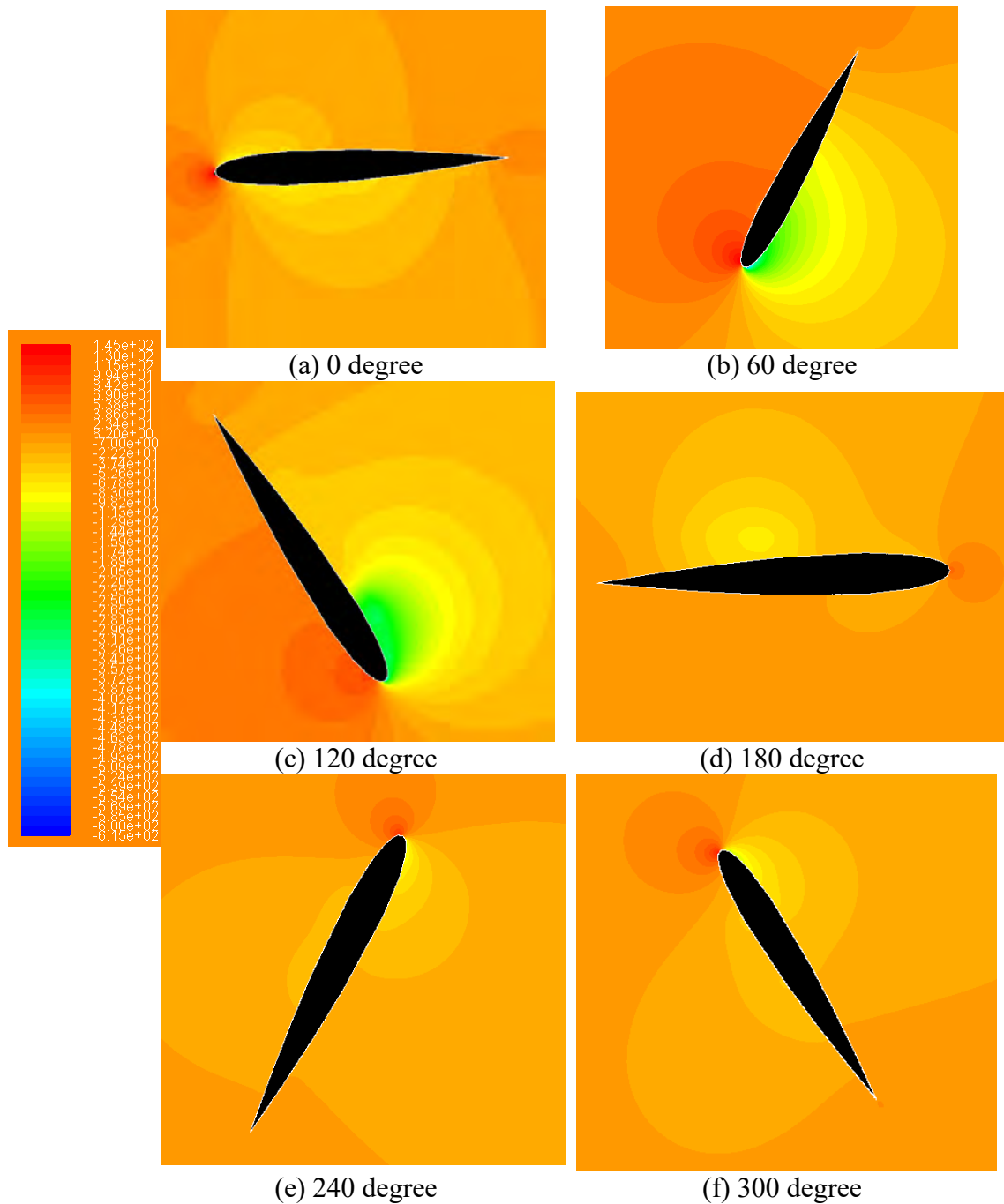


**Fig. 6.17:** Pressure contour of 3 Bladed single layered H – Rotor VAWT; Solidity 0.5 at  $\lambda=3.25$

For solidity 0.7 at  $\lambda=2.5$ , the low pressure becomes even lower at  $\theta=120^\circ$ . This causes a  $C_t$  higher than that found for solidity 0.5 at  $\lambda=3.25$  and  $\theta=120^\circ$ .

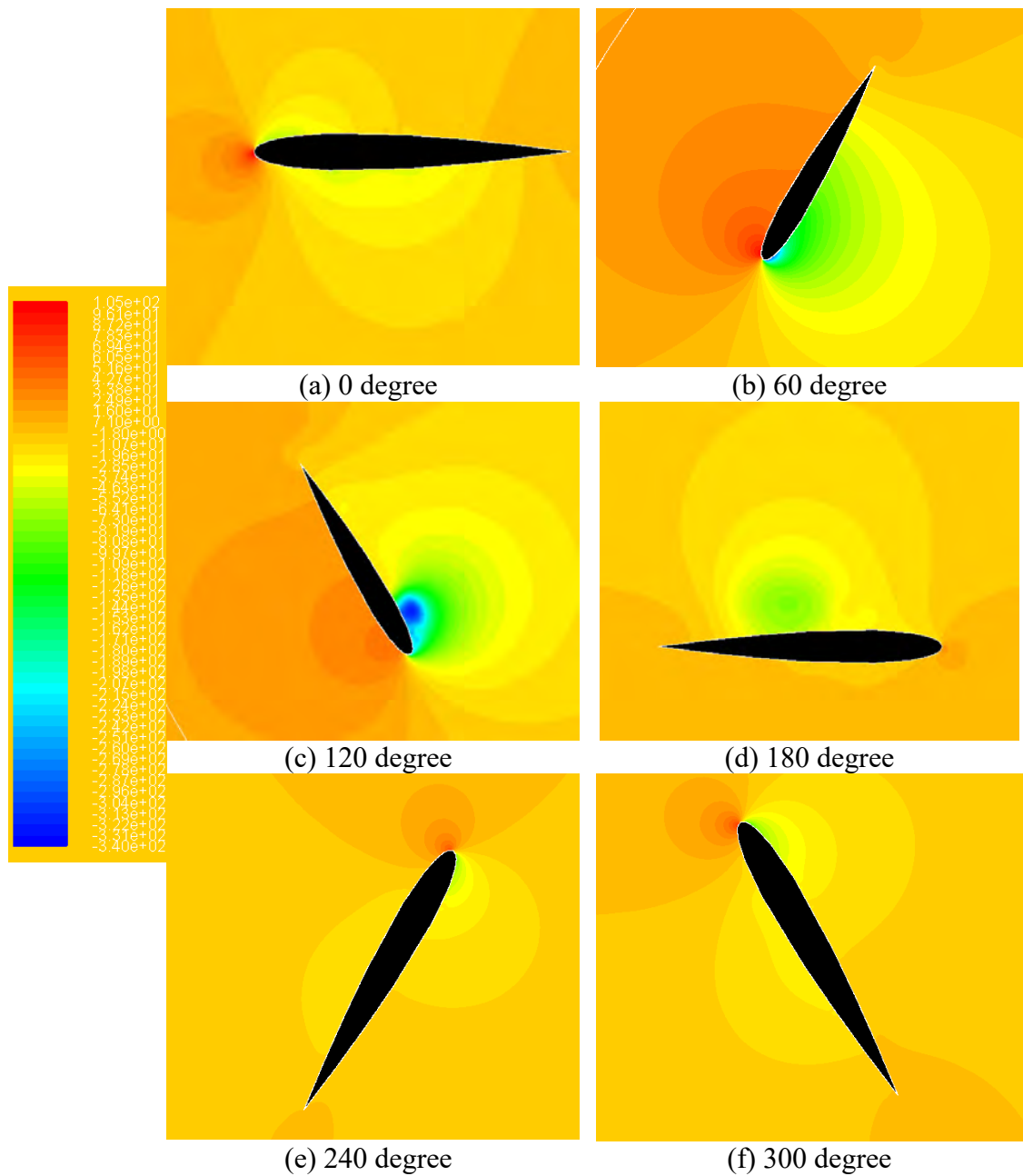


**Fig. 6.18:** Pressure contour of 3 Bladed single layered H – Rotor VAWT; Solidity 0.7,  $\lambda=2.5$

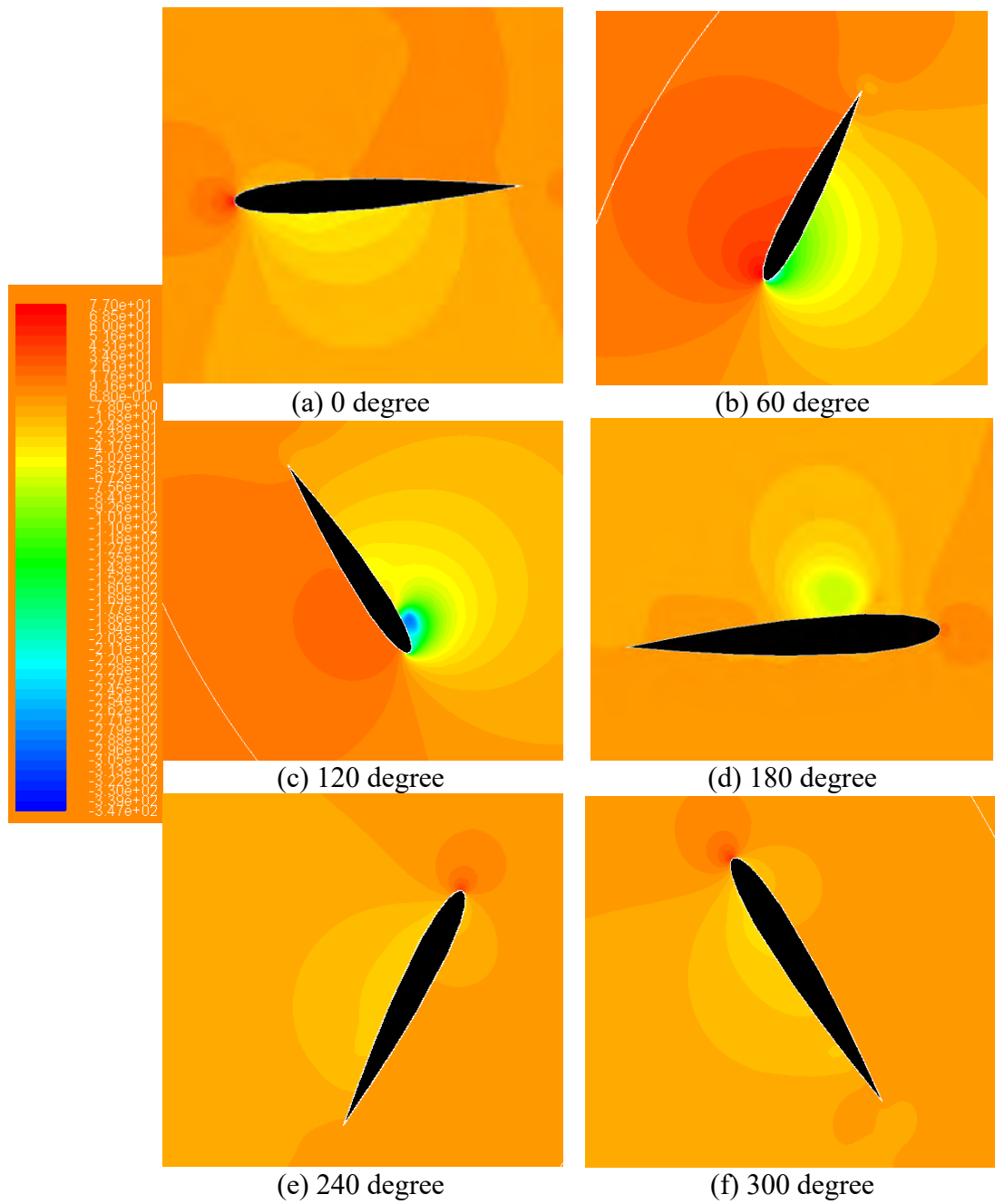


**Fig. 6.19:** Pressure contour of 3 Bladed single layered H – Rotor VAWT; Solidity 1.0,  $\lambda=2.25$



### 6.2.6 Lift and Drag Coefficient

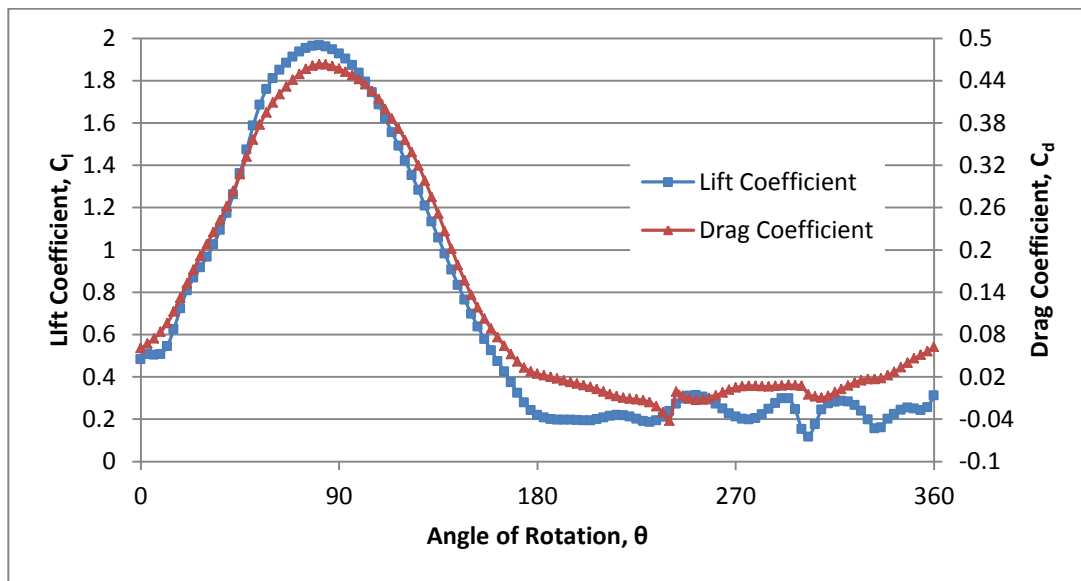


**Fig 6.20:**  $C_l$  and  $C_d$  vs.  $\theta$  for Double Layered (In-line) H-Darrieus VAWT; Solidity 1.0 at  $\lambda=2.25$

Lift coefficient ( $C_l$ ) and Drag coefficient ( $C_d$ ) are shown in Fig. 6.20. It can be seen in the figure that, both  $C_l$  and  $C_d$  are positive in upstream side of the turbine. However, in the downstream side the value of drag coefficient is found negative. As the induced velocity varies for different angle of rotation, the angle of attack on the blade also changes. Hence, these curves show some sharp ups and downs as shown in Fig 6.20.

### 6.3 Performance of Double Layered H-Darrieus Vertical Axis Wind Turbine

#### 6.3.1 Relationship between torque coefficient and tip speed ratio

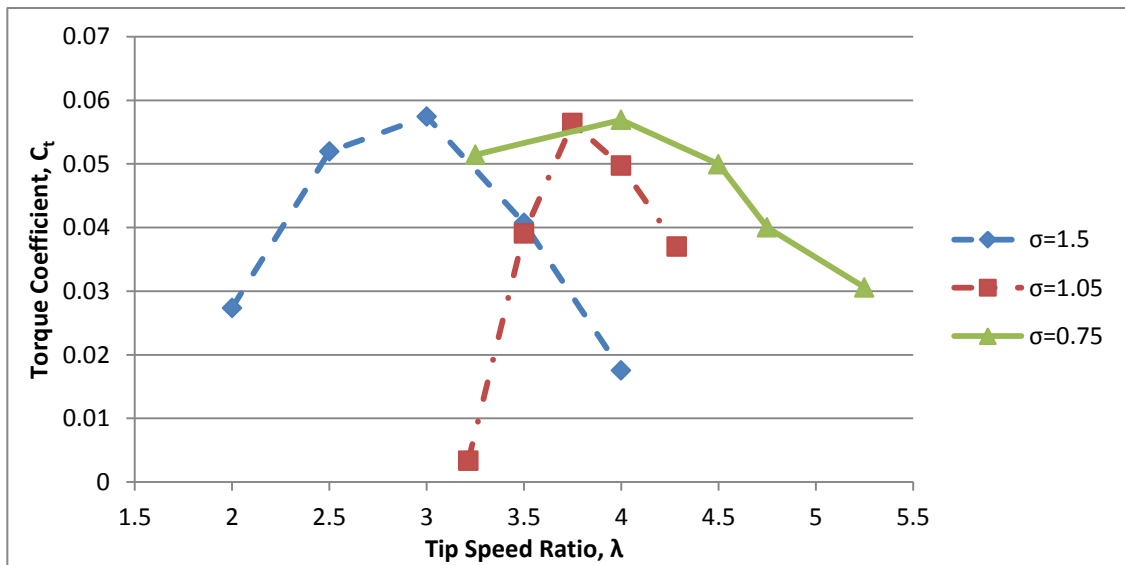


**Fig. 6.21:**  $C_t$  vs.  $\lambda$  for double layered 6 bladed H-rotor VAWT

The performance of double layered H-Darrieus VAWT with solidity 0.75, 1.05 and 1.5 are investigated in this thesis. The change of torque coefficient with tip speed ratio for different solidity VAWT is shown in Fig. 6.16.

For Double Layered H-Darrieus VAWT with solidity 0.75, torque coefficient  $C_t$  is found as 0.051442 at a tip speed ratio,  $\lambda=3.25$ . With the increase in tip speed ratio, the torque coefficient increases to a peak value,  $(C_t)_{\max} = 0.05692$  at  $\lambda=4$ . And, the further increase in tip speed ratio causes the drop in torque coefficient. At  $\lambda=5.25$ , the torque coefficient is equal to 0.030581.

For solidity  $\zeta=1.05$ , the torque coefficient is maximum at  $\lambda=3.75$  and the value of  $(C_t)_{\max}$  is 0.056416. At the tip speed ratio for both lower and higher than  $\lambda=3.75$ , the Double Layered H-rotor VAWT generates torque at a torque coefficient lower than  $(C_t)_{\max}$ . At  $\lambda=3.2144$ ,  $C_t$  is equal to 0.003344 and at  $\lambda=4.28555$ ,  $C_t$  is equal to 0.03702.

The  $C_t$  vs.  $\lambda$  curve for Double Layered H-rotor VAWT with  $\zeta=1.5$  also shows similar nature. First, the torque coefficient increases with the increase in tip speed ratio until a certain limit. Then the further increase in tip speed ratio causes decrease in torque coefficient. At  $\lambda=2$ ,  $C_t$  is equal to 0.027375.  $(C_t)_{\max}= 0.057455$  is achieved at  $\lambda=3.0$ . Then at  $\lambda=4.0$ ,  $C_t$  is equal to 0.0175598.

For the double layered H-rotor VAWT, the maximum torque coefficient remains almost unchanged with the change in solidity, however, the tip speed ratio at which the max torque coefficient is achieved increases with the reduction in solidity.

**Table 6.5:** Relationship between  $C_t$  and  $C_p$  with  $\lambda$  for Double Layered VAWT with  $\zeta = 0.75$

$\lambda$	$C_t$	$C_p$
3.25	0.051442	0.167185
<b>4</b>	<b>0.05692</b>	<b>0.227679</b>
4.5	0.049948	0.224766
4.75	0.040027	0.190127
5.25	0.030581	0.160552

**Table 6.6:** Relationship between  $C_t$  and  $C_p$  with  $\lambda$  for Double Layered VAWT with  $\zeta = 1.05$

$\lambda$	$C_t$	$C_p$
3.2144	0.003344	0.010748
3.5	0.039076	0.136765
<b>3.75</b>	<b>0.056416</b>	<b>0.21156</b>
4	0.049723	0.198893
4.28555	0.03702	0.158651

**Table 6.7:** Relationship between  $C_t$  and  $C_p$  with  $\lambda$  for Double Layered VAWT with  $\zeta = 1.5$

$\lambda$	$C_t$	$C_p$
2	0.027375	0.05475
2.5	0.051936	0.12984
<b>3</b>	<b>0.057455</b>	<b>0.172365</b>
3.5	0.040728	0.142549
4	0.0175598	0.070239

### 6.3.2 Relationship between power coefficient and tip speed ratio

The  $C_p$  vs.  $\lambda$  curve for the Double layered VAWT shows similar nature as Single layered VAWT. The Double Layered H-Darrieus VAWT with solidity 0.75 is studied from  $\lambda=3.25$  to  $\lambda=5.25$ .  $C_p$  is found as 0.1615 at  $\lambda=3.25$  and it becomes maximum at  $\lambda=4$ .  $(C_p)_{\max}$  for the H-Darrieus VAWT with solidity 0.75 is 0.227679. When the turbine rotates at a tip speed ratio higher than  $\lambda=4$ , the power coefficient starts to decrease. At tip speed ratio  $\lambda=5.25$ , the power coefficient reduces to 0.160552.

As the solidity of the vertical axis wind turbine is increased to 1.05, it extracts power with  $C_p=0.010748$  at  $\lambda=3.2144$ . Then for  $\lambda=3.5$  and for  $\lambda=3.75$  the  $C_p$  becomes 0.136765 and 0.21156 respectively. The power coefficient achieved at  $\lambda=3.75$  is maximum and the power coefficient of the VAWT decreases with further increase in tip speed ratio.

The double layered H-Darrieus vertical axis wind turbine with solidity  $\zeta=1.5$  extracts power with a power coefficient 0.05475 when it rotates at  $\lambda=2$ . Then the power coefficient of this VAWT increases until its tangential velocity ( $\Omega R$ ) equal to three times of the free stream velocity (i.e.  $\lambda=3$ ). At  $\lambda=3$ , the power coefficient of this turbine with solidity  $\zeta=1.5$  is maximum and the value is 0.172365. Further increase in tip speed ratio causes decrease in power coefficient and at  $\lambda=4$ ,  $C_p$  becomes 0.070239.

The maximum power coefficients for VAWT with solidity 1.5, 1.05 and 0.75 are found to be 0.172365, 0.21156 and 0.227679 respectively. The  $(C_p)_{\max}$  for VAWT with solidity 1.5, 1.05 and 0.75 are achieved at  $\lambda=3$ , 3.75 and 4 respectively. Hence, it can be understood that, with the decrease in solidity,  $(C_p)_{\max}$  increases and the  $(C_p)_{\max}$  is achieved at lower tip speed ratio.

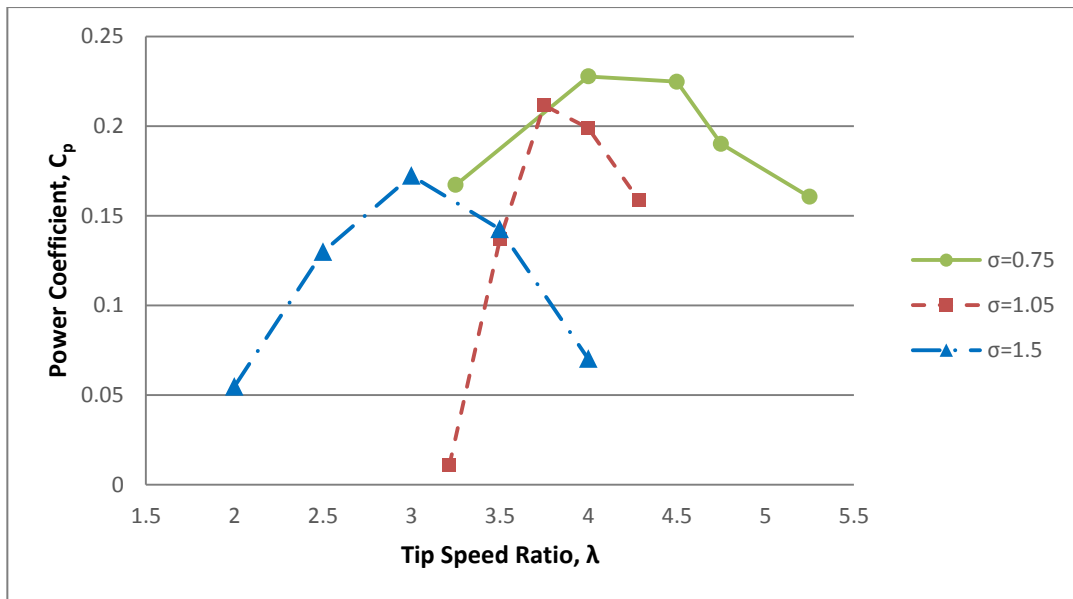


**Fig. 6.22:**  $C_p$  vs.  $\lambda$  for double layered 6 bladed VAWT

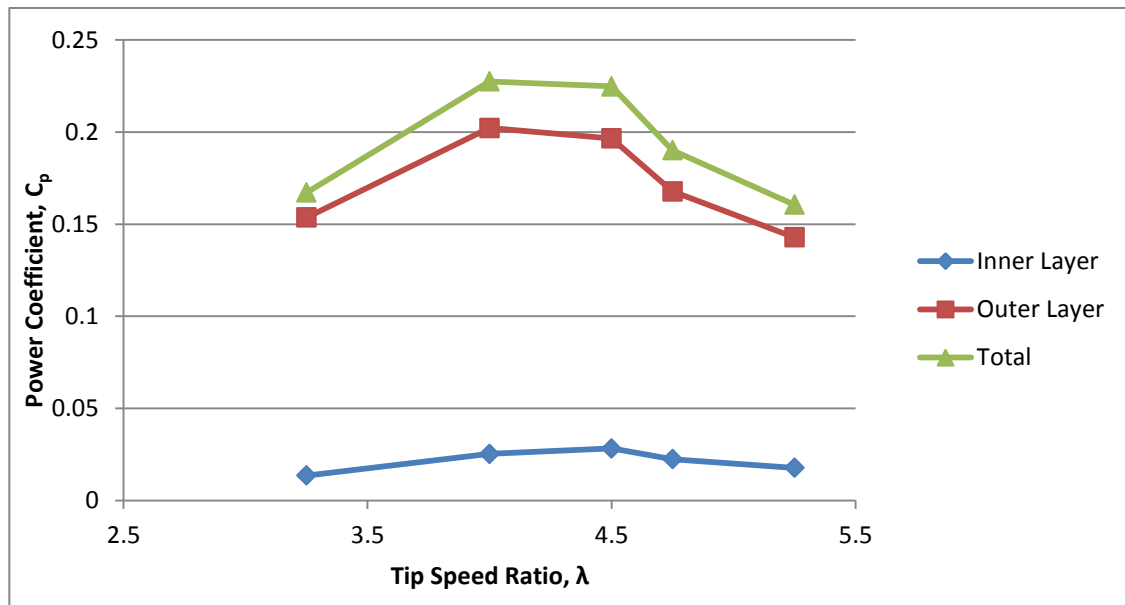
### 6.3.3. Contribution of inner and outer layer to the power coefficient

The power coefficient of inner layer is negligible comparing to the power coefficients of outer layer. For double layered H-rotor VAWT with  $\zeta=0.75$ , power coefficients of inner layer and outer layer are 0.013583 and 0.153602 at  $\lambda=3.25$  as shown in Fig. 6.23. At  $\lambda=4$ , where the VAWT generates power at maximum power coefficient, the inner layer's power coefficient is only 12.4% of the total power coefficient. Though the power coefficient of outer layer is maximum at  $\lambda=4$ , however, power coefficient of inner layer is maximum at  $\lambda=4.5$  and the maximum value is 0.028239. At  $\lambda=5.25$ , the power coefficient of inner layer is 0.017714, which is only 0.1240137 times of the power coefficient of outer layer.

**Table 6.8:** Calculation of  $C_p$  of double layered 6 bladed VAWT with solidity 0.75

$\lambda$	T-inner (Nm)	T-outer (Nm)	T-total (Nm)	$\Omega$ (rad/s)	$P=T\Omega$ (W)	$C_{p\text{-inner}}$	$C_{p\text{-outer}}$	$C_{p\text{-total}}$
(1)	(2)	(3)	(4) = (2) + (3)	(5)	(6) = (4) x (5)	(7) = (2)x(5)/( $\rho v^3$ )	(8) = (3)x(5)/( $\rho v^3$ )	(9) = (7)+(8) Or (6)/( $P_o$ )
3.25	0.086905	0.98275	1.069655	12.62136	13.5005	0.013583	0.153602	0.167185
4	0.130557	1.053011	1.183568	15.53398	18.38552	0.025115	0.202564	0.227679
4.5	0.130489	0.908112	1.038601	17.47573	18.15031	0.028239	0.196527	0.224766
4.75	0.09802	0.73428	0.8323	18.4466	15.3531	0.022391	0.167735	0.190127
5.25	0.070159	0.56574	0.635899	20.38835	12.96493	0.017714	0.142839	0.160552

Here, Available Power ,  $P_o = 0.5\rho Av^3 = 80.752$  W; [ $A=2.06m^2, v=4m/s, \rho=1.225$  kg/m<sup>3</sup>]

**Fig. 6.23:** Inner layer power coefficient, outer layer power coefficient and total power coefficient for  $\zeta=0.75$ 

For double layered H-rotor VAWT with  $\zeta=1.05$ , power coefficients of inner layer and outer layer are respectively -0.01118 and 0.028672 at  $\lambda=3.2144$  as shown in Fig. 6.24. In this case, the power coefficient of inner layer is negative at  $\lambda=3.2144$ . It means the inner layer consumes power instead of generating power at that tip speed ratio. So, the total power coefficient is lower than the power coefficient of outer layer. Inner layer power coefficient is found positive at  $\lambda=3.75$  and the value is 0.012845. It is only

6.08% of the total power coefficient. After that, the power coefficient of the inner layer decreases again and gradually drops to  $(C_p)_{\text{inner}}=0.002871$ . At  $\lambda=4.28555$ , it is found negative again.

**Table 6.9:** Calculation of  $C_p$  of double layered 6 bladed VAWT with solidity 1.05

$\lambda$	T-inner (Nm)	T-outer (Nm)	T-total (Nm)	$\Omega$ (rad/s)	$P=T\Omega$ (W)	$C_p$ -inner	$C_p$ -outer	$C_p$ -total
(1)	(2)	(3)	(4) = (2) + (3)	(5)	(6) = (4) x (5)	(7) = (2)x(5)/(p <sub>o</sub> )	(8) = (3)x(5)/(p <sub>o</sub> )	(9) = (7)+(8) Or (6)/(P <sub>o</sub> )
3.2144	-0.03687	0.094556	0.057683	17.48252	1.008435	-0.01118	0.028672	0.017491
3.5	-0.00372	0.417918	0.414199	19.03726	7.885216	-0.00123	0.137993	0.136765
3.75	0.036311	0.560576	0.596888	20.39627	12.17428	0.012845	0.198311	0.211156
4	0.007607	0.519457	0.527064	21.75687	11.46726	0.002871	0.196023	0.198893
4.28555	-0.00791	0.400315	0.392409	23.31002	9.147053	-0.0032	0.161847	0.158651

Here, Available Power ,  $P_o = 0.5\rho Av^3 = 57.65536W$ ; [ $A=1.4708m^2$ ,  $v=4m/s$ ,  $\rho=1.225 kg/m^3$ ]

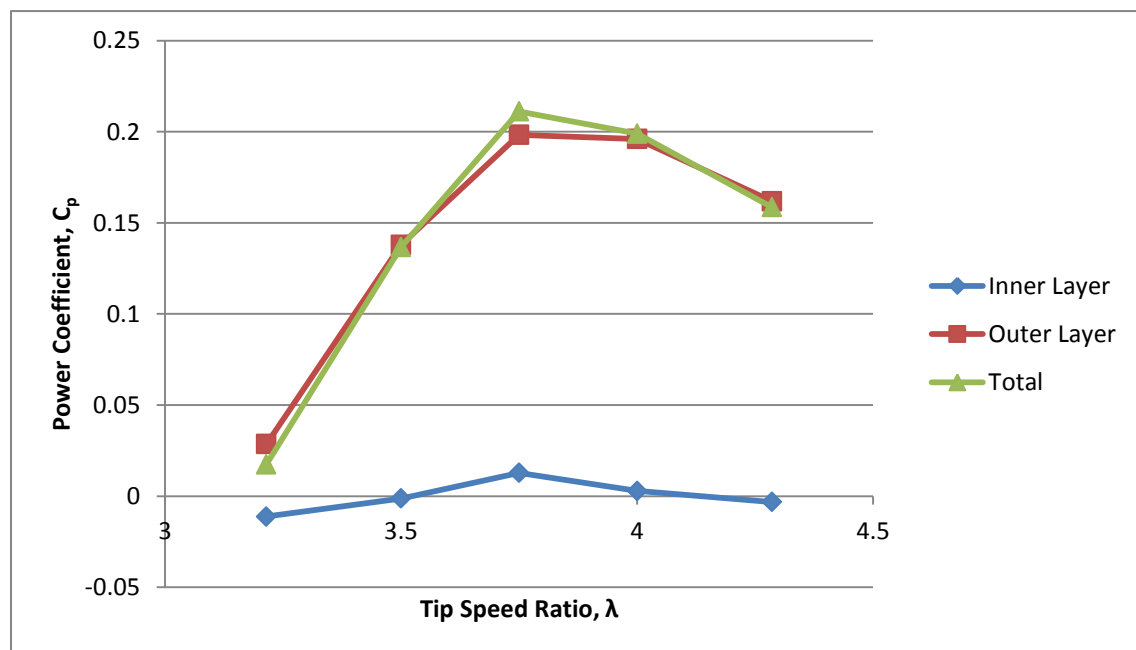


**Fig. 6.24:** Inner layer power coefficient, outer layer power coefficient and total power coefficient for  $\zeta=1.05$

From Fig. 6.25, it can be seen that the inner layer consumes the power that is generated by the outer layer for all the cases except when it rotates at  $\lambda=2.5$  and  $\lambda=3$ . Even at  $\lambda=3$ ,

the power coefficient of inner layer is 0.000611 which is negligible. At tip speed ratio higher than  $\lambda=3$ , the power consumption by the inner layer increases. At  $\lambda=4$ , the inner layer consumes 35.03% of the power generated by the outer layer of the wind turbine.

**Table 6.10:** Calculation of  $C_p$  of double layered 6 bladed VAWT with solidity 1.5

$\lambda$	T-inner (Nm)	T-outer (Nm)	T-total (Nm)	$\Omega$ (rad/s)	$P=T\Omega$ (W)	$C_p$ -inner	$C_p$ -outer	$C_p$ -total
(1)	(2)	(3)	(4) = (2) + (3)	(5)	(6) = (4) x (5)	(7) = (2)x(5)/(p <sub>o</sub> )	(8) = (3)x(5)/(p <sub>o</sub> )	(9) = (7)+(8) Or (6)/(P <sub>o</sub> )
2	-0.00786	0.15017	0.142306	15.53398058	2.21057873	-0.00303	0.057775	0.05475
2.5	0.00874	0.261244	0.269985	19.41748	5.242419	0.004203	0.125637	0.12984
3	0.001059	0.297614	0.298674	23.30097087	6.95939331	0.000611	0.171753	0.172365
3.5	-0.02228	0.234002	0.211722	27.18446602	5.75556182	-0.015	0.15755	0.142549
4	-0.04922	0.1405	0.091282	31.06796117	2.83595961	-0.03787	0.10811	0.070239

Here, Available Power ,  $P_o = 0.5\rho Av^3 = 40.376W$ ; [ $A=1.03m^2$ ,  $v=4m/s$ ,  $\rho=1.225 kg/m^3$ ]

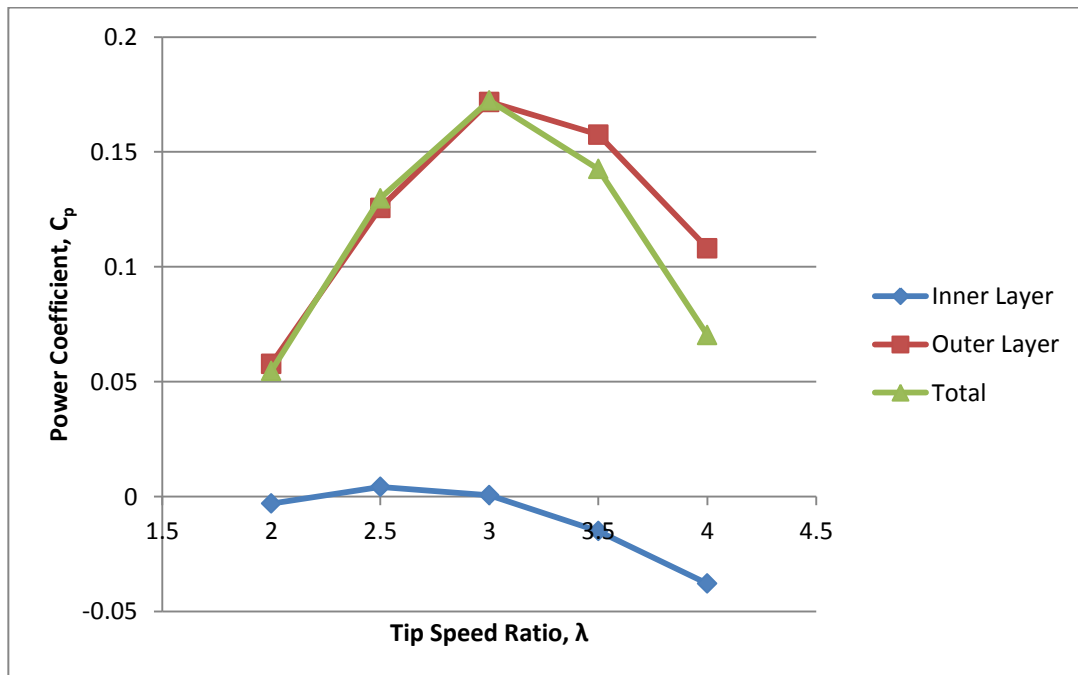
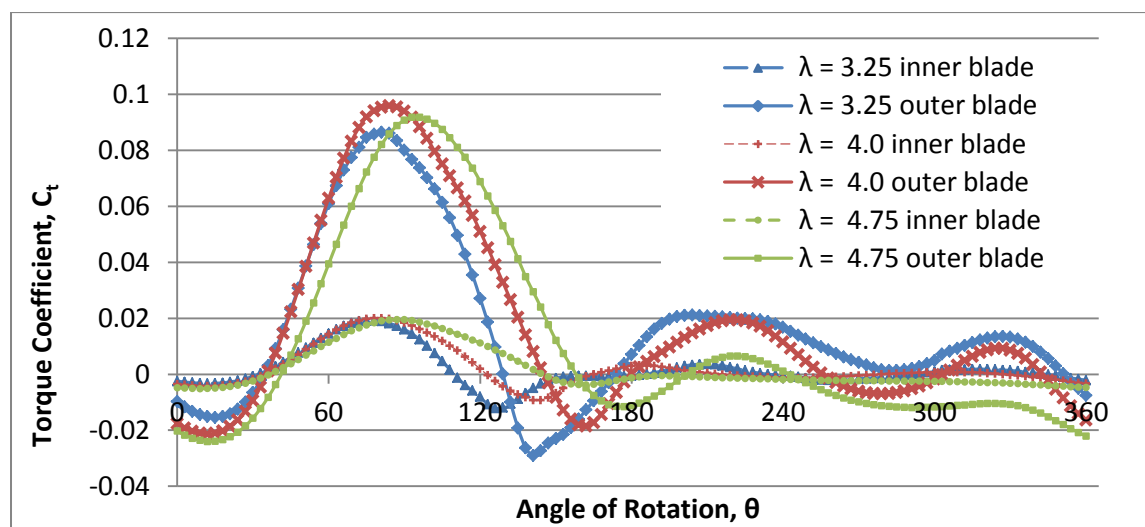


**Fig. 6.25:** Inner layer power coefficient, outer layer power coefficient and total power coefficient for  $\zeta=1.0$



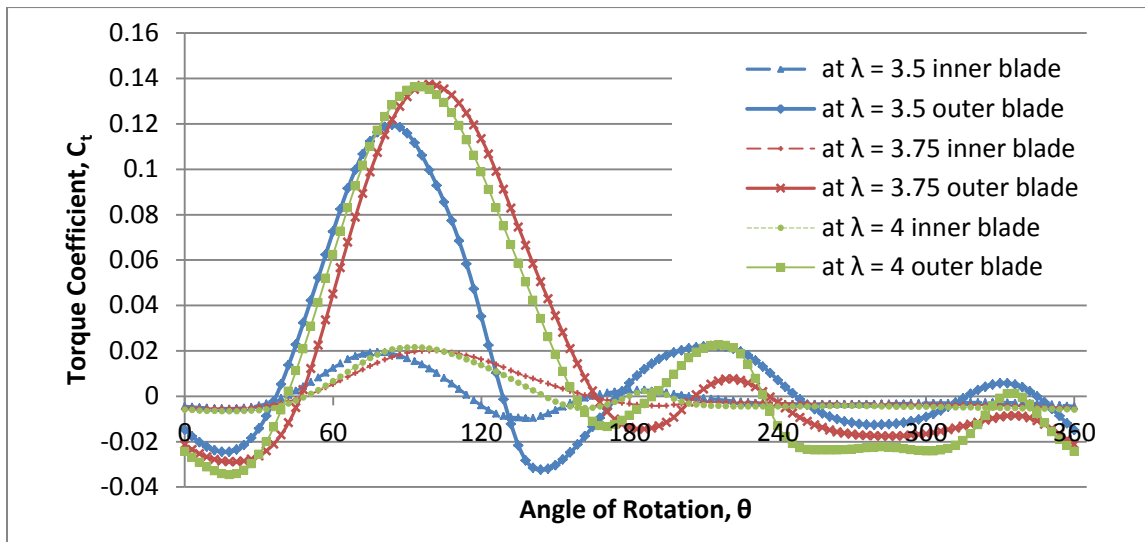
In fact, the inner layer blades are experiencing a lower wind velocity than the velocity experienced by outer layer. As a part of the kinetic energy is being consumed by the outer layer or front layer turbine blades, so, the inner layer blades get less amount of energy to extract power. This can be clearly seen in the figures from fig 6.23 to Fig. 6.25 where, the contribution of inner layer blades to the total power coefficient is very low and somewhere negative.

### 6.3.4 Relationship between torque coefficient and angle of rotation



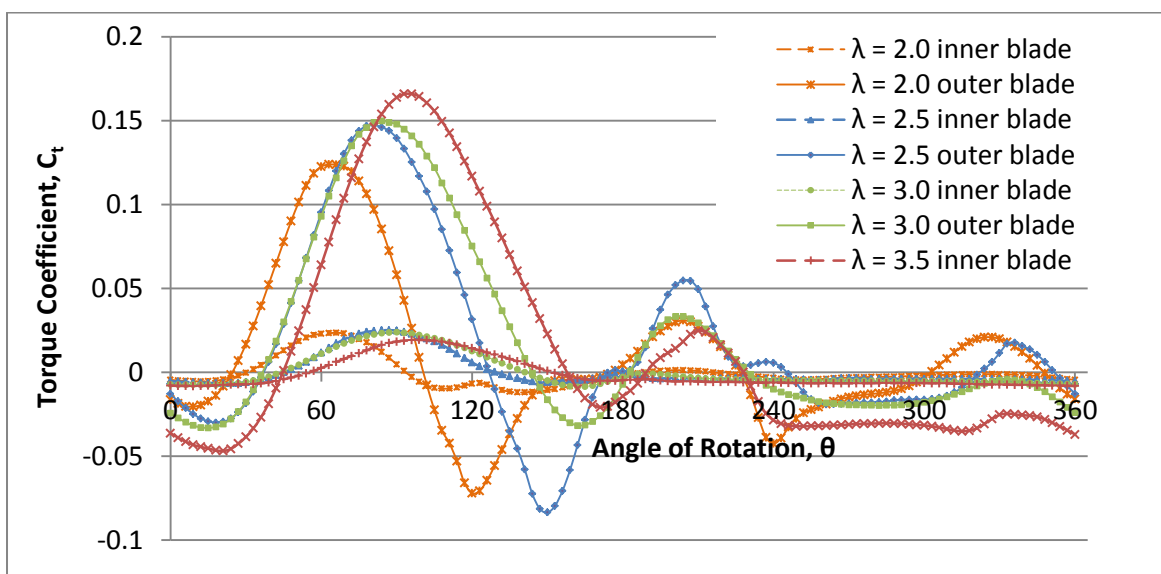
**Fig. 6.26:**  $C_t$  vs.  $\theta$  for  $\zeta=0.5$  Double layered H-Darrieus VAWT (max  $C_p$  at  $\lambda=4.0$ )

Fig. 6.26 to 6.28 shows the change in  $C_t$  of a single blade of each layer of Double layered H-Darrieus turbine with its angle of rotation ( $\theta$ ). For double layered H-rotor VAWT with solidity 0.75, peak value of  $C_t$  for outer layer blade is 0.095889 at  $\lambda=4$  and at  $\theta=84^\circ$  and peak value of  $C_t$  for inner layer blade is 0.019991 at  $\lambda=4$  and at  $\theta=78^\circ$ .



**Fig. 6.27:**  $C_t$  vs.  $\theta$  for  $\zeta=1.05$  Double layered H-Darrieus VAWT (max  $C_p$  at  $\lambda=3.75$ )

From Fig. 6.27, for a double layered VAWT with  $\zeta=1.05$ , the peak  $C_t$  for inner layer blade and outer layer blade are respectively 0.021585 and 0.137452. The outer layer blade achieves its peak  $C_t$  when it rotates at tip speed ratio 3.75 and its angular position is,  $\theta=99^\circ$ . The inner layer blade's peak  $C_t$  is achieved for  $\lambda=4.0$  and at angle of rotation  $\theta=93^\circ$ .



**Fig. 6.28:**  $C_t$  vs.  $\theta$  for  $\zeta=1.5$  Double layered H-Darrieus VAWT (max  $C_p$  at  $\lambda=3.0$ )

When solidity is further increased to  $\zeta=1.5$ , the peak  $C_t$  of an individual outer layer blade is found 0.17 for the conditions  $\lambda=4$  and at  $\theta=97^\circ$ . The inner layer blade gains its peak  $C_t$  when tangential velocity ( $\Omega R$ ) is 3.75 times of the free stream velocity (i.e.  $\lambda=3.75$ ) and when its angular position is,  $\theta=90^\circ$ . The value of peak  $C_t$  of inner layer blade is 0.0239.

It is clear that the maximum part of the torque is generated by the blade when it is in upstream side of the wind turbine. It is because the blade faces maximum induced velocity in the upstream side, which is almost equal to the free stream velocity. Nevertheless, when it moves to the downstream side the induced velocity falls as a portion of kinetic energy of wind has already been used by the blades at upstream side for power generation. Velocity contours are shown in Fig. 6.29 to Fig. 6.34 and the velocity vectors around the blade are shown in Fig.6.35 to 6.40.

One important observation is the torque created by the inner layer blades is always lower than the outer layer blades. The reason behind this also lies in the reduced induced velocity at the inner layer blades. Even at the downstream side the  $C_t$  is negative for inner layer blades. This means, the inner layer blades at the downstream side use the power in order to rotate, which is generated by the blades at upstream side.

It is shown in the Fig. 6.26, the maximum torque coefficient, which is achieved by an outer layer blade, is in between 78 degree to 96 degree angle of rotation. For the solidity  $\zeta=0.75$ , the  $(C_p)_{\max}$  is achieved at  $\lambda=4$ . The  $C_t$  of the individual outer layer blade is also found to be the highest at that tip speed ratio ( $\lambda=4$ ). The maximum  $C_t$  that is achieved by an individual outer layer blade, is 0.0958894 at  $\theta=84^\circ$  and the maximum  $C_t$  that is achieved by an individual inner layer blade at the same tip speed ratio, is

0.0199914 at  $\theta=78^\circ$  which is also the highest among the maximum  $C_t$ 's at different tip speed ratios.

On the contrary, the maximum  $C_t$ , which is achieved by an individual outer layer blade for  $\zeta=1.05$  and  $\zeta=1.5$ , is not achieved at the same tip speed ratio at which the power coefficient is maximum. Rather, it is achieved at higher tip speed ratio. Though the peak  $C_t$  of an individual blade is higher at a tip speed ratio higher than  $\lambda=3.5$  for VAWT with  $\sigma=1.5$ , yet, the average  $C_t$  of the blade becomes lower as the value of negative  $C_t$  is also higher.

From the Fig. 6.26 to 6.28, it is evident that, the peak value of torque coefficient of an individual blade of double layered H-Darrieus Vertical Axis Wind Turbine increases with the increase in solidity.

The peak  $C_t$  of a blade of the double layered H-rotor VAWT is lower than the peak  $C_t$  of a blade of the single layered H-rotor VAWT. The outer layer blades of Double Layered H-Darrieus VAWT generate positive torque in the downstream side of the turbine, even at higher solidity. This is clearly an advantage of the double layered H-rotor VAWT.

### 6.3.5 Velocity Contour and Velocity Vectors

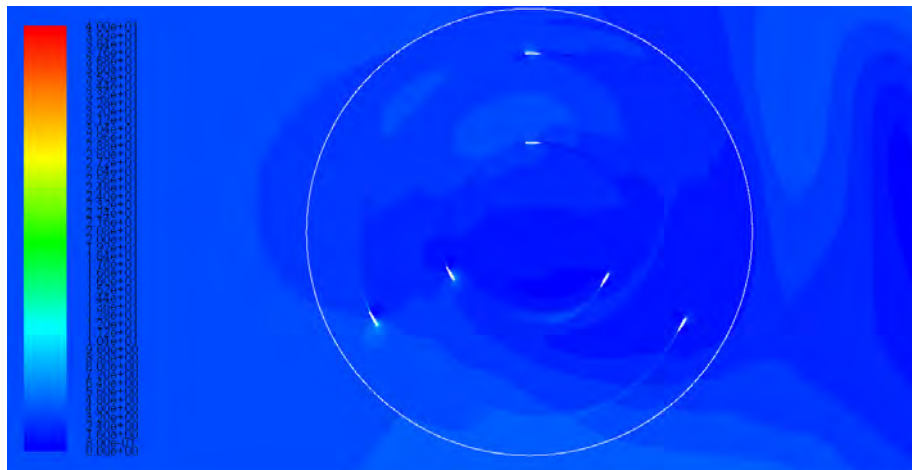


**Fig. 6.29:** Velocity contour of 6 Bladed Double layered H – Rotor VAWT; Solidity 0.75,  $\lambda=4.5$ (0 degree)



**Fig. 6.30:** Velocity contour of 6 Bladed Double layered H – Rotor VAWT;  
Solidity 0.75,  $\lambda=4.5$ (60 degree)

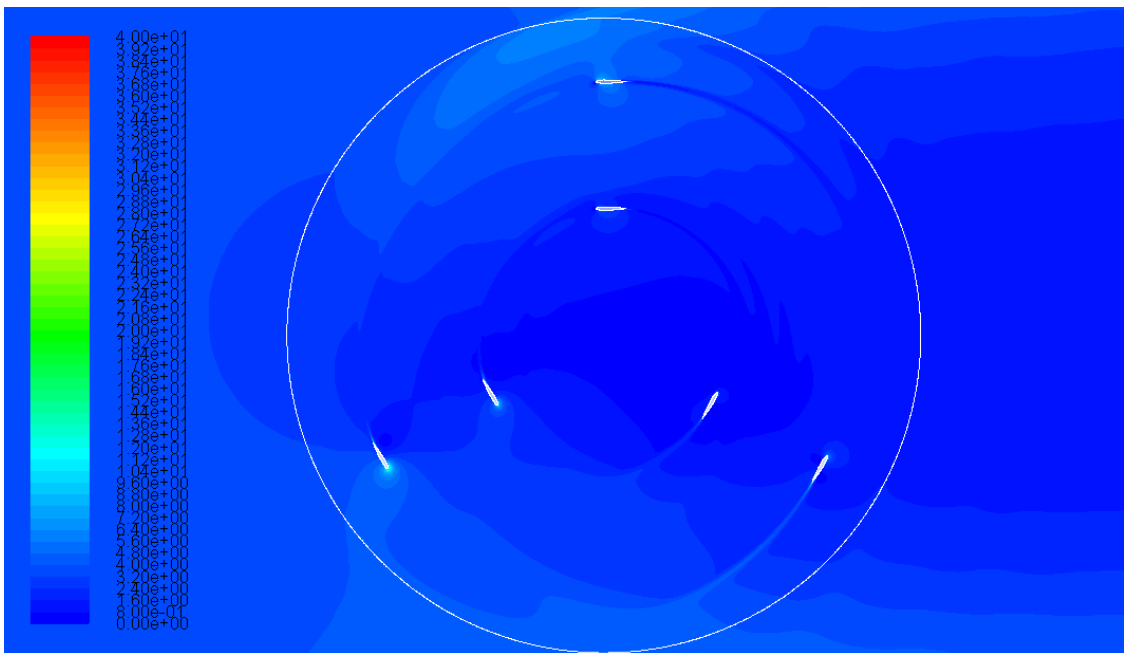


**Fig. 6.31:** Velocity contour of 6 Bladed Double layered H – Rotor VAWT;  
Solidity 1.05,  $\lambda=3.75$ (0 degree)

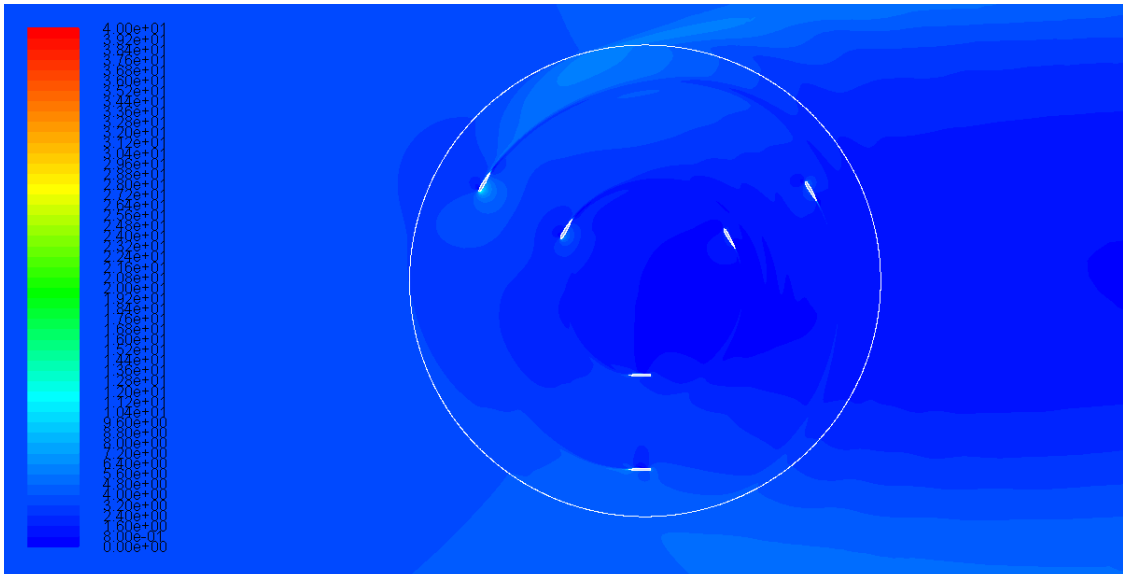


**Fig. 6.32:** Velocity contour of 6 Bladed Double layered H – Rotor VAWT;  
Solidity 1.05,  $\lambda=3.75$ (60 degree)

The velocity contours depicted in the figures for Fig. 6.29 to Fig. 6.34 show that, at downstream side the velocity of wind decreases, as a portion of the kinetic energy of wind is used by the upstream turbine blades for generating torque and power which is similar to the Single Layered H-Darrieus VAWT. The inner layer blades fronting lower velocity wind than the outer layer blades. This is a reason for the lower power coefficient of the inner layer blades. Velocity vectors around the blade are shown in Fig. 6.35 to Fig. 6.40.

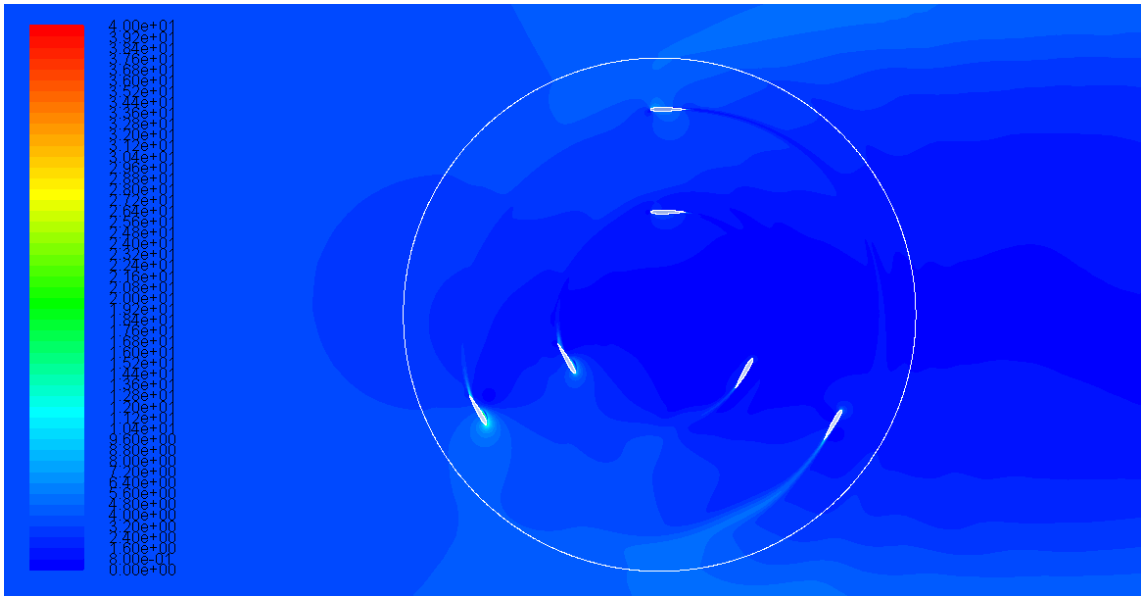


**Fig. 6.33:** Velocity contour of 6 Bladed Double layered H – Rotor VAWT; Solidity 1.5,  $\lambda=3(0 \text{ degree})$

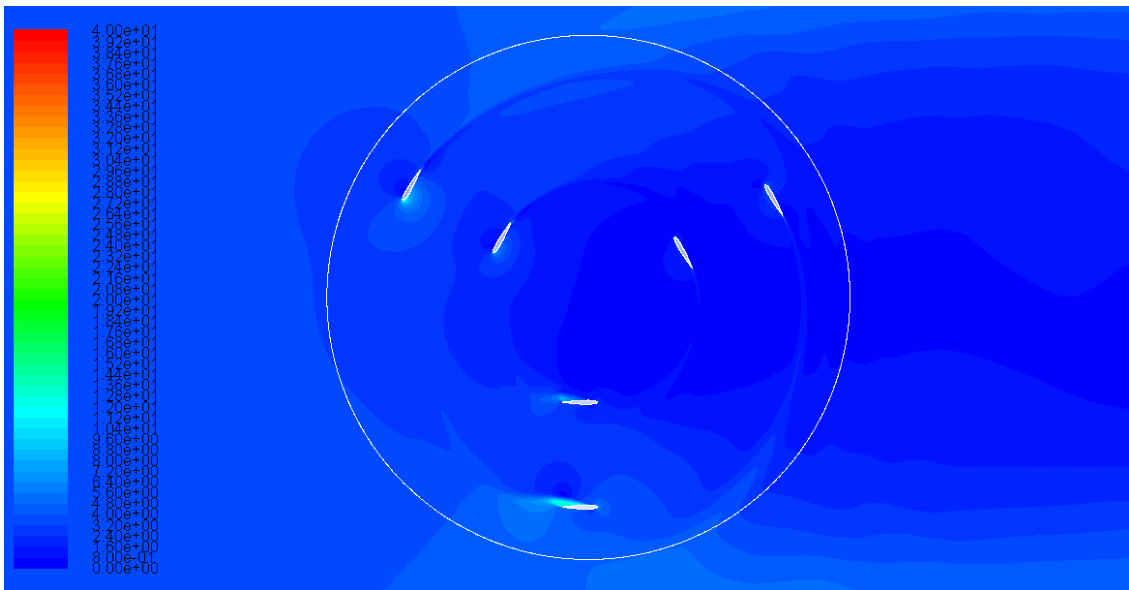


**Fig. 6.34:** Velocity contour of 6 Bladed Double layered H – Rotor VAWT; Solidity 1.5,  $\lambda=3(60 \text{ degree})$

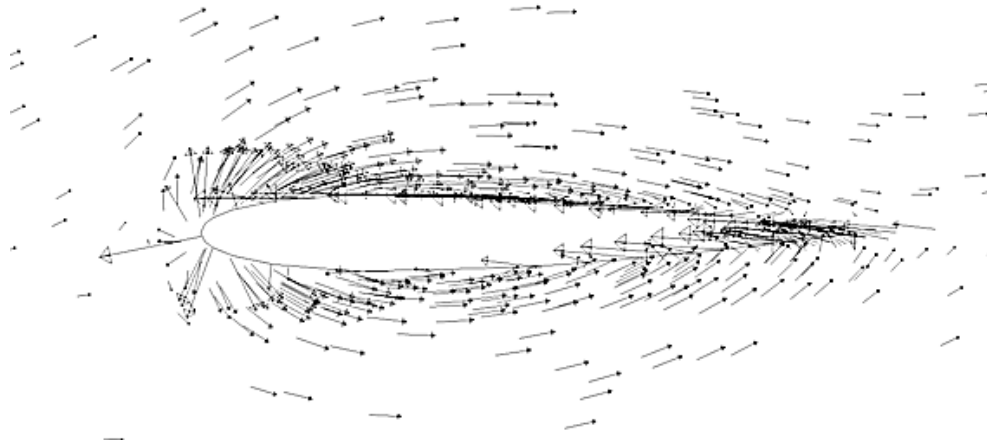


**Fig. 6.35(a):** Velocity vector of 6 Bladed Double layered H – Rotor VAWT; Solidity 0.75,  $\lambda=4.5$  (outer layer blades at 0 degree)

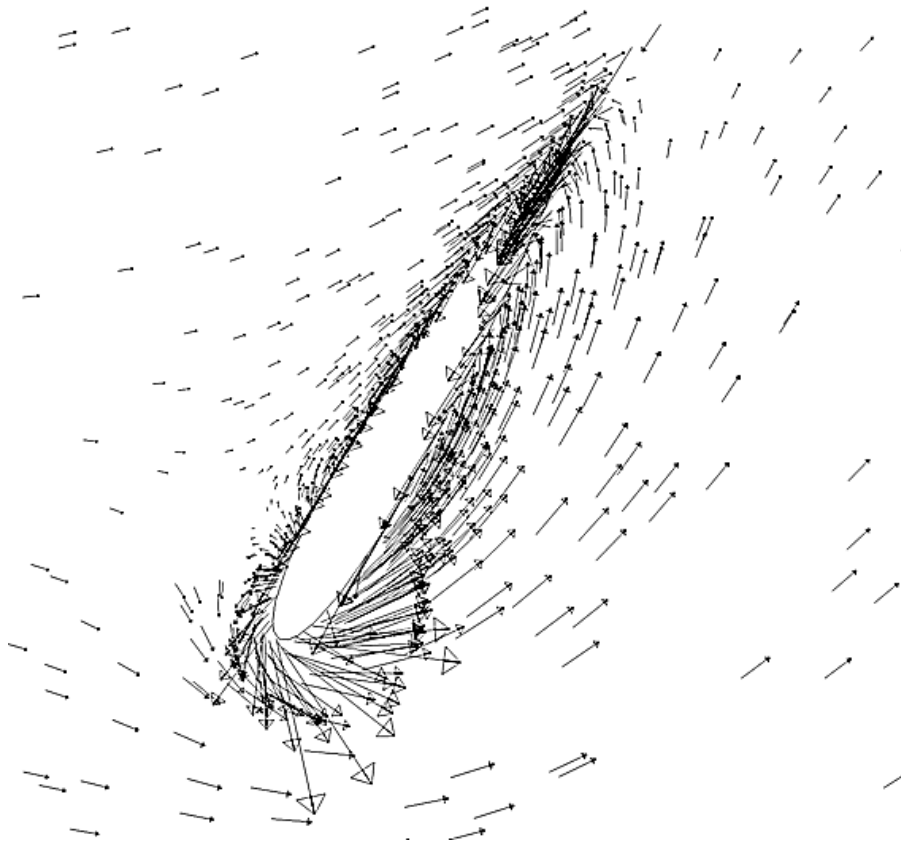


**Fig. 6.35(b):** Velocity vector of 6 Bladed Double layered H – Rotor VAWT; Solidity 0.75,  $\lambda=4.5$  (outer layer blades at 60 degree)



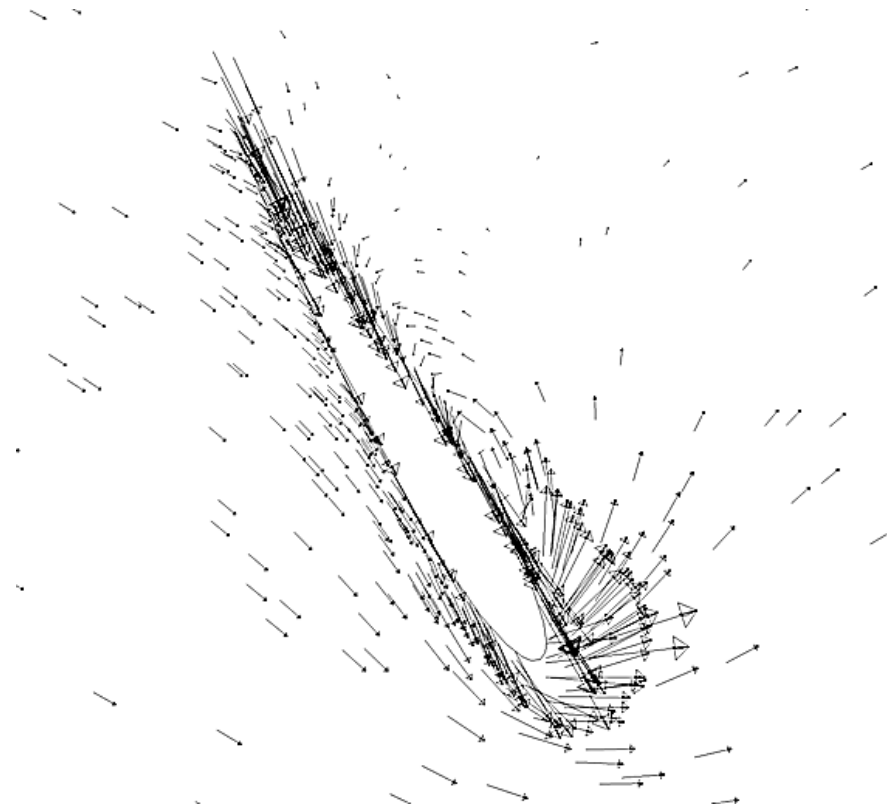


**Fig. 6.35(c):** Velocity vector of 6 Bladed Double layered H – Rotor VAWT; Solidity 0.75,  $\lambda=4.5$  (outer layer blades at 120 degree)

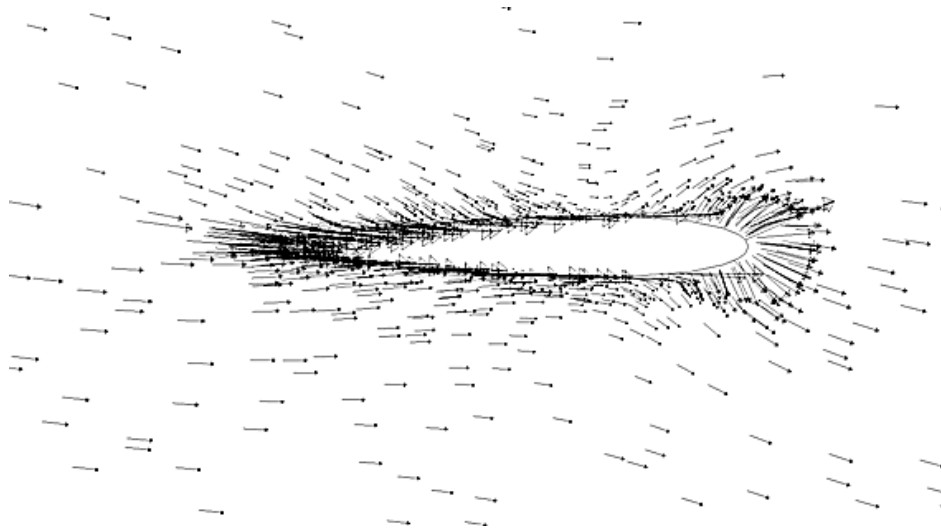


**Fig. 6.35(d):** Velocity vector of 6 Bladed Double layered H – Rotor VAWT; Solidity 0.75,  $\lambda=4.5$  (outer layer blades at 180 degree)

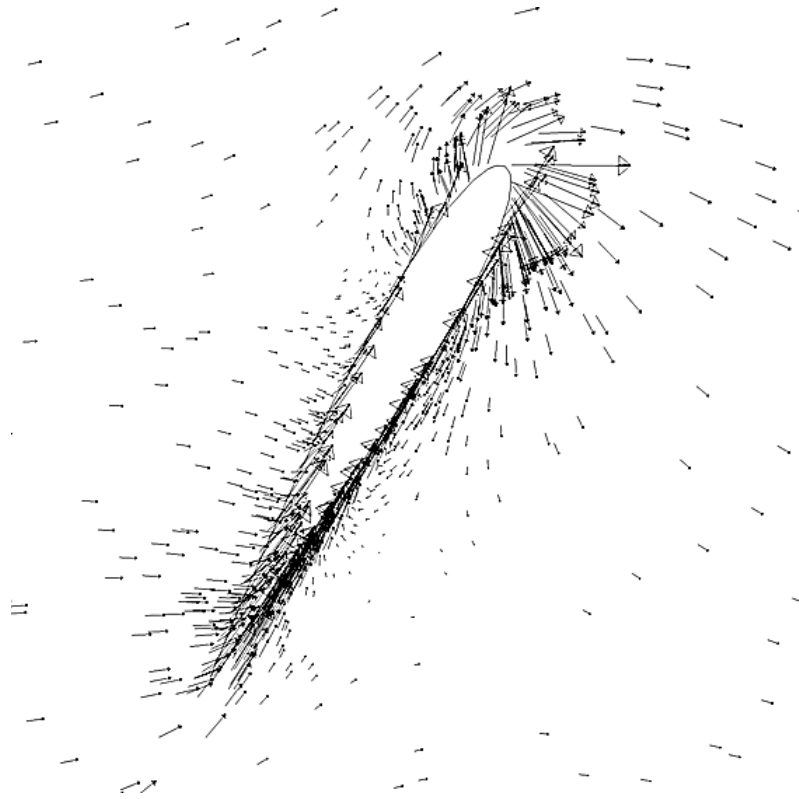


**Fig. 6.35(e):** Velocity vector of 6 Bladed Double layered H – Rotor VAWT; Solidity 0.75,  $\lambda=4.5$  (outer layer blades at 240 degree)

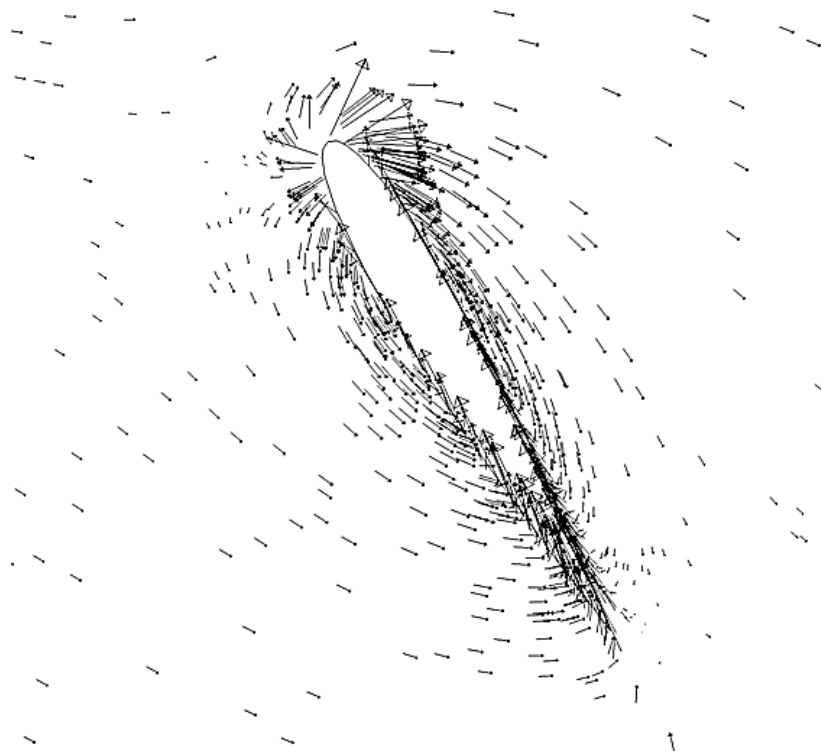


**Fig. 6.35(f):** Velocity vector of 6 Bladed Double layered H – Rotor VAWT; Solidity 0.75,  $\lambda=4.5$  (outer layer blades at 300 degree)

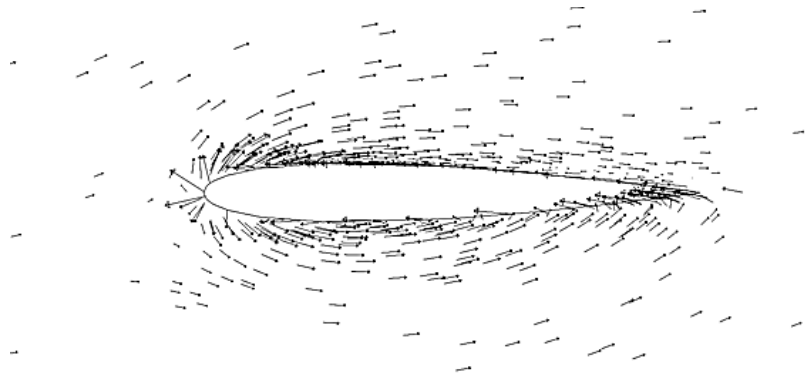


**Fig. 6.36(a):** Velocity vector of 6 Bladed Double layered H – Rotor VAWT; Solidity 0.75,  $\lambda=4.5$  (inner layer blade at 0 degree)

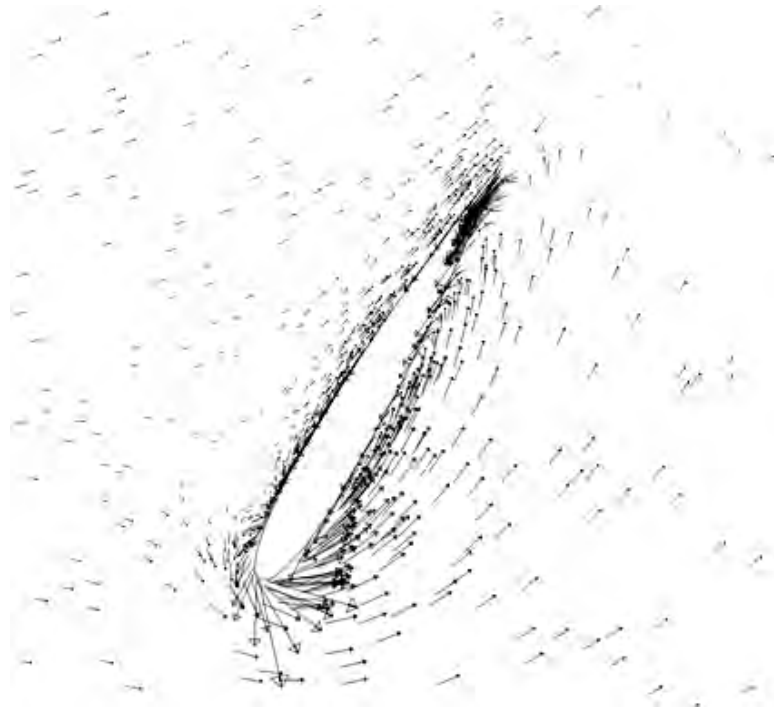


**Fig. 6.36(b):** Velocity vector of 6 Bladed Double layered H – Rotor VAWT; Solidity 0.75,  $\lambda=4.5$  (inner layer blade at 60 degree)



**Fig. 6.36(c):** Velocity vector of 6 Bladed Double layered H – Rotor VAWT; Solidity 0.75,  $\lambda=4.5$  (inner layer blade at 120 degree)

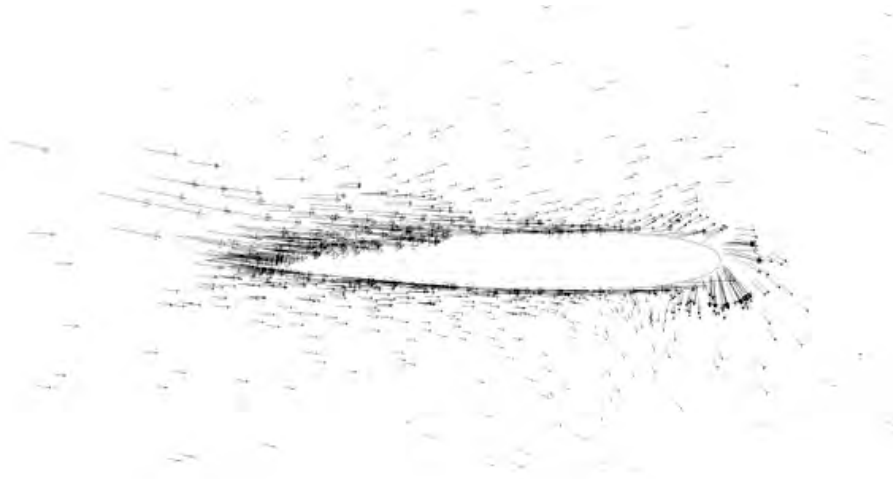


**Fig. 6.36(d):** Velocity vector of 6 Bladed Double layered H – Rotor VAWT; Solidity 0.75,  $\lambda=4.5$  (inner layer blade at 180 degree)

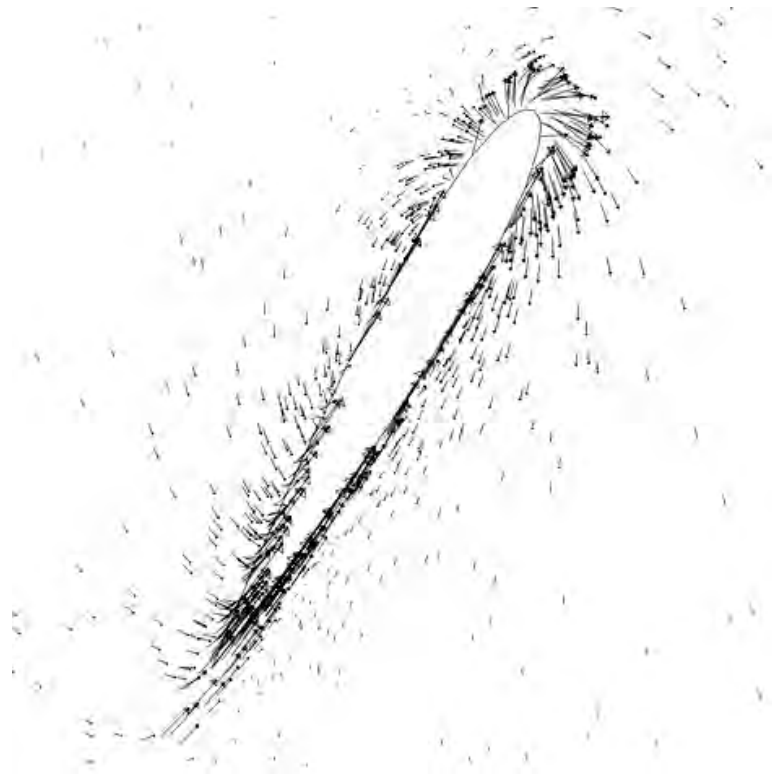


**Fig. 6.36(e):** Velocity vector of 6 Bladed Double layered H – Rotor VAWT; Solidity 0.75,  $\lambda=4.5$  (inner layer blade at (a) 240 degree)

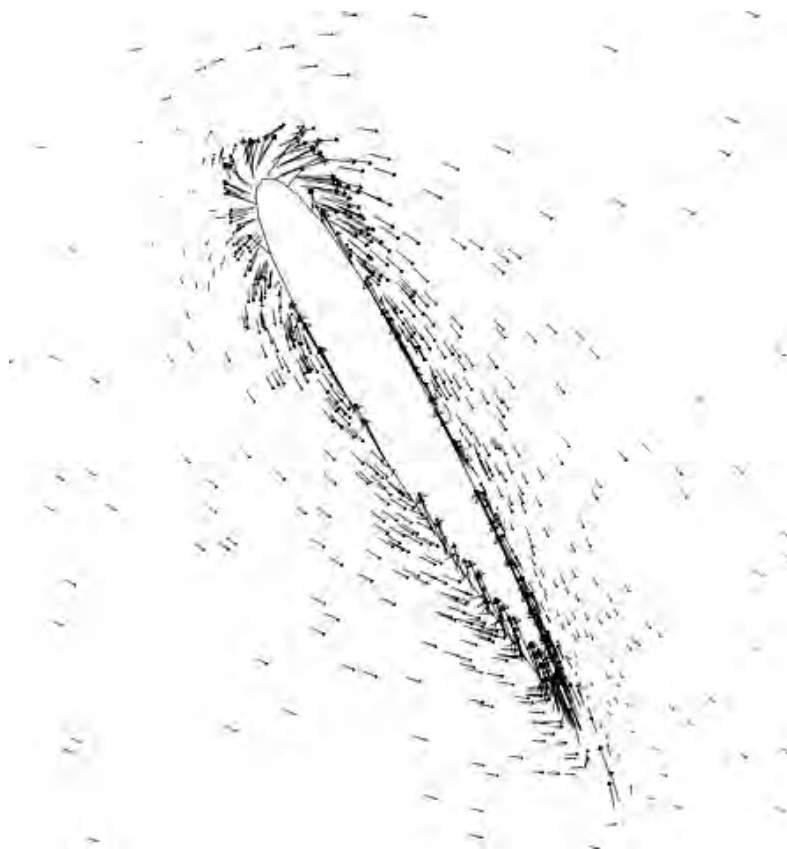


**Fig. 6.36(f):** Velocity vector of 6 Bladed Double layered H – Rotor VAWT; Solidity 0.75,  $\lambda=4.5$  (inner layer blade at 300 degree)

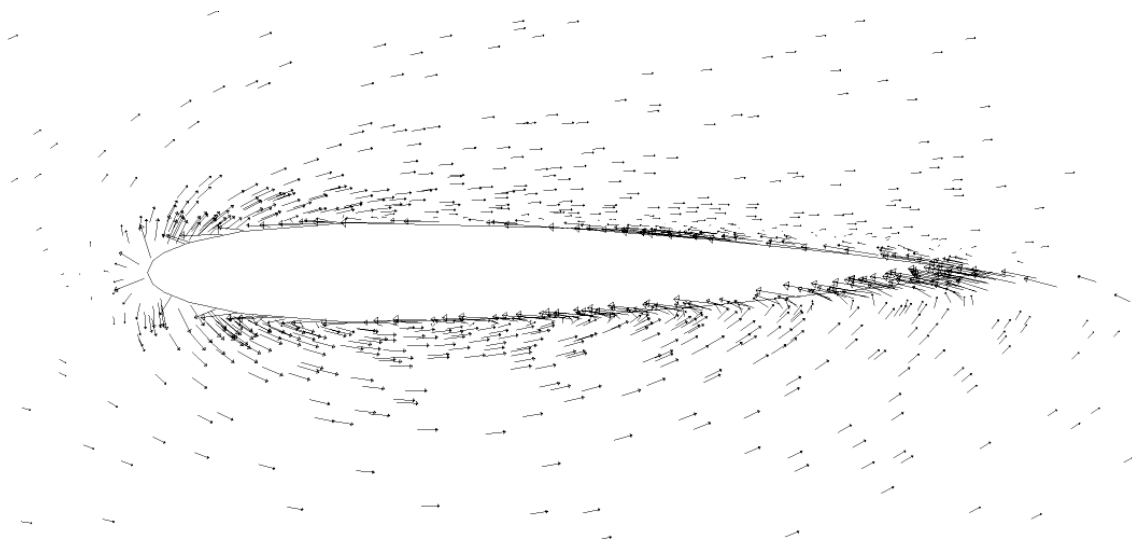


**Fig. 6.37(a):** Velocity vector of 6 Bladed Double layered H – Rotor VAWT; Solidity 1.05,  $\lambda=3.75$  (inner layer blades at 0 degree)

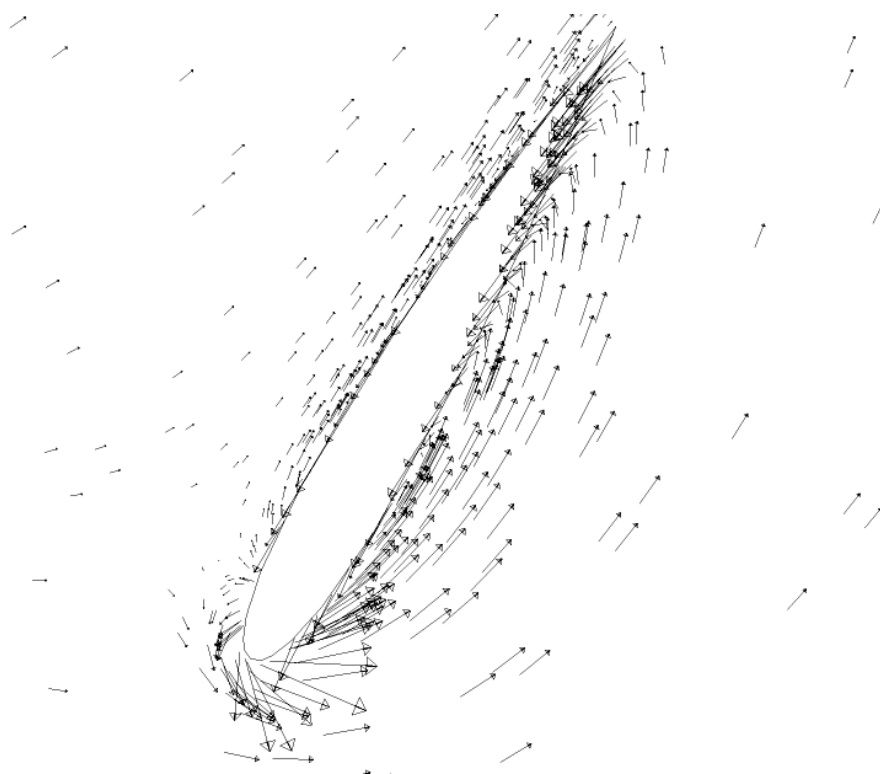


**Fig. 6.37(b):** Velocity vector of 6 Bladed Double layered H – Rotor VAWT; Solidity 1.05,  $\lambda=3.75$  (inner layer blades at 60 degree)

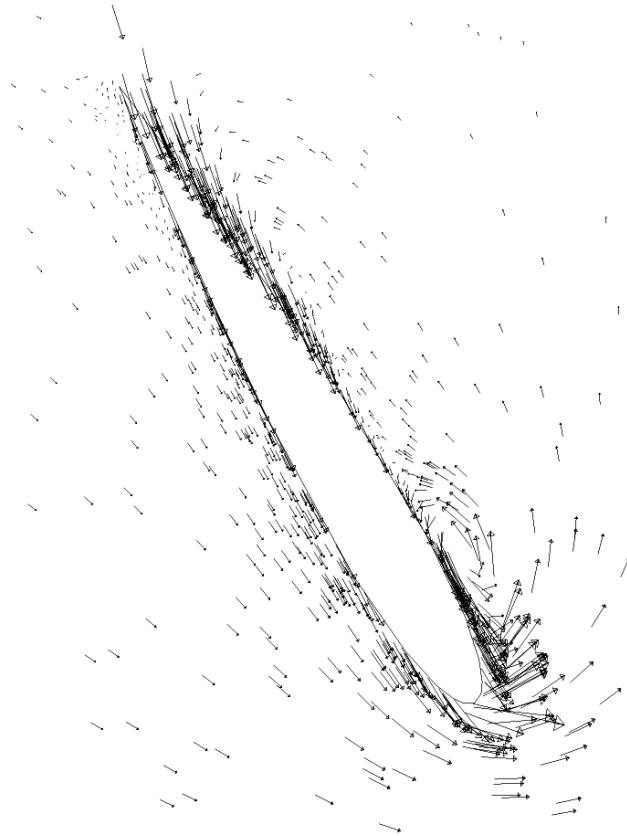


**Fig. 6.37(c):** Velocity vector of 6 Bladed Double layered H – Rotor VAWT; Solidity 1.05,  $\lambda=3.75$  (inner layer blades at 120 degree)

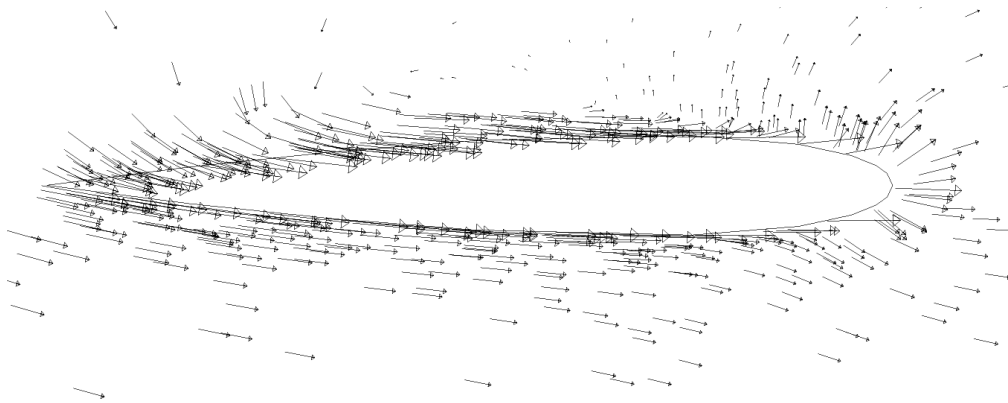


**Fig. 6.37(d):** Velocity vector of 6 Bladed Double layered H – Rotor VAWT; Solidity 1.05,  $\lambda=3.75$  (inner layer blades at 180 degree)

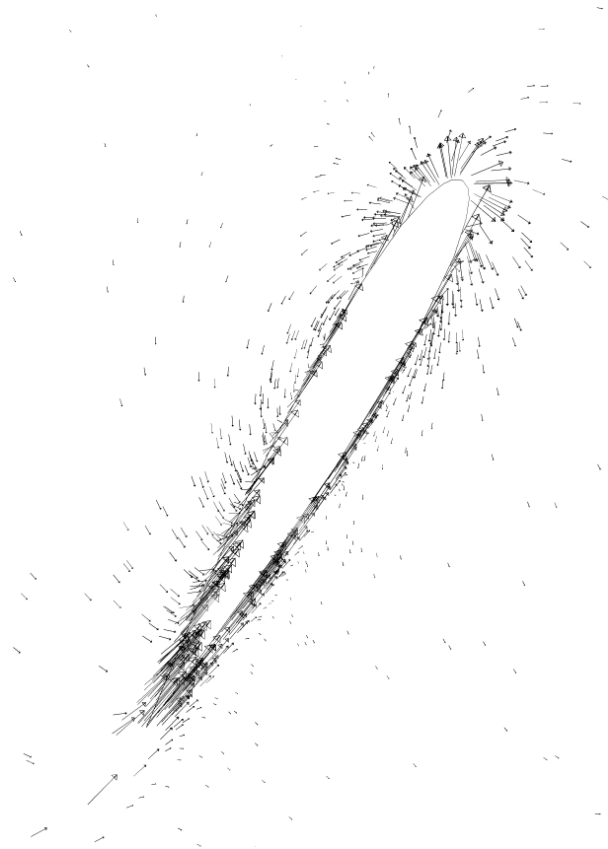


**Fig. 6.37(e):** Velocity vector of 6 Bladed Double layered H – Rotor VAWT; Solidity 1.05,  $\lambda=3.75$  (inner layer blades at 240 degree)

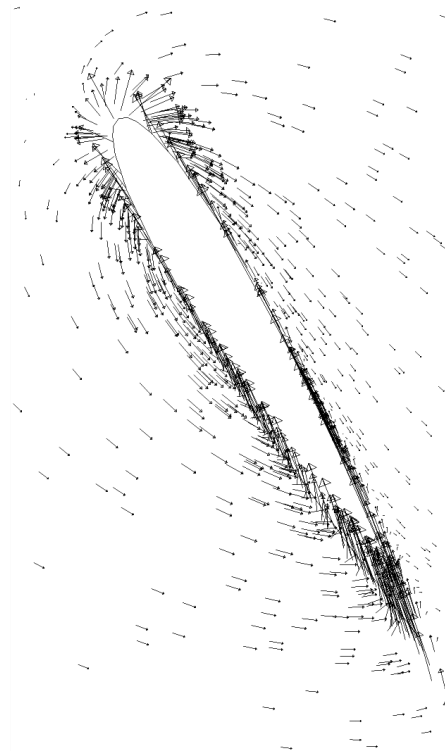


**Fig. 6.37(f):** Velocity vector of 6 Bladed Double layered H – Rotor VAWT; Solidity 1.05,  $\lambda=3.75$  (inner layer blades at 300 degree)



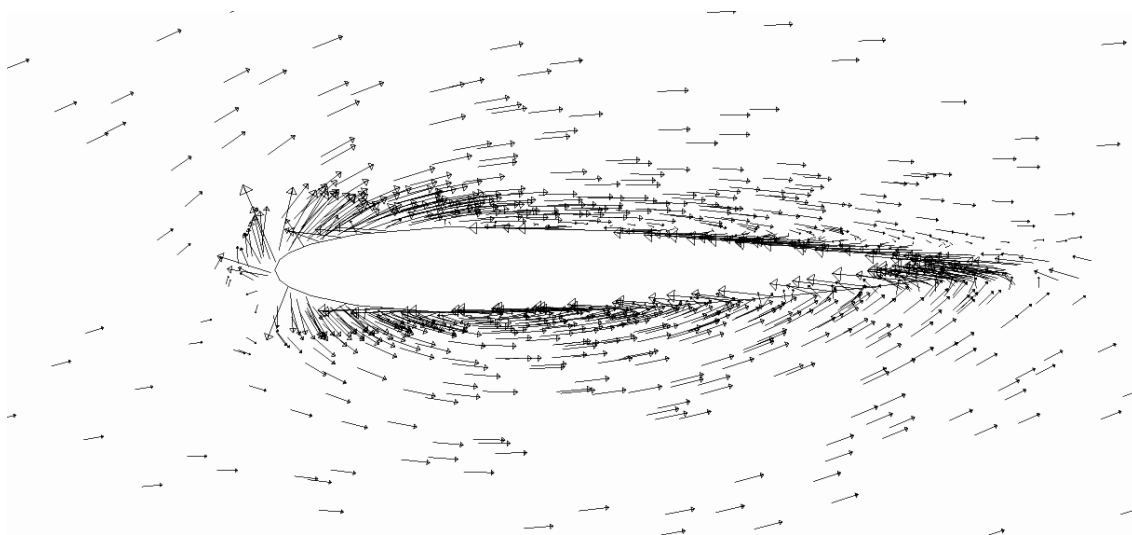


**Fig. 6.38(a):** Velocity vector of 6 Bladed Double layered H – Rotor VAWT; Solidity 1.05,  $\lambda=3.75$  (outer layer blades at 0 degree)

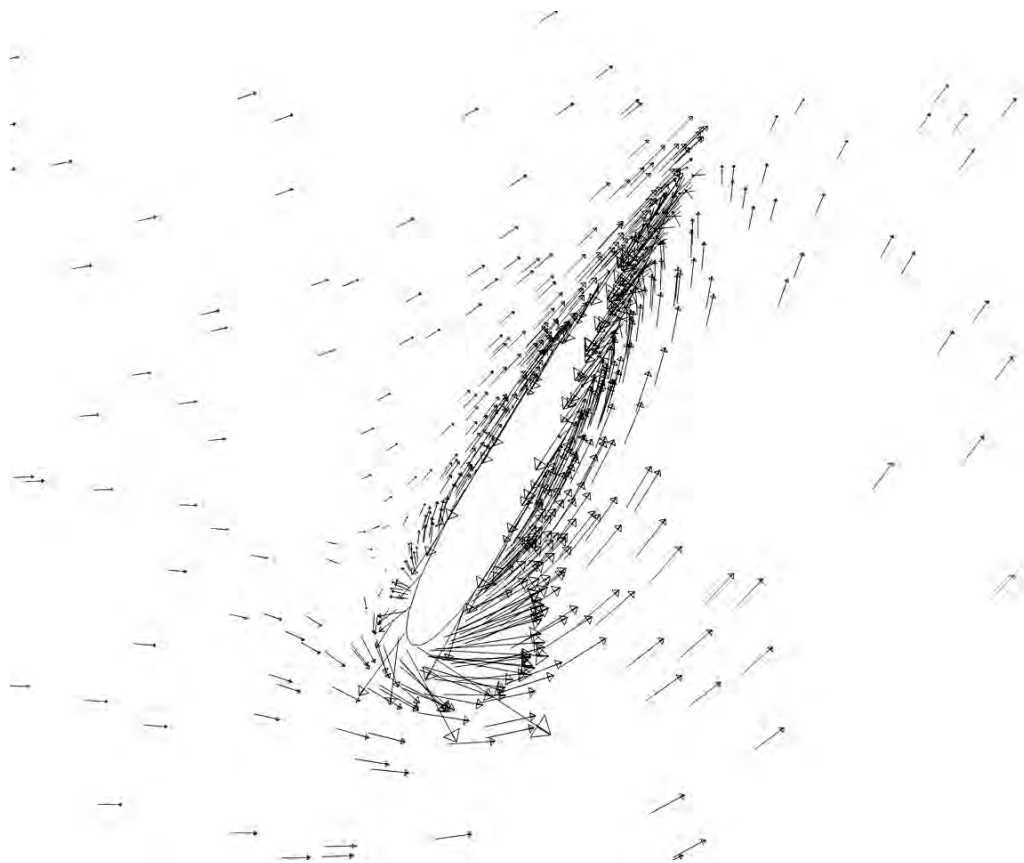


**Fig. 6.38(b):** Velocity vector of 6 Bladed Double layered H – Rotor VAWT; Solidity 1.05,  $\lambda=3.75$  (outer layer blades at 60 degree)

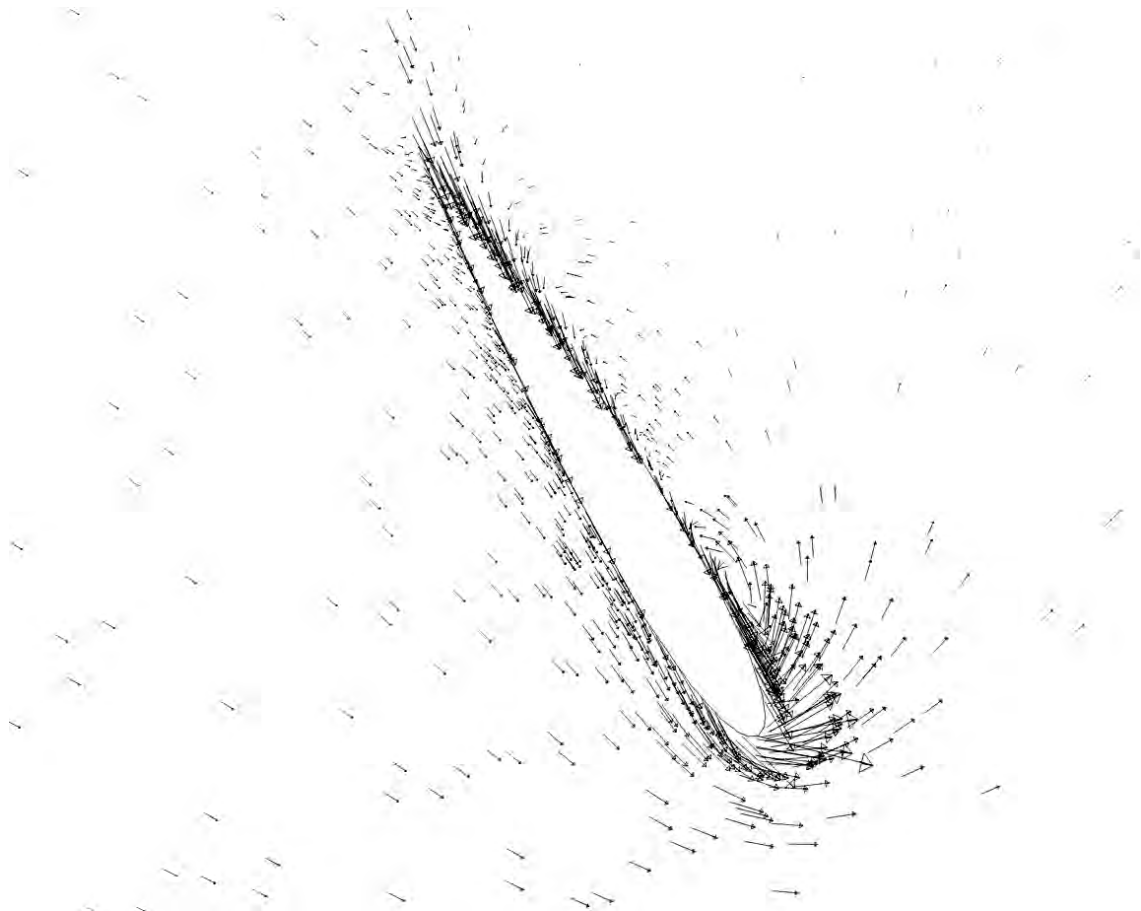


**Fig. 6.38(c):** Velocity vector of 6 Bladed Double layered H – Rotor VAWT; Solidity 1.05,  $\lambda=3.75$  (outer layer blades at 120 degree)

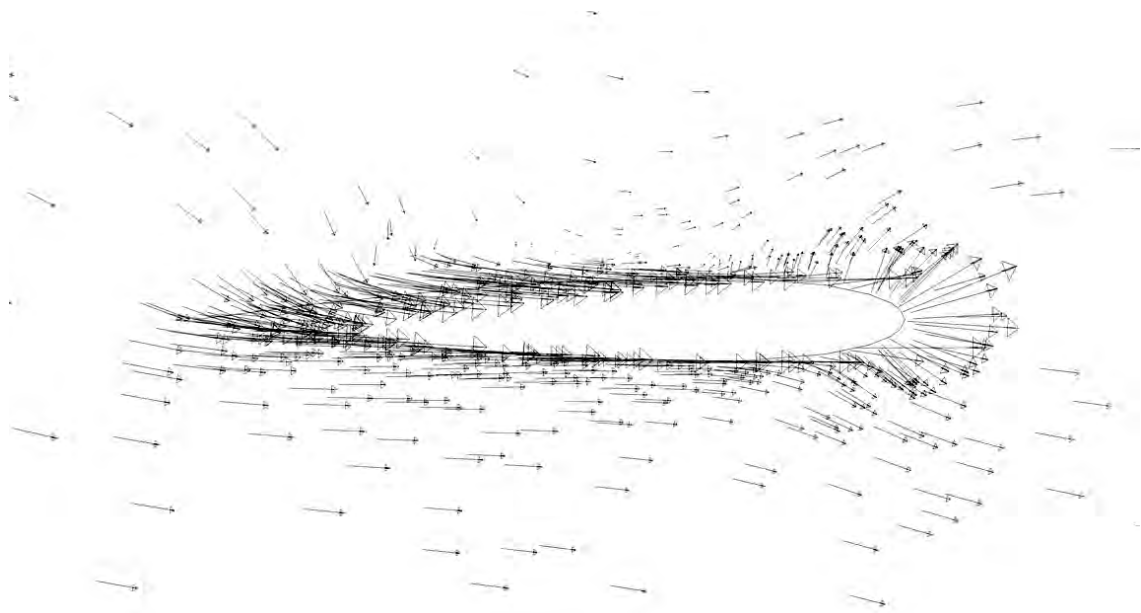


**Fig. 6.38(d):** Velocity vector of 6 Bladed Double layered H – Rotor VAWT; Solidity 1.05,  $\lambda=3.75$  (outer layer blades at 180 degree)

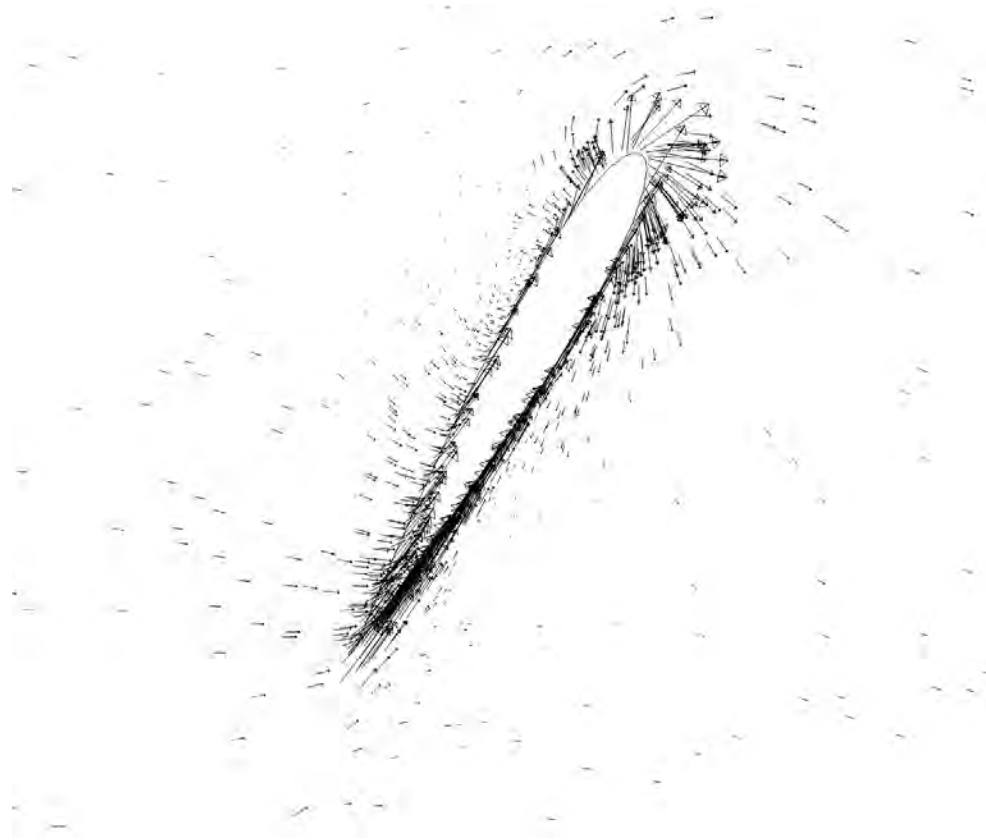


**Fig. 6.38(e):** Velocity vector of 6 Bladed Double layered H – Rotor VAWT; Solidity 1.05,  $\lambda=3.75$  (outer layer blades at 240 degree)

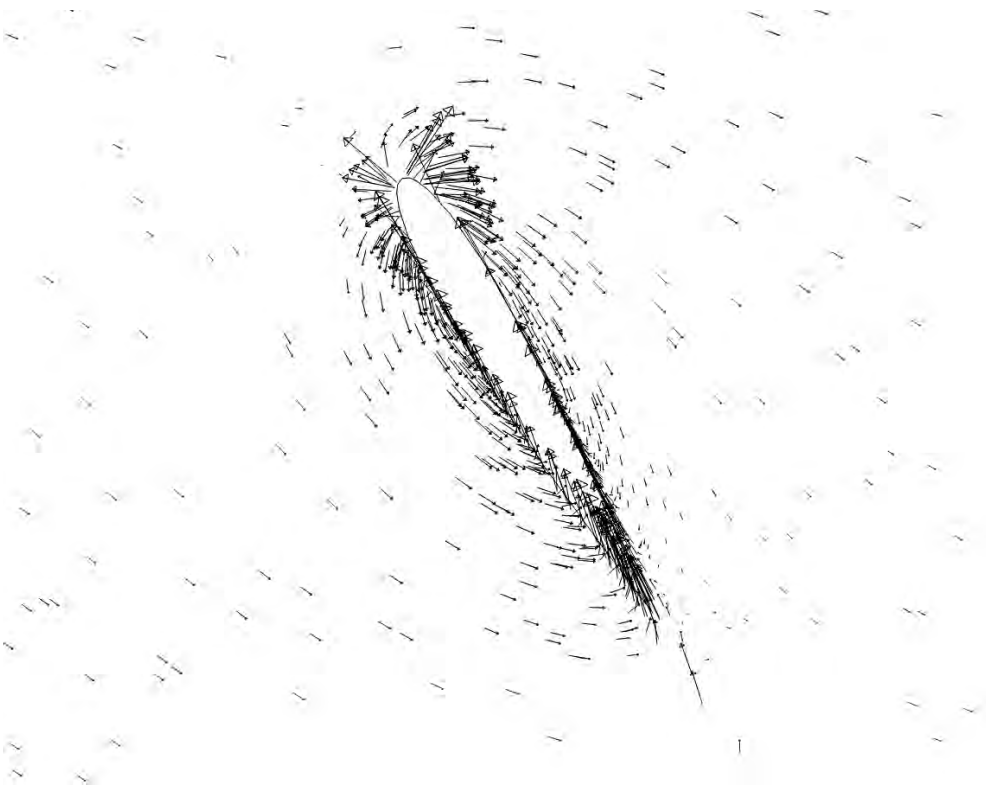


**Fig. 6.38(f):** Velocity vector of 6 Bladed Double layered H – Rotor VAWT; Solidity 1.05,  $\lambda=3.75$  (outer layer blades at 300 degree)

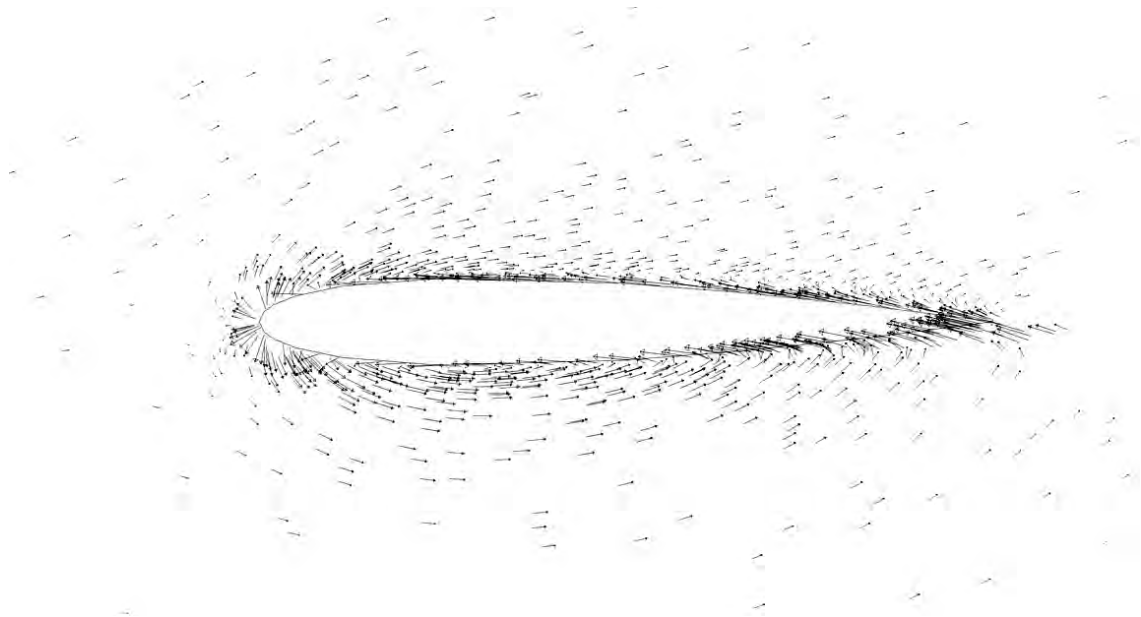


**Fig. 6.39(a):** Velocity vector of 6 Bladed Double layered H – Rotor VAWT; Solidity 1.5,  $\lambda=3.0$  (inner layer blades at 0 degree)

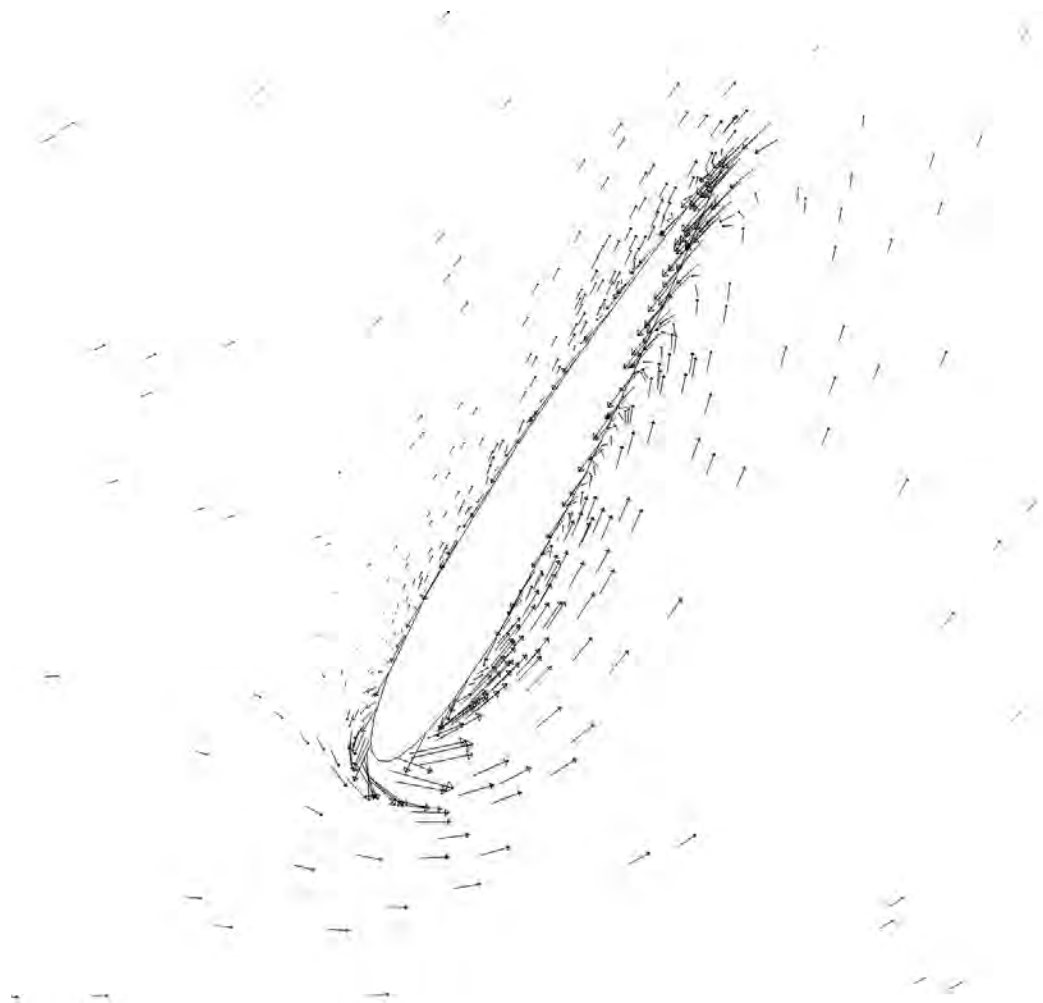


**Fig. 6.39(b):** Velocity vector of 6 Bladed Double layered H – Rotor VAWT; Solidity 1.5,  $\lambda=3.0$  (inner layer blades at 60 degree)

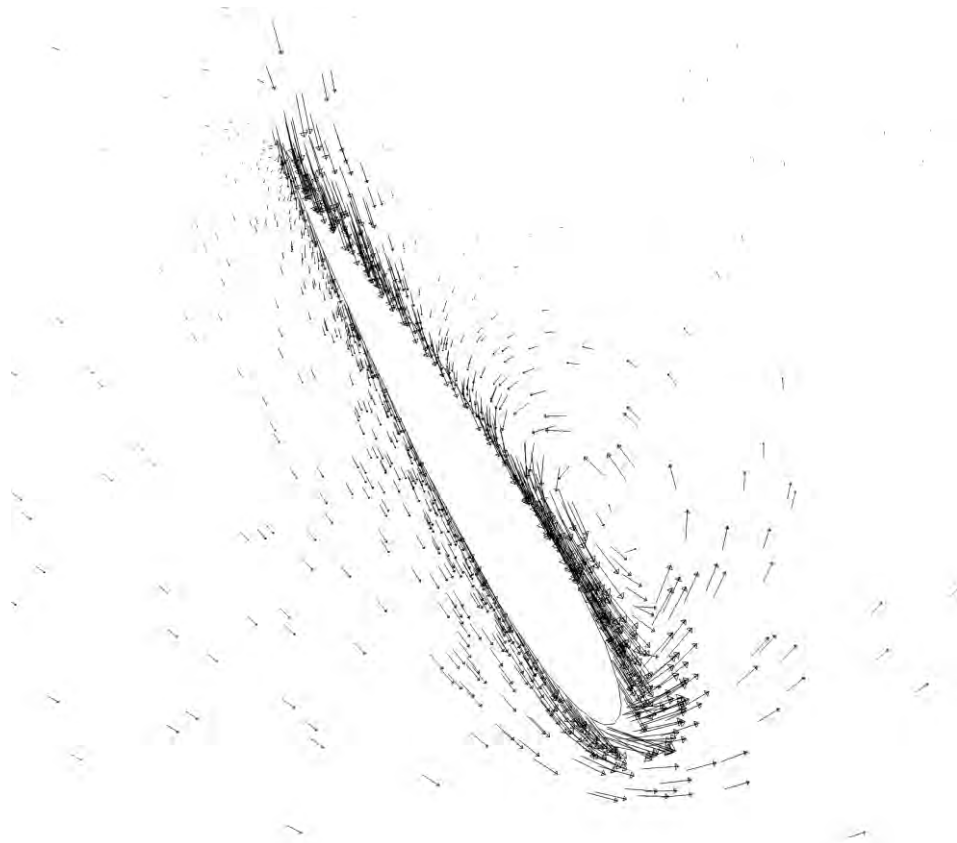


**Fig. 6.39(c):** Velocity vector of 6 Bladed Double layered H – Rotor VAWT; Solidity 1.5,  $\lambda=3.0$  (inner layer blades at 120 degree)

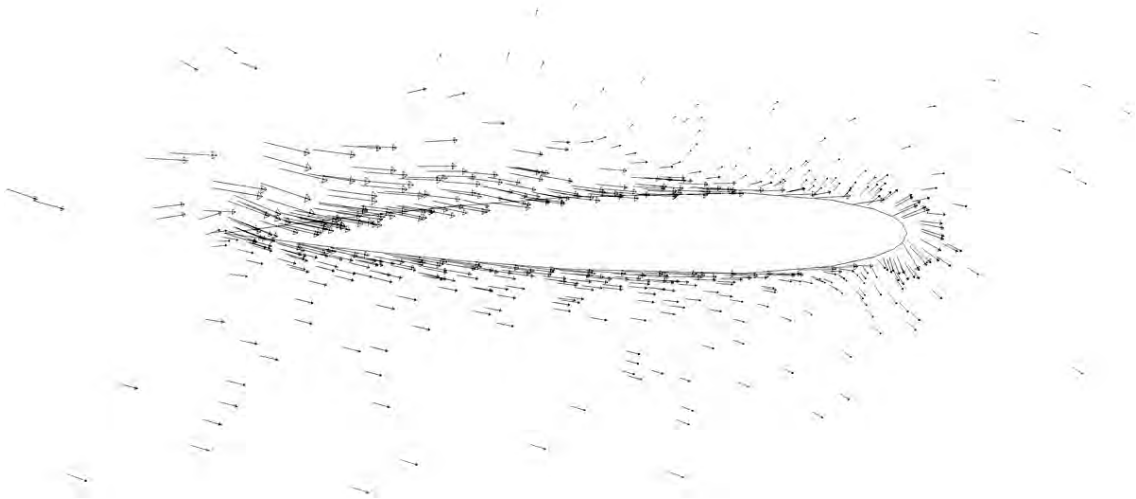


**Fig. 6.39(d):** Velocity vector of 6 Bladed Double layered H – Rotor VAWT; Solidity 1.5,  $\lambda=3.0$  (inner layer blades at 180 degree)

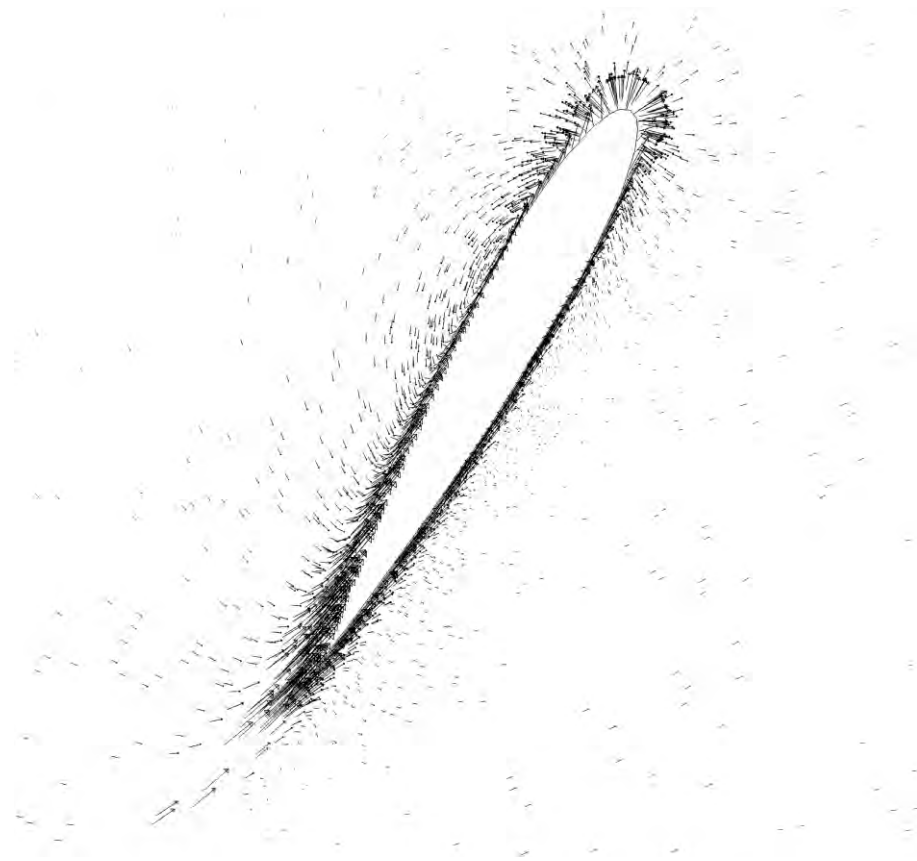


**Fig. 6.39(e):** Velocity vector of 6 Bladed Double layered H – Rotor VAWT; Solidity 1.5,  $\lambda=3.0$  (inner layer blades at 240 degree)

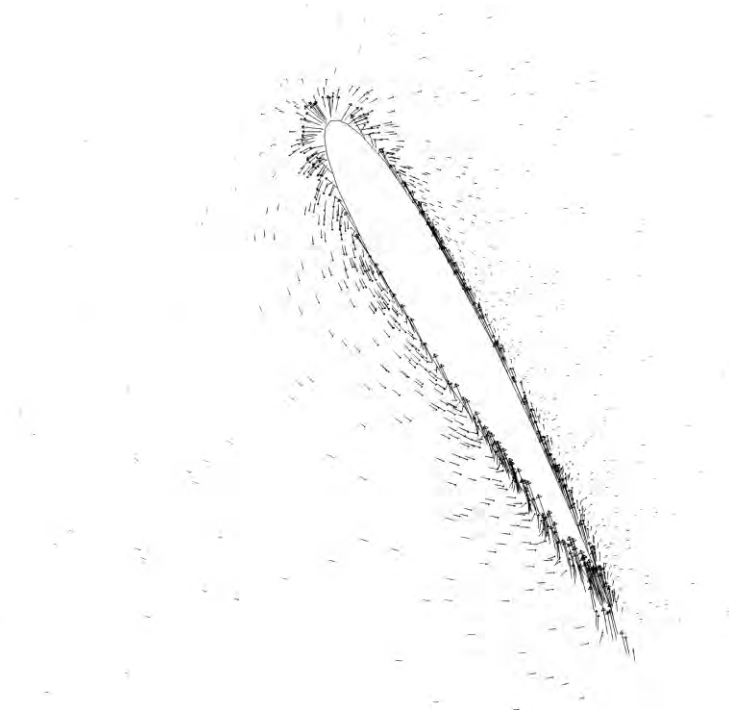


**Fig. 6.39(f):** Velocity vector of 6 Bladed Double layered H – Rotor VAWT; Solidity 1.5,  $\lambda=3.0$  (inner layer blades at 300 degree)

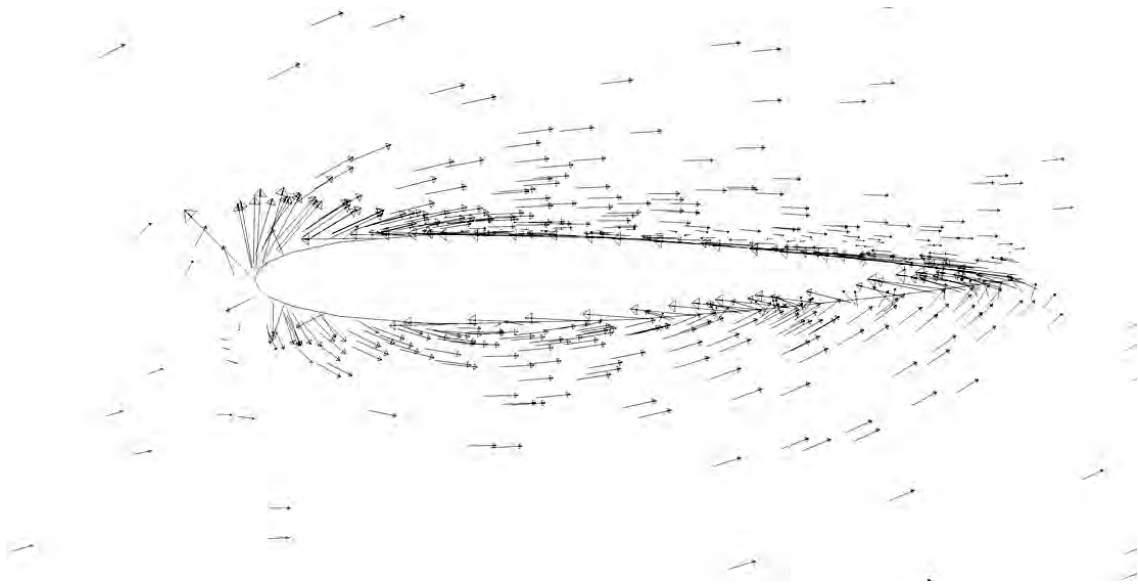


**Fig. 6.40(a):** Velocity vector of 6 Bladed Double layered H – Rotor VAWT; Solidity 1.5,  $\lambda=3.0$  (outer layer blades at 0 degree)

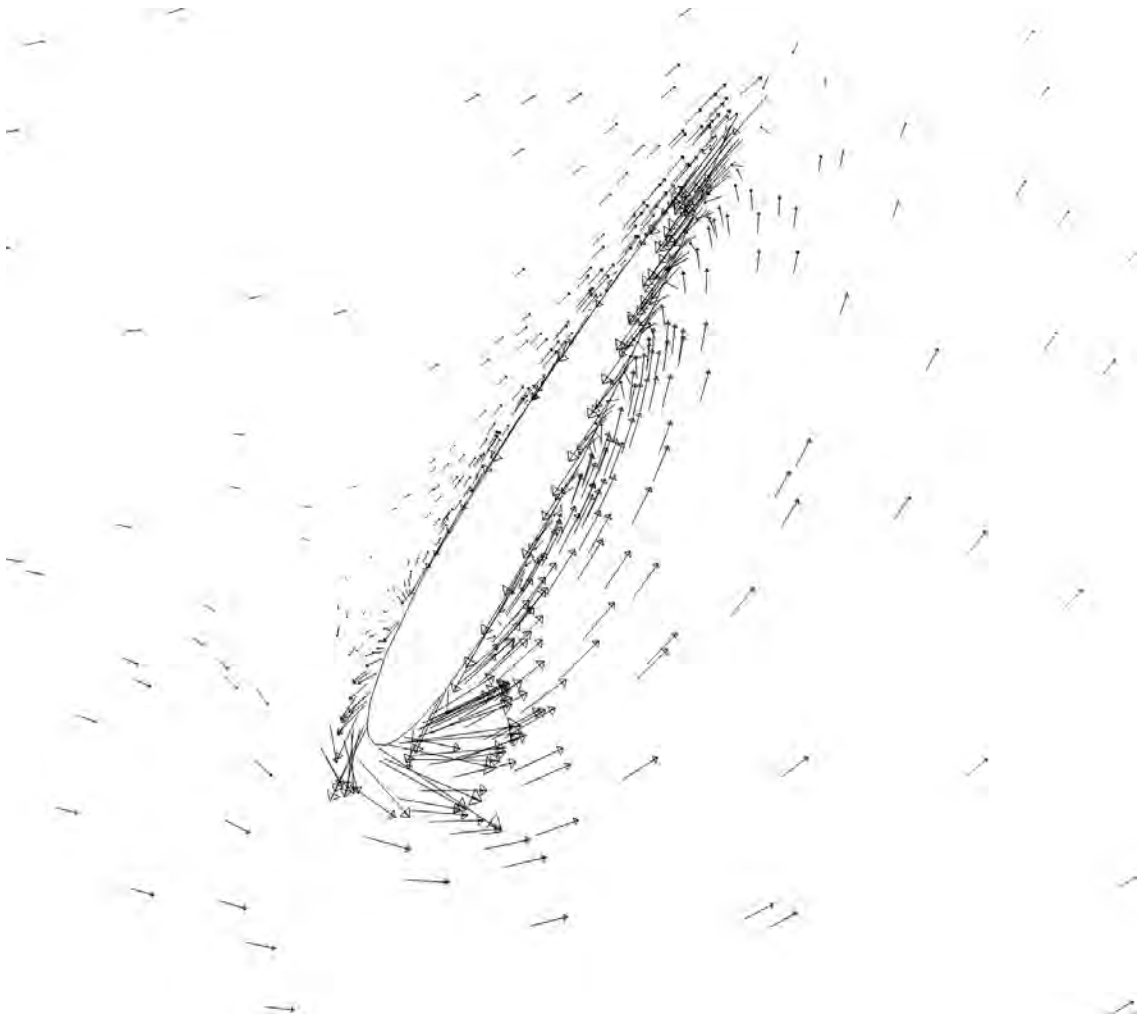


**Fig. 6.40(b):** Velocity vector of 6 Bladed Double layered H – Rotor VAWT; Solidity 1.5,  $\lambda=3.0$  (outer layer blades at 60 degree)

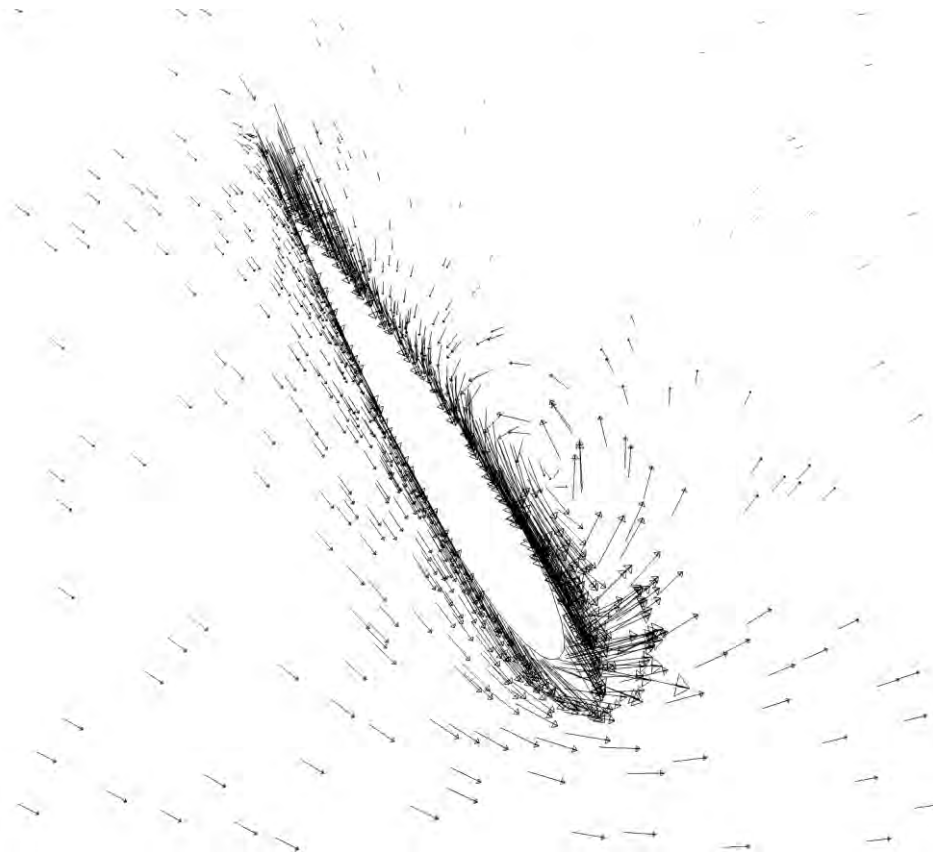


**Fig. 6.40(c):** Velocity vector of 6 Bladed Double layered H – Rotor VAWT; Solidity 1.5,  $\lambda=3.0$  (outer layer blades at 120 degree)

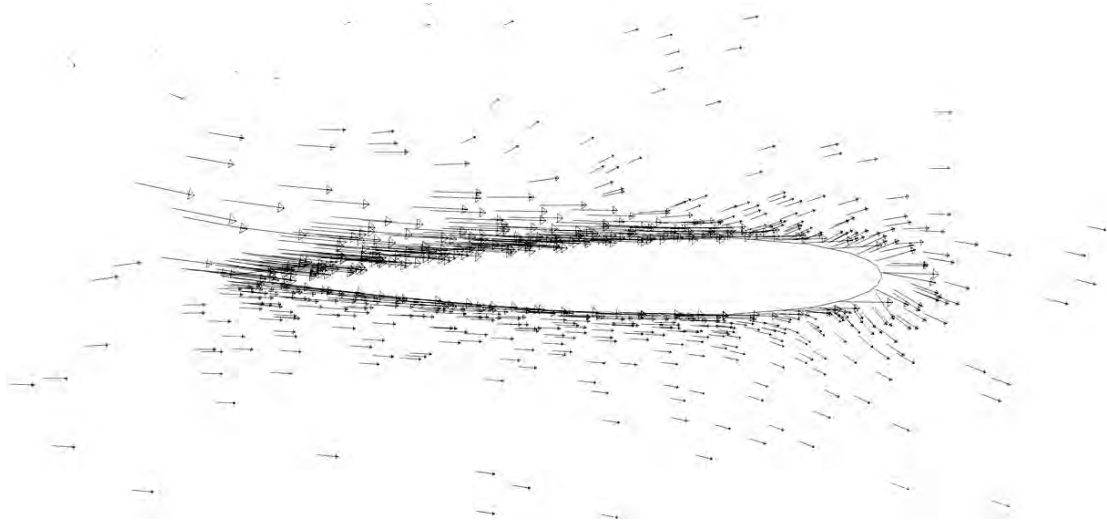


**Fig. 6.40(d):** Velocity vector of 6 Bladed Double layered H – Rotor VAWT; Solidity 1.5,  $\lambda=3.0$  (outer layer blades at 180 degree)



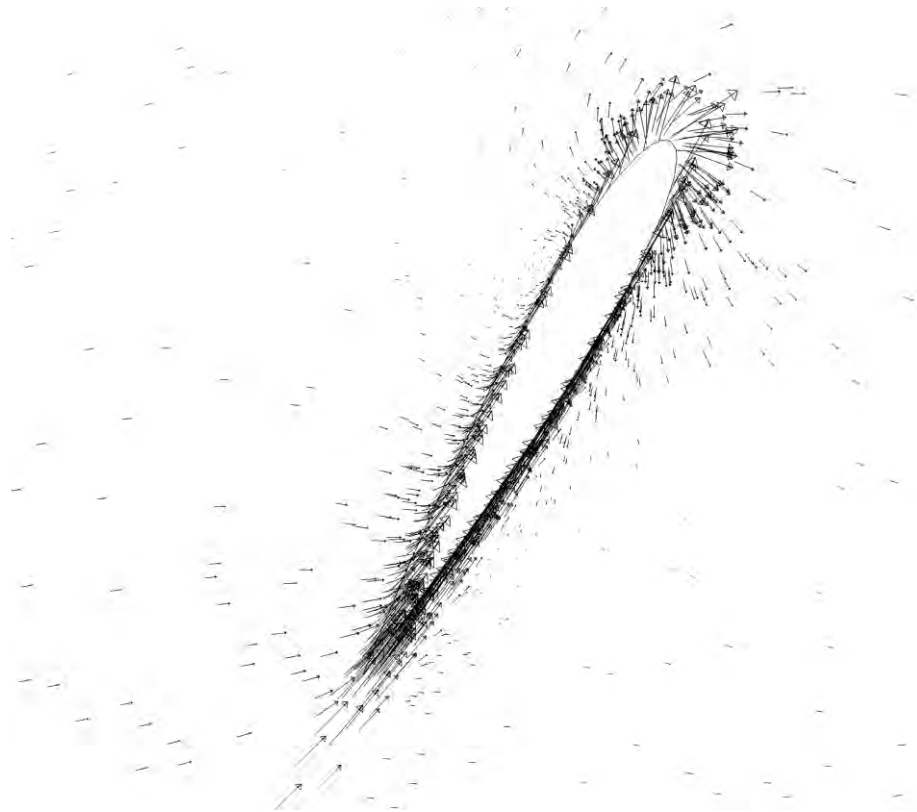


**Fig. 6.40(e):** Velocity vector of 6 Bladed Double layered H – Rotor VAWT; Solidity 1.5,  $\lambda=3.0$  (outer layer blades at 240 degree)

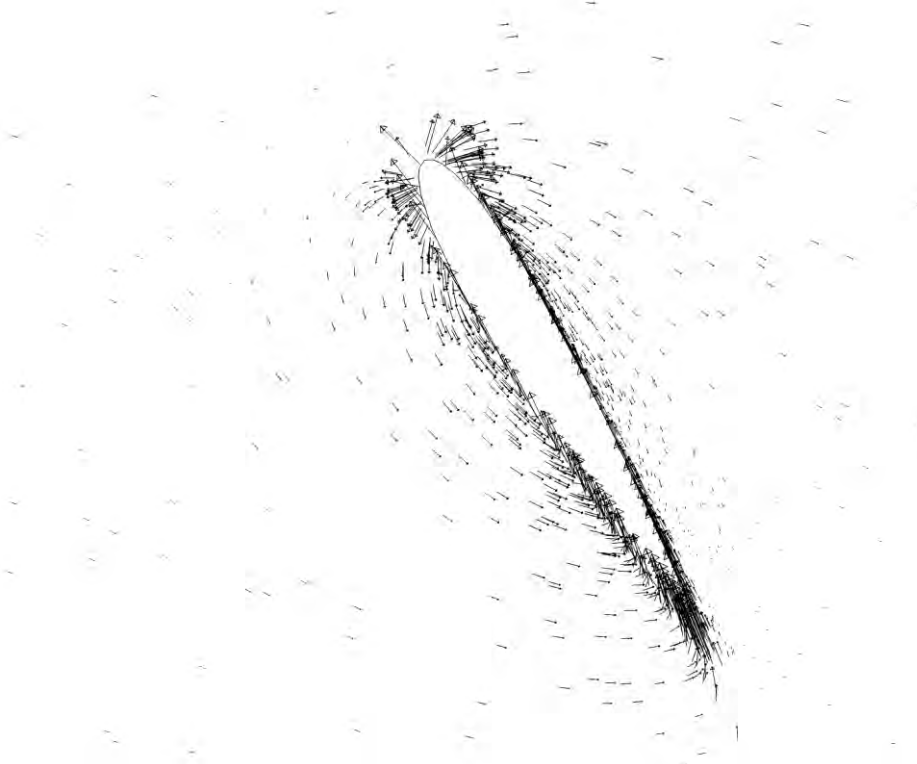


**Fig. 6.40(f):** Velocity vector of 6 Bladed Double layered H – Rotor VAWT; Solidity 1.5,  $\lambda=3.0$  (outer layer blades at 300 degree)

### 6.3.6 Pressure Contour

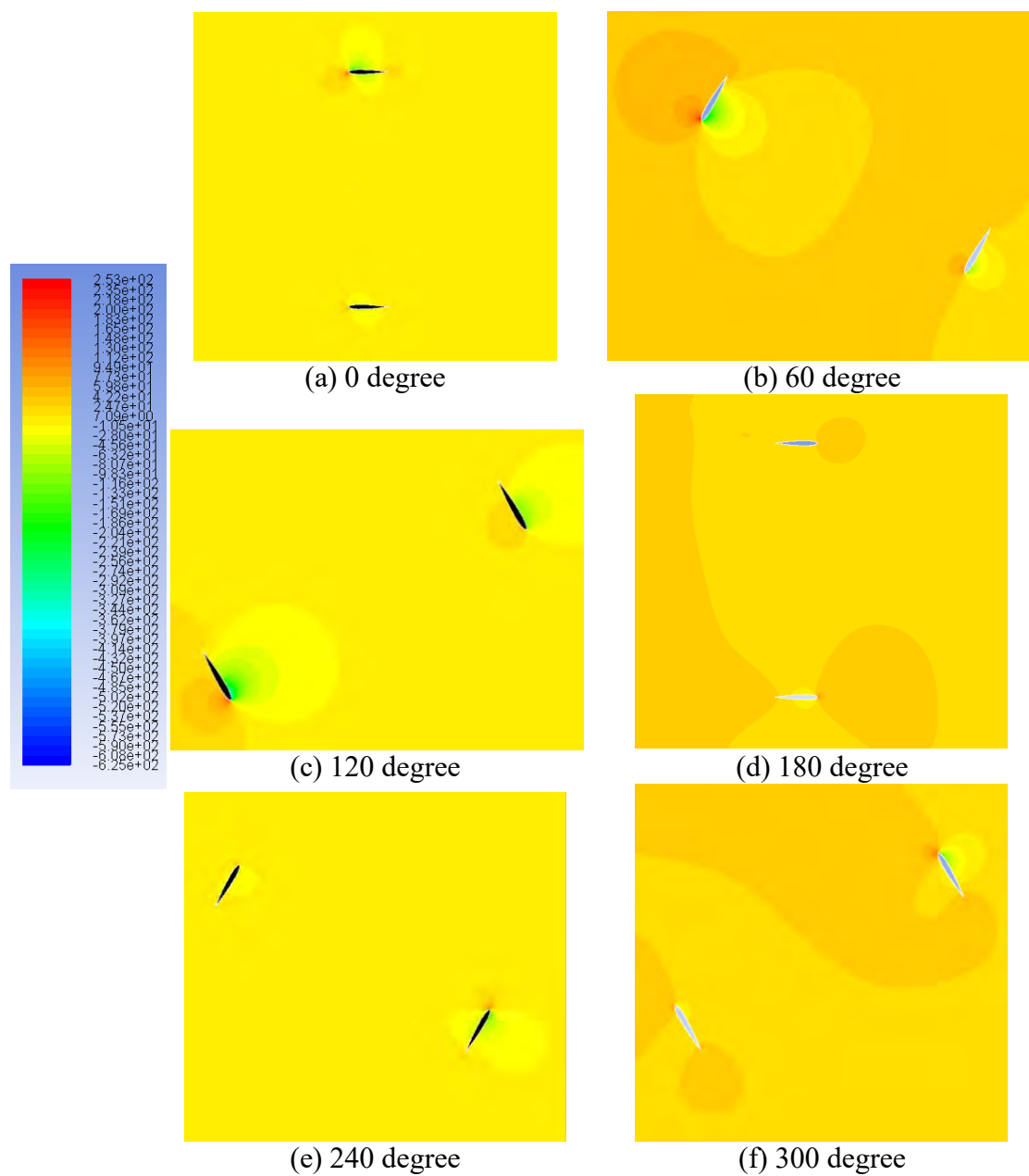


**Fig. 6.41:** Pressure contour of 6 Bladed Double layered H – Rotor VAWT; Solidity 0.75 at  $\lambda=4.5$

Pressure Contours for the double layered H-rotor VAWT with solidity 0.75, 1.03 and 1.5 are shown in Fig. 6.41 to Fig. 6.43. Pressure contours at angle of rotation  $0^{\circ}$ ,  $60^{\circ}$ ,  $120^{\circ}$ ,  $180^{\circ}$ ,  $240^{\circ}$  and  $300^{\circ}$  are shown in these figures.

It is obvious from the pressure contours for double layered H – Rotor VAWT that, at  $\theta=60^{\circ}$  there is high pressure zone in front of the blades which causes a negative axial force and hence, a negative torque. At  $\theta=60^{\circ}$ , the pressure difference leads to a higher axial force of the turbine blade and at  $\theta=120^{\circ}$ , the pressure difference is still higher, however, it works on different part of the blade surface, which causes drop in axial force and hence, torque as well as torque coefficient. At  $\theta=180^{\circ}$ , this pressure difference is very small which leads to almost zero lift force but there is high pressure zone at the leading edge of the blade, which causes negative torque. When the blades come to  $\theta=240^{\circ}$  the pressure difference started to increase again, however, this time it gives a lift outward direction of the turbine considering the high pressure zone at the inner surface near leading edge of the turbine blade is still present. Hence, a small axial force causes a small positive torque as shown in the Fig. 6.26. A small pressure difference causing small axial force is still present when the position of the blades is at  $\theta=300^{\circ}$ .

It is clearly noticeable that, the pressure difference at the inner layer blade side is less than the outer layer blade side for all angular position. This causes the lower torque coefficient for inner layer blades as shown in Fig. 6.26 to Fig. 6.28.

From the  $C_t$  vs.  $\theta$  curve, we can see that the positive torque is generated by blades when they are in upstream half cycle. In the figure of contours, we can see similar outcome for the angle corresponding to  $\theta=60^{\circ}$  and  $\theta=120^{\circ}$ . We can also see, as we increase the

solidity, the high and low pressure zones experience more surface area of the turbine blade resulting the higher torque coefficient for higher solidity wind turbines.

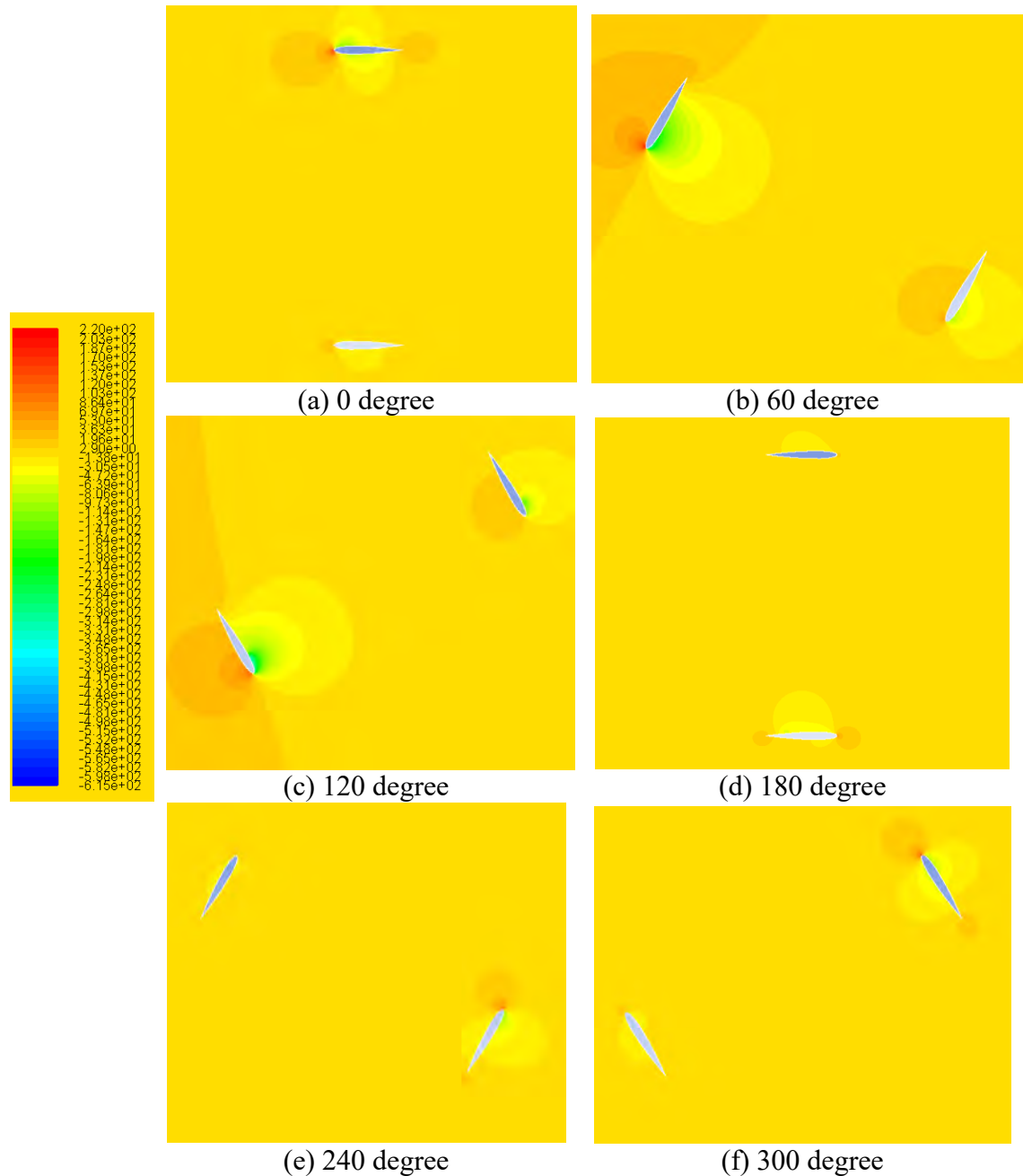


**Fig. 6.42:** Pressure contour of 6 Bladed double layered H – Rotor VAWT; Solidity 1.05 at  $\lambda=3.75$

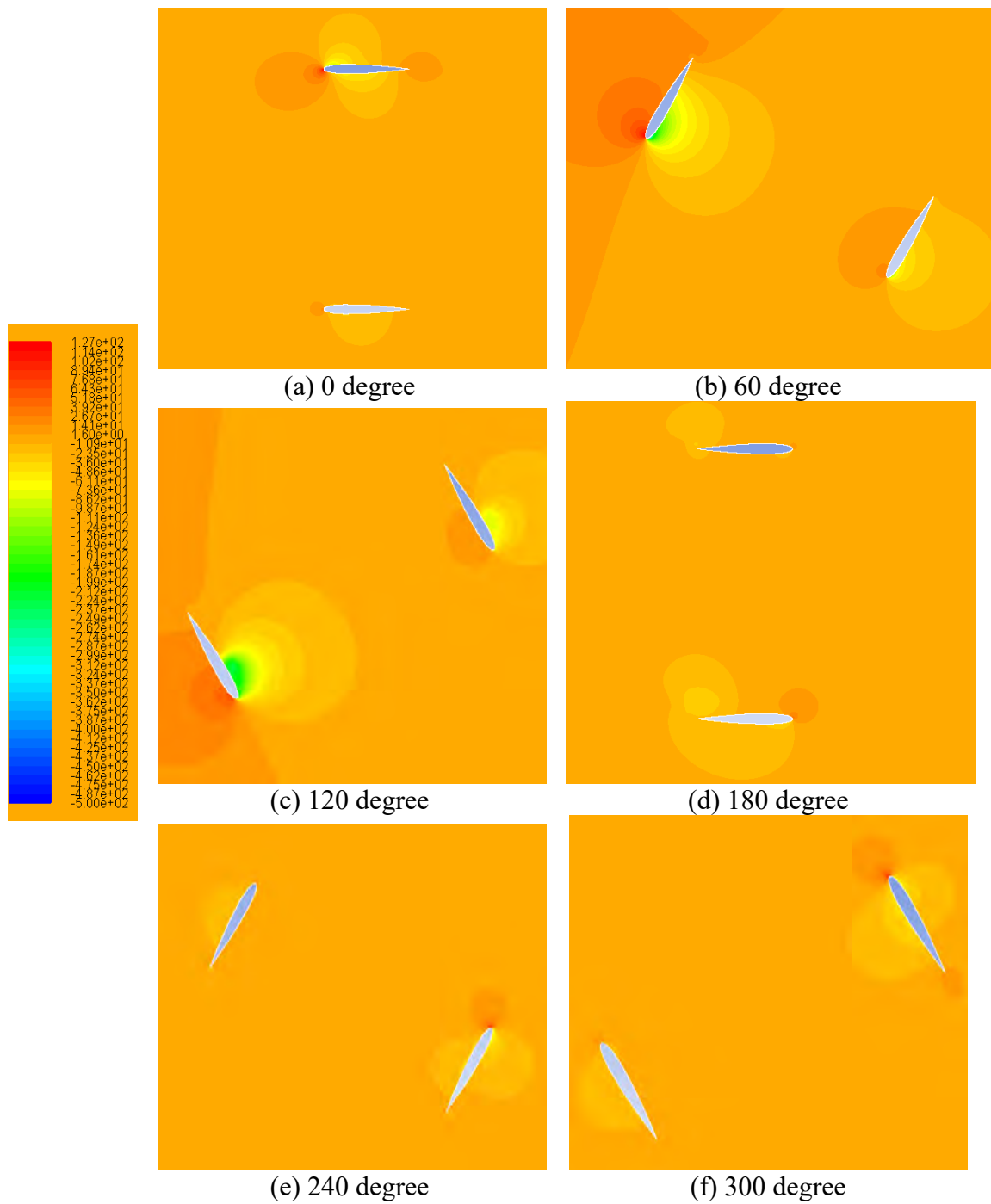


**Fig. 6.43:** Pressure contour of 6 Bladed double layered H – Rotor VAWT; Solidity 1.5 at  $\lambda=3$

For the double layered wind turbine, when the outer layer blades have low pressure zone on surface near to the center, the inner layer blades have the high pressure zone far from the center. That means the low pressure zone of outer layer blade and the high

pressure zone of inner blades are in between the two layers. Later, these two zones interact with each other and decrease the pressure difference on both outer and inner layer blade by decreasing the pressure of high pressure zone for inner layer blade and by increasing the pressure of low pressure zone for the outer layer blade. As a result the tangential force decreases and hence, the  $C_t$  of double layered H-rotor VAWT is lower than the  $C_t$  of single layered H-rotor VAWT.

### 6.3.7 Lift and Drag Coefficient

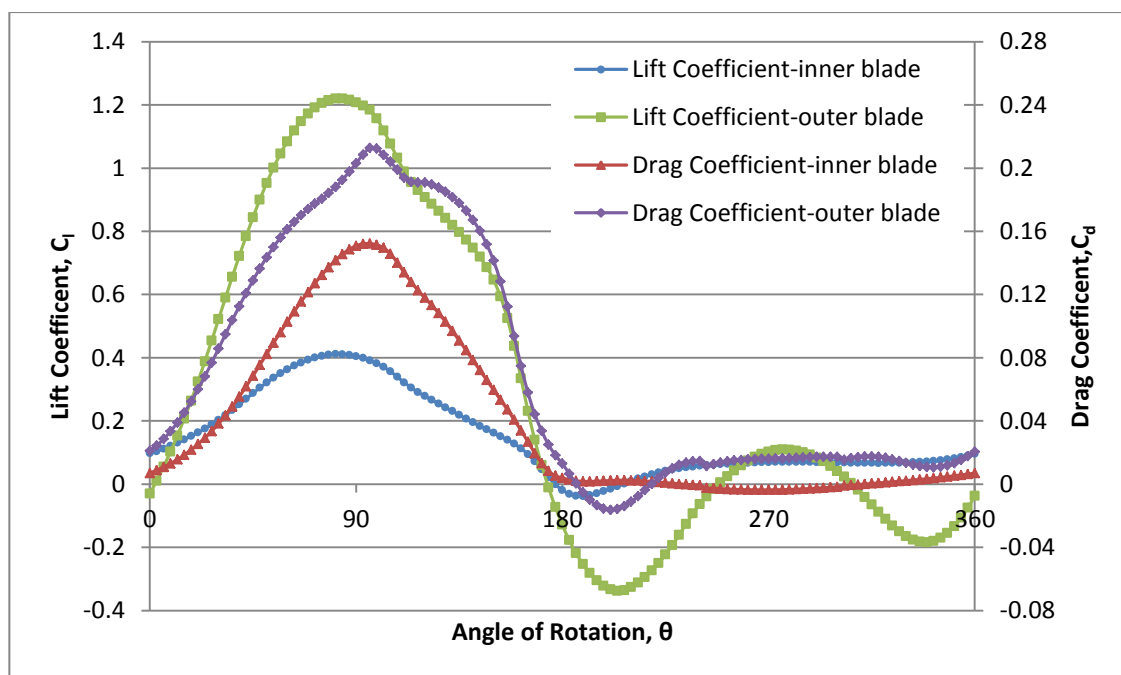


**Fig 6.44:**  $C_l$  and  $C_d$  vs.  $\theta$  for Double Layered (In-line) H-Darrieus VAWT; Solidity 1.5 at  $\lambda=3.0$

Lift coefficient ( $C_l$ ) and Drag coefficient ( $C_d$ ) for Double Layered H-Darrieus in-line VAWT with solidity 1.5 rotating at a tip speed ratio 3.0 are shown in Fig. 6.44.  $C_l$  and  $C_d$  for outer layer blades are higher than that of inner layer blades.

### 6.4 Comparison between single layered and double layered H-Darrieus VAWT

In Fig. 6.45, Fig. 6.46 and Fig. 6.47 are respectively showing the comparison of the  $C_t$  for  $(C_p)_{\max}$ , the  $\lambda$  for the  $(C_p)_{\max}$  and the  $(C_p)_{\max}$  with the change in solidity ( $\zeta$ ) for the

Single Layered H-Darrieus VAWT and the Double Layered H-Darrieus VAWT. The  $C_t$  for  $(C_p)_{\max}$  of single layered VAWT with solidity  $\zeta=1$  is 1.13 times higher than the  $C_t$  for  $(C_p)_{\max}$  of double layered H-rotor VAWT with solidity  $\zeta=1.05$ . However, the  $(C_p)_{\max}$  for double layered H-Darrieus VAWT is achieved at the tip speed ratio 66.67% higher than the tip speed ratio at which the single layered H-Darrieus achieves its  $(C_p)_{\max}$ . Hence, at unit solidity,  $(C_p)_{\max}$  for single layered VAWT is lower than  $(C_p)_{\max}$  for double layered VAWT.

The double layered 6 bladed VAWT achieves maximum  $C_p$  at a tip speed ratio higher than the tip speed ratio at which the single layered 3 bladed VAWT achieves its  $(C_p)_{\max}$  as shown in fig 6.46. The  $\lambda$  for  $(C_p)_{\max}$  for the Double Layered H-rotor VAWT with solidity 0.75 and 1.05 are respectively 60% and 66.67% higher than the  $\lambda$  for  $(C_p)_{\max}$  for Single Layered H-rotor VAWT with solidity 0.7 and 1.0.

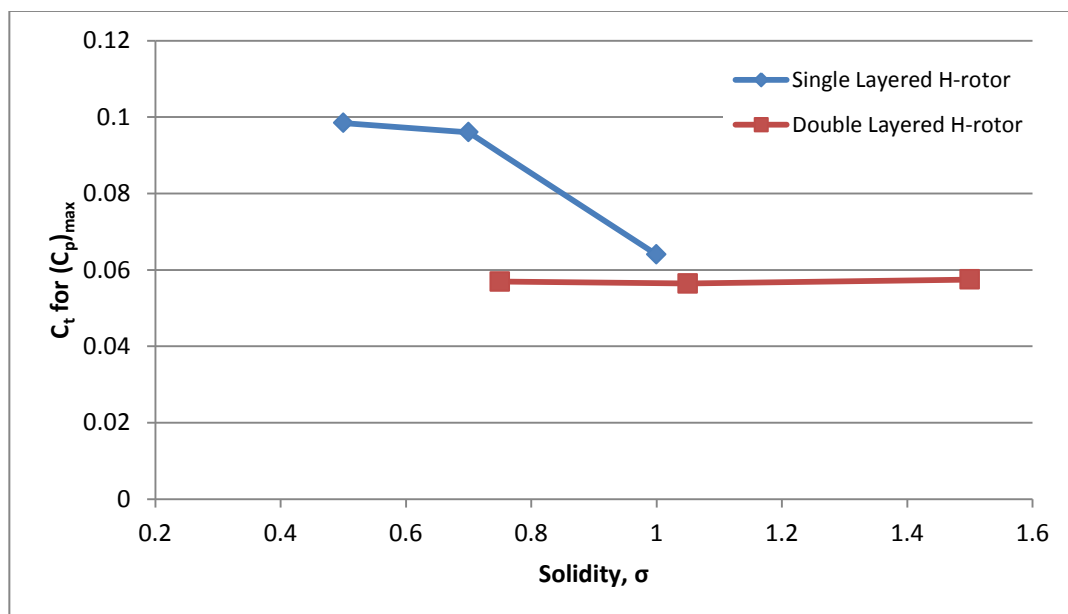


**Fig 6.45:** Comparison of  $C_t$  for  $(C_p)_{\max}$  with the change of solidity

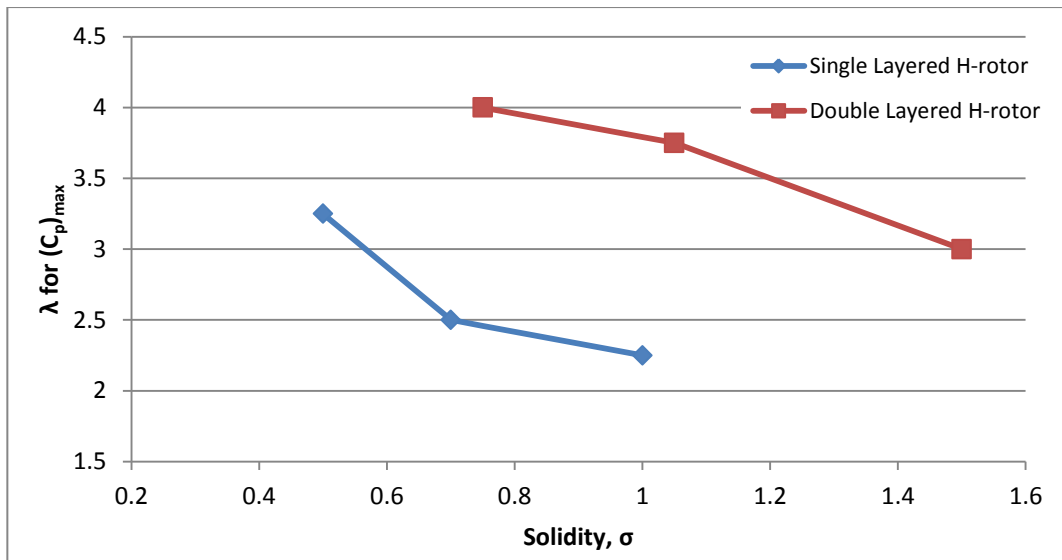


**Fig 6.46:** Comparison of  $\lambda$  for  $(C_p)_{max}$  with the change of solidity

The maximum power coefficient decreases with the increase in solidity. The comparison of  $(C_p)_{max}$  for single layer 3 bladed and double layered 6 bladed H-Darrieus type VAWT is shown in Fig. 6.47. With decrease in solidity, maximum  $C_p$  of single layer VAWT increases stiffly, while, the maximum  $C_p$  for double layer VAWT increases at a slower rate. Interestingly, the  $(C_p)_{max}$  for double layered 6 bladed VAWT with higher solidity is higher than the  $(C_p)_{max}$  for single layered 3 bladed VAWT.

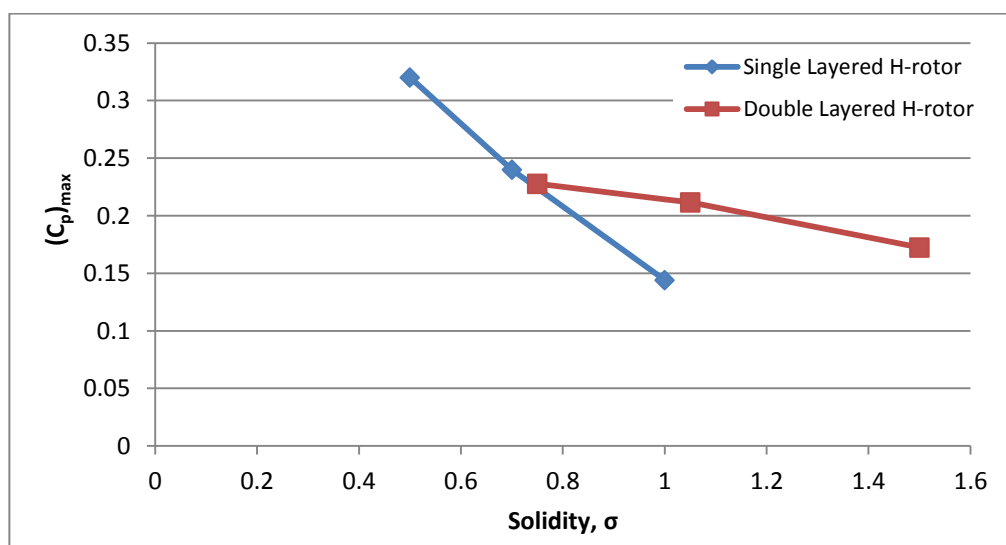


**Fig 6.47:** Comparison of  $(C_p)_{max}$  with the change of solidity



### 6.5 Performance of Double Layered H-Darrieus VAWT with Staggered Layers

The performance of a new model of Double layered Staggered H-Darrieus VAWT with solidity  $\zeta=1.5$  is investigated. For this model, the inner layer blades are  $60^\circ$  ahead of the outer layer blades. The comparisons of torque coefficient and power coefficient between the Double Layered (in-line) H-Darrieus VAWT and Double Layered (staggered) H-Darrieus VAWT are shown in the table 6.10.

**Table 6.10:**  $C_t$  and  $C_p$  of different types of Double Layered H-Darrieus VAWT with solidity,  $\sigma=1.5$

$\lambda$	Double Layered In-line VAWT		Double Layered Staggered VAWT	
	$C_t$	$C_p$	$C_t$	$C_p$
2.0	0.027375	0.05475	0.024782	0.049564
2.5	0.051936	0.12984	<b>0.058389</b>	0.145973
3	<b>0.057455</b>	<b>0.172365</b>	0.057518	<b>0.172554</b>
3.5	0.040728	0.142549	0.042975	0.150414
4	0.01756	0.070239	0.014249	0.056994

#### 6.5.1 Relationship between torque coefficient and tip speed ratio

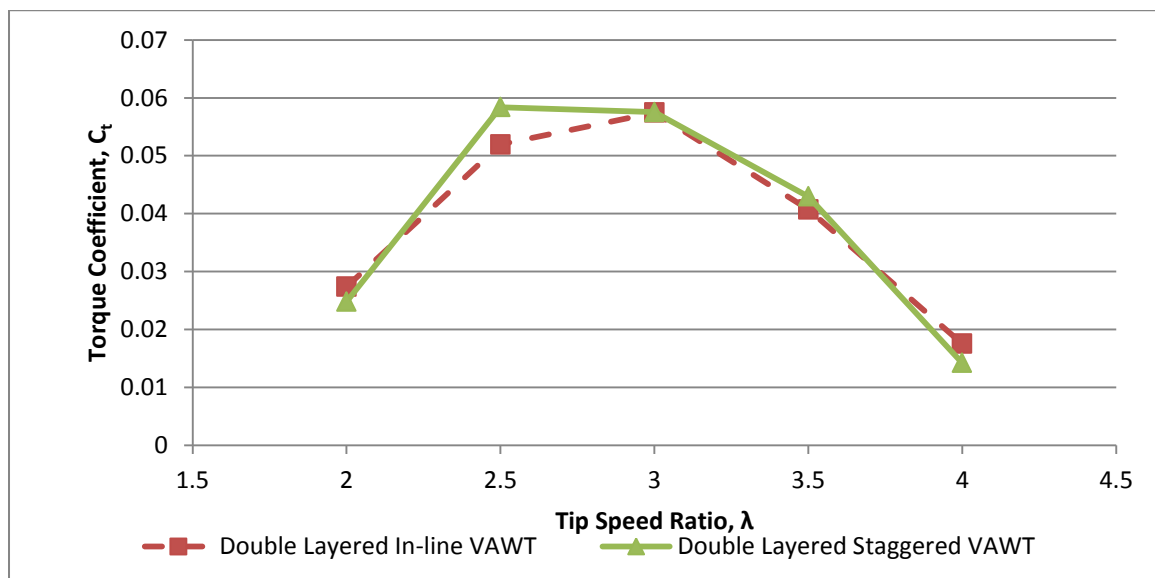


**Fig. 6.48:**  $C_t$  vs.  $\lambda$  for different H-Darrieus VAWT at  $\zeta=1.5$

From Fig. 6.48 we can see that, the torque coefficients of the Double Layered (Staggered) H-rotor are higher than the torque coefficients of Double Layered (in-line) H-rotor rotating at a tip speed ratio of 2.5, 3 and 3.5. For the  $\lambda=2$  and  $\lambda=4$ , the torque coefficients of the Double Layered (Staggered) H-rotor are lower than the torque coefficients of the Double Layered (in-line) H-rotor. The maximum torque coefficient of Double Layered (Staggered) H-rotor is achieved at  $\lambda=2.5$ , though the maximum torque coefficient of Double Layered (in-line) H-rotor is achieved at  $\lambda=3.0$ . The maximum torque coefficient of Double Layered (staggered) H-rotor is 1.016256 times of the value of maximum torque coefficient of Double Layered (in-line) H-rotor.

### 6.5.2 Relationship between power coefficient and tip speed ratio

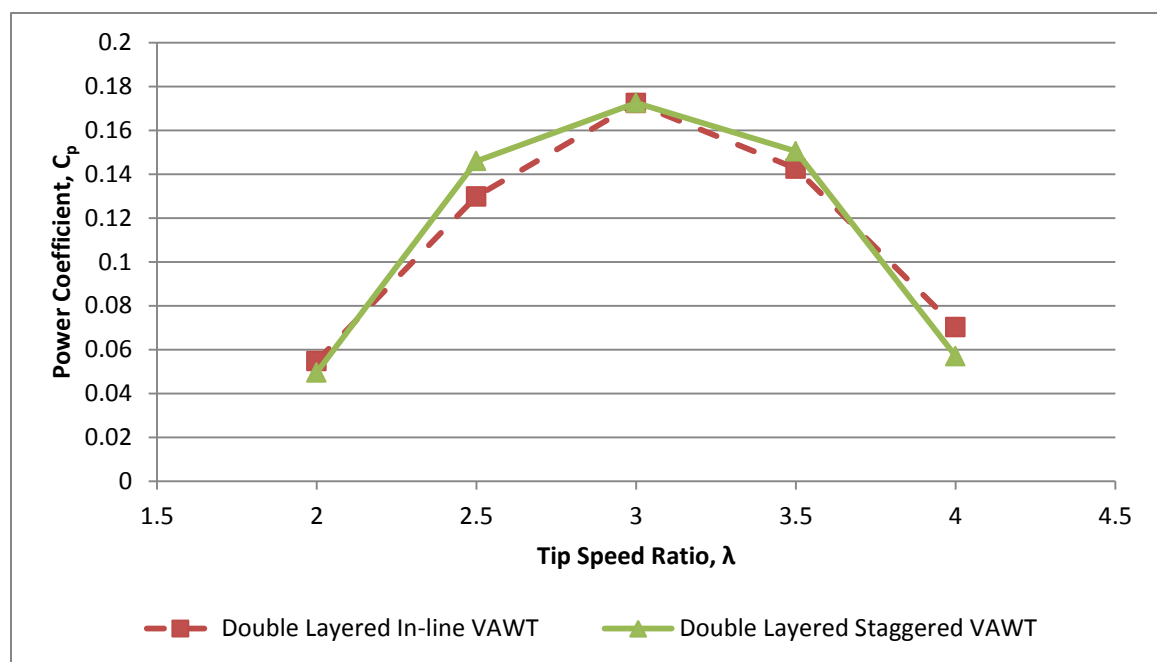


**Fig. 6.49:**  $C_p$  vs.  $\lambda$  for different H-Darrieus VAWT at  $\zeta=1.5$

For the double layered (staggered) H-rotor VAWT, the  $(C_p)_{\max} = 0.172554$  at the  $\lambda=3$ , at the  $\lambda=2.5$ , the  $C_p=0.145973$  and at the  $\lambda=3.5$ , the  $C_p=0.150414$ . So, near to the tip speed ratio, power coefficient changes very little and over a range of tip speed ratio (from  $\lambda=2.5$  to  $\lambda=3.5$ ), the power coefficient varies in between 0.145973 and 0.172554.

This difference is only 15.4% of maximum power coefficient and 2.66% of available power. Whereas, for the double layered (staggered) H-rotor VAWT, This difference of power coefficient is in between  $\lambda=2.5$  and  $\lambda=3.5$ , which is only 24.67% of the maximum power coefficient and 4.25% of the available power.

As shown in the Fig.6.48 and 6.49, the tip speed ratio remains same for extracting maximum power. Even the  $(C_p)_{\max}$  values of the both double layered VAWTs are almost same. The maximum torque coefficient is achieved at lower tip speed ratio for double layered staggered VAWT than the tip speed ratio for double layered in-line VAWT. The positive side of the double layered staggered VAWT is, its power coefficient does not change as rapidly as it changes for the double layered in-line VAWT. So, with the fluctuations of the tip speed ratios (i.e. rotational speed of turbine for a constant wind velocity) the power output is possible without any significant reduction in the power coefficient.

### 6.5.3. Contribution of inner and outer layer blades to the power coefficient

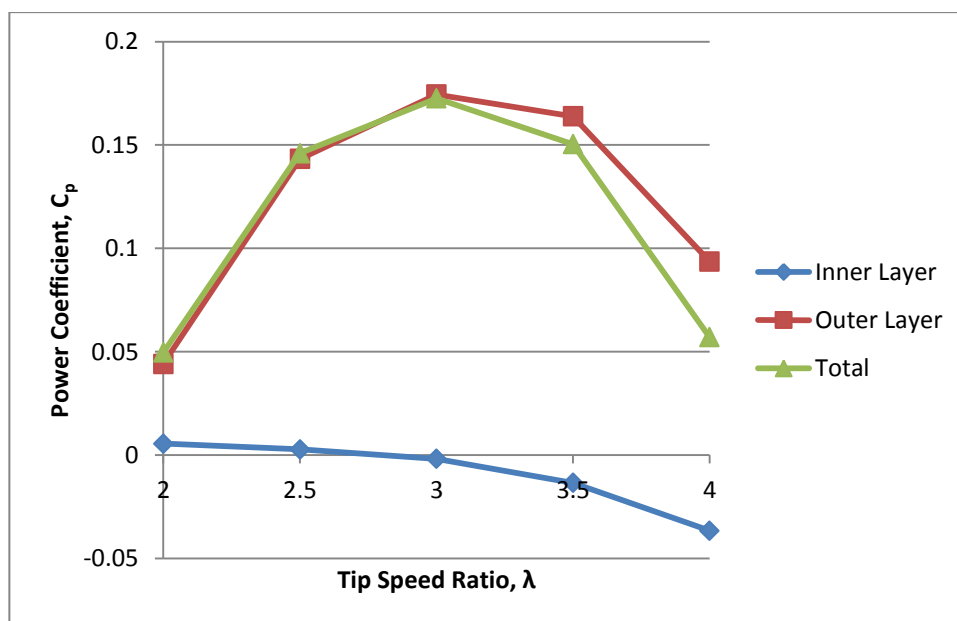


**Fig. 6.50:** Inner layer power coefficient, outer layer power coefficient and total power coefficient for Double Layered (staggered) VAWT with  $\zeta=1.5$

Fig. 6.39 shows the power coefficient of the inner layer, outer layer and total value. It is observed that, the power coefficient of the inner layer is higher at the lower tip speed ratio and the power coefficient of the outer layer increases with the tip speed ratio until  $\lambda=3$  and then again decreases. At the higher tip speed ratio, the inner layer consumes the power produced by the outer layer and hence the total power coefficient reduces.

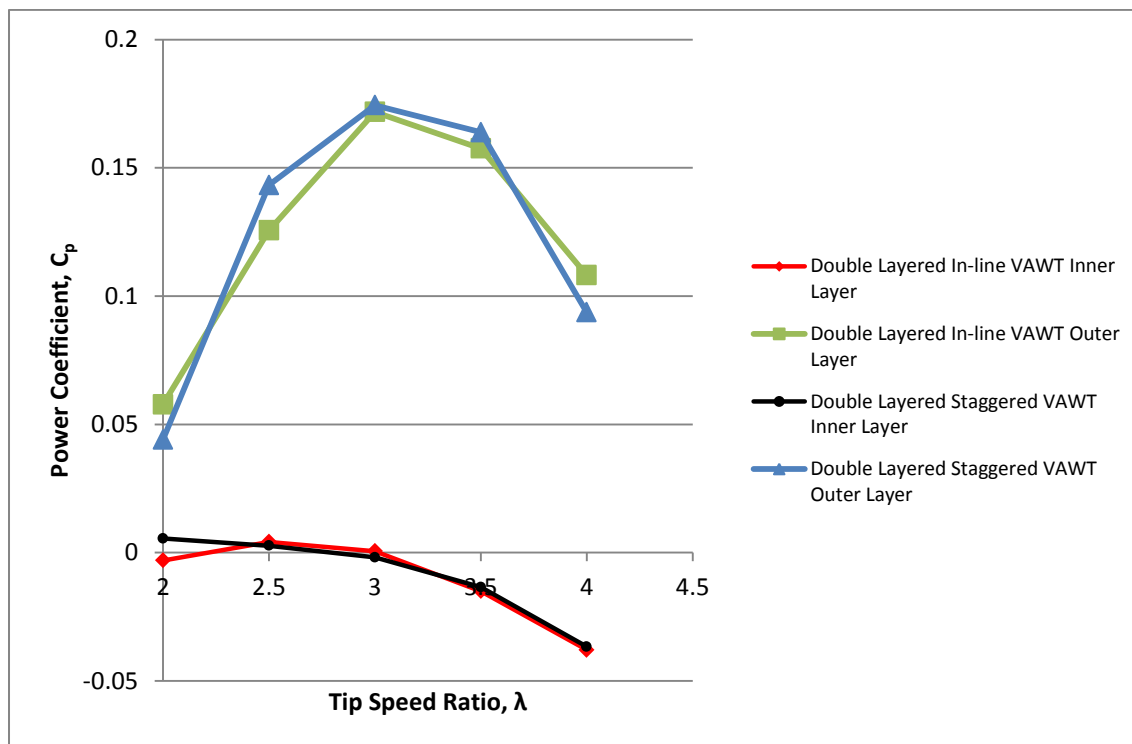


**Fig. 6.51:** Inner layer power coefficient and outer layer power coefficient for Double Layered VAWTs with  $\zeta=1.5$

Fig 6.51 shows the comparison of  $C_p$  of the inner and the outer layer of the Double Layered Staggered H-rotor and Double Layered in-line H-rotor VAWT. The power coefficient of the inner layer of Double Layered Staggered H-rotor is lower than the Double Layered in-line H-rotor VAWT at tip speed ratio above  $\lambda=2.5$ . Below  $\lambda=2.5$  the power coefficient of inner layer of Double Layered Staggered H-rotor is higher

comparatively. From  $\lambda=2.5$  to  $\lambda=3.5$ , the power coefficient of outer layer of Double Layered Staggered H-rotor VAWT is higher comparatively.

#### 6.5.4 Relationship between torque coefficient and angle of rotation

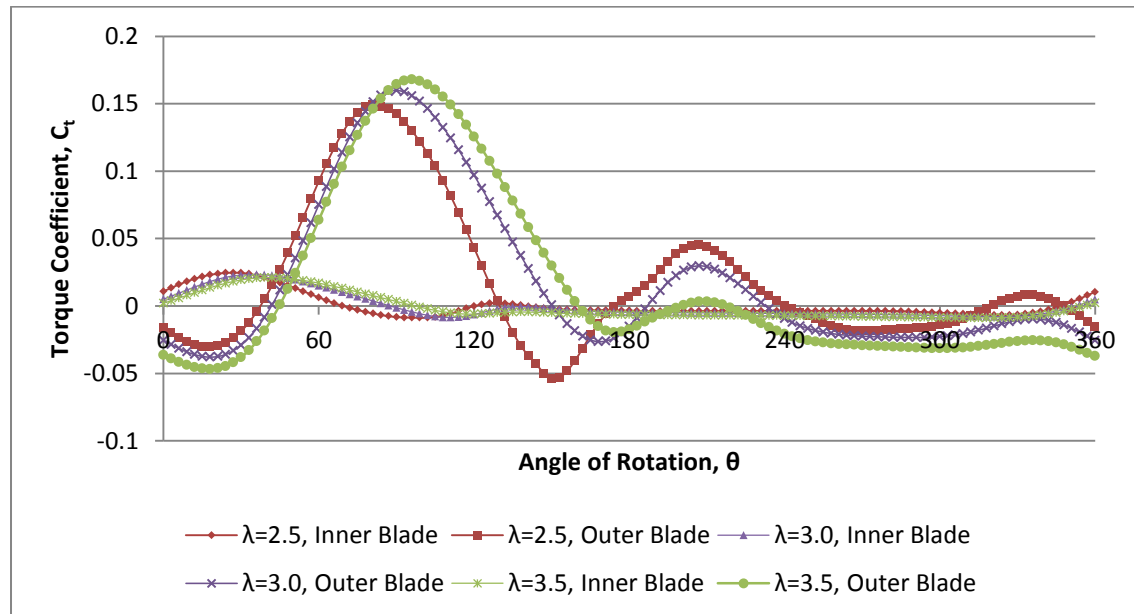


**Fig. 6.52:**  $C_t$  vs.  $\theta$  for Double layered (Staggered) H-Darrieus VAWT with  $\zeta=1.5$

From Fig. 6.52, it can be seen that, as the inner layer blade is  $60^\circ$  ahead of the outer layer blade, the inner layer can produce torque to rotate the outer layer when the angle of rotation is from  $0^\circ$  to  $45^\circ$ . Whereas, for double layered in-line VAWT, both inner and outer layer blades consume power at those angle of rotation. This decreases the fluctuation of torque generated by the wind turbine. At the same time, this positive  $C_t$  of inner layer blades of double layered staggered VAWT at angle of rotation is from  $0^\circ$  to  $45^\circ$  causes a raise to the average  $C_t$ . Though the average  $C_p$  of the inner layer blade of the double layered staggered VAWT is very low and even negative as like as the double layered in-line VAWT as shown in Fig. 6.39, the  $C_p$  of the outer layer blades of double layered staggered VAWT is higher than the  $C_p$  for the outer layer blades of double layered in-line VAWT at  $\lambda=2.5$  to  $\lambda=3.5$ . So, it can be said that, there is a passive

influence of inner layer blades to the power coefficient of the outer layer blades, which leads to a higher total maximum power coefficient of the machine.

### 6.5.5 Velocity Contour and Velocity Vectors

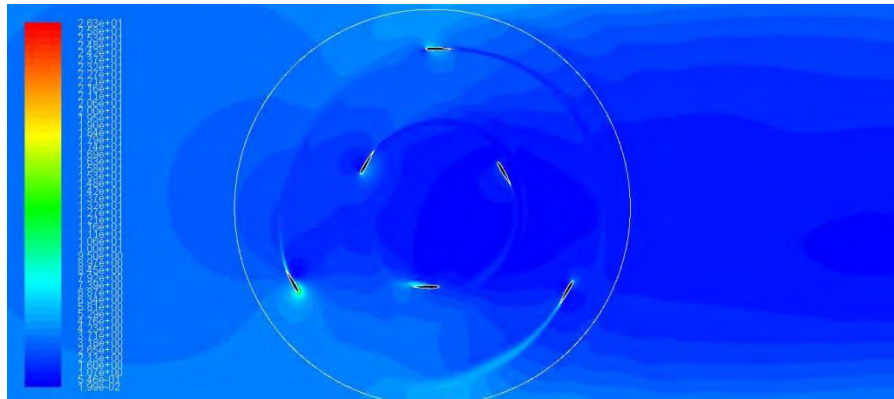


**Fig. 6.53:** Velocity contour of 6 Bladed Double layered H – Rotor VAWT; Solidity 1.0,  $\lambda=3.0(0 \text{ degree})$

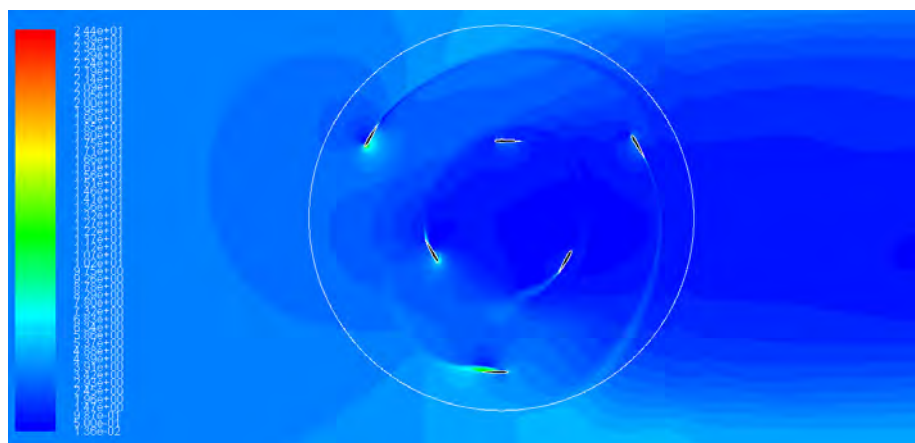


**Fig. 6.54:** Velocity contour of 6 Bladed Double layered H – Rotor VAWT; Solidity 1.0,  $\lambda=3.0(60 \text{ degree})$

The velocity contours depicted in the figures for Fig. 6.40 to Fig. 6.41 show the velocity contour around the Double Layered H-Darrieus VAWT. These show that, as the wind flows to downstream its velocity reduces. Hence the blades mostly generate power at upstream side. The velocity vectors around each blade are shown in Fig. 6.55 to Fig. 6.56.

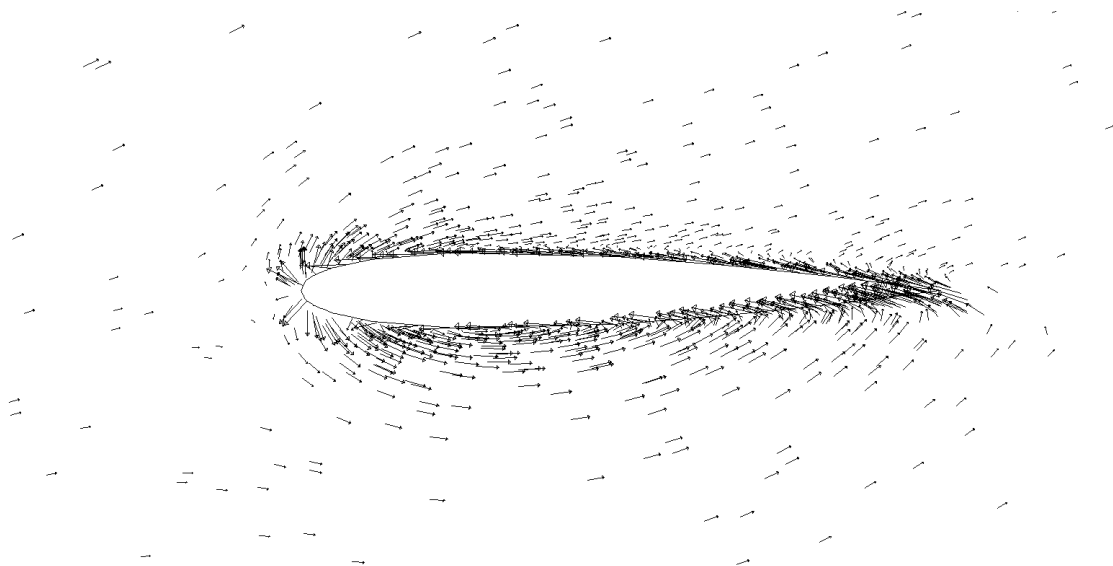


**Fig. 6.55(a):** Velocity vector of 6 Bladed Double layered Staggered H – Rotor VAWT;  
Solidity 1.5,  $\lambda=3.0$  (inner layer blades at 0 degree)

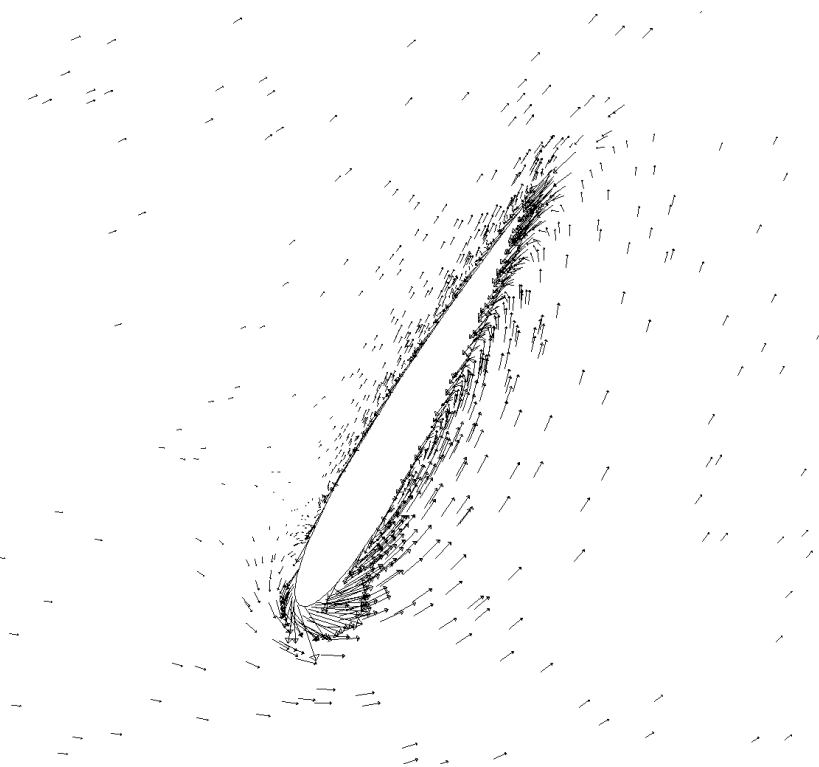


**Fig. 6.55(b):** Velocity vector of 6 Bladed Double layered Staggered H – Rotor VAWT;  
Solidity 1.5,  $\lambda=3.0$  (inner layer blades at 60 degree)

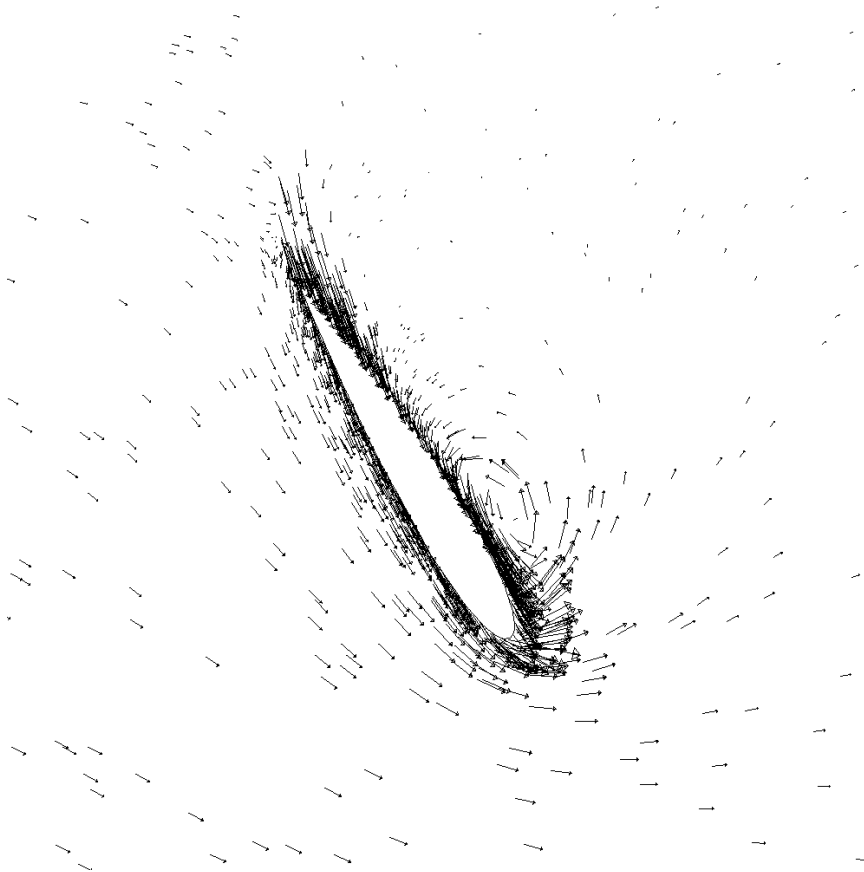


**Fig. 6.55(c):** Velocity vector of 6 Bladed Double layered Staggered H – Rotor VAWT;  
Solidity 1.5,  $\lambda=3.0$  (inner layer blades at 120 degree)

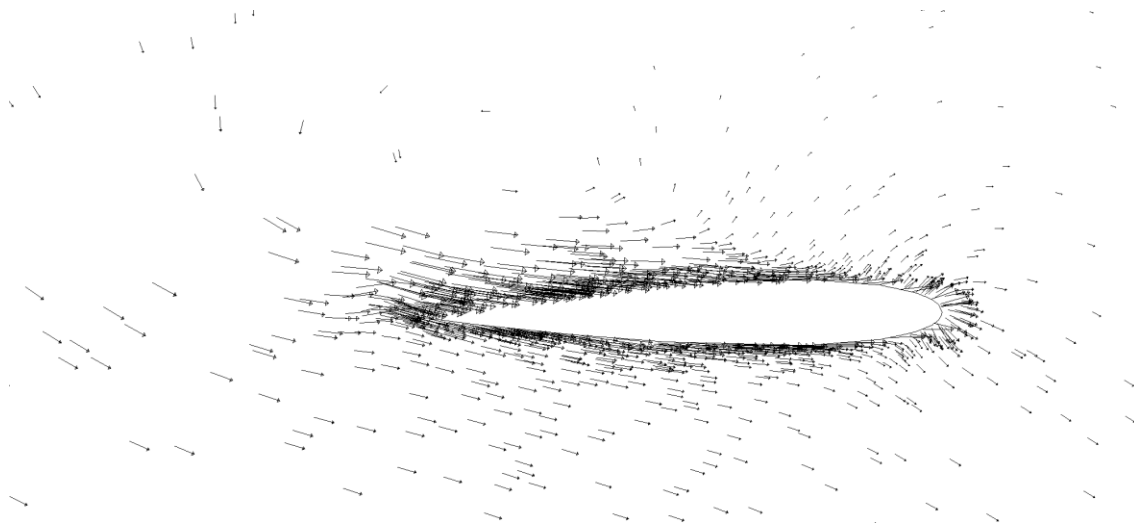


**Fig. 6.55(d):** Velocity vector of 6 Bladed Double layered Staggered H – Rotor VAWT;  
Solidity 1.5,  $\lambda=3.0$  (inner layer blades at 180 degree)





**Fig. 6.55(e):** Velocity vector of 6 Bladed Double layered Staggered H – Rotor VAWT;  
Solidity 1.5,  $\lambda=3.0$  (inner layer blades at 240 degree)



**Fig. 6.55(f):** Velocity vector of 6 Bladed Double layered Staggered H – Rotor VAWT;  
Solidity 1.5,  $\lambda=3.0$  (inner layer blades at 300 degree)

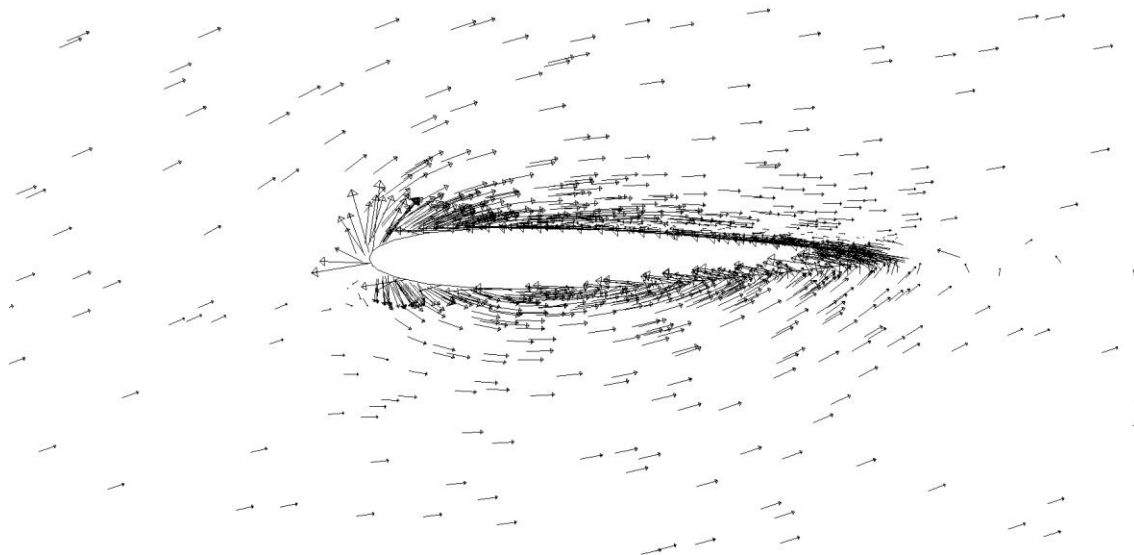


**Fig. 6.56(a):** Velocity vector of 6 Bladed Double layered Staggered H – Rotor VAWT; Solidity 1.5,  $\lambda=3.0$  (outer layer blades at 0 degree)

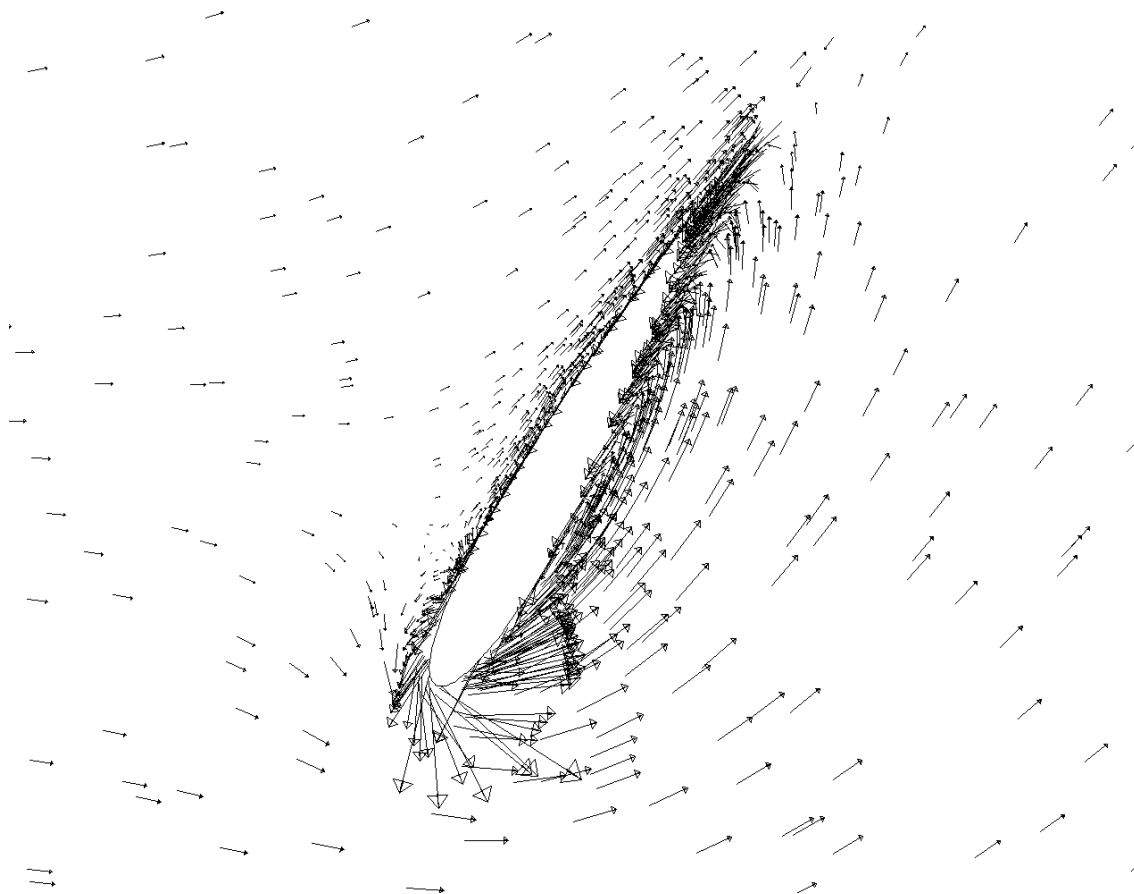


**Fig. 6.56(b):** Velocity vector of 6 Bladed Double layered Staggered H – Rotor VAWT; Solidity 1.5,  $\lambda=3.0$  (outer layer blades at 60 degree)

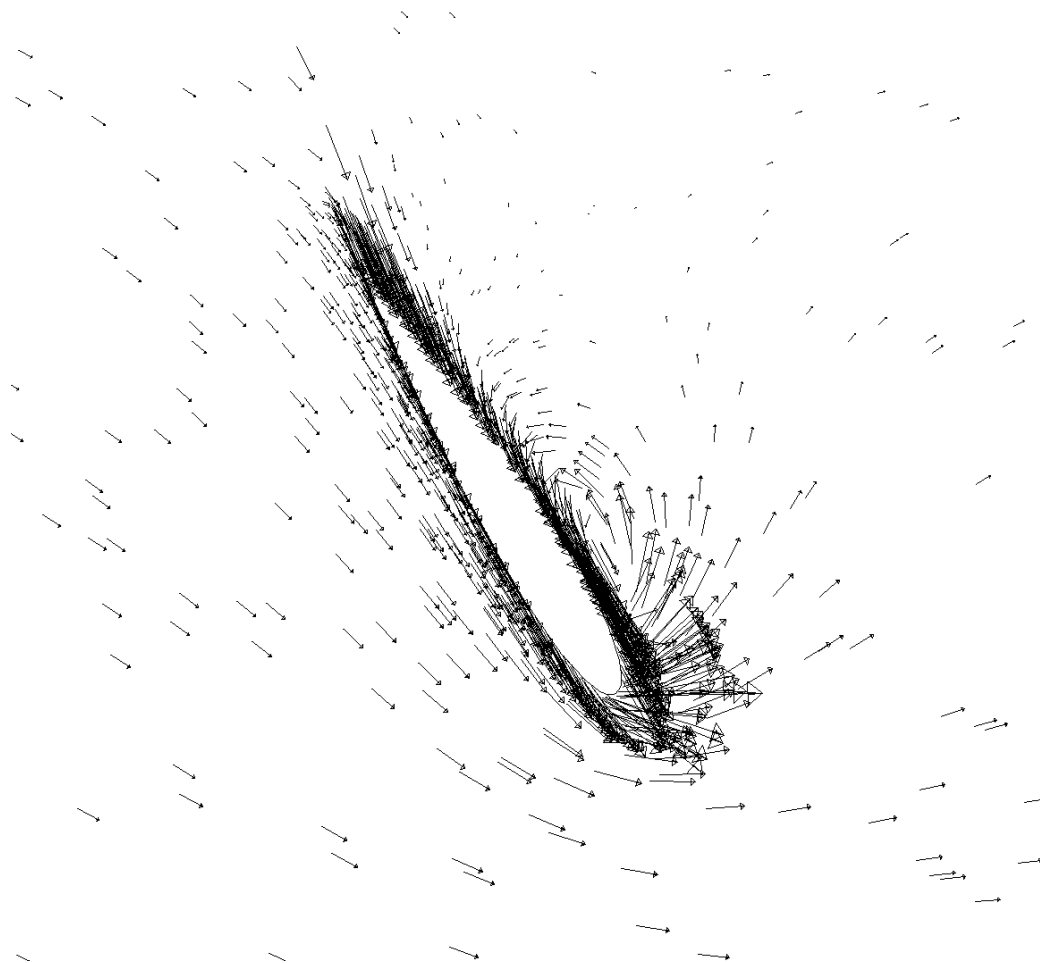


**Fig. 6.56(c):** Velocity vector of 6 Bladed Double layered Staggered H – Rotor VAWT;  
Solidity 1.5,  $\lambda=3.0$  (outer layer blades at 120 degree)

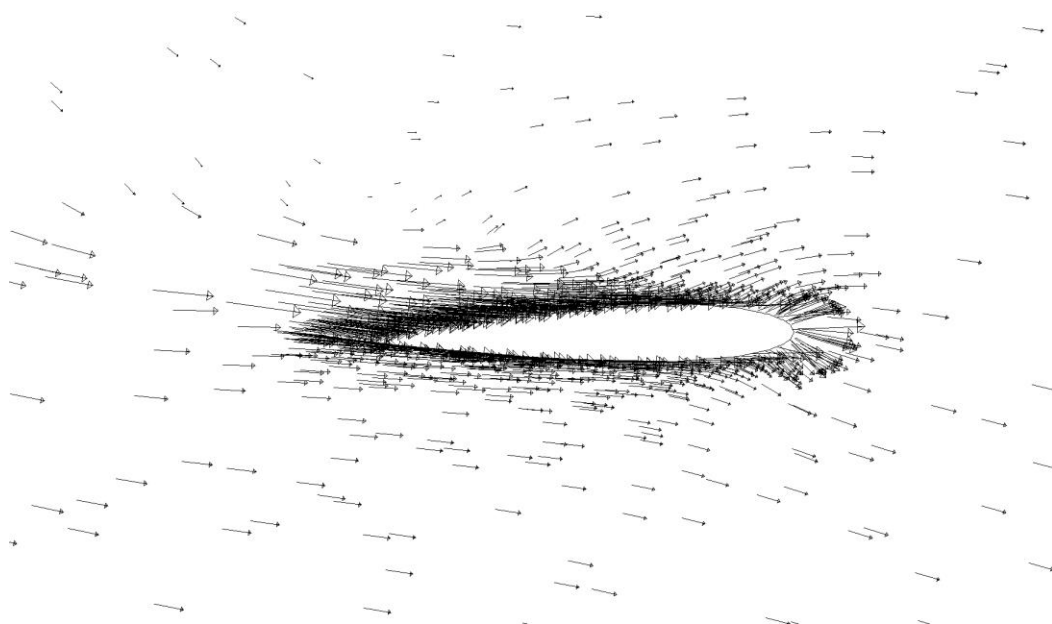


**Fig. 6.56(d):** Velocity vector of 6 Bladed Double layered Staggered H – Rotor VAWT;  
Solidity 1.5,  $\lambda=3.0$  (outer layer blades at 180 degree)

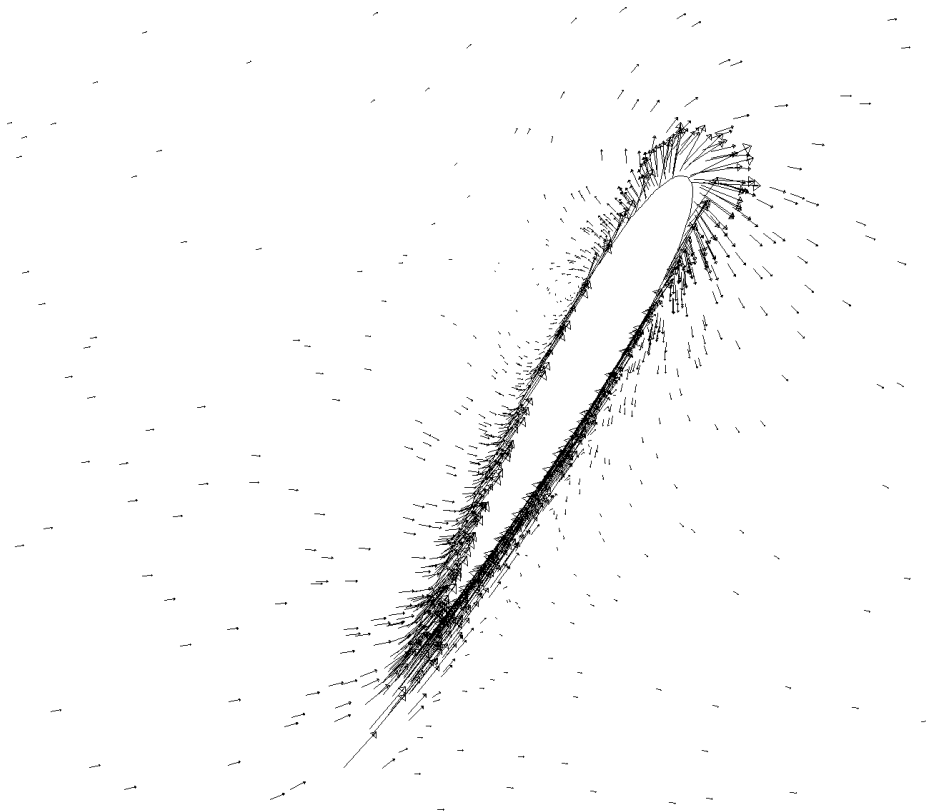


**Fig. 6.56(e):** Velocity vector of 6 Bladed Double layered Staggered H – Rotor VAWT;  
Solidity 1.0,  $\lambda=3.0$  (outer layer blades at 240 degree)

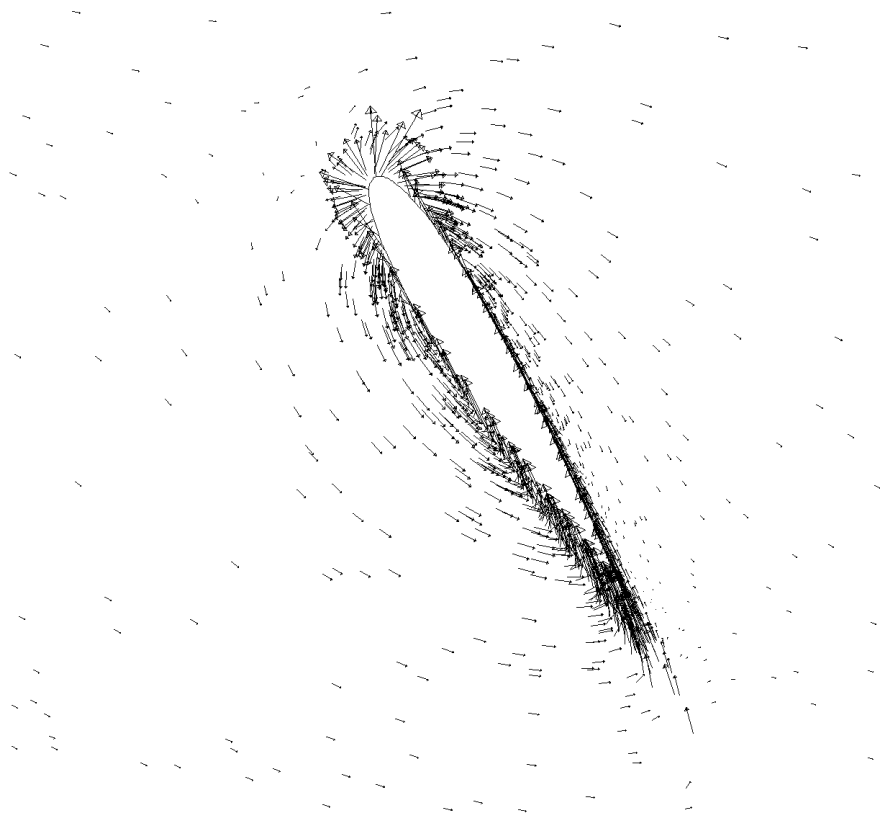


**Fig. 6.56(f):** Velocity vector of 6 Bladed Double layered Staggered H – Rotor VAWT;  
Solidity 1.5,  $\lambda=3.0$  (outer layer blades at 300 degree)

### 6.5.6 Pressure Contour

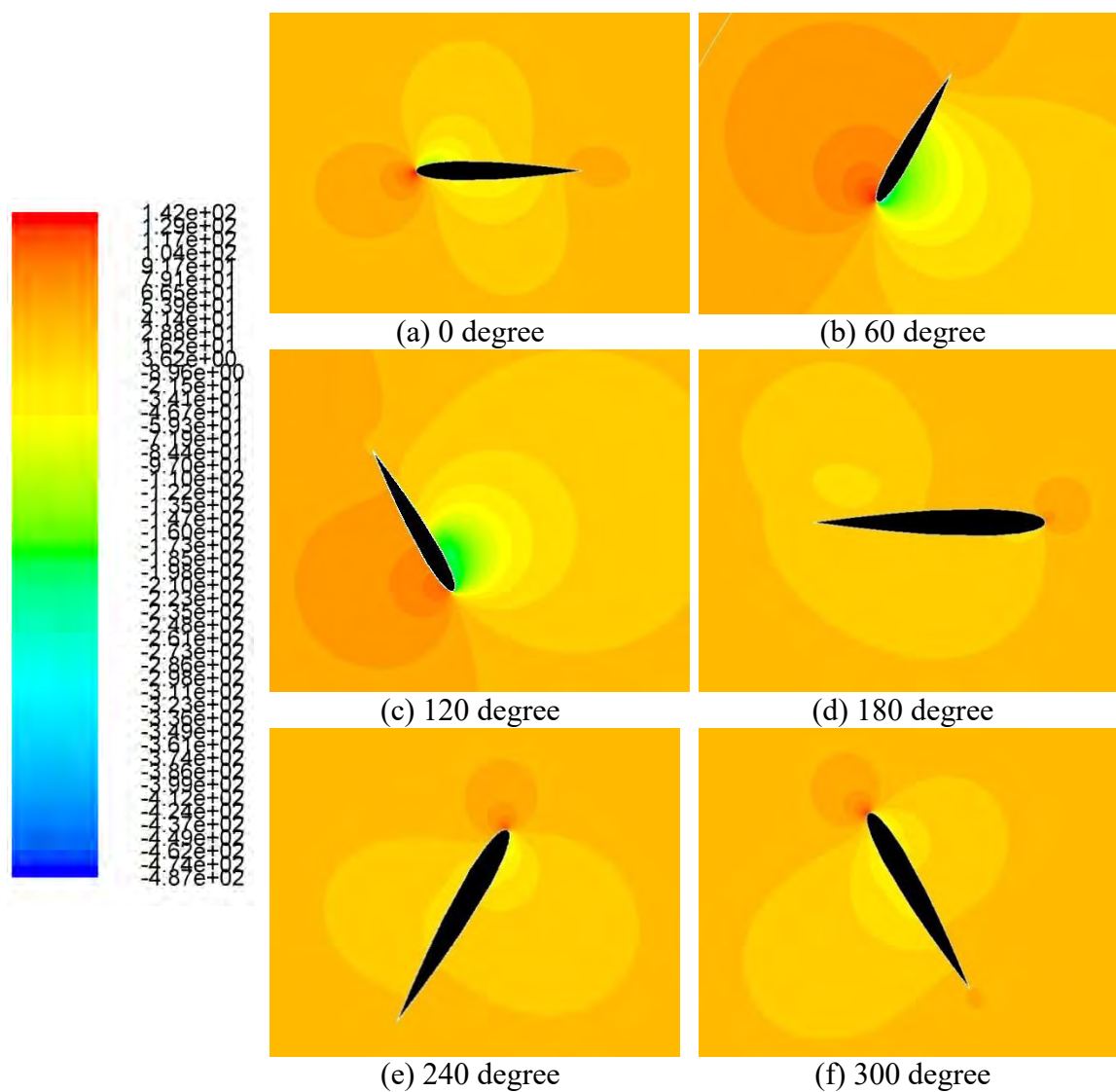


**Fig 6.57:** Pressure contour of outer layer blades of Double layered staggered H – Rotor VAWT; Solidity 1.5 at  $\lambda=3.0$

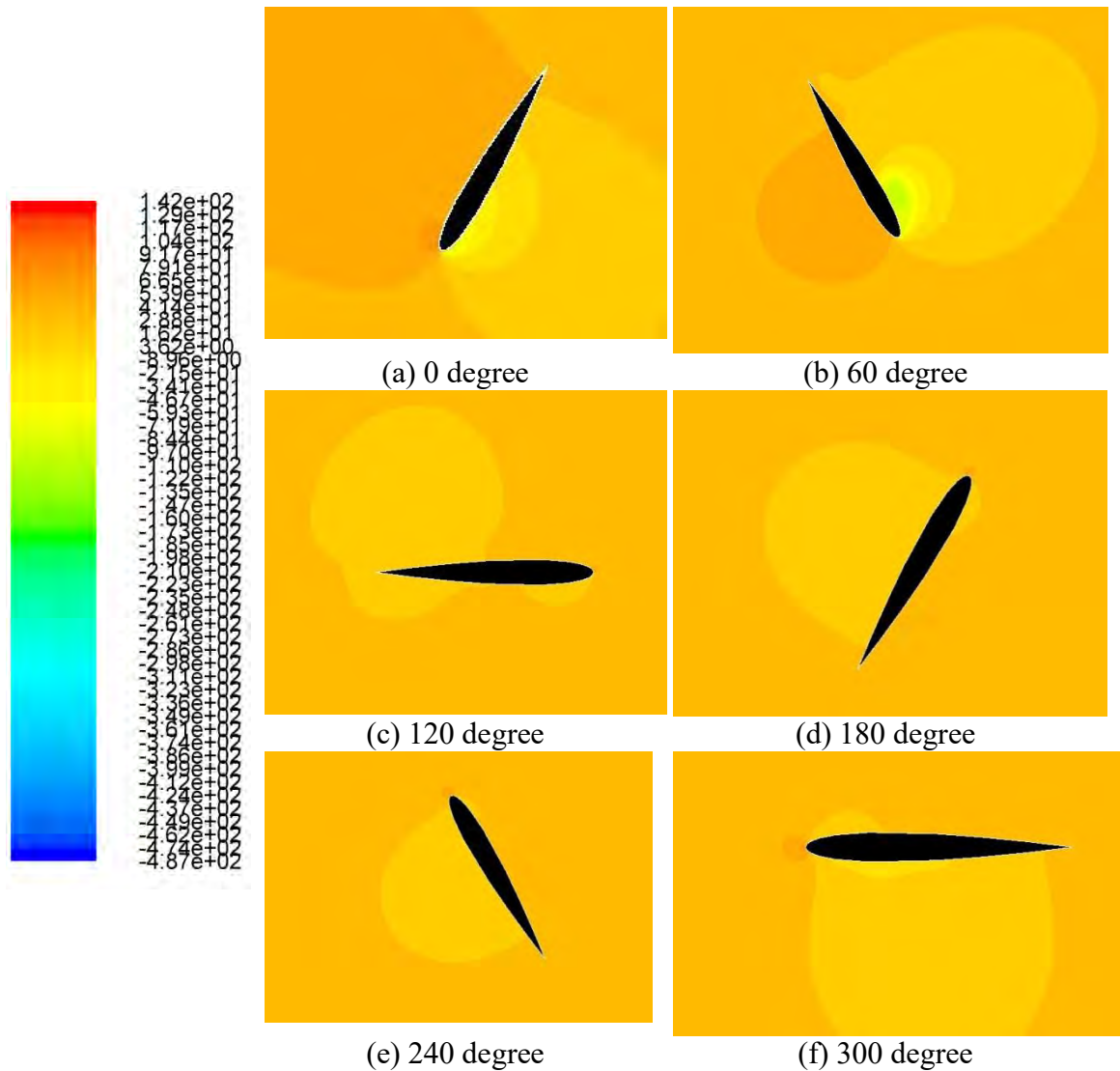


**Fig 6.58:** Pressure contour of outer layer blades of Double layered staggered H – Rotor VAWT; Solidity 1.5 at  $\lambda=3.0$

The Pressure contours of the double layered staggered VAWT with  $\zeta=1.5$  at  $\lambda=3.0$  is shown in figures from Fig. 6.57 to Fig. 6.58. This is similar as the pressure contour of double layered in-line VAWT with  $\zeta=1.5$  at  $\lambda=3.0$ . Low pressure zone is visible in front of the blades when those are at angular position  $\theta=60^\circ$  and  $\theta=120^\circ$ . At other angular positions shown in Fig. 6.57 and Fig. 6.58, a high pressure zone is visible in front of the blade, which oppose the blade rotation and consumes torque to rotate. This is graphically shown in sub-article 6.5.4. Pressure difference on the surface of the outer layer blades is higher than the pressure difference on the surface of the inner layer

blades as shown in these figures. For that reason, the power coefficient of the inner layer is lower than the power coefficient of the outer layer as shown in sub-article 6.5.4.

### 6.5.7 Lift and Drag Coefficient

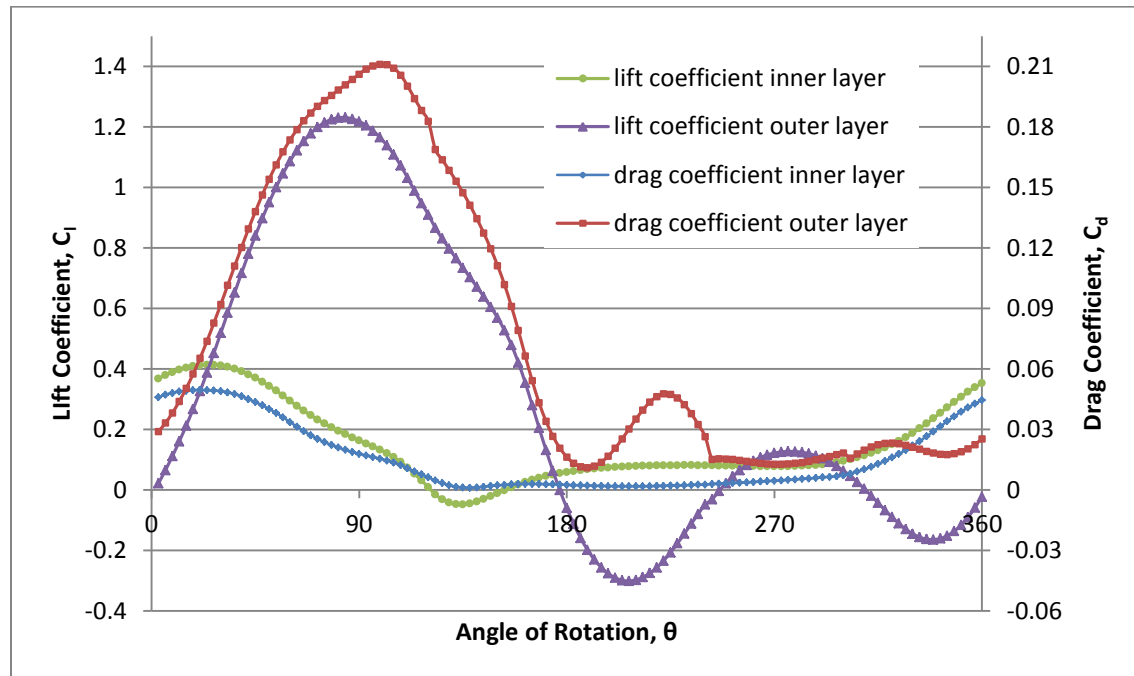


**Fig 6.59:**  $C_l$  and  $C_d$  vs.  $\theta$  for Double layered (Staggered) H-Darrieus VAWT; Solidity 1.5 at  $\lambda=3.0$

Lift coefficient ( $C_l$ ) and Drag coefficient ( $C_d$ ) for Double Layered H-Darrieus Staggered VAWT with solidity 1.5 rotating at a tip speed ratio 3.0 are shown in Fig. 6.59.  $C_l$  and  $C_d$  for outer layer blades are higher than that of inner layer blades. Outer layer blades are showing similar  $C_l$  curve as the Double Layered in-line H-rotor. Peak value of  $C_d$  of inner layer blade of Double layered staggered H-rotor is lower than the peak value of  $C_d$  of inner layer blade Double layered in-line H-rotor.

CHAPTER: 7

# CONCLUSION



## 7.1 Conclusion

The performance of the novel concept of the six bladed double layered H-Darrieus vertical axis wind turbine (VAWT) is numerically investigated in this thesis and can be concluded as:

1. The maximum power coefficient of both single layered H-Darrieus VAWT and double layered H-Darrieus VAWT increases with decrease in solidity. The rate of increase in power coefficient for Double layered H-Darrieus VAWT is lower than the rate of increase for single layered H-Darrieus VAWT. Double layered H-rotor VAWT can achieve higher maximum power coefficient than single layered H-rotor VAWT at higher solidity VAWT. Besides, from the rates of change in power coefficient it is found that, at lower solidities (i.e.  $\zeta=0.5$  and  $\zeta=0.7$ ) the maximum power coefficient of single layered H-rotor VAWT is higher.
2. The maximum torque generated by the single layered vertical axis wind turbine increases sharply with decrease in solidity.
3. The maximum torque coefficient for double layered H-Darrieus VAWT remains almost unchanged with the decrease in solidity.
4. The tip speed ratio ( $\lambda$ ) for  $(C_p)_{\max}$  of double layered H-rotor VAWT is higher than the  $\lambda$  for  $(C_p)_{\max}$  of single layered H-rotor VAWT.
5. In case of double layered VAWT, each blade generates positive torque at the downstream side of the wind turbine, whereas each blade of single layered H-rotor VAWT consumes torque at the downstream side. Though the inner layer blades of Double Layered H-rotor do not generate high torque as like as the outer layer blades, it helps the outer layer blades to generate positive torque at the downstream side.

6. The maximum power coefficient of Double Layered Staggered H-Darrieus VAWT is almost equal to the maximum power coefficient of the Double Layered in-line H-Darrieus VAWT. However, when the tip speed ratio is either increased or decreased from the  $\lambda$  for  $(C_p)_{\max}$ , the power coefficient of Double Layered Staggered H-Darrieus VAWT initially decreases at a slower rate than the Double Layered in-line H-Darrieus VAWT up to a certain change in tip speed ratio. Hence, it can be concluded that, the Double Layered Staggered H-Darrieus VAWT is capable of generating stable power coefficient over a range of tip speed ratio.

This work shows the way to the future researchers to invent a wind turbine of higher efficiency.

**RECOMMENDATIONS:**

Future researchers may alter the followings to invent a better H-Darrieus vertical axis wind turbine.

1. Ratio of Blade chord length to blade spacing.
2. Angular position of the inner layer blades and outer layer blades
3. Consider pitching of inner layer and outer layer blades.
4. Blade with different chord length for different layer.

Further researches on this novel double layered concept will improve its performance and it will be able to generate power with higher power coefficient.

## REFERENCES

- [1] Manwell, J.F., McGowan, J.G. and Rogers, A.L., *Wind Energy Explained*, John Wiley & Sons Ltd., UK, 2009.
- [2] Mandal, A.C., Islam, M.Q., *Aerodynamics and Design of Wind Turbine*, chap.8, pp. 153-256, BUET, Dhaka, 2001.
- [3] Templin, R.J., “Aerodynamic Performance Theory for the NRC Vertical-Axis wind Turbine”, National Resource Council of Canada, report LTRA-LA-160, June 1974.
- [4] Wilson, R.E. and Lissaman, P.B.S., “Applied Aerodynamics of Wind Power Machines”, Oregon State University, Corvallis, Oregon 9731, USA, May 1974.
- [5] Strickland, J.H., “The Darrieus Turbine: A performance Prediction Model Using Multiple Streamtubes”, Sandia Laboratories Report, SAND75-0431, October 1975.
- [6] Paraschivoiu, I., “Double Multiple Streamtube Model for Darrieus Wind Turbine”, Proceedings of second DOE/NASA Wind Turbine Dynamics Workshop, Cleveland, February 24-26, 1981, pp. 18-24.
- [7] Mandal, A.C. and Islam, M.Q., “Flow Curvature Effect on Darrieus Wind Turbine with Blade Pitching”, RERIC International Energy Journal, Vol. 10, No. 2, 61-73, December 1988.
- [8] Gosselin, R., Dumas, G. and Boudreau, M., “Parametric Study of H-Darrieus Vertical–Axis Turbines Using uRANS Simulation”, 21st Annual Conference of the CFD Society of Canada, Sherbrooke, Quebec, 2013, pp. 1-16.
- [9] Beri, H. and Yao, Y., “Double Multiple Stream Tube Model and Numerical Analysis of Vertical Axis Wind Turbine”, Energy and Power Engineering, Vol. 3, pp. 262-270, 2011.
- [10] Conaill E. Soraghan, William E. Leithead, Hong Yue and Julian Feuchtwang, “Double Multiple Streamtube Model for Variable Pitch Vertical Axis Wind Turbines”, American Institute of Aeronautics and Astronautics
- [11] Lanzafame, R., Mauro, S. and Messina, M., “2D CFD Modeling of H-Darrieus Wind Turbines using a Transition Turbulence Model”, Energy Procedia, 45, pp. 131 – 140, 2014.
- [12] Mălăeș, I. and Dumitrescu, H., “Numerical Simulation of VAWT Flow Using Fluent”, U.P.B. Sci. Bull., Series D, Vol. 76, Iss. 1, 2014.

- [13] Mălăeșel, I., Dumitrescu, H. and Cardos, V., “Numerical Simulation of Vertical Axis Wind Turbine at Low Speed Ratios”, *Global Journal of Researches in Engineering: I Numerical Methods*, Vol. 14, Iss. 1 pp. 9-20, 2014.
- [14] Migliore, P.G. and Fritschen, J.R., “Darrieus Wind Turbine Airfoil Configurations”, Solar Energy Research Institute, Golden, Colorado, USA, No. SERI/TR-11045-1, 1982.
- [15] Danao, L.A., Qin, N. and Howell, R., “A Numerical Study of Blade Thickness and Camber Effects on vertical Axis Wind Turbines”, *Journal of Power and Energy*, 226(7), 867-881, 2012.
- [16] Chen, Y. and Lian, Y., “Numerical Investigation of vortex Dynamics in an H-rotor Vertical Axis Wind Turbine”, *Engineering Application of Computational Fluid Mechanics*, 2015.
- [17] Mohamed, M.H., “Performance investigation of H-rotor Darrieus turbine with new airfoil shapes”, *Energy*, 47, 522-530, 2012.
- [18] Mohamed, M.H., Ali, A.M. and Hafiz, A .A., “CFD analysis for H-rotor Darrieus turbine as a low speed wind energy converter, *Engineering Science and Technology*”, an International Journal, 18, 1-13, 2015.
- [19] Abu-El-Yazied, T.G., Ali, A.M., Al-Ajmi, M.S., Hassan, I.S., “Effect of Number of Blades and Blade Chord Length on the Performance of Darrieus Wind Turbine”, *American Journal of Mechanical Engineering and Automation*, 2(1), 16-25, 2015.
- [20] Dominy, R., Lunt, P., Bickerdyke, A. and Dominy, J., “Self- starting capability of a Darrieus turbine”, *Proceedings of the I MECH E part A : journal of power and energy*, 221 (1). pp. 111-120, 2007.
- [21] Li, S. and Li, Y., “Numerical Study on Performance Effect of Solidity on the Straight-bladed Vertical Axis Wind Turbine”, *IEEE*, 2010.
- [22] Castelli, M.R., Betta, S.D. and Benini, E., “Effect of Blade Number on a straight-Bladed Vertical-Axis Darrieus Wind Turbine”, *World Academy of Science, Engineering and Technology*, vol. 6, 2012-01-20.
- [23] Amet, E., Maître, T., Pellone, C. and Achard, J.L., “2D Numerical Simulations of Blade-Vortex Interaction in a Darrieus Turbine”, *Journal of Fluids Engineering*, Vol. 131, pp. 111103-1 ~ 111103-15, November 2009.
- [24] [[https://en.wikipedia.org/wiki/Blade\\_element\\_theory](https://en.wikipedia.org/wiki/Blade_element_theory)].
- [25] Versteeg, H. K. and Malalasekera, W., *An Introduction to Computational Fluid Dynamics*, Pearson Education Limited, England, 2007.

- [26] Harlow, F. H. and Welch, J. E., "Numerical Calculation of Time-dependent Viscous Incompressible Flow of Fluid with Free Surface", *Phys. Fluids*, Vol. 8, pp. 2182–2189, 1965.
- [27] ANSYS FLUENT Theory Guide, ANSYS Inc., November 2011, USA.
- [28] Rhie, C. M. and Chow, W. L., "Numerical Study of the Turbulent Flow Past an Airfoil with Trailing Edge Separation", *AIAA Journal*. 21(11). 1525–1532. November 1983.
- [29] Ragheb, M., "Optimal Rotor Tip Speed Ratio", Lecture notes of Course no. NPRE 475, Department of Nuclear, Plasma and Radiological Engineering, University of Illinois at Urbana-Champaign, USA.